Physik-Department

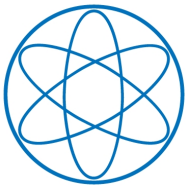

Central Production of Two-Pseudoscalar Meson Systems at the COMPASS Experiment at CERN

Dissertation von Alexander Austregesilo

Technische Universität
München

TECHNISCHE UNIVERSITÄT MÜNCHEN
Physik-Department E18

Central Production of Two-Pseudoscalar Meson Systems at the COMPASS Experiment at CERN

Alexander Austregesilo

Vollständiger Abdruck der von der Fakultät für Physik der Technischen Universität München zur Erlangung des akademischen Grades eines

Doktors der Naturwissenschaften

genehmigten Dissertation.

Vorsitzende: Univ.-Prof. Dr. N. Brambilla

Prüfer der Dissertation:

1. Univ.-Prof. Dr. S. Paul
2. Univ.-Prof. Dr. L. Fabbietti

Die Dissertation wurde am 31.7.2014 bei der Technischen Universität München eingereicht und durch die Fakultät für Physik am 20.10.2014 angenommen.

For my grandfather
Dr. Henrique M. Austregesilo

Abstract

The question of the existence of glueballs is one of the unsolved problems in modern particle physics and can be regarded as a stringent test for quantum chromodynamics. Especially the supernumerous states in the light scalar meson spectrum are candidates for the observation of mixing effects between $q\bar{q}$ mesons and pure gluonic bound states. On the other hand, the existence and the properties of many resonances in this sector are disputed. The COMPASS experiment was proposed to make significant contributions to this field.

COMPASS is a fixed-target experiment at the CERN SPS which focused on light-quark hadron spectroscopy during the data taking periods in 2008 and 2009. A world-leading data set was collected with a 190 GeV/c hadron beam impinging on a liquid hydrogen target in order to study, inter alia, the central production of glueball candidates in the light meson sector. Especially the double-Pomeron exchange mechanism is well suited for the production of mesons without valence-quark content. To this end, we select events with two protons and two pseudoscalar mesons in the final state from the COMPASS data set recorded with an incident proton beam. Several selection criteria are compared in order to enhance the double-Pomeron component in the centrally produced sample. The angular distribution of the decay of these systems into $\pi^+\pi^-$ and K^+K^- is decomposed in terms of partial-wave amplitudes, where particular attention is paid to the inherent mathematical ambiguities. They can be naturally resolved by using the information from the related $\pi^0\pi^0$ final state. The resulting distributions yield unprecedented precision, most notably on the relative phase between the partial-wave amplitudes. For the first time, an analysis in narrow bins of the squared four-momentum transfer is possible, which provides information about the dynamics of the production process.

Furthermore, we show that a mass-dependent fit of the obtained S-wave intensity distribution alone, as it was done in the past, can be achieved by substantially different models. Only if the intensities of the S- and D-wave amplitudes as well as their relative phase are fitted simultaneously, resonant states can be distinguished from non-resonant background. With this method, we obtain realistic Breit-Wigner parameters for the scalar mesons above 1 GeV/c^2, especially in the K^+K^- channel. A combination of the results with precision data from elastic scattering experiments may be able to elucidate the entire sector of light scalar mesons.

Zusammenfassung

Die Frage nach der Existenz von Glueballs ist eines der ungelösten Probleme der modernen Teilchenphysik und kann als eine zwingende Prüfung für Quantenchromodynamik angesehen werden. Vor allem die überzähligen Zustände im Spektrum leichter skalarer Mesonen sind Kandidaten für die Beobachtung von Mischeffekten zwischen $q\bar{q}$-Mesonen und rein-gluonischen gebundenen Zuständen. Andererseits sind das Vorhandensein und die Eigenschaften vieler Resonanzen in diesem Sektor umstritten. Das COMPASS-Experiment wurde entworfen, um bedeutend in diesem Bereich beizutragen.

COMPASS ist ein Fixed-Target-Experiment am CERN SPS, das sich während der Datennahmeperioden 2008 und 2009 auf Hadronen-Spektroskopie mit leichten Quarks konzentrierte. Ein weltweit führender Datensatz wurde mit einem $190\,\mathrm{GeV}/c$ Hadronenstrahl gesammelt, der auf ein Flüssigwasserstoff-Target auftraf, um unter anderem die zentrale Produktion von Glueball-Kandidaten im Sektor leichter Mesonen zu untersuchen. Vor allem der Doppel-Pomeron-Austauschmechanismus ist bekanntlich für die Produktion von Mesonen ohne Valenz-Quark-Inhalt geeignet. Zu diesem Zweck wählen wir Ereignisse mit zwei Protonen und zwei pseudo-skalaren Mesonen im Endzustand aus dem Datensatz, der mit einem Protonenstrahl bei COMPASS erfasst wurde. Mehrere Auswahlkriterien werden verglichen, um die Doppel-Pomeron Komponente in dem zentral-produzierten Sample anzureichern. Die Winkelverteilung des Zerfalls dieser Systeme in $\pi^+\pi^-$ und K^+K^- wird in Partialwellenamplituden zerlegt, wobei besonderes Augenmerk auf den inhärenten mathematischen Ambiguitäten liegt. Diese können durch die Verwendung von Informationen aus dem verwandten $\pi^0\pi^0$ Endzustand gelöst werden. Die daraus resultierenden Verteilungen besitzen bisher unerreichte Präzision, vor allem die der relative Phase zwischen den Partialwellenamplituden. Zum ersten Mal ist eine Untersuchung in schmalen Bereichen des Vierimpulsübertrags möglich, welche Informationen über die Dynamik des Produktionsprozesses ermöglicht.

Darüber hinaus zeigen wir, dass ein massenabhängiger Fit der erhaltenen S-Wellenintensitätsverteilung allein, wie es in der Vergangenheit geschehen ist, durch grundlegend unterschiedliche Modelle erreicht werden kann. Nur wenn man die Intensitäten der S- und D-Wellenamplituden sowie ihre relative Phase gleichzeitig betrachtet, werden Resonanzzustände von nicht-resonantem Untergrund unterschieden. Mit dieser Methode erhalten wir realistische Breit-Wigner-Parameter für die skalaren Mesonen über $1\,\mathrm{GeV}/c^2$, vor allem im K^+K^- Endzustand. Eine Kombination der Ergebnisse mit präzisen Daten aus Experimenten mit elastischer Streuung kann in der Lage sein, den gesamten Sektor der leichten skalaren Mesonen aufzuklären.

Contents

Chapter 1

Spectroscopy of Light Scalar Mesons

The Standard Model represents the current understanding of the fundamental processes in nature. It describes the dynamics of particles under the influence of the strong, weak and electro-magnetic forces. The success of the unified electro-weak theory was crowned in 2012 by the discovery of a particle at the CERN Large Hadron Collider (LHC) which is consistent with the predicted Higgs boson [1, 2].

Quantum chromodynamics (QCD), the part of the Standard Model responsible for the strong interaction, was developed 40 years ago [53]. It is formulated in analogy to quantum electrodynamics (QED), with quarks that carry a colour charge, and gluons which mediate the force between the quarks, as degrees of freedom. However, two important differences with respect to QED prevent the deduction of the hadron spectrum from QCD. First of all, it is a non-abelian gauge theory, which manifests itself in the colour charge of the gluons and their ability to interact among themselves. In combination with a growing coupling constant for low energies [27], this leads to the fact that perturbative techniques cannot be applied. In this domain, the quarks and gluons are confined into colour-neutral hadrons, which are the relevant degrees of freedom. Precise knowledge of the hadron spectrum is therefore essential in order to understand the strong interaction at low energies.

This introduction summarises selected topics that are important for this work. Extensive reviews on the methods and results in light scalar meson spectroscopy can be found in [74] and [81].

1.1 Theoretical Approach

In the following, we will introduce a series of models and concepts which aim at deducing the spectrum of hadrons. We will focus on spinless mesons with positive parity, the so-called scalar sector. In addition to that, we will restrict ourselves to light mesons, consisting only of up, down or strange quarks. This field is still under heavy debate, even though it plays a fundamental role in QCD and is important for nucleon-nucleon interaction [83]. One of the consequences of QCD are bound systems of gluons, the so-called glueballs, which ought to exist due to the before-mentioned self-interaction. Nearly all models predict the lightest glueball to have scalar quantum numbers, but a unique identification with a physical state has not been possible to the present day [81]. The existence of glueballs is one of the unsolved problems in modern particle physics and can be regarded as a stringent test for QCD.

1.1.1 Multiplets and Constituent Quarks

Light mesons can be grouped into multiplets of the SU(3) flavour symmetry. For this purpose, the light and nearly mass-degenerate up and down quarks are treated as an isospin $I = \frac{1}{2}$ doublet, while the heavier strange quark is an isospin $I = 0$ singlet with the strangeness quantum number -1. In addition, the parity quantum number $P = +1$ describes the behaviour of the quark wave function under spatial inversion. Anti-quarks have the opposite parity.

These quarks are combined with anti-quarks, for which all quantum numbers are reversed, in order to form the observable mesons. The total intrinsic spin S can hereby be either 0 or 1, and couples with the relative orbital angular momentum $\vec{L}$ between the quark and the antiquark to the total spin of the meson $\vec{J}$.

$$\vec{J} = \vec{S} + \vec{L}, \qquad |L - S| \leq J \leq |L + S| \tag{1.1}$$

The parity of the meson is defined as the product of intrinsic parities of the constituent quarks multiplied with the parity of the spatial wave function

$$P = P_q \cdot P_{\bar{q}} \cdot (-1)^L = (-1)^{L+1} \ . \tag{1.2}$$

Neutral mesons are eigenstates of the charge conjugation operator, which transforms particles into their anti-particles and vice versa. Their eigenvalue is determined by the product of the symmetry behaviour of the spatial and spin wave functions and can be expressed as

$$C = (-1)^{L+S} \ . \tag{1.3}$$

Customarily, charged mesons are attributed with the C-parity of their neutral isospin partner. Finally, it is useful to introduce the generalised G-parity as C-parity followed by a rotation of $180°$ around the I_2 axis in isospin space [72], which implies a reversal of the charge sign. The G-parity is approximately conserved by the strong interaction.

$$G = (-1)^{L+S+I} \tag{1.4}$$

Its eigenvalue is multiplicative and -1 for pions. We can therefore use the relation for mesons decaying into a number n_π of pions

$$G = (-1)^{n_\pi} \ . \tag{1.5}$$

Within the flavour SU(3) group, a set of states with the same quantum numbers J^{PC} form a nonet of mesons. Due to the SU(3) symmetry, they can be grouped into an octet and a singlet state. For example, the nine pseudoscalar mesons in the ground state with $J^{PC} = 0^{-+}$ can be represented as orthogonal SU(3) eigenstates [72]. In this formalism, the physical states η and η' are represented as mixtures of the flavour eigenstates η_8 and η_1. The nonet is often illustrated in a plane spanned by the third component of Isospin, I_3, and by the strangeness quantum number (cf. Figure 1.1).

This scheme can be applied in a similar fashion to the vector ($J^{PC} = 1^{--}$) and tensor ($J^{PC} = 2^{++}$) mesons. Both nonets have a nearly ideal mixing angle of $35.3°$. As a consequence, one of the physical states is purely $s\bar{s}$ ($\phi(1020)$, $f_2'(1525)$), while the other ($\omega(782)$, $f_2(1270)$) is composed of u and d quarks only. The observed mass difference between both states of about $250\,\mathrm{MeV}/c^2$ supports this scheme experimentally [72].

The success of this model for the description of both mesons and baryons ultimately led to the establishment of quarks as the building blocks of strongly interacting matter. The constituent quark model can not only describe the pattern of the experimentally observed

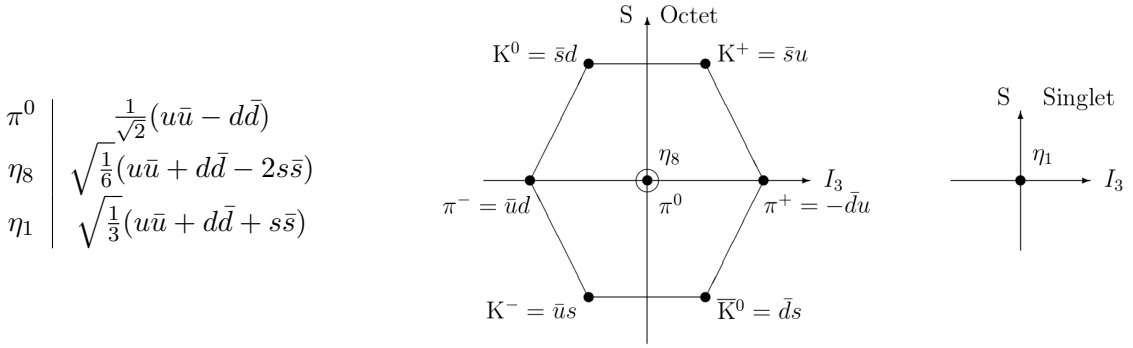

Figure 1.1: The nonet of pseudoscalar mesons [74]. The upright S on the vertical axis signifies the strangeness.

states, but can even be used to calculate properties of the hadrons like e.g. magnetic moments and explain their masses at least qualitatively.

However, the scalar sector is very controversially discussed within the constituent quark model. Especially the series of established [26] scalar isoscalar ($I = 0, J^{PC} = 0^{++}$) states

$$f_0(500), f_0(980), f_0(1370), f_0(1500), f_0(1710) \tag{1.6}$$

seems to be impossible to incorporate into conventional quark-model nonets. Even if the $f_0(500)$ is described by elastic $\pi\pi$ scattering and the $f_0(980)$ as an eventual $K\bar{K}$ molecule or tetra-quark state [72], the remaining three resonances cannot belong to the same $q\bar{q}$ nonet. For these super-numerous states, mixing effects with states beyond the constituent quark model, e.g. scalar isoscalar glueballs, could be important in order to explain the observed spectrum.

If the model is extended to incorporate constituent gluons, at least two of them can form a bound system with C-parity +1 [81]. Only colour singlet states are considered, as they might be observable in experiments. If one assumes further that the ground state is formed by gluons in a relative S-wave, the lightest glueball in this model can have $J^{PC} = 0^{++}, 0^{-+}$ or 2^{++}. It can therefore contribute to the mixing scheme in the scalar sector. Several different explanations are proposed in the literature [81], but a definite consensus could not yet be reached. This is partly due to the imprecise experimental knowledge about the existence and properties of the scalar isoscalar resonances.

1.1.2 Effective QCD

Another group of theoretical approaches uses approximate symmetries to transform the QCD Lagrangian into an effective theory, where the hadrons are the relevant degrees of freedom. Perturbative calculations can then be used at low energies which is not possible within pure QCD. In general, these theories are only valid within a limited energy regime and rely on experimentally determined constants.

The most prominent example is Chiral Perturbation Theory. It identifies the experimentally observed pseudoscalar mesons as the Goldstone-bosons of a spontaneously broken chiral symmetry [58]. As this symmetry is also explicitly broken through the masses of the light quarks, the bosons acquire mass as well.

The mechanism of chiral symmetry breaking can be explained within the Linear Sigma Model[1]. The light scalar nonet appears here as chiral partner to the pseudoscalar one [26].

[1]Named after the scalar isoscalar meson σ [55], an old name for the $f_0(500)$

Hence, the $f_0(500)$ is sometimes called the "Higgs boson of strong interaction" in these models, as its role is similar to the Higgs particle in electro-weak symmetry breaking. Namely, it is responsible for a large part of the light hadron masses. A reliable picture of the light scalar mesons is indispensable for these models in order to derive the hadronic manifestations of QCD.

1.1.3 QCD on the Lattice

A different approach to solve the QCD Lagrangian are numerical simulations, so-called Lattice QCD (LQCD) calculations. These ab initio methods currently provide the most reliable means [79] to study the hadron spectrum. The quark and gluon fields are simulated on an Euclidean space-time lattice, which is used to evaluate correlation functions. In imaginary time, the obtained energy levels quickly converge towards the ground state, but even excited states can be measured with increasing precision. Yet, most of the methods deal with stable particles. Exploring dynamical properties like decay widths or phase shifts has only become possible in the last few years [49].

Systematic errors due to discretisation, finite lattice spacing and periodic boundary conditions can be controlled via extrapolation methods. Most calculations also use heavier u and d quark masses than those found in nature [47] in order to avoid computationally expensive vacuum loops. Therefore, an extrapolation towards the physical point is required in addition. The computed pion mass is usually quoted as a measure for this scaling.

By mapping the continuous symmetries onto discrete transformation properties of the cubic lattice, even the spin, parity and charge conjugation quantum numbers of the states can be determined. However, also with this method, the scalar sector with vacuum quantum numbers $J^{PC} = 0^{++}$ seems to be the most difficult to handle. It is prone to large fluctuations and numerical instabilities.

In general, the LQCD efforts towards glueball spectroscopy can be grouped into two fields. One approach deals with a quark-less Yang-Mills theory in order to determine the pure glueball spectrum. A prominent example can be found in [79], where the identification of a large variety of J^{PC} states was achieved. The obtained spectrum is illustrated in Figure 1.2. The lowest lying resonance has indeed the quantum numbers 0^{++} and a mass of $1730\,\mathrm{MeV}/c^2$ with a comparatively small error. It therefore supports the conclusion of the constituent quark model regarding the supernumerous f_0 states. However, these (so-called) quenched approximations cannot clarify mixing effect with conventional $q\bar{q}$ mesons.

Analyses in the second field try to take the entire dynamics of QCD into account, including both quarks and gluons on the lattice. Considerable efforts are currently ongoing to understand the hadron spectrum with these unquenched approaches. In addition to the mass spectrum, also the relative size of overlaps with certain operators yields information about the internal structure of the extracted states [47]. Especially operators which are proportional to the chromo-magnetic part of the QCD field-strength tensor indicate a gluonic component of the resonances. No definite result has been obtained so far for isoscalar scalar states [48], but a remarkable precision is reached already for isovector mesons. The current degree of detail is not matched by experimental results in the field of hadron spectroscopy.

1.2 Central Exclusive Production

Scattering experiments have helped to understand the composition of particles and the structure of interactions since the very beginning. Without knowledge of the elementary quarks and gluons, consistent scattering theories were able to describe the experimental observations.

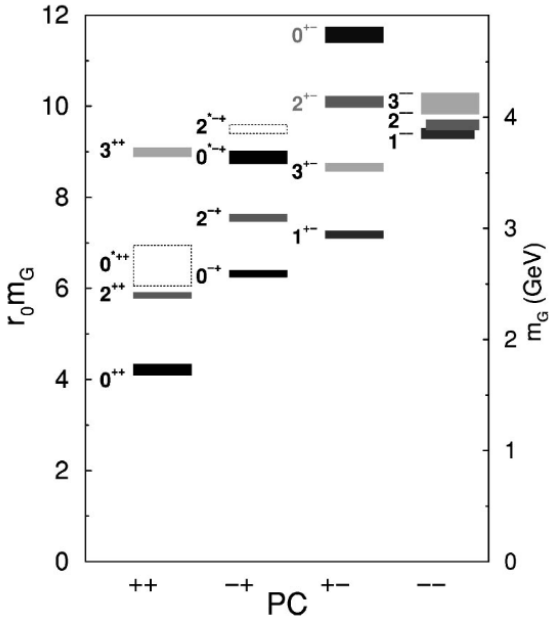

Figure 1.2: Mass spectrum of glueballs, simulated in a quark-less theory on the lattice [79].

After leading to the establishment of QCD, they still provide an important phenomenological tool to understand the Strong Interaction in the confined regime.

In this section, we will introduce the basic terms necessary to understand the central production reaction, which is used in this work to study scalar mesons. We will also present an overview of central production experiments and discuss their results.

1.2.1 Scattering Theory: Reggeon and Pomeron

The two-body scattering process

$$1 + 2 \to 3 + 4 \tag{1.7}$$

is completely characterised by the two independent Lorentz-invariant Mandelstam variables

$$\begin{aligned} s &= (P_1 + P_2)^2 \\ t &= (P_1 - P_3)^2 \end{aligned} \tag{1.8}$$

with the particle four-momenta $P_{1,2,3}$ [43]. The squared four-momentum transfer t is negative. For equal particles with mass m, the squared centre-of-mass energy s is larger than $4m^2$.

The analytic amplitude $A(s,t)$ for the reaction relates the s-channel process (1.7) to the t-channel process

$$1 + \bar{3} \to \bar{2} + 4 \tag{1.9}$$

via crossing symmetry. The resonances in the t-channel have an important impact on the scattering cross section in the s-channel. Regge theory describes these resonances as poles in the complex angular momentum plane whose locations vary with t. The approximately linear dependences $\alpha(t)$ in this plane are called Regge trajectories, and they can be associated with the exchange of quasi-particles, often called Reggeons ($\mathbb{R}$) [43]. For positive integer values of the angular momentum, particles with squared mass t correspond to experimentally observable states. The Chew-Frautschi plot in Figure 1.3 shows the degenerate trajectories for

the combinations of isospin and C-parity corresponding to the ρ, a_2 and f_2 mesons in pion-pion scattering. Other meson trajectories (π, $b_1(1235)$, etc.) are parallel but cross the vertical axis at lower values of J. The linearity allows a simple extrapolation to the physical region of the s-channel where $t < 0$.

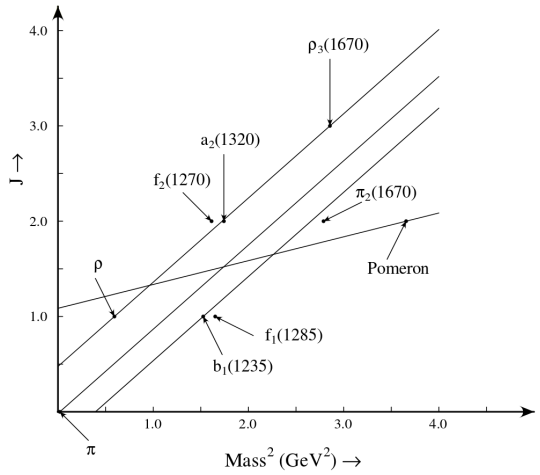

Figure 1.3: Chew-Frautschi plot with partly degenerate Regge trajectories and the Pomeron trajectory [34].

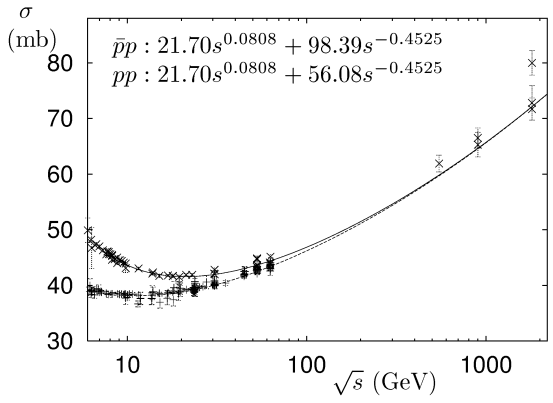

Figure 1.4: Total cross section of pp and $p\bar{p}$ (reproduced with permission from [43]).

With the optical theorem, the total cross section for a hadronic reaction can be directly calculated from the imaginary part of the elastic scattering amplitude at $t = 0$. According to Regge theory, this results in a behaviour of the total cross section as

$$\sigma(s) \propto s^{\alpha(0)-1} \ . \tag{1.10}$$

Since the leading trajectories have an intercept around 0.5, the hadronic cross section should fall approximately like $1/\sqrt{s}$. This is in agreement with experimental observations up to energies of $\sqrt{s} \approx 10\,\text{GeV}$. Beyond that, a logarithmic rise of the total cross section was measured by several hadron scattering experiments (cf. Figure 1.4). This triggered the postulation of a new trajectory which crosses the vertical axis slightly above 1. This so-called Pomeron ($\mathbb{P}$) trajectory is parametrised as

$$\alpha_{\mathbb{P}}(t) = 1 + \epsilon_{\mathbb{P}} + \alpha'_{\mathbb{P}} t \ , \tag{1.11}$$

and the data is well described with $\epsilon_{\mathbb{P}} \approx 0.08$ [43]. The apparent violation of unitarity of a cross section rising with energy is avoided by a slowly decreasing value of $\epsilon_{\mathbb{P}}(s)$. This effect can be explained by the exchange of multiple Pomerons at higher energies. In addition, the Regge contribution becomes insignificant compared to mechanisms described by perturbative QCD for very large energies and transverse momenta [43].

The slope parameter $\alpha'_{\mathbb{P}} = 0.25\,\text{GeV}^{-2}$ is determined by fitting the elastic scattering cross section as a function of t for a fixed energy [43]. Even though the Pomeron trajectory is shallower than the meson trajectories (cf. Figure 1.3), no physical particle could yet be associated with it. Since it has the quantum numbers of the vacuum ($I = 0, C = +$), the Pomeron is often brought into connection with glueball candidates. In QCD terms, it can be modelled as a two-gluon interaction but the direct derivation of Regge theory from quantum chromodynamics is so far unresolved.

1.2.2 Double-Pomeron Exchange

The concept of Regge theory can be generalised for inelastic events, where additional particles are produced. Pomeron exchange dominates for high energies and t less than about $1\,\mathrm{GeV}^2$. In this domain, we speak of diffractive dissociation if one of the initial particles stays intact while the other produces a system of hadrons (cf. Figure 1.5).

The main focus of this work are inelastic reactions where both particles stay intact and almost undisturbed. In these central exclusive reactions, two Reggeons are radiated from the initial state, collide and form a system of hadrons (cf. Figure 1.6). Especially if the energies are high enough for the scattering to be dominated by the double-Pomeron contribution, the reaction is ideal to study the production of glueballs owing to the glue-rich nature of the Pomeron without valence quarks. Furthermore, the quantum numbers of the central system are constrained to $I^G = 0^+$, $J^{PC} = 0^{++}, 2^{++}, 4^{++}$,.. and the process therefore selects the controversially discussed scalar isoscalar sector. However, the energy threshold for double-Pomeron scattering is much higher than for single diffraction and subject to debates. Central (exclusive) production and double-Pomeron exchange (DPE) are often used synonymously in the literature, but we will maintain this important differentiation.

In Figures 1.5 and 1.6, we use the notation $p_{\mathrm{f(ast)}}$ and $p_{\mathrm{s(low)}}$ to distinguish the scattered beam and target protons in the final state. In addition, the intermediate states X are introduces which decay into hadrons. We chose the production of two pions for this example, since it has the largest cross section and plays a prominent role in this work. As both processes have the same particles in the final state, diffractive dissociation will be an important background for the study of central exclusive production.

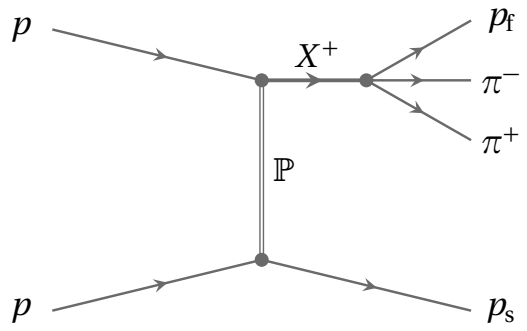

Figure 1.5: Diffractive dissociation with Pomeron exchange.

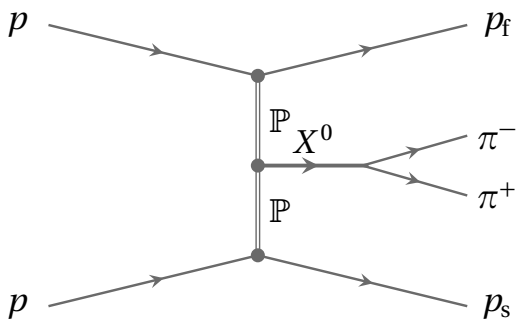

Figure 1.6: Central exclusive production with double-Pomeron exchange.

Two kinematic variables can help to distinguish between the two production mechanisms. The reduced longitudinal momentum x of the final-state particles in the centre-of-mass frame, often also noted x_{F} because of its introduction by R. Feynman [51], is defined as

$$x_{\mathrm{F}} = \frac{p_{\mathrm{L}}}{p_{\mathrm{L(max)}}} = \frac{2p_{\mathrm{L}}}{\sqrt{s}} \ . \tag{1.12}$$

For double-Pomeron exchange reactions, $|x_{\mathrm{F}}|$ should be close to unity for both outgoing protons. $(1 - x_{\mathrm{F}})$ is sometimes called $x_{\mathbb{P}}$ [43].

The rapidity y is an alternative kinematic variable [40] to describe high-energy collisions. It is defined for particles with non-zero transverse momentum with respect to the beam axis z

as

$$y = \frac{1}{2} \ln \frac{E + p_z}{E - p_z}. \tag{1.13}$$

The rapidity has the advantage that it transforms additively under boosts along the z direction. Consequently, the rapidity difference between two particles remains invariant under longitudinal boosts. If not specified otherwise, we will evaluate the rapidity in the centre-of-mass frame of the reaction as well. If the protons loose only a small fraction $(1 - x_\mathrm{F})$ of their momenta, no other particle in the reaction can be in the same region of rapidity. Distinctive rapidity gaps larger than two units therefore characterise double-Pomeron exchange reactions.

1.2.3 Central Production in Experiments

Double-Pomeron Exchange at ISR (CERN)

The first evidence for double-Pomeron exchange processes was observed at the world's first hadron collider, the CERN[2] Intersecting Storage Rings (ISR). The reaction $pp \to p\pi^+\pi^- p$ was studied with five different energies from $\sqrt{s} = 23.4\,\mathrm{GeV}$ to $\sqrt{s} = 63.4\,\mathrm{GeV}$ in order to allow for two large rapidity gaps $\Delta y > 2$ [46]. Even though single-diffraction processes dominate at all studied energies, it was possible to enrich the DPE sample by requiring both protons to have $|x_F| > 0.9$. In addition, both pions had to be detected in the rapidity region $|y| < 1$. Resonances in the $p\pi$ systems could be efficiently suppressed by these requirements. Furthermore, no obvious correlation was observed between the azimuthal angles of the scattered protons for this enriched sample. Also the momentum transfers at the two proton vertices showed an independent behaviour. This lead to the conclusion that the two proton vertices factorise, which was expected for DPE. Angular distributions of the pions suggested that the central $\pi^+\pi^-$ system is produced mainly in an S-wave ($J = 0$). A signal in the mass region of the $f_2(1270)$ could also be discerned in the invariant mass distribution. The lack of data hindered the precise extraction of resonance parameters at this stage. However, by proving the existence of DPE, the experiments helped to establish the phenomenological Regge model.

A large sample of 3 million events was later collected at the ISR by a different experimental setup [78] at the highest available centre-of-mass energy of $\sqrt{s} = 63.4\,\mathrm{GeV}$. Figure 1.7 shows the invariant mass spectrum of the central $\pi^+\pi^-$ system in a semi-logarithmic scale. It rises rapidly from threshold and peaks around $0.5\ \mathrm{MeV}/c^2$. A sharp drop of about one order of magnitude is observed in the region of the $f_0(980)$ meson, another one around $1.5\,\mathrm{GeV}/c^2$. The enhancement around $1.3\,\mathrm{GeV}/c^2$ could be due to the $f_2(1270)$, even though it appears to be broader.

A partial-wave analysis has been performed in order to disentangle the contributions with different spins in the di-pion mass spectrum. Following a simple DPE model, only the allowed $J^{PC} = 0^{++}$ and 2^{++} corresponding to S- and D-waves, respectively, and the magnetic quantum number $M = 0$ were used. No attempt has been made to extract the $J = 4$ contribution [78]. The results confirmed the previously observed dominant S-wave. In order to extract the resonant contributions, mass-dependent amplitudes were fitted to the S- and D-wave intensities as well as their interference term. The S-wave could be modelled entirely with a fixed $f_0(980)$ and another broad resonance around $1.4\,\mathrm{GeV}/c^2$ interfering with a coherent non-resonant component. No conclusive answer could be obtained for the D-wave components.

Nonetheless, the results were combined with elastic $\pi\pi$ scattering data (cf. Section 1.3.3) in an extensive analysis of the resonant components of the S-wave from threshold to $1.6\,\mathrm{GeV}/c^2$ [16]. The data provides significant extra information especially in the region around $1\,\mathrm{GeV}/c^2$, where

[2] European Organisation for Nuclear Research

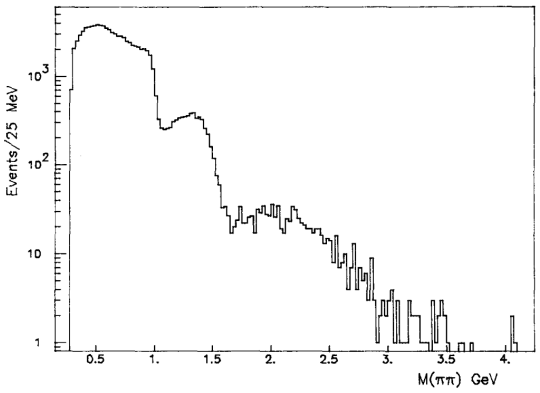

Figure 1.7: Invariant mass spectrum of $\pi^+\pi^-$ events at $\sqrt{s} = 63.3\,\text{GeV}$ [78].

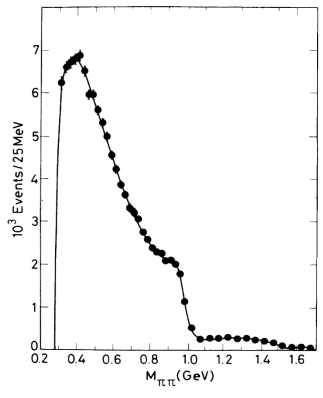

Figure 1.8: $\pi\pi$ S-wave from [78] with fit [16].

elastic scattering is controlled by interference effects between S- and P-wave. In the unitary analysis, the double-Pomeron production of the di-pion final state acts as severe constraint through the crucial $K\bar{K}$ threshold region. As a result, two broad objects $\epsilon(900)$ and $\epsilon'(1430)$ and two narrow resonances were claimed, which were called $S_1(991)$ and $S_2(988)$. This is contradicted by recent studies [83] which confirm only the $f_0(500)$ and the $f_0(980)$. However, the occurrence of three states below $1\,\text{GeV}/c^2$ was treated as definite evidence for dynamics beyond the constituent quark model at that time. Even though this involved analysis lacked precision data, its parametrisation of the $\pi\pi$ S-wave is still widely used in experiments (e.g. [9]).

Double-Pomeron Exchange at CERN SPS

Experiments at the next generation CERN hadron collider Sp$\bar{\text{p}}$S[3] [67, 29] continued to investigate double-Pomeron exchange in order to gain insight into scattering processes at $\sqrt{s} = 630\,\text{GeV}$. However, the accessible mass range far beyond the resonant region for light mesons did not allow for further input to spectroscopic studies.

On the other hand, the fixed-target experiments carried out with the SPS[4] proton beam at CERN produced a large number of new results. pp and $\pi^- p$ reactions were studied with beam energies between 85 GeV ($\sqrt{s} = 12.7\,\text{GeV}$) and 450 GeV ($\sqrt{s} = 29.1\,\text{GeV}$). The detectors were able to reconstruct a variety of final states, including charged and neutral particles. In this short review, we will exemplarily focus on the central production of two pions as it was studied in great detail and is also an important part of this work.

First of all, the large number of recorded events allowed a detailed comparison of the invariant mass distributions depending on beam type and momentum. After removing the obvious $p\pi$ resonances from the data sample, the same features appeared as described above. In addition, a dominant peak at the position of the $\rho(770)$ can be discerned for the lowest energies (cf. Figure 1.9). This isospin $I = 1$ state is evidence for the importance of other Regge trajectories at these energies as it cannot be produced via double-Pomeron exchange. However, the relative intensity quickly vanishes with increasing $\sqrt{s}$. It can be explained by the contribution of two pion trajectories to the production of $\rho(770)$ which should scale with $1/s^2$ [74]. The dominant enhancement at threshold which remains for higher energies was treated as an indication for s-independent Pomeron-Pomeron scattering. Fits to these invariant mass dis-

[3]Super Proton Antiproton Synchrotron
[4]Super Proton Synchrotron

tributions with interfering Breit-Wigner resonances and non-resonant background terms could describe the shape and helped to quantify the $\sqrt{s}$-dependence [14].

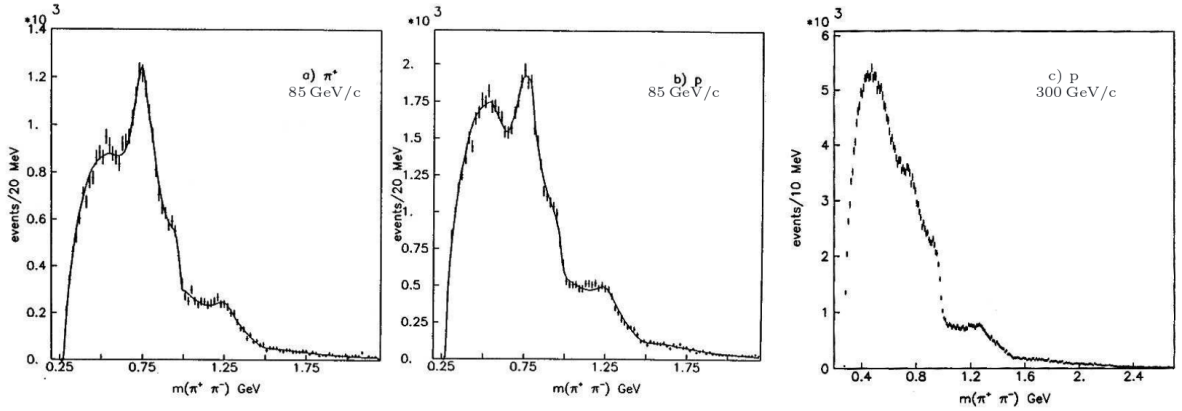

Figure 1.9: The $\pi^+\pi^-$ mass distribution with (a) 85 GeV/c π^+, (b) p, or (c) 300 GeV/c p beam [74].

A partial-wave analysis in narrow mass bins was used to separate the S-wave from states with spin 1 and 2. Subsequently, the remaining intensity distribution was interpreted with interfering Breit-Wigner resonances and an exponential background. Similarly to other final states, a minimal set of three states ($f_0(980)$, $f_0(1370)$, $f_0(1500)$) was needed to describe the $\pi^+\pi^-$ S-wave (cf. Figure 1.10). The inclusion of another Breit-Wigner function further improved the fit and helped to established the $f_0(1710)$ meson as a scalar isoscalar resonance [21]. A coupled-channel analysis of the S-wave in $\pi^+\pi^-$ and K^+K^- final states yielded essentially the same results with four required poles [19]. The branching fractions of the scalar resonances were determined which permitted conclusions on their quark content. However, the method of deriving a complex amplitude from a one-dimensional mass distribution and ignoring the relative phase with respect to the other components is met with criticism [81].

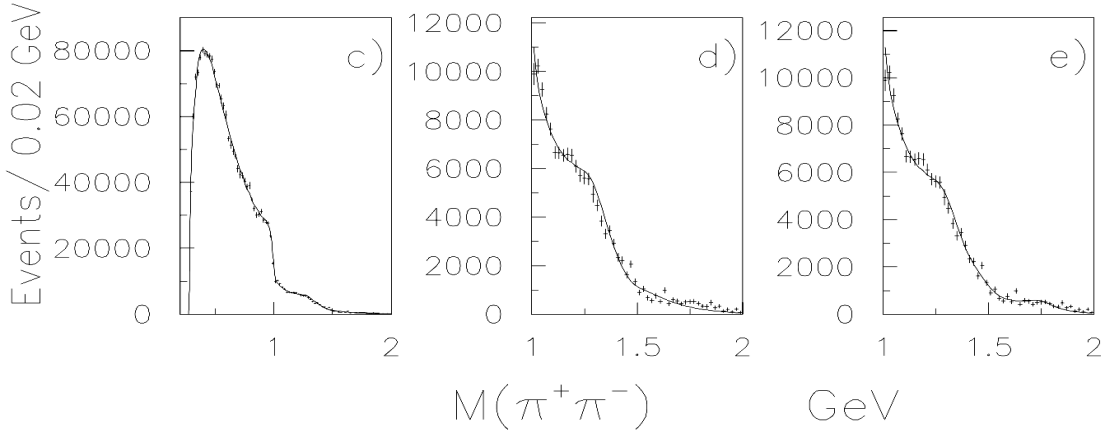

Figure 1.10: c) and d) The $\pi^+\pi^-$ S-wave with fit using three Breit-Wigner functions plus non-resonant background, e) using four Breit-Wigner functions plus non-resonant background [21].

In addition to the analysis of the angular distribution of the decay products, the data gave insights into the production characteristics. In this context, established $q\bar{q}$ states behave

differently than the glueball candidates $f_0(1500)$ and $f_2(1900)$ which lead to the figurative name "glueball-filter". It was suggested that the observed effect was driven primarily by the variable dP_T [37], defined as the difference of the transverse momenta of the exchange particles from the slow and the fast proton vertices with respect to the beam axis in the centre-of-mass frame (cf. Figure 1.11). Under the assumption that DPE was the leading contribution in central production, this would imply a vectorial interaction [39]. On the other hand, the dP_T-dependence can be explained by an effect of the angle between the two proton scattering planes ϕ in the overall centre-of-mass system. This angle is directly related to the kinematic properties of the reaction and may select different domains [74]. Some unresolved points will be addressed in this work.

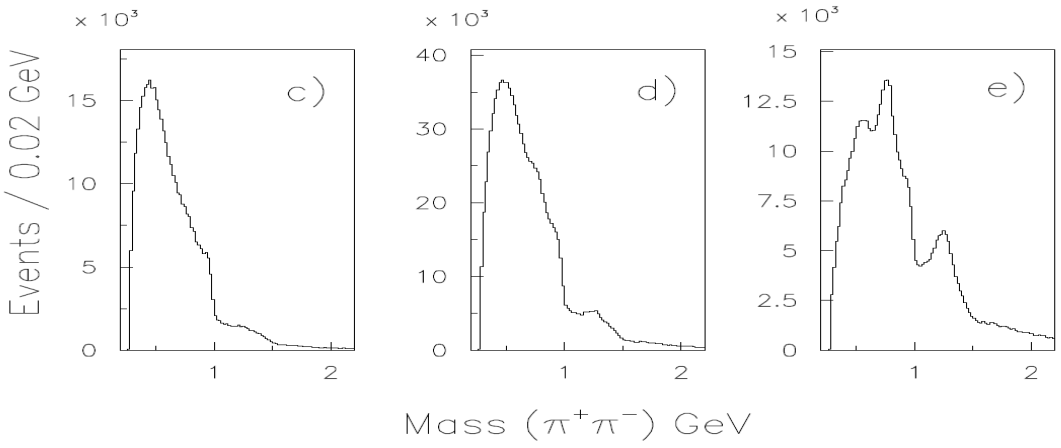

Figure 1.11: $\pi^+\pi^-$ mass spectrum for $dP_\mathrm{T} < 0.2\,\mathrm{GeV}/c$ (c), $0.2\,\mathrm{GeV}/c < dP_\mathrm{T} < 0.5\,\mathrm{GeV}/c$ (d) and $dP_\mathrm{T} > 0.5\,\mathrm{GeV}/c$ (e) [37].

Double-Pomeron Exchange at RHIC, Tevatron and LHC

Central exclusive production recently regained interest as a clean source for scalar states which are not necessarily mesons. Already before the start of LHC, the dynamics of Higgs particle production was studied in this context [68]. The angle between the two scattering planes ϕ is considered to be a direct measure for the spin-parity of the produced state. Especially the combination of Regge theory and perturbative techniques is thereby important [60].

On the other hand, hadron colliders indisputably provide the ideal environment for the study of double-Pomeron exchange. Experiments with a large coverage in rapidity in combination with detectors surrounding the beam pipe in the forward region may be able to measure the exclusive production of mesons down to masses of $1\,\mathrm{GeV}/c^2$. However, dedicated low-intensity runs with defocused beams are needed to avoid background from hard collisions. As this is not the main focus of the experiments, only very limited data and resources are available for a meson-spectroscopy analysis. Figure 1.12 shows a $\pi^+\pi^-$ spectrum with and without the requirement for rapidity gaps measured by the ALICE experiment [93]. As expected, the $\rho(770)$ signal is indeed completely suppressed in the case of two rapidity gaps. Yet, the outgoing protons cannot be measured with the present setup and the amount of data is far from sufficient for a dedicated partial-wave analysis.

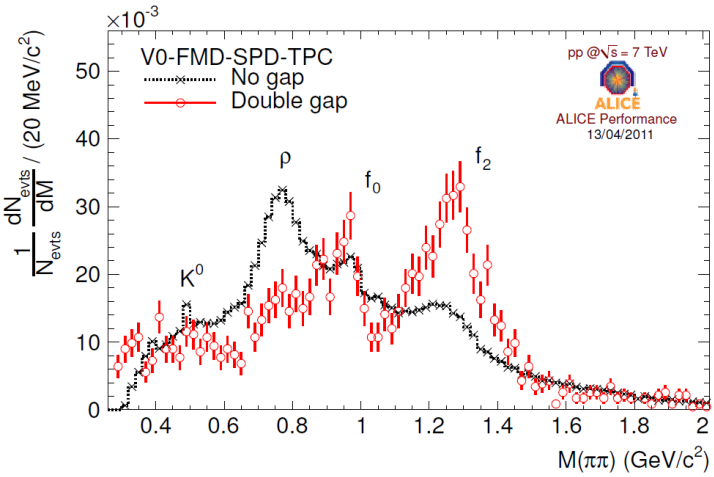

Figure 1.12: Invariant mass spectrum of $\pi^+\pi^-$ events at $\sqrt{s} = 7\,\text{TeV}$ [93].

1.3 Further Experimental Access to the Scalar Sector

Apart from the central exclusive production, other so-called glue-rich reactions were suggested, which should be suited to study glueballs in experiments. In addition to that, elastic $\pi\pi$ scattering data are used in combined analyses. As they are not subject of this work, we will only briefly summarise the impact of results from these processes on the current understanding of scalar mesons.

1.3.1 $p\bar{p}$ Annihilation

Several experiments (e.g. Crystal Barrel [10] at LEAR[5]) used proton-antiproton annihilation in order to produce a system of mesons. If the annihilation happens at rest, only the lowest angular momentum states contribute to the process which is beneficial for the identification of resonances. However, many open questions arise from the theoretical basis of this production process. To this end, the decay branching fractions between nearly all two-meson final states were measured.

As the quark-antiquark pairs annihilate into gluons, they interact and may form bound states. In this context, the narrow $f_0(1500)$ resonance was extensively studied in $p\bar{p}$-annihilation experiments [11]. However, a direct connection to the production of glueballs could not be established. The process seems to be dominated by a mere rearrangement of quarks [74], which is naïvely understandable with the OZI rule [82]. The $\overline{\text{P}}$ANDA[6] experiment will hopefully be able to resolve the open questions in this field within the next decade [50].

1.3.2 Initial-State Radiation in Heavy-Flavour Decays

At electron-positron colliders, charmonium and bottomonium states are produced copiously. Apart from CP-violation studies, the experiments can also be used to study hadron spectroscopy through the decay products. The narrow and therefore unambiguously identifiable initial states strongly constrain the quantum numbers of the reaction and simplify the analysis.

[5] Low-Energy Antiproton Ring at CERN
[6] AntiProton ANnihilation at DArmstadt

Especially radiative decays of the J/ψ meson should provide a clean environment for gluonic excitations in the light-quark sector, as the OZI rule suppresses direct decays of the $c\bar{c}$ [74]. If the photon is detected, the remaining two-gluon system should be able to form a glueball. On the other hand, the dominance of initial-state radiation is experimentally not proven.

1.3.3 $\pi\pi$ Scattering

Pion-pion scattering is experimentally challenging as the initial state does not consist of stable particles. The topology can, however, be embedded in other processes. The prime example was explored by the CERN-Munich collaboration [64], whose data are still used for parametrisations of the $\pi\pi$ S-wave in many analyses (cf. Section 6.1.3). A π^- beam is scattered off a proton target, producing a di-pion system and a recoiling neutron. This charge-exchange reaction is dominated by one-pion-exchange (cf. Figure 1.13) and is therefore suited for the determination of $\pi\pi$ amplitudes. Many resonances contribute to the process via the intermediate state X and can be disentangled by the angular properties of their decay. The method is often called phase-shift analysis, since especially the interference between the complex-valued amplitudes for different spins provides a powerful tool.

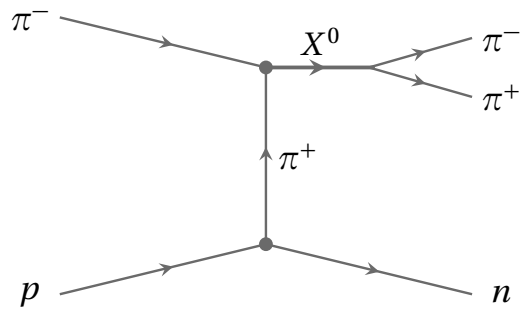

Figure 1.13: One-pion exchange with embedded $\pi\pi$ scattering (here: s-channel).

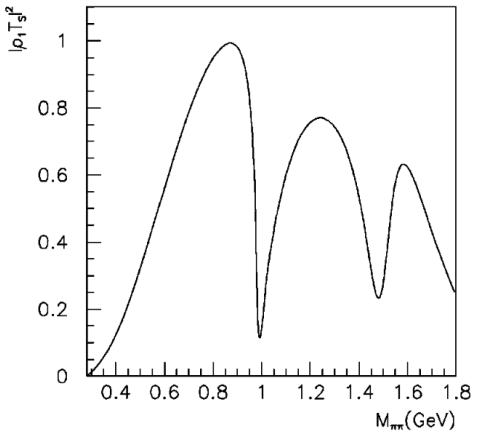

Figure 1.14: Squared $\pi\pi$ S-wave amplitude with 6 poles [76].

Supplementary information from $K^+ \to \pi^+\pi^- e^+\nu_e$ decays [88] is used to constrain the low-energy behaviour of the scattering amplitudes [74]. The limited available phase space for this reaction combined with the well understood weak decay results in very precise data in the threshold region.

In contrast to the production experiments mentioned above, elastic scattering has to fulfil unitarity, i.e. the conservation of probability. As a consequence, the $\pi\pi$ amplitude has to vanish close to threshold. This effect is often called Adler zero [5], and is well confirmed experimentally. The obtained amplitudes (cf. Figure 1.14) cannot be directly applied to different processes, where small di-pion masses are often enhanced. However, the Watson theorem [103] relates the phase of production processes below the first inelastic threshold to elastic scattering.

Chapter 2

COMPASS with Hadron Beams

But an unambiguous answer to the question:
"do glueballs exist and what is their mass spectrum" has not yet been given.
[...]
The proposed experiment will make many significant contributions to this field.
from the COMPASS proposal [25]

The COmmon Muon and Proton Apparatus for Structure and Spectroscopy (COMPASS) [25] was proposed partly as a continuation of the efforts of the fixed-target experiments at CERN SPS in the field of light scalar mesons (cf. Section 1.2.3). After focusing on the spin structure of nucleons [25] with a polarised muon beam in the first years of operation, the collaboration turned its attention towards light-meson spectroscopy in 2008 and 2009. In the following chapter, we will introduce the experimental setup with emphasis on the newly introduced parts for the hadron spectroscopy programme. A detailed description of the apparatus can be found in [3] and [6].

A novel detector type, the PixelGEM detector, was introduced in COMPASS in order to improve the tracking of hadrons scattered at very small angles and, at the same time, to reduce the material in the beam. In the second part of this chapter, we will describe the new beam tracking system and evaluate its performance in the high-intensity hadron beam. Especially the investigation concerning an observed degradation during operation and the resulting improvements will be summarised.

Finally, the methods to calibrate tracking detector positions in order to ensure precise reconstruction of charged particles along the spectrometer will be discussed. It is a vital prerequisite for the results of this work and refined procedures will positively influence the accuracy of future analyses.

2.1 Experimental Setup and Upgrades

As a modern hadron spectroscopy experiment, COMPASS was designed to precisely measure light mesons and baryons with masses up to $3\,\mathrm{GeV}/c^2$. Positive and negative hadron beams impinging on liquid hydrogen or solid-state targets can excite states via several different production processes. While reactions mediated by the strong interaction like diffractive dissociation and central production (cf. Section 1.2.2) dominate the cross section, photo-production in the Coulomb field of heavy nuclei (Pb, Ni) can also be selected to probe the inner structure of the produced hadrons [7].

2.1.1 Beam and Target

The CERN SPS can deliver both positively and negatively charged secondary hadron beams with an intensity of up to 10^7 particles per second and a momentum of 190 GeV/c to the experimental zone of COMPASS. The positive hadron beam consists of 74.6% protons, 24.0% pions and 1.4% kaons at the COMPASS target [6] and is used for the main part of this work. However, a comparison with the negatively charged beam composed out of 96.8% pions, 2.4% kaons and 0.8% anti-protons is beneficial for studies of the production process.

Two differential Cherenkov counters (CEDAR) in the beam line are used to identify the incoming hadrons. A combination of gas pressure and diaphragm settings selects the Cherenkov rings of one type of particle in each device. The acceptance of the detectors limits the allowed beam divergence for particle identification.

A 40 cm long cylindrical Mylar cell with a diameter of 35 mm containing liquid hydrogen at its boiling point is used as a proton target for the presented data set. The thickness of hydrogen along the beam axis corresponds to 4.5% of a radiation length and 5.5% of a nuclear interaction length [6]. The target is surrounded by two concentric barrels of scintillator slabs with radii of 12 cm and 75 cm, respectively. This Recoil Proton Detector (RPD) measures the slow proton p_s with polar angles between 50° and 90°. The energy loss in the target walls and the inner scintillator barrel limits the lowest detectable momentum of recoil protons to about 0.3 GeV/c, which translates into a minimal four-momentum transfer to the target of 0.07 GeV$^2/c^2$ [6].

2.1.2 Charged Particle Tracking

A set of silicon micro-strip detectors is used for precise vertex reconstruction. 12 planes upstream and 8 planes downstream of the target guarantee a spatial resolution below 10 µm for the track position and a resolution for the squared four-momentum transfer to the target of $7 \cdot 10^{-3}$ GeV$^2/c^2$ [6]. In 2009, all silicon stations were cooled down to about 200 K using liquid nitrogen in order to reduce radiation damage. As a consequence, a drastic reduction of noise and a significant improvement in performance was observed.

The final-state particles are mostly emitted in forward direction and detected by a two-stage magnetic spectrometer. This ensures flat acceptance and high resolution in a broad kinematic range. The spectrometer is equipped with a variety of gaseous tracking detectors. Modern micro-pattern gaseous detectors [92] with spatial resolutions below 100 µm are able to measure scattered hadrons close to the beam region. Several different types of medium- and large-sized multi-wire proportional counters and drift detectors with an active area of up to $5 \times 3\,\mathrm{m}^2$ complete the kinematic coverage in both spectrometer parts. Scintillating fibre detectors improve the time resolution necessary in the high-intensity environment with trigger rates up to 30 kHz.

2.1.3 Calorimetry and Particle Identification

Both spectrometer parts feature electromagnetic calorimeters (ECAL1+2), which enables the measurement of photons emitted from the target in an angle between 1 and 100 mrad with respect to the beam axis. In combination with the segmentation into 4568 modules, neutral hadrons (e.g. π^0, η) in the final state can be reconstructed with almost the same precision as their charged counterparts.

In order to identify the charged hadrons in the final state, a ring-imaging Cherenkov (RICH) detector is installed in the first spectrometer stage. It allows the separation of pions, kaons and protons with a momentum below 50 GeV/c. However, the low momentum threshold of 9 GeV/c

for the identification of kaons poses a more stringent limitation for the studies presented later in this work.

The detection of neutral particles emitted in the region of negative rapidities is hampered by the fact that the first electromagnetic calorimeter is installed 14 m downstream of the target. Since 2012, this drawback has been cured with the implementation of a new, large-angle acceptance ECAL0 [54]. For charged particles, the aperture of the first spectrometer magnet SM1 also restricts the acceptance for negative rapidities.

Figure 2.1 illustrates the experimental setup as it was used during the data taking periods with hadron beams in 2008 and 2009. It does not show the two CEDAR detectors which are installed approximately 30 m upstream of the target.

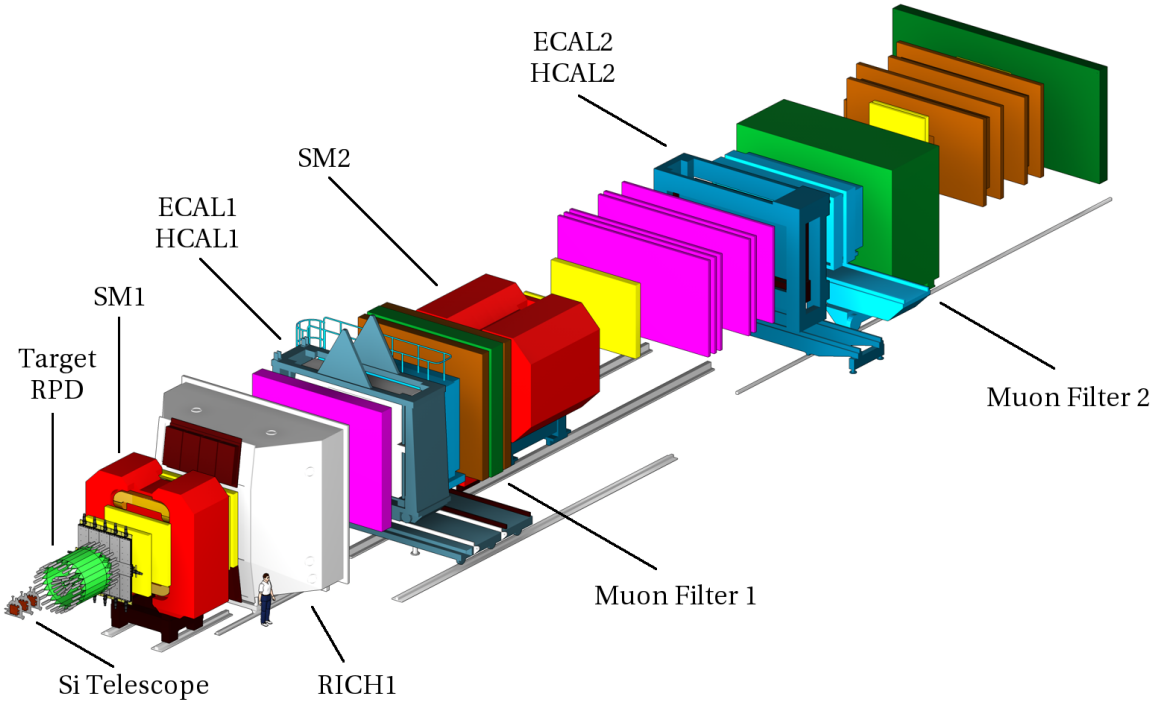

Figure 2.1: Rendered image of the COMPASS spectrometer setup for the hadron spectroscopy programme [6]. The beam enters from the left.

2.2 The PixelGEM Beam-Tracking System

The gas electron multiplier (GEM) technology [92] combines the detector properties of gas amplification with photo-lithographic production techniques. Its main advantage arises from the fact that amplification and detection of the signal are separated in different stages inside the gas volume. The amplification takes place in a thin insulating polymer foil which is chemically etched with a high density matrix of holes and metal coated on both sides. By applying a potential difference of around 500 V between the two sides of the foil, a strong electric field is generated inside the holes. The electrons of the primary ionised gas molecules are guided by the field lines into a GEM hole where multiplication takes place causing a propagating

avalanche. Gains of up to 10^4 can be achieved with single foils, multiple foils are stacked in order to reach gains of 10^5 and a stable operation at the same time.

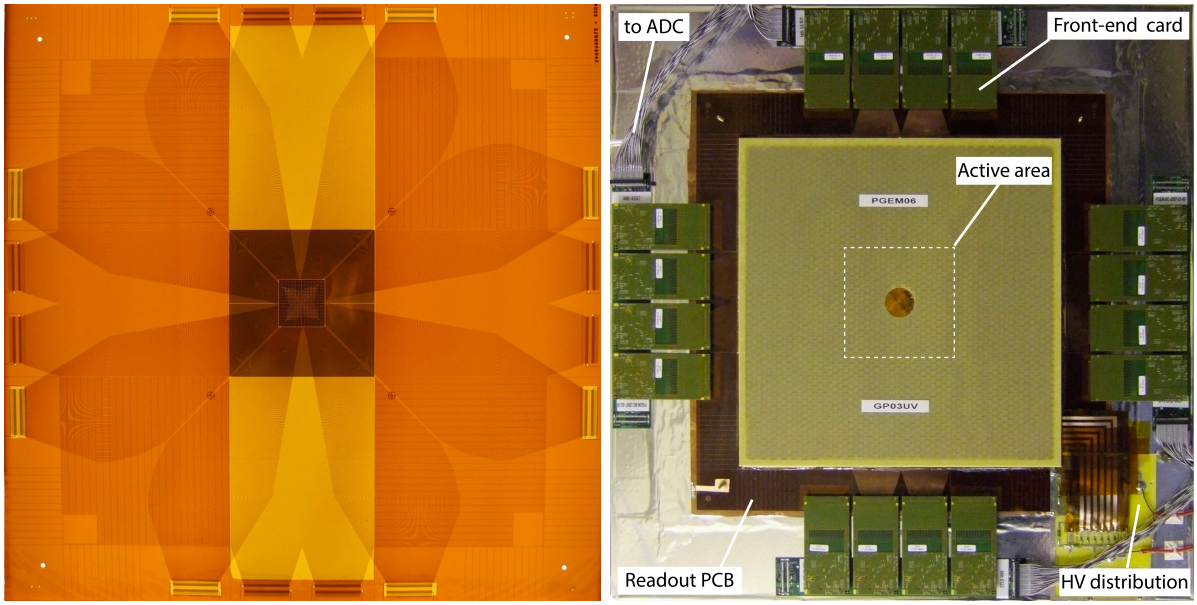

(a) Readout foil

(b) Assembled PixelGEM detector

Figure 2.2: PixelGEM detector [6].

COMPASS was the first experiment which used the GEM technology in a large scale. A system of 22 detectors with an active area of $31 \times 31\,\mathrm{cm}^2$ each and a 2-dimensional strip readout was operated successfully for several years [70]. However, a dead zone with a diameter of 5 cm had to be implemented in the centres in order to reduce the channel occupancy in the high-intensity beams. For the hadron programme in 2008 and 2009, the novel PixelGEM detector was developed with a fully active area of $10 \times 10\,\mathrm{cm}^2$ and a pixelised readout in the central part (cf. Figure 2.2). Through charge sharing, 1024 squared pads with a lateral length of 1 mm are able to detect scattered particles in the vicinity of the beam with a spatial resolution of 120 µm [18]. A set of 5 detectors was installed along the spectrometer as a replacement for more massive scintillating fibre detectors in order to minimise the material budget and therefore secondary interactions. They play an important role for the precise reconstruction of the fast proton p_f in central production reactions.

We will focus here on the performance observed during the operation of the PixelGEM detectors in the hadron beam for two years and the following high-intensity muon beam periods. A detailed description of the PixelGEM setup can be found in [59].

2.2.1 Commissioning and Performance

One PixelGEM detector was installed between the target and the first spectrometer magnet in order to provide an additional space point between the silicon micro-strip trackers and the tracking stations in the first spectrometer arm. The 4 remaining detectors were grouped in pairs, mounted back-to-back and rotated by an angle of 45° around the beam axis. One of these stations was installed up-, the other downstream of the second spectrometer magnet SM2 (cf. Figure 2.3).

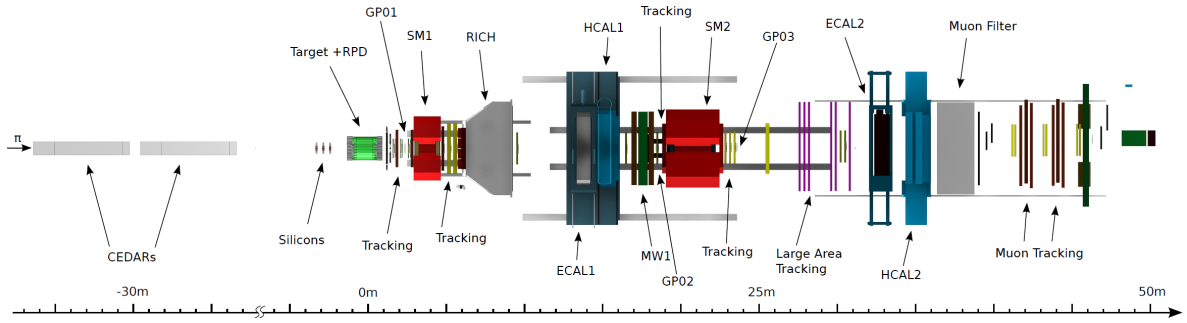

Figure 2.3: The COMPASS spectrometer setup seen from the top [97]. GP01,2,3 indicate the locations of the PixelGEM detectors.

An extensive analysis of the performance of the complete PixelGEM tracking system was presented in [99]. With a spatial resolution of around 90 µm and a background-corrected plateau efficiency above 99%, the detectors exceeded the design specifications in a low-intensity hadron beam ($5 \cdot 10^5$ particles/s). In nominal beam conditions, these performance benchmarks were slightly worsened by the current necessary to keep the GEM foils on their potential. Summarising, the PixelGEM detector system was operated successfully during the two years of hadron beam. It improved the acceptance of the spectrometer for beam tracks and particles scattered at very small angles, which is an important prerequisite for the analysis presented in this work.

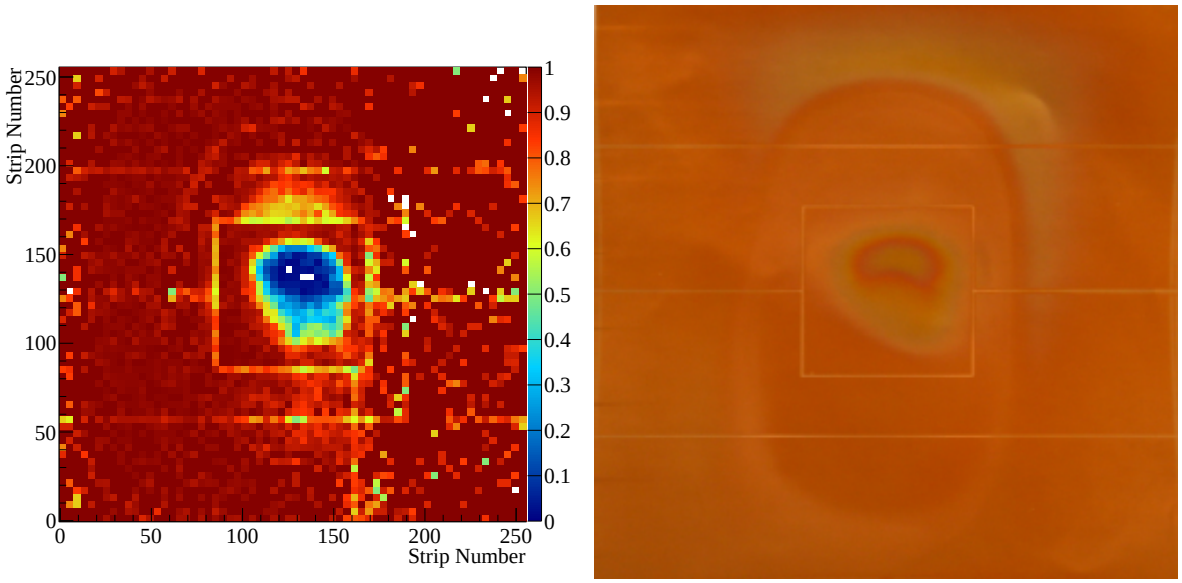

(a) Detection efficiency

(b) Deposit on the bottom of the third GEM foil

Figure 2.4: Aging effects in GP03XY [97].

After the completion of the hadron spectroscopy programme in 2009, the PixelGEM detector stations GP02 and GP03 remained in the spectrometer as a supplement. However, a decrease in the signal amplitude and thus the detection efficiency developed in a few detectors during the next two year of operation in a beam of up to $2 \cdot 10^7$ muons per second.

The shape in the centre (cf. Figure 2.4) apparently follows the occupancy distribution in the hadron beam [97]. In addition, an oval structure with a radius of about 3 cm is clearly observed in all detectors (cf. Figure 2.5). The planes were facing the beam back-to-back with an angle of 45°, which proves that the origin of this structure can only be related to something detector-external.

A decrease in performance of gaseous detectors correlated with radiation is often a sign for gas impurities in the detector volume [91]. As the gas tightness of the detectors was carefully tested during construction, the gas distribution system in the experimental zone can be a possible source for contaminations. With overpressure around 200 mbar, leakages of up to 30 ml/h were found and eliminated [97]. On the other hand, a direct correlation between the affected detectors and the leaks could not be proven.

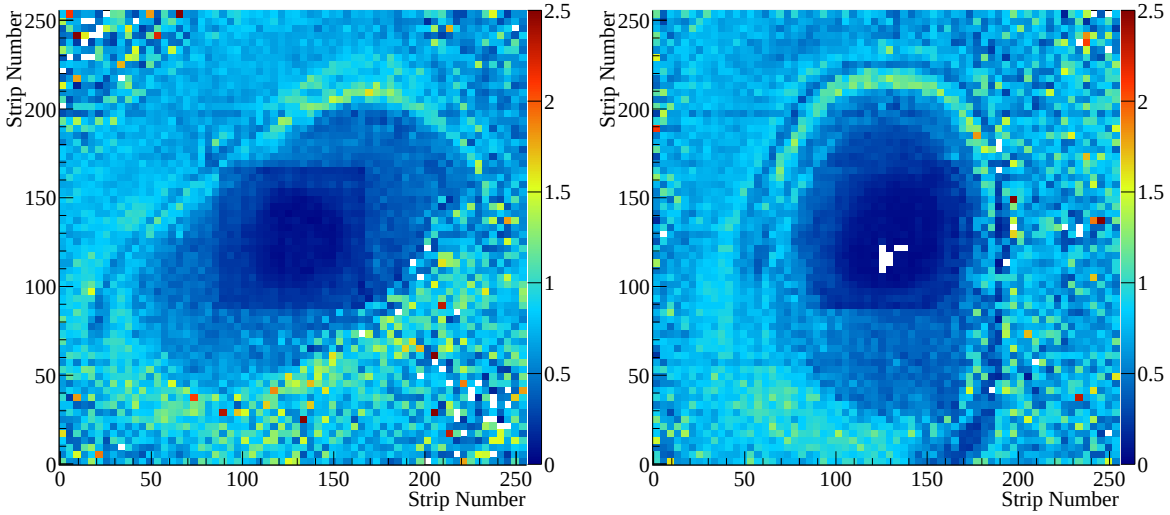

(a) GP03UV (b) GP03XY

Figure 2.5: Signal amplitude in arbitrary units [97].

2.2.2 Examination of Irradiated Detector

As the degradation of the performance was not recoverable, the detector with the worst signs was dismounted and examined in the laboratory. The position dependence of the signal amplitude could be directly reproduced with a focused X-ray source. In addition, measurements of the GEM foil currents showed a decreased amplification capability which indicated a physical or chemical alteration of the GEM foils themselves. However, a deposit on the readout foil which hinders the charge collection could not be completely excluded [97].

Opening of the affected detector revealed considerable amounts of a sealant[1], which was applied to the closed detector from the outside and apparently entered through leaking joints. This silicone based rubber is known to be prone to out-gassing, even though no negative effect on detector performances has been reported previously when it was used in very small quantities [32].

[1] Dow Corning 1-2577 Conformal Coating

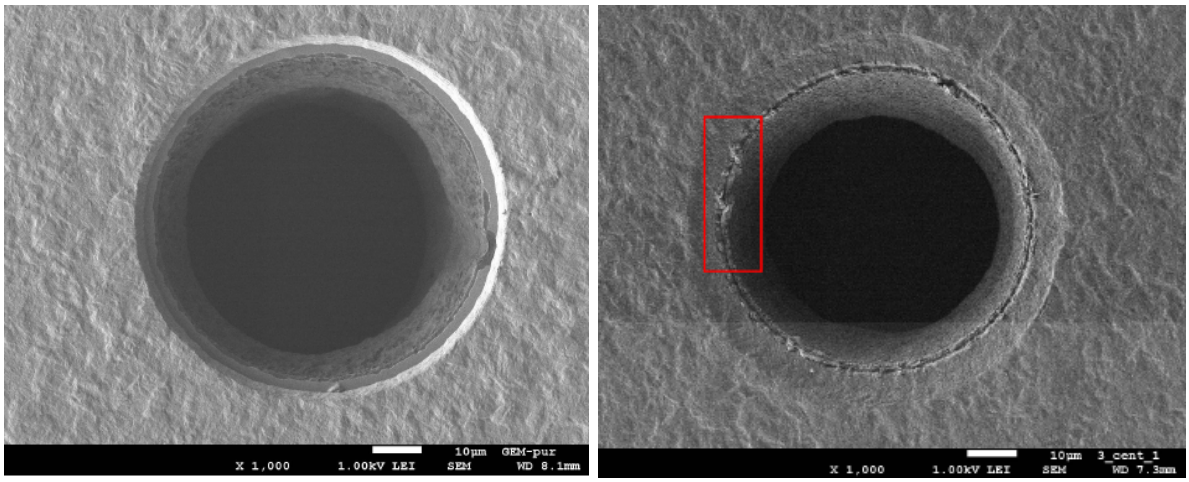

(a) Unused GEM foil (b) Irradiated GEM foil

Figure 2.6: SEM images of a GEM hole [44].

Furthermore, a deposit was found on all GEM foils and the readout plane, with increasing quantity from top to bottom. Its shape matches exactly the pattern of low efficiency regions seen in Figure 2.4. Especially the outline of the ring shape is as sharp as the distance between single GEM holes, a fact that does not find a correspondent in the experimental setup.

Pieces of the affected GEM foils were examined with a scanning electron microscope (SEM) and energy-dispersive X-ray spectroscopy (EDX) and compared to a sample of an unused foil. In addition to an enlarged rim around the GEM holes, deposits with sizes in the order of $1 - 10\,\mu\text{m}$ were seen both at the edge of the GEM holes and on the copper surface in between them (cf. Figure 2.6). Traces of silicon and sulphur could be detected on the irradiated samples [44]. Large percentages of carbon and oxygen on the previously pure copper surface indicate an organic coating. The silicone sealant can be responsible for these effects, even though it has no sulphur component. The crystalline structures (cf. red box in Figure 2.4b) built up by the sulphur contamination were traced back to the production of the readout plane, were sulphuric acid is used to remove remnants of glue on the pixel area. The comparison with SEM images of copper exposed to a high concentration of hydrogen sulphide [98] supports this conclusion (cf. Figure 2.7). Specifically which deposit is responsible for the performance deterioration could not be deduced at this stage.

2.2.3 Aging Studies in the Laboratory

In order to establish the effect of single substances on the performance of GEM detectors, the observed aging effects should be reproduced under controlled conditions in the laboratory. To this end, a modular detector with replaceable GEM foils was irradiated with X-ray intensities of up to $5 \cdot 10^7/\text{s}$ [96] for several days to reach accumulated charges comparable to the detectors in COMPASS. As the ambient air pressure and temperature lead to gain variations, the environmental conditions are recorded and corrected for. A well defined contamination can be brought into the gas circuit with a flushed box.

Preliminary measurements (cf. Figure 2.8) showed a successful operation of the system. However, a substantial decrease of the gain was observed already without additional contamination [96]. The visible alteration of the irradiated GEM foil surface indicates an aging effect, whose source is still under study.

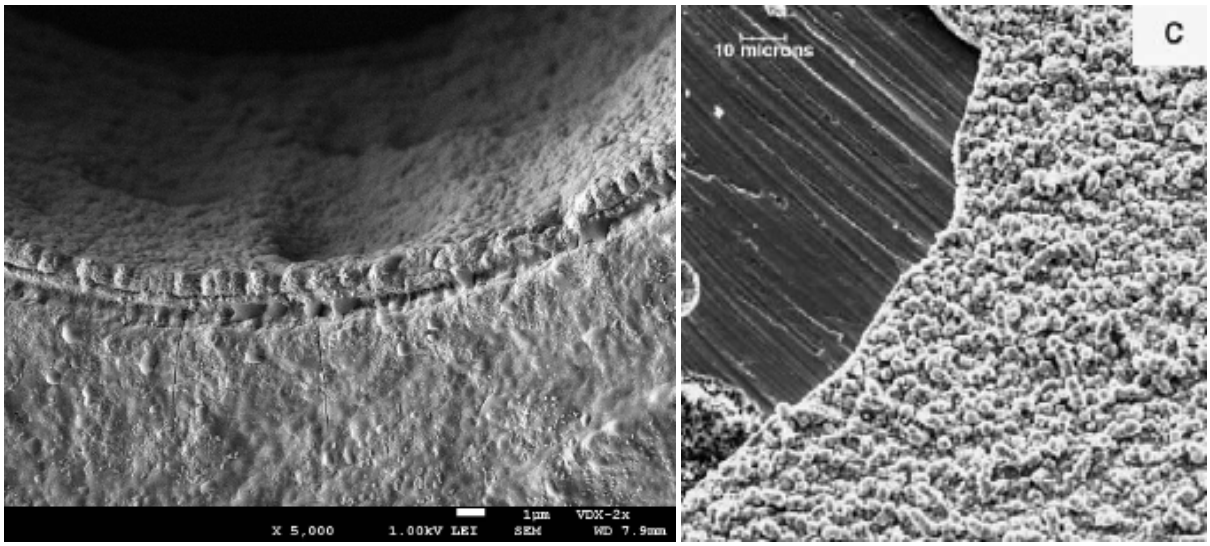

(a) Irradiated GEM foil [97] (b) Copper exposed to H_2S [98]

Figure 2.7: SEM images of sulphur deposit on copper.

2.2.4 Modification to Production

It was found out that the composition of the used glue[2] was changed by its manufacturer after it was certified for out-gassing [32]. It therefore constituted an additional risk for contamination. Finally, four entirely new detectors were built with special care concerning impurities in the gas volume. A different, certified glue[3] was applied in predefined portions using a dispenser robot. The same glue was also used in small quantities to seal the detector from the outside. Two new detectors replaced the deficient station GP03 for the 2012 run with hadron beam. In addition, one detector was added to GP01 in order to complete the station. The development of any deficiency could not be observed so far.

2.3 Spectrometer Alignment

In total, the COMPASS spectrometer uses more than 200 tracking detector planes to reconstruct charged particle trajectories. A trigonometric survey provides their position within the experimental setup with a precision down to 1 mm. However, many detectors reach up to two orders of magnitude better spatial resolutions. In addition, their physical fixations are affected by their weight, temperature variations and a strong magnetic field. In order to achieve an optimal track reconstruction performance, corrections to the position and orientation of the tracking detectors in space are mandatory. In the following section, we will describe the official software alignment procedure [6], which was applied to the reconstruction of the analysed data set.

[2] Araldite AY103-1
[3] Stycast 1266

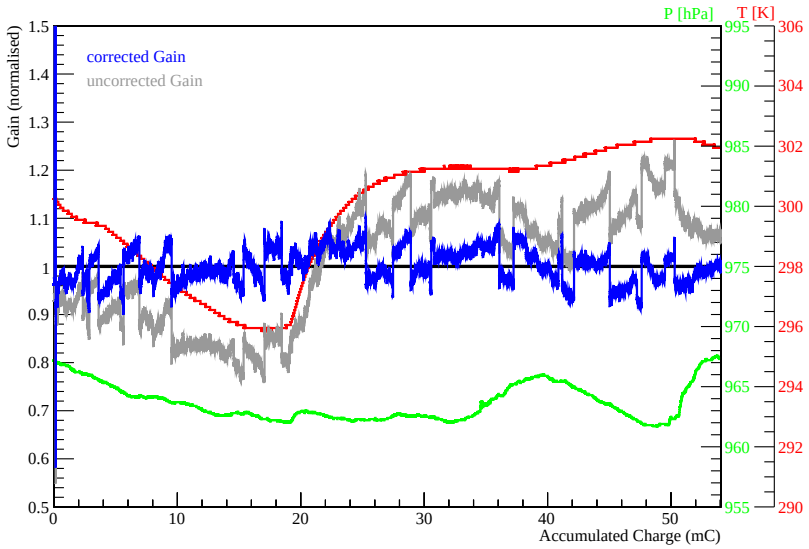

Figure 2.8: Gain measurement corrected for temperature and pressure variations [96].

2.3.1 Alignment Method

The starting point of the software alignment is a sample of tracks reconstructed with preliminary detector positions. Typically, it consists of 10^4 to 10^6 trajectories. For all detector planes, corrections for a translation along the measured coordinate, a rotation around the beam axis, and the effective pitch are possible. The effective pitch accounts for a possible inclination of the detector plane with respect to the beam axis. Only the position along the beam axis is difficult to determine in the forward spectrometer geometry. It is usually kept fixed unless the residual distribution of a given plane indicates a large deviation.

The corrections are determined by minimising the weighted sum of squared errors χ^2 of all tracks in the sample. The Millipede program [28] is used to perform this fit, which can have more than 1000 parameters. In a linear model, the matrix describing the problem is large but sparsely populated and can therefore be analytically inverted. A new set of tracks is reconstructed with the obtained corrections and the procedure is iterated until the parameters converge and become negligible compared to the detector resolution. Four detector planes with a large lever arm have to be kept at fixed positions to prevent a collective drift of the entire coordinate system.

The COMPASS alignment is started with special data recorded with the spectrometer magnets switched off. In this case, straight tracks can be safely assumed in order not to bias the momentum reconstruction. A widely defocused muon beam and the trigger on the beam and veto counters reach a broad illumination of all detector planes. Afterwards, additional corrections are generated for the detector planes downstream of the target in the magnetic field, which not only shifts the positions of the mechanical support of some detectors, but also influences the internal processes of charge propagation in gaseous detectors. The effect is strongest for the small-area trackers in the fringe field of SM1 where the Lorentz-force acting on drifting and amplified charges results in an apparent translation of the detector planes of up to 400 µm. For these detectors, a correction in form of an effective shift is applied, since the distortion is approximately uniform over the active area of the respective detector [6].

As a last step, the detector positions and orientations are finalised on a track sample as it is used for the analysis. This ensures the right weighting of detector contributions to the reconstructed data set. The vertex reconstruction in the target is also optimised. For the hadron-beam data taking period, the entire procedure was repeated approximately every two weeks, mainly after longer periods of access to the experimental zone when detectors were moved or replaced.

2.3.2 Time-Dependent Alignment

Displacements of up to 50 µm have been observed for the silicon micro-strip detectors during the course of one day. Since this is a multiple of their spatial resolution, a time-dependent alignment has been introduced in order to profit from the full vertexing capabilities. Corrections to the positions of the silicon planes are generated for each run, which can span a period of up to 3 hours. As an example, Figure 2.9 illustrates the movements of the five silicon tracker stations in the vertical plane as a function of time. A correlation with the ambient temperature measured nearby in the experimental area is evident. Since the same starting values are used for all processed runs, the continuity of the curves further supports the validity of these corrections. Especially for final states with only one charged track [7, 100], the precision for vertex reconstruction is substantially increased. As a result, specially events with scattering angles below 1 mrad can be reconstructed with considerably reduced background (cf. Figure 2.10). The different solid targets (Ni, W) can be nicely resolved.

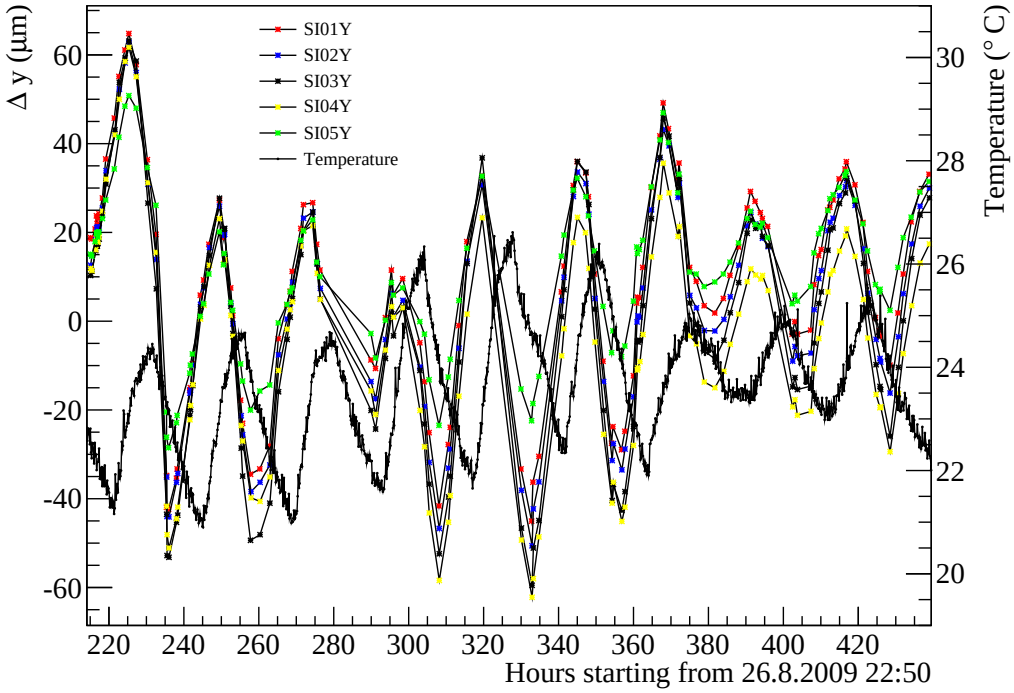

Figure 2.9: Silicon micro-strip detector alignment vs. time.

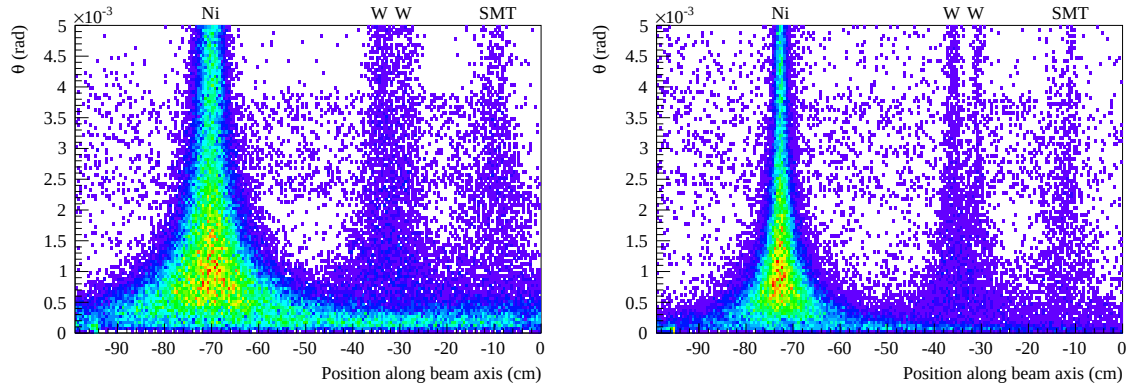

(a) standard reconstruction

(b) run-by-run alignment

Figure 2.10: Scattering angle as a function of the reconstructed primary vertex position along the beam axis [6].

Chapter 3

Data Selection

COMPASS recorded data with a 191 GeV/c proton beam in 2008 and 2009. A two week long pilot run in 2008 was intended as a test and the trigger composition was changed several times. In 60% of these data, the same trigger was used as in the eight week long main data taking campaign in 2009. In addition, the trigger rate could be increased by approximately 50% in 2009. For this reason, the pilot run data amounts to less than 10% of the total sample. Even though the analysis has been started on this considerably smaller data set, it is neglected for the final results as it requires a different treatment concerning both selection and simulation.

A rough estimate of the available luminosity can be calculated based on the number of scattering centres in the target volume per area. The total number of incident beam particles measured by a counting unit connected to the scintillating fibre detector upstream of the experimental zone is approximately 10^{13} for the analysed data set. Taking into account the fraction of protons in the positively charged hadron beam of about 75%, an integrated luminosity of approximately $12\,\mathrm{pb}^{-1}$ of proton-proton reactions was available in 2009. Due to trigger and reconstruction efficiencies as well as dead-times, the effective luminosity was reduced by about a factor of ten [8].

3.1 Event Topology

3.1.1 Trigger

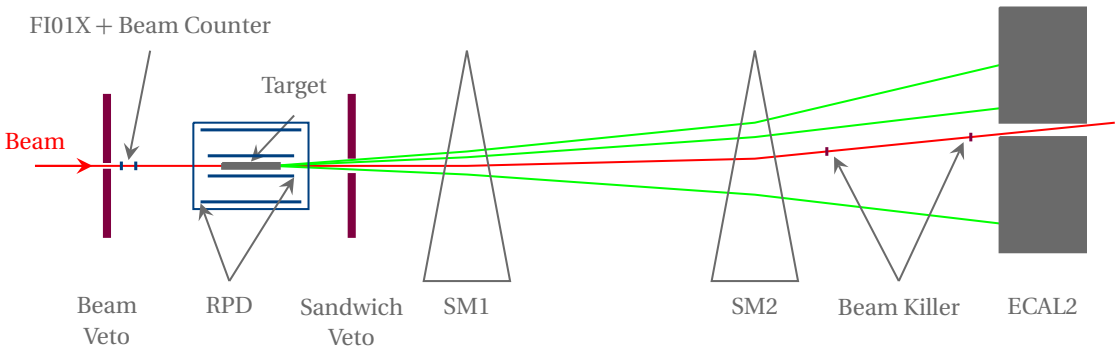

Figure 3.1: DT0 trigger scheme: Trigger (blue) and Veto (purple) components [59]. In the spectrometer, a non-interacting beam track (red) and an event with three charged tracks (green) is drawn for illustration.

The principal trigger used to record the data is called DT0[1]. It requires a signal from an incoming beam proton in a scintillator disc with 3.2 cm radius which was placed approximately 7 m upstream of the target. The horizontal plane of the scintillating fibre detector upstream of the target (FI01X) is used in coincidence. A signal from a particle recoiling from the target and hitting both barrels of the recoil proton detector (RPD) system indicates an interaction within the target volume. Since the recoil proton has to be able to leave the target with enough energy to penetrate the inner barrel and reach the outer scintillator slabs, this results in a minimum value for the squared four-momentum transfer to the target proton of about $0.07\,\mathrm{GeV}^2/c^2$.

Furthermore, a veto system helps to select only clean and reconstructable events. It blocks events with one or more beam particles outside of the target region or particles traversing the spectrometer without any interaction. If one or more particles leave the target with a polar angle of more than 180 mrad with respect to the beam axis, the event is outside of the spectrometer acceptance and discarded by the sandwich veto detector [95]. Figure 3.1 illustrates the trigger scheme with all components and particle trajectories for exemplary events.

During the data taking periods, few other triggers were also recorded for calibration purposes. These include non-interacting beam particles, particles from the halo of the beam and a random trigger. However, about 95% of the recorded events fulfilled the DT0 criteria and were used in the analysis presented in this work.

3.1.2 Primary-Vertex Reconstruction

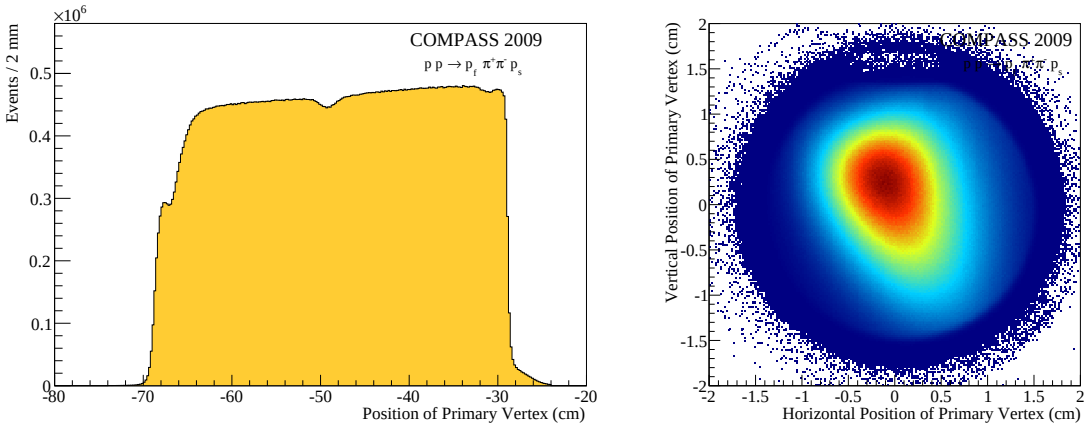

(a) Longitudinal projection

(b) Transverse projection

Figure 3.2: Primary vertex distribution.

For the analysis described in this work, the events are required to have exactly one reconstructed primary vertex within the physical boundaries of the liquid hydrogen target in order to avoid ambiguities in the RPD reconstruction (cf. Section 3.1.3). In addition, the vertex has to have exactly three reconstructed outgoing particle tracks whose charge sum matches the incident positive beam. Figure 3.2 shows the spatial distribution for the accepted vertices along the beam axis (a) and in the transverse plane (b). A dip can be observed near $-50\,\mathrm{cm}$, which reflects a minor inefficiency of the RPD trigger. At this position, light guides are attached to the scintillator slabs for calibration. In the transverse plane, the vertex distribution follows

[1] Diffractive Trigger 0

the beam profile which is centred on the target. The filling level of liquid hydrogen can be discerned in the upper part.

3.1.3 Particle Identification

The positive hadron beam with a momentum of 191 GeV/c consists of 74.6% protons, 24.0% pions and 1.4% kaons [6] at the COMPASS target. The experimental setup includes a set of two differential Cherenkov detectors (CEDAR) located upstream of the target in order to distinguish between the different beam components. However, one of the CEDAR detectors was used to positively identify pions in the beam for a part of the data recording period. Hence, we require a positive proton signal in only one of the CEDARs for the event selection. The settings have to be adapted time-dependently, which is realised by means of a data base. The combination of efficiency and geometrical acceptance of the CEDAR detectors was measured to be close to 90% [6].

The recoil proton detector represents the most important contribution to the diffractive reaction trigger DT0. In addition, the specific energy loss spectra in the outer barrel of the RPD can be used to identify the recoiling protons. With elastic scattering data, it was verified that the vast majority of the recoil particles are protons [6]. With this information, the time-of-flight measurement between both barrels allows the reconstruction of the four-momentum of the recoil proton which is later used in evaluating the energy and momentum balance (cf. Section 3.1.4). Only events with exactly one charged track in the RPD were accepted in order to avoid ambiguities.

Of the three tracks leaving the primary vertex, two have positive charge. They have to be distinguished using the information provided by the ring imaging Cherenkov (RICH) detector in order to assign the right mass to the particles. However, the present RICH setup only allows reliable particle identification up to 50 GeV/c. On the other hand, the beam proton is expected to transfer only a small fraction of its momentum in central production reactions and therefore remains the most energetic particle in the reaction. Hence, the proton cannot be identified directly. In exchange, the other positive particle can be identified as either pion or kaon in about 60% of the events.

As the hadronic cross section for pion production is by more than one order of magnitude larger than that for kaons [13], misidentification of other particles as π^+ does not play a significant role for the channel studied in this work. A simple comparison of the likelihoods $\mathcal{L}$ for the pion, kaon, proton or background hypotheses of the positive track is enough to select a clean sample of $\pi^+\pi^-$ events. In Figure 3.3, the momentum distributions of the identified sample are compared with events for which a mere assignment of the proton mass to the faster positive particle was used. The low momentum threshold of 2.8 GeV/c for pion identification is thereby reflected by the suppression of the enhancement at 180 GeV/c in the momentum distribution of the fast proton p_f (cf. Figure 3.3b). In combination with the characteristics of the central production reaction, this selection criterion will be reconsidered in Section 3.3.

Due to its much smaller cross section [13], the identification of produced kaon pairs requires more attention. First of all, the lower momentum threshold at 9.5 GeV/c severely limits the kaon identification capabilities of the RICH detector in the COMPASS setup. In addition, the probability for the misidentification of a π^+ as a K^+ can create a large impurity in the sample. If it is evaluated with the pure particle samples as described in [66], the misidentification probability rises tremendously for momenta above 40 GeV/c (cf. Figure 3.4). Consequently, the number of misidentified pions may even exceed the expected number of kaons. This pion background can be suppressed by applying a threshold on the ratio of the likelihoods $\mathcal{L}_{K^+}/\mathcal{L}_\mathrm{other}$. The momentum distribution of identified kaons is shown in Figure 3.5 for increasing likelihood

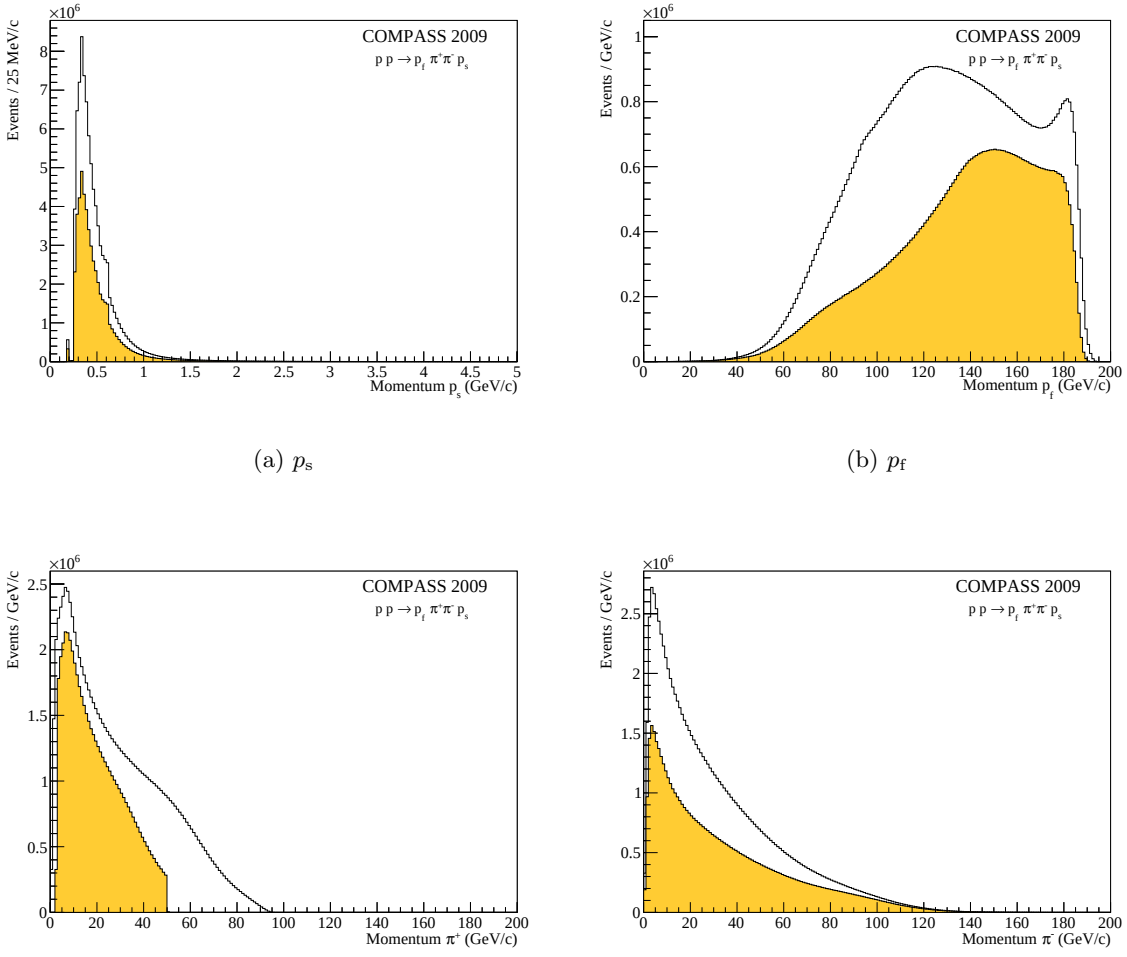

(a) p_s

(b) p_f

(c) π^+

(d) π^-

Figure 3.3: Laboratory momentum distributions for the reaction $pp \to p_\mathrm{f}\pi^+\pi^-p_\mathrm{s}$ with all selection cuts applied (filled) and without the RICH identification of π^+ (open).

thresholds. Only for the final value of 1.30, the unphysical enhancement towards high momenta owing to misidentified pions is completely suppressed (cf. also Figure 4.9). Even higher values of this ratio do not improve the purity of the sample, while valid events are lost uniformly along the K^+ momentum. With this identification scheme, the negative particle can be safely attributed as K^- owing to the conservation of strangeness in hadronic reactions.

3.1.4 Four-Momentum Conservation

The beam energy is not measured in the COMPASS hadron beam setup. In order to guarantee the exclusivity of the measurement, the total energy of all measured final-state particles is summed up. A clear peak at 192 GeV is obtained (cf. Figure 3.6), which reflects the mass of the target proton added to the beam energy. Only the events whose energy sum lies within the boundaries of three standard deviations around the maximum are accepted. The width of the exclusivity peak of about 1.6 GeV is mainly given by the intrinsic momentum spread of the beam line and is far larger than the resolution of the spectrometer (cf. Chapter 4).

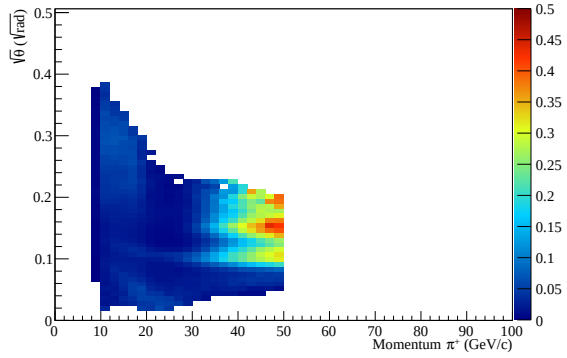

Figure 3.4: Misidentification probability for π^+ as K^+ with $\mathcal{L}_{K^+} > 1.00\,\mathcal{L}_{\pi^+}$ depending on p_{lab} and polar angle θ w.r.t. beam axis.

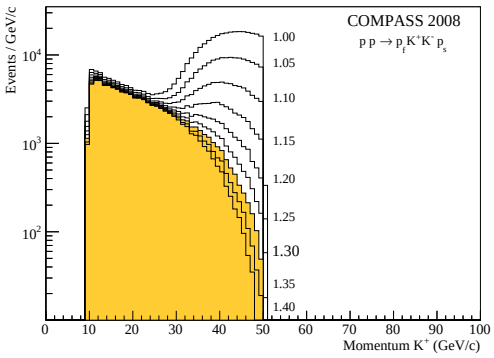

Figure 3.5: Momentum distribution of identified K^+ with different likelihood thresholds after all selection cuts.

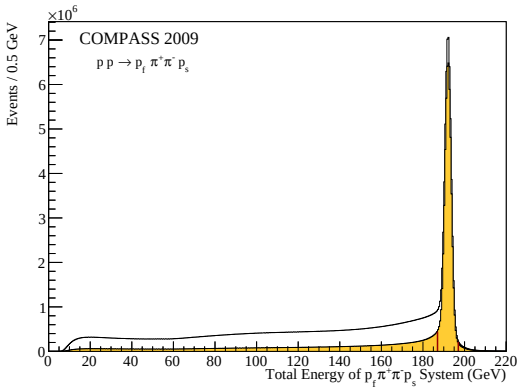

Figure 3.6: Energy sum of the selected sample (filled), $\pm 3\sigma$ indicated by bars, without azimuthal cut (open).

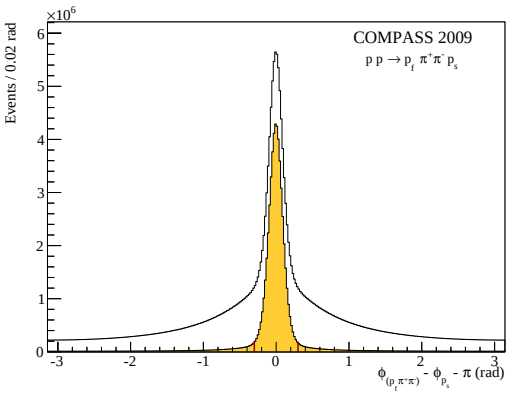

Figure 3.7: Azimuthal correlation between p_{s} and the $p_{\text{f}}\pi^+\pi^-$ system (filled), $\pm 3\sigma$ indicated by bars, without energy cut (open).

In addition, the information provided by the RPD is used to correlate the azimuthal angle ϕ of the recoil proton with the one of the forward going three body system $p_{\text{f}}\pi^+\pi^-$. As they should be back-to-back for exclusive reactions, a peak at 180° can be observed in the angle difference (cf. Figure 3.7). The requirement that the angle lies around 3 standard deviations ($\sigma_\phi \approx 0.1\,\text{rad}$) around the maximum has a big overlap with the requirement for energy balance. The combined application of both cuts guarantees an exclusive sample. For the case of di-pion production, the contribution from additional final-state particles which escape the detection lies below 5% with these cuts.

In total, approximately $9 \cdot 10^7$ exclusive events with the required topology of four outgoing charged tracks were recorded in 2009. In more than $5 \cdot 10^7$ events, one positive track can be identified as a pion. The positive kaon could be identified for about $8 \cdot 10^5$ events. We will examine these data samples in detail in the following section, before revisiting the particle identification methods for centrally produced events (cf. Section 3.3).

3.2 Diffractive Dissociation of Beam Protons

Without further selection criteria, diffractive dissociation of the incident proton dominates the proton-proton cross section at $\sqrt{s} = 18.9\,\mathrm{GeV}$. This reaction provides access to the excited baryon spectrum, which is as important for the understanding of QCD as the meson spectrum. Baryons as three-quark systems may be sufficiently complex to reveal physics which is hidden in the meson sector [73]. Complementary to existing photo-production experiments, hadron-induced reactions can help to complete the knowledge about the baryon spectrum. Poorly known parameters of excited baryons like their widths and branching ratios can become accessible. In this case, especially the $N\pi\pi$ decay modes are important to reach high-mass and high-angular-momentum states.

Since baryon spectroscopy is not the prime focus of this work, only a selection of relevant kinematic spectra will be presented in the following. All distributions show the data sample selected with the criteria introduced above, including the identification of the positive meson by the RICH detector. The data set serves as a starting point for a dedicated partial-wave analysis [17, 104].

3.2.1 N^* and Δ Resonances

At first, we focus on the $p_\mathrm{s}\pi^+\pi^-$ final state. The squared four-momentum transfer t from the beam to the target proton peaks at low values which is characteristic for the dominant diffractive scattering [43]. The sharp cut at $0.07\,\mathrm{GeV}^2/c^2$ is created by the acceptance of the recoil proton detector as the central trigger element (cf. Figures 3.8a-c). Events below this threshold which passed the selection are presumably triggered by delta electrons or pile-up events.

On the other hand, the t distribution shows a strong dependence on the invariant mass of the produced $p_\mathrm{f}\pi^+\pi^-$ system. This is illustrated by fitting the sum of two exponential functions to the t distributions in mass bins of $10\,\mathrm{MeV}/c^2$. Figure 3.8 shows the fitted values for the exponential slopes (d), their relative contribution (e) and the reduced χ^2 as a measure for the goodness of fit (f) as a function of the three-body mass. Near threshold, the t distribution is completely dominated by a component with a steep slope. However, the simple model is clearly not sufficient to describe the data (cf. Figure 3.8a), which is also reflected in the χ^2 distribution. For masses above $1.8\,\mathrm{GeV}/c^2$, two exponents with slopes around $-11\,(\mathrm{GeV}/c)^{-2}$ and $-4.5\,(\mathrm{GeV}/c)^{-2}$ fit the data with high accuracy (cf. Figure 3.8c). A similar behaviour was seen in the diffractive dissociation of a negative pion beam into a three-pion system [59].

In the mass region below $2\,\mathrm{GeV}/c^2$, the t distribution is modified by the occurrence of baryon resonances, which can be seen especially in the relative strength of the two fitted exponential curves (cf. Figure 3.8e). The invariant mass distribution of the $p_\mathrm{f}\pi^+\pi^-$ system shows visible enhancements as well (cf. Figure 3.9a). As a partial-wave analysis is needed in order to determine spin and parity of the resonances, we can only list possible states with relevant $N\pi\pi$ decay modes which can be found in the Review of Particle Physics [26]. In the 2012 issue, a new naming scheme for baryons was introduced to specify the intrinsic properties J^P and to be independent of the formation reaction. It will be employed in the following.

Since the dominating Pomeron exchange does not transfer isospin [43], only N^* states with $I = \frac{1}{2}$ are taken into account. Even if we consider only states whose existence is certain or at least very likely[2], the prominent peak around $1.7\,\mathrm{GeV}/c^2$ could contain contributions from $N(1700)\,3/2^-$, $N(1710)\,1/2^+$ and $N(1720)\,3/2^+$. The masses and widths of these states are only known with an uncertainty of $50 - 100\,\mathrm{MeV}/c^2$. The less pronounced peak around

[2] i.e. these states have **** and *** ratings in the PDG [26]

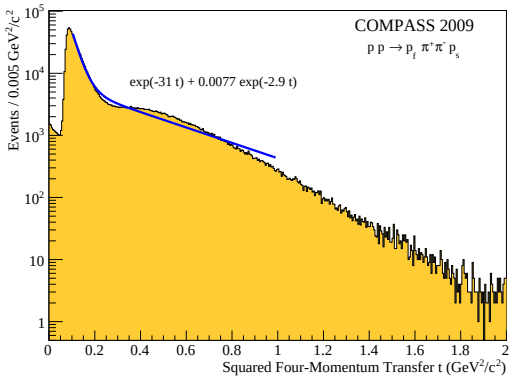

(a) $m_{p_f\pi^+\pi^-} < 1.40\,\mathrm{GeV}/c^2$

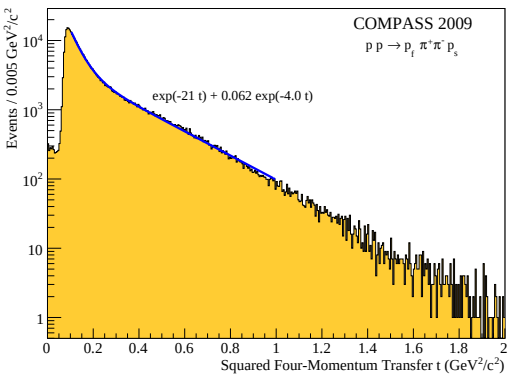

(b) $1.50\,\mathrm{GeV}/c^2 < m_{p_f\pi^+\pi^-} < 1.51\,\mathrm{GeV}/c^2$

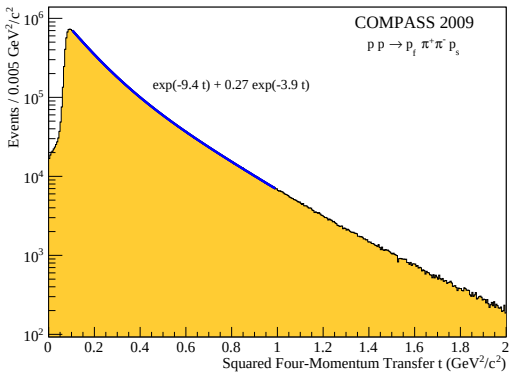

(c) $2.00\,\mathrm{GeV}/c^2 < m_{p_f\pi^+\pi^-} < 2.01\,\mathrm{GeV}/c^2$

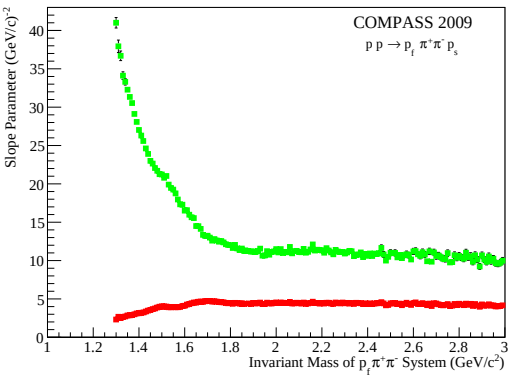

(d) Slopes parameters b_1 (green) and b_2 (red)

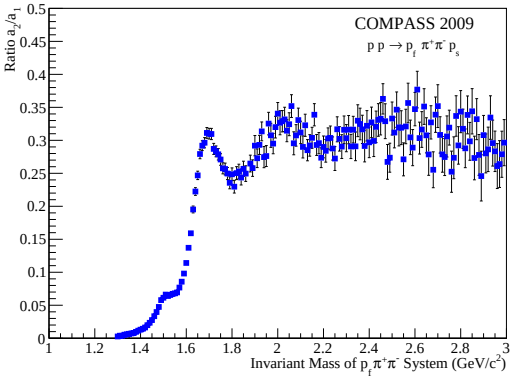

(e) Ratio $\frac{a_2}{a_1}$

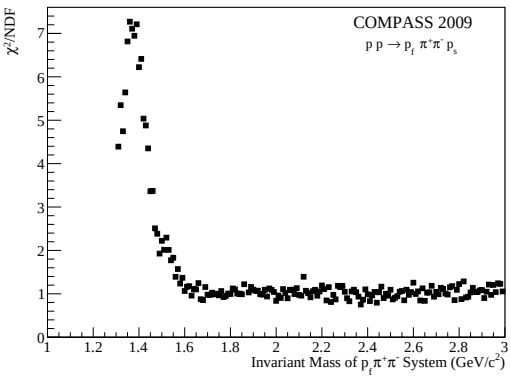

(f) χ^2/NDF

Figure 3.8: t distributions with fit of $a_1e^{-b_1t}+a_2e^{-b_2t}$ (blue) in the range $[0.1, 1.0]\,\mathrm{GeV}^2/c^2$ (a-c), parameters of the fit in $10\,\mathrm{MeV}/c^2$ bins of the $p_f\pi^+\pi^-$ mass (d-f).

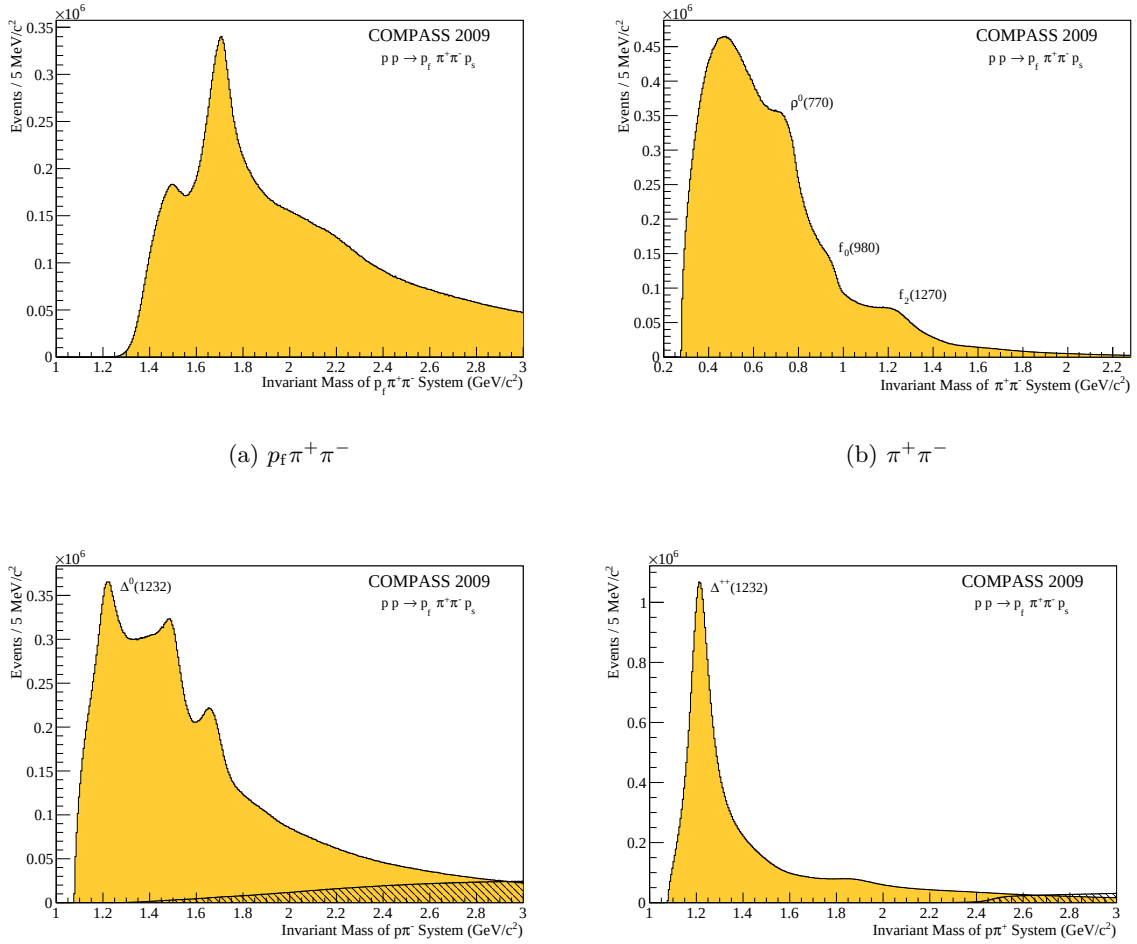

(a) $p_\mathrm{f}\pi^+\pi^-$

(b) $\pi^+\pi^-$

(c) $p_\mathrm{f}\pi^-$ ($p_\mathrm{s}\pi^-$ hatched)

(d) $p_\mathrm{f}\pi^+$ ($p_\mathrm{s}\pi^+$ hatched)

Figure 3.9: Invariant mass spectra for the $p_\mathrm{f}\pi^+\pi^-p_\mathrm{s}$ final state.

$1.5\,\mathrm{GeV}/c^2$ may include the well explored $N(1520)\,3/2^-$, $N(1520)\,1/2^-$ and even a shoulder towards lower masses stemming from the Roper resonance $N(1440)\,1/2^+$ [87]. The enhancement at $2.2\,\mathrm{GeV}/c^2$ could be a sign for the highly excited states $N(2190)\,7/2^-$, $N(2220)\,9/2^+$ and $N(2250)\,9/2^-$ which were mainly studied in $N\pi$ decays so far. Additional baryon resonances may be hidden beneath these peaking structures. Since nearly all quantum numbers can be produced in this reaction, a partial-wave analysis of the data sample is very challenging. On the other hand, it might be the only way to confirm the existence of these states or to determine their properties precisely.

A common approach to formulate the amplitudes for a partial-wave analysis assumes the isobar model, which describes the decay of a diffractively produced resonance through a series of two-body decays. The intermediate states, the eponymous isobars, are either modelled using knowledge from other experiments [59] or fitted themselves [69]. For the case of an excited N^* resonance decaying into three hadrons, both $N\pi$ as well as $\pi\pi$ resonances are possible as intermediate states (cf. Figure 3.10).

The invariant mass distribution of the $\pi^+\pi^-$ system shows clear signatures for the $\rho(770)$, $f_0(980)$ and $f_2(1270)$ mesons (cf. Figure 3.9b). Since these resonances play also an important

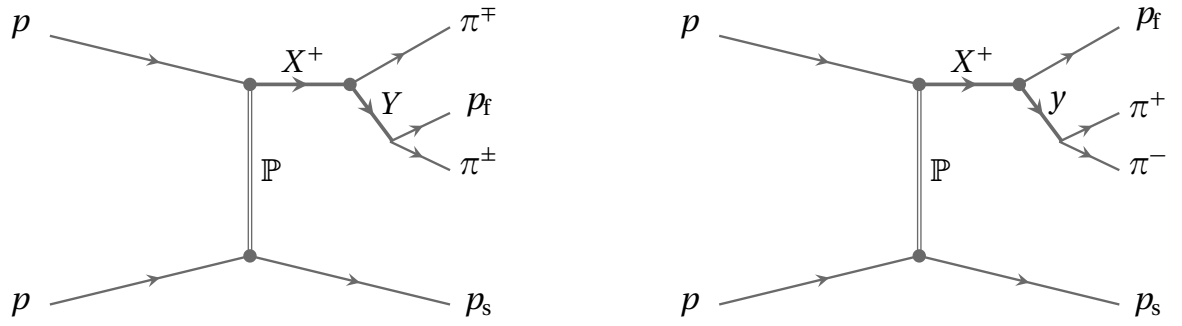

(a) Baryonic isobar Y, two possibilities

(b) Mesonic isobar y

Figure 3.10: Diffractive proton dissociation into $p\pi^+\pi^-$ in the isobar model.

role in the central-production analysis, we will discuss the influence of diffractive dissociation as a background later in this work.

The observation of excited baryons in the $p\pi$ subsystems is striking. The invariant mass spectrum of the $p_\mathrm{f}\pi^-$ system (cf. Figure 3.9c) shows a very prominent $\Delta^0(1232)\,3/2^+$ baryon, but at least two peaks formed by other nucleon excitations like the $N(1535)\,1/2^-$, $N(1650)\,1/2^-$ and $\Delta(1700)\,3/2^-$ can be discerned. As both $I = \frac{1}{2}$ and $I = \frac{3}{2}$ (Δ) are possible as intermediate states, the unambiguous identification is even more speculative without a dedicated partial-wave analysis.

Only $I = \frac{3}{2}$ resonances can be formed by the doubly charged $p_\mathrm{f}\pi^+$ combination (cf. Figure 3.9d). The invariant mass distribution is dominated by the $\Delta^{++}(1232)\,3/2^+$ resonance, even though an enhancement around $1.9\,\mathrm{GeV}/c^2$ is evidence for the presence of higher excitations. Since Δ^{++} production seems to represent a large fraction of the data, [74] suggested it as a possibility to obtain the Reggeon-exchange contribution to the central production process. However, the Δ^{++} as intermediate state in the decay of an N^* resonance does not allow conclusions of this kind.

No resonant structures can be discerned for the $p_\mathrm{s}\pi^\pm$ combinations (cf. hatched histograms in Figures 3.9c and d). The kinematic limits for the identification of the π^+ by the RICH detector allow only masses above $2.4\,\mathrm{GeV}/c^2$ in the $p_\mathrm{s}\pi^+$ system.

3.2.2 Baryon Resonances with Strangeness

If one positive particle is identified as a kaon, strangeness conservation implies the production of a kaon pair in the reaction. This enables us to study decays of excited N^* baryons into intermediate states with strangeness. The narrow $\Lambda^0(1520)\,3/2^+$ in the invariant mass spectrum of the $p_\mathrm{f}\,K^-$ subsystem (cf. Figure 3.11a) can even be treated as a quasi-stable final-state particle in a two-body analysis. Signs for higher-mass baryon excitations with strangeness are discernible around 1.7 and $1.8\,\mathrm{GeV}/c^2$. No resonances are allowed in the $p_\mathrm{f}\,K^+$ subsystem. The three-particle invariant mass with a threshold around $2\,\mathrm{GeV}/c^2$ neither shows evidence for resonant components.

The K^+K^- invariant mass distribution exhibits a very narrow $\phi(1020)$ peak with a width of approximately $5\,\mathrm{MeV}/c^2$ (cf. Figure 3.11b). Also this vector meson with hidden strangeness is an indication for the isobaric decay of N^* resonances above $2\,\mathrm{GeV}/c^2$, which are studied in [8]. The other structures in the spectrum, which may for example arise from K^+K^- decays of $f_2(1270)$, $f_0(1500)$ and $f_2'(1525)$ mesons, will be discussed in detail in Chapter 7.

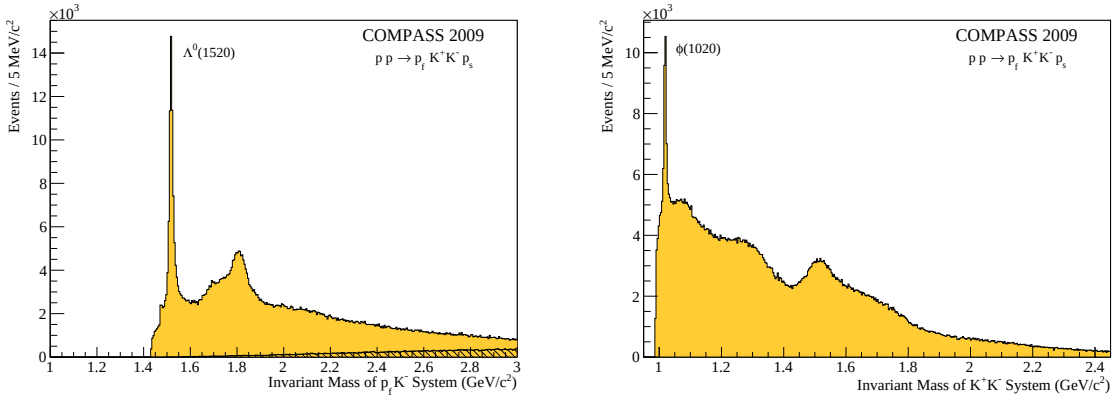

(a) $p_\mathrm{f}K^-$ ($p_\mathrm{s}K^-$ hatched) (b) K^+K^-

Figure 3.11: Invariant mass spectra for the $p_\mathrm{f}K^+K^-p_\mathrm{s}$ final state.

3.3 Selection of Central Production

Since the trigger was not sensitive to a specific production mechanism, additional kinematic cuts are indispensable in order to enrich the central-production component. Various approaches have been used in the past and were examined with our data. Most of the methods showed a large overlap, but none was able to successfully single out a pure double-Pomeron exchange sample for the centre-of-mass energy of $\sqrt{s} = 18.9\,\mathrm{GeV}$. However, a final choice can only be reached after effects of the diffraction background component on the partial-wave decomposition are observed in Chapter 5.

We will focus on the selection of centrally produced di-pion systems for the rest of this chapter. The discussion of the kaon-pair production will be resumed in Chapter 7.

3.3.1 Invariant-Mass Cut

The invariant mass spectrum of the $p_\mathrm{f}\pi^+$ subsystem shows a dominant $\Delta^{++}(1232)$ peak (cf. Figure 3.9d). The production of baryon resonances is also obvious in the $p_\mathrm{f}\pi^-$ subsystem (cf. Figure 3.9c). Similar contributions were also reported for data recorded by the OMEGA spectrometer [21], where an invariant mass of at least $1.5\,\mathrm{GeV}/c^2$ was required for the $p_{\mathrm{f,s}}\pi^\pm$ (short: $p\pi$) combinations in order to enrich the centrally produced $\pi^+\pi^-$ system in the sample. Even though this mass cut cannot suppress the diffractive-dissociation component completely, the final results do not change significantly when the threshold is increased to $2.0\,\mathrm{GeV}/c^2$.

A qualitative comparison of our $p_\mathrm{f}\pi^\pm$ invariant mass spectra with the ones observed with the WA102 experiment [21] at $\sqrt{s} = 29.1\,\mathrm{GeV}/c^2$ reveals a considerable suppression of the masses above $2\,\mathrm{GeV}/c^2$ with respect to the peak height of the baryon resonances in the COMPASS data. It is, however, difficult to judge whether the different $\sqrt{s}$-dependence of the competing production processes (cf. Section 1.2.2) is responsible for this difference. The requirement for a fast proton scattered in forward direction, which was used as a part of the trigger in the OMEGA setup [21], can also have a similar effect.

In order to be able to compare the analyses of both experiments, we decided to adopt the same kinematic cuts for the selection of the centrally produced system at first. Figure 3.12a illustrates the momentum distribution of the proton p_f for events where the $p\pi$ combinations

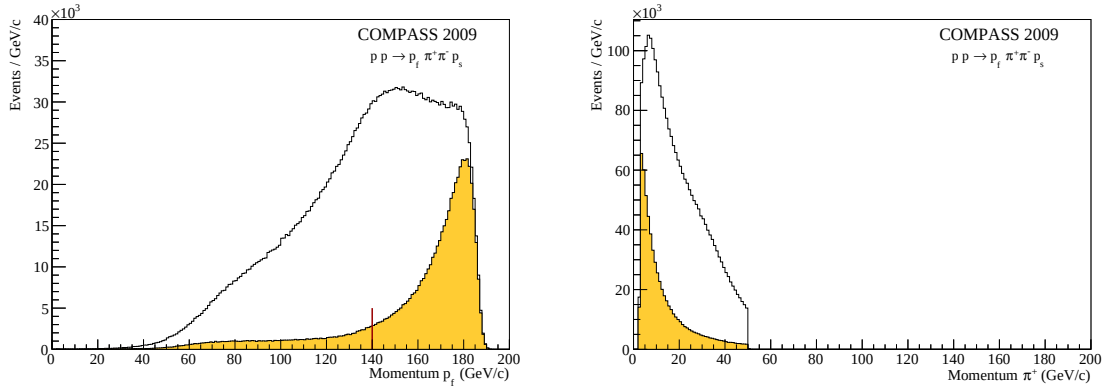

(a) p_f (b) π^+

Figure 3.12: Momenta in laboratory frame for events with identified π^+, $m(p\pi) > 1.5\,\mathrm{GeV}/c^2$ (filled).

have an invariant mass above $1.5\,\mathrm{GeV}/c^2$. As expected for centrally produced events, the distribution peaks at values near the beam momentum of $191\,\mathrm{GeV}/c$. The momentum of p_f is limited by the minimum momentum required for the other charged particles to reach the first spectrometer magnet. In addition, the RICH detector has a momentum threshold of $2.8\,\mathrm{GeV}/c$ for the π^+ to be identified. On the other hand, the long tail of the momentum distribution towards low momenta has to be cut at $140\,\mathrm{GeV}/c$ in order to suppress events with a fast π^-. The requirement for a large proton momentum alone is not sufficient to select central production reactions, in contrast it can even accentuate the baryon resonances in the $p_\mathrm{f}\pi^-$ subsystem (cf. Figure 3.13).

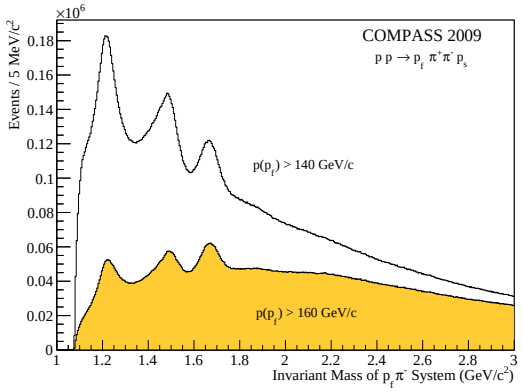

Figure 3.13: Invariant mass spectrum of $p_\mathrm{f}\pi^-$ with momentum cut for p_f.

In Section 3.1.3, we used the RICH detector to distinguish the two forward-going particles p_f and π^+ in the final state. After the additional removal of low masses in the $p\pi$ subsystems, the particles are clearly separable by their momentum in the laboratory frame. The momentum distribution for the proton p_f peaks at values close to the beam energy while the majority of produced positive pions has much lower momenta. The assignment is therefore unique, the RICH identification can be omitted. By this measure, the data set which satisfies the

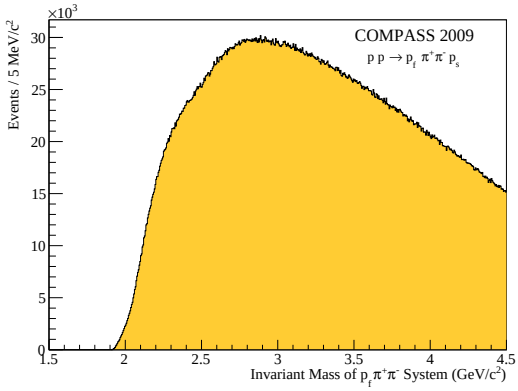

Figure 3.14: Invariant mass spectrum of the $p_\mathrm{f}\pi^+\pi^-$ system with $m(p\pi) > 1.5\,\mathrm{GeV}/c^2$.

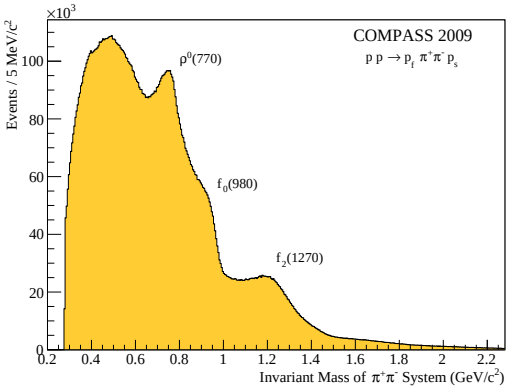

Figure 3.15: Invariant mass spectrum of the $\pi^+\pi^-$ subsystem with $m(p\pi) > 1.5\,\mathrm{GeV}/c^2$.

requirement of a $p\pi$ mass above $1.5\,\mathrm{GeV}/c^2$ is enlarged by approximately 40% to about $1.4 \cdot 10^7$ events. Especially the low-momentum threshold of the RICH detector and its non-perfect efficiency are avoided. Furthermore, a peak is observed in the momentum distribution of the fast proton p_f (cf. Figure 3.3b) without explicit identification of the positive pion. This acts as a clear sign for a contribution of central production to the data set. Nevertheless, the event is discarded if one of the tracks is unmistakably identified as a kaon, which happens in around 2.4% of the cases.

The effect of the requirement for a large invariant mass of the $p\pi$ systems on the $p_\mathrm{f}\pi^+\pi^-$ invariant mass spectrum is shown in Figure 3.14. The distribution starts at a mass of about $2\,\mathrm{GeV}/c^2$ and no obvious resonant behaviour can be discerned, which is expected for central-production reactions. The squared four-momentum transfer distribution does not change for three-body masses above $2\,\mathrm{GeV}/c^2$ (cf. Figure 3.8).

Figure 3.15 shows the $\pi^+\pi^-$ invariant mass spectrum of the centrally produced events. The peaks due to the $\rho(770)$ and the $f_2(1270)$ resonances as well as the sharp drop in intensity near the $f_0(980)$ meson due to the $K\bar{K}$ threshold can be clearly recognised. The spectrum appears to fit the scaling of the meson production cross sections with $\sqrt{s}$ [74] observed at the OMEGA spectrometer with different beam energies (cf. Figure 1.9). The production of $\rho(770)$ decreases rapidly with increasing $\sqrt{s}$, which is explained by a Reggeised pion-pion contribution ($\approx 1/s^2$). On the the other hand, the enhancement at low $\pi^+\pi^-$ masses as well as the $f_0(980)$ remain practically unchanged, a fact that is characteristic for s-independent Pomeron-Pomeron scattering. A quantitative comparison is, however, not possible at this stage, since the spectra are not corrected for acceptance.

3.3.2 Alternative Criteria for the Selection of Central Production

The effect of an invariant-mass cut on the $p\pi$ subsystems of $1.5\,\mathrm{GeV}/c^2$ on the Feynman x_F distributions for the fast and the slow protons as well as the di-pion system is shown in Figure 3.16. Very similar to the distribution from [21], the $\pi^+\pi^-$ system lies well within $|x_F| \leq 0.25$ and can therefore be regarded as centrally produced. The requirement for a minimal momentum of the fast proton p_f of $140\,\mathrm{GeV}/c$ alone already kinematically restricts the central system to this region. On the other hand, it apparently enhances baryon resonances in the $p_\mathrm{f}\pi^\pm$ systems (cf. Figure 3.13). An additional selection criterion is absolutely necessary.

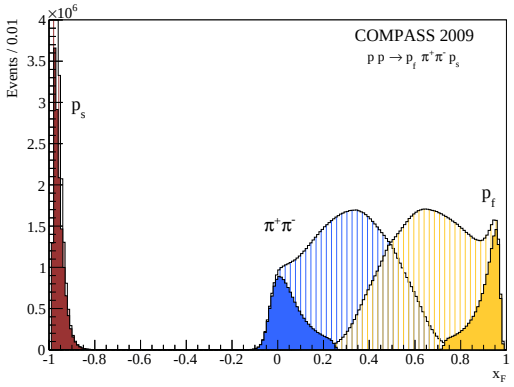

Figure 3.16: Feynman x_F distributions, $m(p\pi) > 1.5\,\mathrm{GeV}/c^2$ (filled).

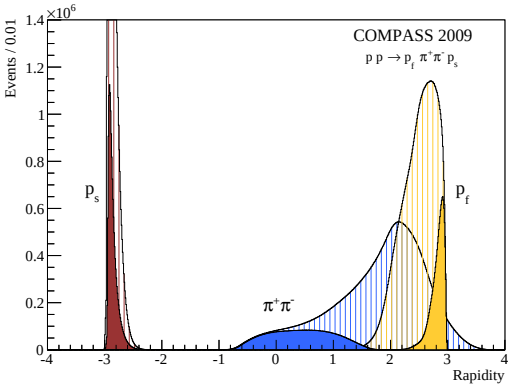

Figure 3.17: Rapidity distributions, $m(p\pi) > 1.5\,\mathrm{GeV}/c^2$ (filled).

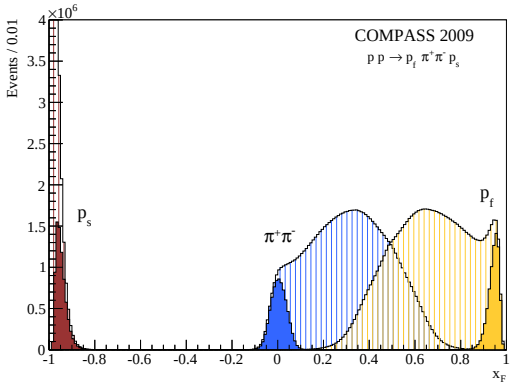

Figure 3.18: Feynman x_F distributions, $|y(p) - y(\pi)| > 2$ (filled).

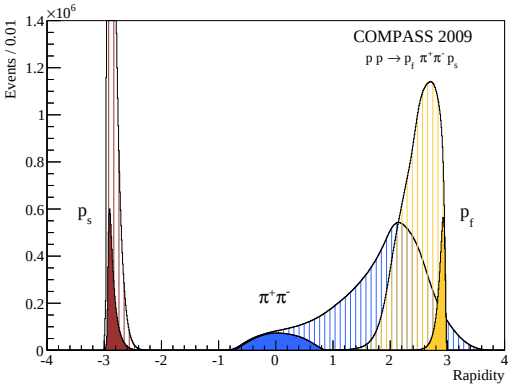

Figure 3.19: Rapidity distributions, $|y(p) - y(\pi)| > 2$ (filled).

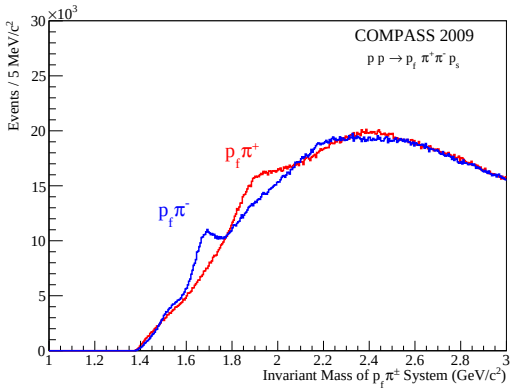

Figure 3.20: $p_\mathrm{f}\pi^\pm$ invariant mass spectra with $|y(p) - y(\pi)| > 2$.

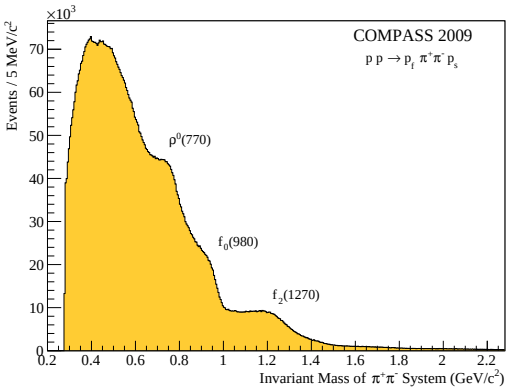

Figure 3.21: Invariant mass spectrum of the $\pi^+\pi^-$ subsystem with $|y(p) - y(\pi)| > 2$.

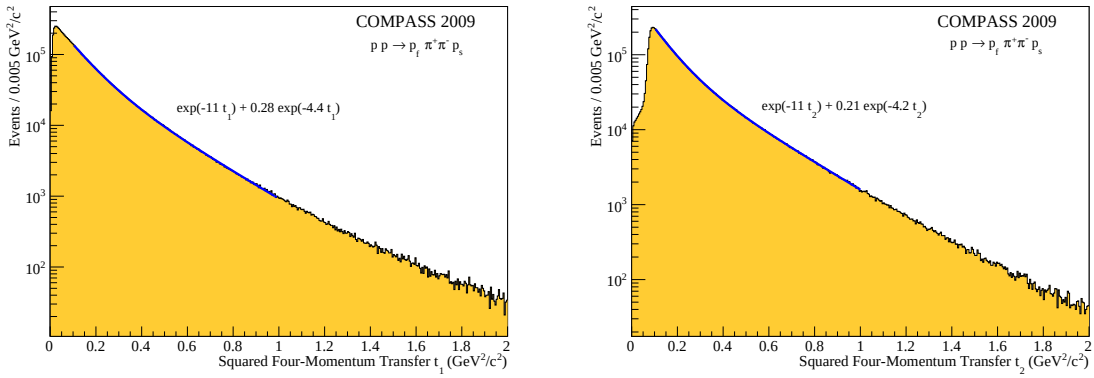

(a) $t_1 = -(p_{\mathrm{beam}} - p_{\mathrm{f}})^2$ (b) $t_2 = -(p_{\mathrm{target}} - p_{\mathrm{s}})^2$

Figure 3.22: Distribution of squared four-momentum transfers t_1 and t_2 for events with $|y(p) - y(\pi)| > 2$.

In the centre-of-mass frame of the proton-proton reaction, the rapidity interval $[-3, 3]$ is kinematically accessible in COMPASS. A small rapidity gap between the p_{f} and the $\pi^+\pi^-$ system is visible for the sample selected by the invariant-mass cut (cf. Figure 3.17). However, only the occurrence of rapidity gaps Δy larger than two units between the protons and either central pion is a clear sign for a dominant double-diffractive contribution [43]. If we explicitly select events with this requirement, the sample is reduced to $7.5 \cdot 10^6$ events, and the x_{F}- and y-distributions become almost symmetric (cf. Figure 3.18 and 3.19). The $p_{\mathrm{f}}\pi^{\pm}$ combinations show only very little evidence for baryonic resonances above $1.6\,\mathrm{GeV}/c^2$ (cf. Figure 3.20), and the three-body invariant mass threshold is even increased to about $3\,\mathrm{GeV}/c^2$. The $\rho(770)$ contribution to the $\pi^+\pi^-$ invariant mass spectrum is greatly reduced compared to the enhancement at threshold (cf. Figure 3.21), which is a sign for a dominant double-Pomeron exchange component. On the other hand, only very little data remain for invariant $\pi^+\pi^-$ masses above $1.6\,\mathrm{GeV}/c^2$.

Furthermore, the shape of the squared four-momentum transfer distribution from the beam to the central system t_1 becomes very similar to the one from the target proton t_2 for these events. The only major difference is caused by the trigger threshold at $t_2 \approx 0.07\,\mathrm{GeV}^2/c^2$. Figure 3.22 shows the two distributions with double-exponential fits in the interval $[0.1, 1.0]\,\mathrm{GeV}^2/c^2$. Both exhibit the typical slopes and ratios for diffractive reactions that are mediated by Pomeron exchange in Regge theory. The observed reaction is therefore symmetric with respect to beam and target, which is consistent with central production. In contrast, this symmetry is not observed for the selection via the $p\pi$ invariant mass cut. Additional observations in favour of requiring explicit rapidity gaps to select central-production events will be presented in Chapter 5.

An equivalent approach to select double-Pomeron exchange events in the analysis of data from very early central-production experiments at NAL[3] was introduced by Chew [33]. With a $205\,\mathrm{GeV}/c$ hadron beam, the experimental conditions were very similar to the ones in COMPASS. However, only a rough estimation of the total cross section could be achieved with 191 centrally produced events. The variables $Z_{A,B}$ were introduced as

$$Z_{A,B} \equiv \ln \frac{s}{s_{1,2}} \tag{3.1}$$

[3]National Accelerator Laboratory, now FNAL or Fermilab

with the squared invariant masses $s_{1,2}$ formed by the central system together with one of the final-state protons. Since qualitative arguments given by Regge theory require $x_{\mathbb{P}}$ to be larger than 0.9 for Pomeron exchange (cf. Section 1.2.2), the DPE region is located in the triangle between $Z_{A,B} \geq 2.3$. The third side of this triangle is given by the phase space constraint, which depends on the total available energy for the reaction. Figure 3.23a illustrates this limit as a function of beam momentum in the laboratory frame. The accessible region with the 191 GeV/c COMPASS beam is substantial. The data set selected by rapidity gaps larger than two units has a large overlap with the selected region and therefore confirms the postulation of a DPE contribution (cf. Figure 3.23b). In [33], it is also shown that this requirement approximately translates into an invariant mass cut on the $p\pi$ subsystems of greater than 1.5 GeV/c^2. In turn, the centrally produced di-pion mass can be as large as 2 GeV/c^2.

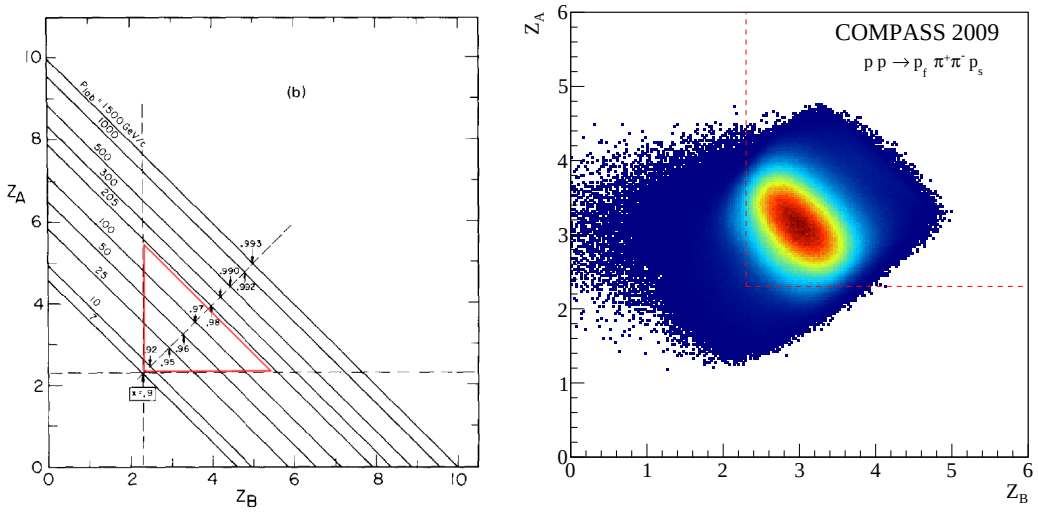

(a) DPE [33], highlighted region accessible with COMPASS

(b) Data with $|y(p) - y(\pi)| > 2$, DPE region within dashed lines

Figure 3.23: Triangle plot defining the double-Pomeron exchange region.

A recent theoretical work [75] evaluates differential distributions for the reaction $pp \to p\pi^+\pi^- p$ in a Regge approach. For the double-Regge exchange contribution to the cross section, which includes $\mathbb{PP}$, $\mathbb{RP}$ and $\mathbb{RR}$ scattering processes, detailed predictions for the kinematic distributions are presented. Especially the rapidity distributions of the produced pions are used to disentangle the different contributions. While they all overlap at $\sqrt{s} = 5.5\,\text{GeV}$[4] (cf. Figure 3.24), a component dominated by Pomeron-Pomeron scattering can be selected in the rapidity region $|y(\pi)| < 1$ for $\sqrt{s} = 200\,\text{GeV}$[5]. This requirement was also tested on the selection of COMPASS data, which lies in between the two cases with with $\sqrt{s} = 18.9\,\text{GeV}$. Diffractive resonance production, which dominates the cross section for low energies ($\sqrt{s} < 20\,\text{GeV}$), is not included in the intentionally simplified Regge framework [75]. However, qualitative statements are made also on the rapidity distributions of the pions produced by this reaction. The contribution from double-Regge exchange processes tends to be along the diagonal $y(\pi^+) = y(\pi^-)$,

[4] corresponding to $\overline{\text{P}}$ANDA energy
[5] Relativistic Heavy Ion Collider (RHIC) energy

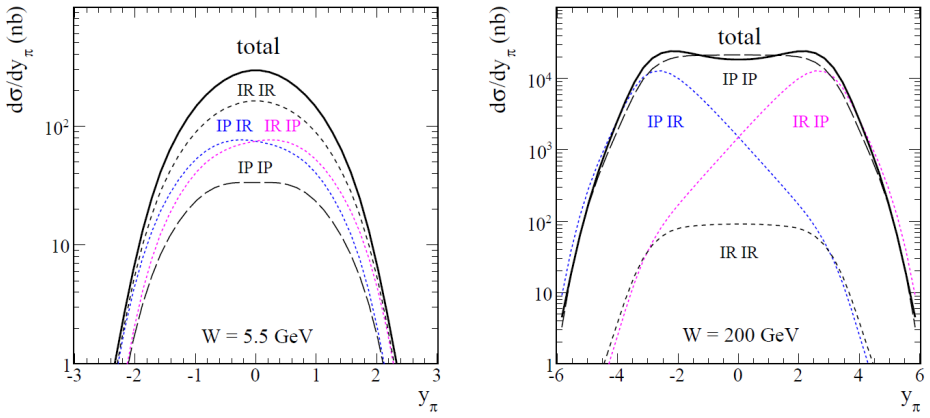

Figure 3.24: Rapidity distributions of pions at different centre-of-mass energies [75].

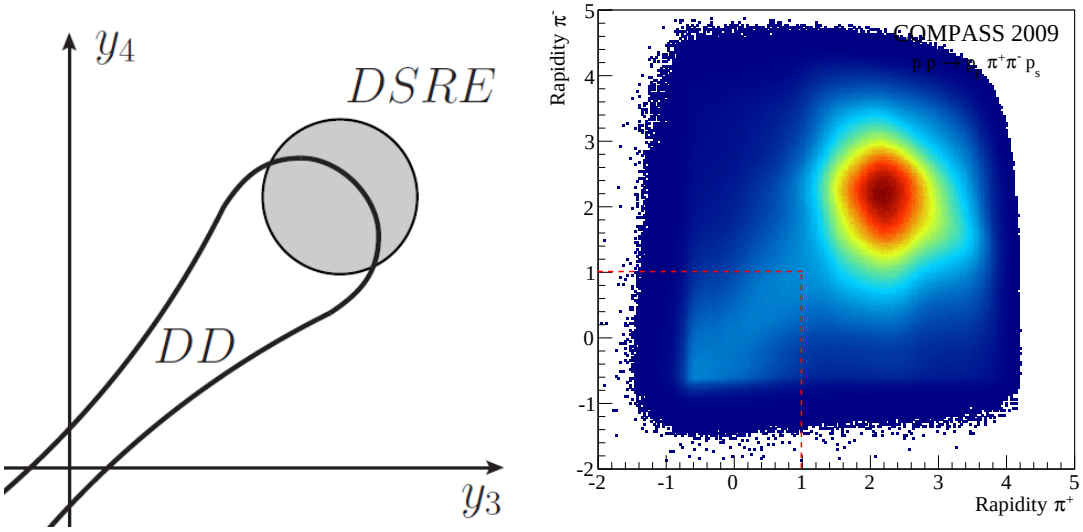

(a) Double-diffraction (DD) and diffractive single-resonance excitation (DSRE) regions for the pion rapidities $y_{3,4}$ [75]

(b) Data, DD within dashed line

Figure 3.25: Rapidity distribution for both pions in the reaction.

with DPE near the origin (cf. Figure 3.25a). Events with an excited beam proton, so-called single-diffraction reactions, can be found with pion rapidities close to the beam rapidity and are thus kinematically separated. In Figure 3.25b, this effect is confirmed with COMPASS data. Apart from the dominant diffractive dissociation reactions near $y_{3,4} = 3$, a second component can be clearly discerned around the origin. For backward rapidities, the acceptance at COMPASS is sharply limited by the aperture of the first spectrometer magnet at $y_{3,4} \approx -0.7$.

Modern theoretical works on central production, as e.g. discussed in [60] and followed up in Section 4.1.3, use a combination of constraints on rapidity and Feynman x_F to specify the reaction. For our data, the requirement for both pions to have absolute rapidities below unity together with the lower limit for x_F of the protons of 0.9 is almost equivalent with the selection of minimal rapidity gaps of two units as discussed above. However, it is often easier to implement as a trigger in experiments or as a cut in numerical simulations.

In this work, we will study the centrally produced sample selected by an invariant mass cut on the $p\pi$ subsystems in order to maintain the possibility to compare the results to the experiments at the CERN OMEGA spectrometer. In Chapter 5, we observe effects of the diffractive dissociation component on the partial-wave analysis which lead to the application of the stricter criterion, i.e. the requirement for rapidity gaps of at least two units. However, the selection of a pure double-Pomeron exchange sample without signs of $\rho(770)$ production could not be achieved with any kinematic cuts.

3.3.3 Glueball Filter

As introduced in Section 1.2.3, Close and Kirk [37] observed a dependency of the produced states on the transverse momentum difference dP_T of the exchange particles in data recorded by the OMEGA spectrometer at CERN. In particular for small dP_T, known $q\bar{q}$ states like $f_2(1270)$ were claimed to be suppressed relative to the $f_0(980)$ meson and the glueball candidates $f_0(1500)$ and $f_2(1950)$.

If we bin the centrally produced data selected with the identical $p\pi$ invariant mass cut in terms of dP_T, we can also observe this effect (cf Figure 3.26). The intensities of the $\rho(770)$ and $f_2(1270)$ signals clearly decrease in the limit $dP_T \to 0$, while the enhancement at threshold and the sharp drop around $1\,\mathrm{GeV}/c^2$ remain stable. Only a small fraction of events with $\pi^+\pi^-$ masses above $1.5\,\mathrm{GeV}/c^2$ can be found with $dP_T < 0.2\,\mathrm{GeV}/c$. However, a quantitative conclusion can only be drawn after the data are decomposed into partial waves.

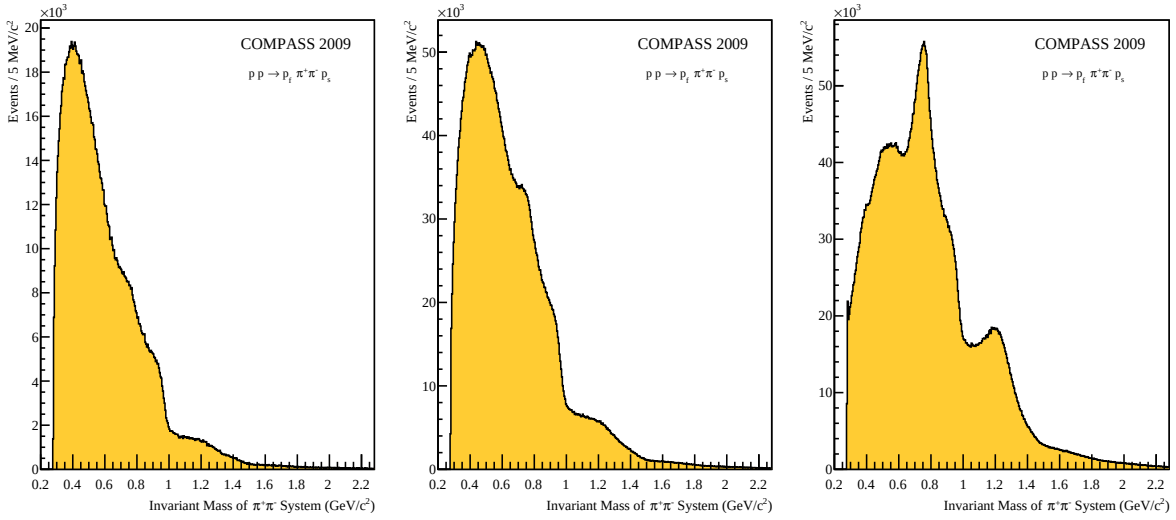

Figure 3.26: $m_{\pi^+\pi^-}$ for $dP_T < 0.2\,\mathrm{GeV}/c$ (left), $0.2 < dP_T < 0.5\,\mathrm{GeV}/c$ (centre) and $dP_T > 0.5\,\mathrm{GeV}/c$ (right).

The dependence on dP_{T} is kinematically related to the azimuthal angle ϕ between the slow- and the fast-proton scattering planes defined in the pp centre-of-mass system by the relation [71]

$$\cos\phi = \frac{dP_{\mathrm{T}}^2 - P_{\mathrm{T}}^2}{4t_1 t_2} \ . \tag{3.2}$$

Figure 3.27 shows this angle as a function of the invariant mass of the centrally produced $\pi^+\pi^-$ system. The $q\bar{q}$ mesons $\rho(770)$ and $f_2(1270)$ are dominant for small values of ϕ, while the enhancement at low masses is produced in reactions with $\phi = 180°$. The $f_0(980)$ meson seems to show a constant behaviour as a function of ϕ. [74] explains this discrepancy as a variation in momentum transfer, which selects different regimes of the production mechanisms. Short-range quark or gluon exchange between the two Pomerons for large transfers compete with the exchange of meson trajectories for more peripheral collisions. Similar effects are observed in the diffractive production of $\rho(770)\pi$ systems [59], where the peak of the $a_1(1260)$ meson is also considerably altered as a function of the squared four-momentum transfer.

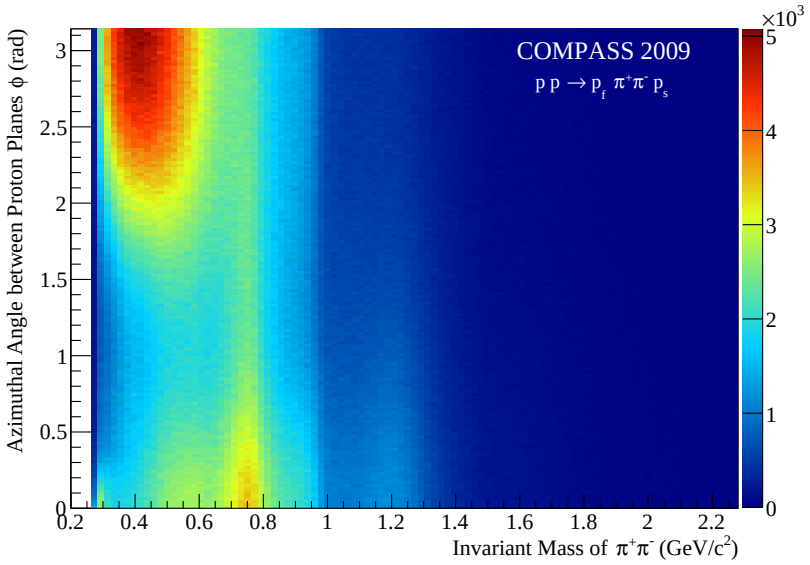

Figure 3.27: Dependence of azimuthal angle ϕ on di-pion invariant mass.

The kinematic origin of these dependencies was quantified by Kaidalov et al. [68] using the tools of Regge phenomenology. Following this, we have constructed an alternative set of amplitudes and applied the formalism to our data. This new approach will be introduced in Chapter 8. In the past, however, the amplitudes of the reaction were constructed without the information of this additional degree of freedom. For the main analysis presented in this work, we will restrict ourselves to the decay kinematics of the central two-pseudoscalar meson systems and neglect the production variable ϕ.

3.4 Neutral Particles in the Final State

In addition to excellent charged-particle tracking capabilities, COMPASS is also equipped to detect high energetic photons in a broad kinematic range. This can be used to reconstruct the decays of centrally produced neutral particles into photons. However, owing to geometrical acceptance and material in the flight path between the interaction point and the electromagnetic calorimeters, the reconstruction efficiency is about one order of magnitude lower than for the corresponding charged particles [6]. Nevertheless, the data serve as an independent confirmation of the charged-particle analyses since a different part of the apparatus is used to reconstruct these final-states. In addition, Bose symmetry allows only even orbital angular momentum states of two identical pseudo-scalar mesons. This limits the quantum numbers of the produced resonances accordingly.

We use a data selection scheme that was developed and approved by the COMPASS experiment for the analysis of the baryon spectrum [104] in order to support the results of the $\pi^+\pi^-$ analysis presented in this work. Apart from that, we do not expect a gain in information from the quantitatively inferior data.

3.4.1 $pp \to p_\mathrm{f}\,\pi^0\pi^0\,p_\mathrm{s}$

A total number of about $1.6 \cdot 10^6$ events was reconstructed in the $p_\mathrm{f}\,\pi^0\pi^0\,p_\mathrm{s}$ final state. Apart from effects due to the different acceptance, the kinematic distributions for $\pi^0\pi^0$ production show many similarities with the ones of the corresponding $\pi^+\pi^-$ channel. The $\Delta^+(1232)$ resonance dominates the $p_\mathrm{f}\pi^0$ invariant mass spectrum (cf. Figure 3.28), where both combinations are filled into one histogram. At least two peaks for baryon resonances with higher masses can be discerned around $1.5\,\mathrm{GeV}/c^2$ and $1.7\,\mathrm{GeV}/c^2$. The $\pi^0\pi^0$ invariant mass itself exhibits a striking but expected difference with respect to the $\pi^+\pi^-$ system at the $\rho(770)$ mass, which is not allowed to decay into two identical particles (cf. Figure 3.29). Apart from that, the shapes coincide nicely.

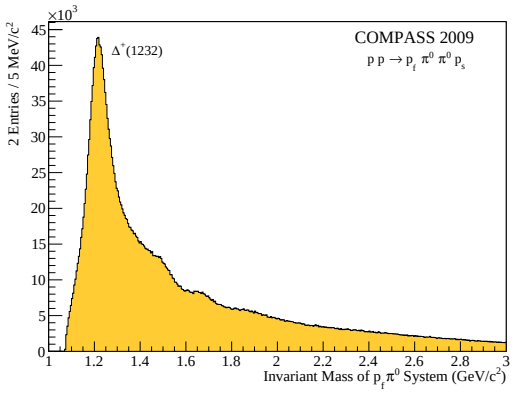

Figure 3.28: Invariant mass of $p_\mathrm{f}\pi^0$ systems.

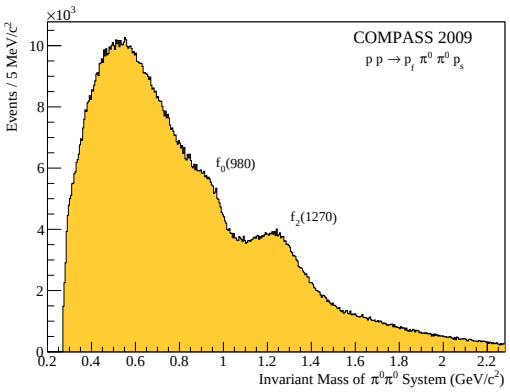

Figure 3.29: Invariant mass of $\pi^0\pi^0$ system.

The difference in acceptance between charged and neutral pion reconstruction can be observed directly in the x_F distribution of the centrally produced subsample (cf. Figure 3.30). Due to the comparably large distance of 14 m between the target and ECAL1, almost no π^0 can be detected if they are emitted backwards relative to the proton-proton centre-of-mass system ($x_\mathrm{F} < 0$). The requirement for the $p\pi^0$ masses to be at least $1.5\,\mathrm{GeV}/c^2$ is only fulfilled by about $2 \cdot 10^5$ events, and their invariant mass distribution is heavily distorted. As it can be seen in Figure 3.31, the enhancement for $\pi^0\pi^0$ masses below $800\,\mathrm{MeV}/c^2$ is almost completely

suppressed by this acceptance effect. Nonetheless, we will present the results of a partial-wave analysis of this sample in Chapter 5.

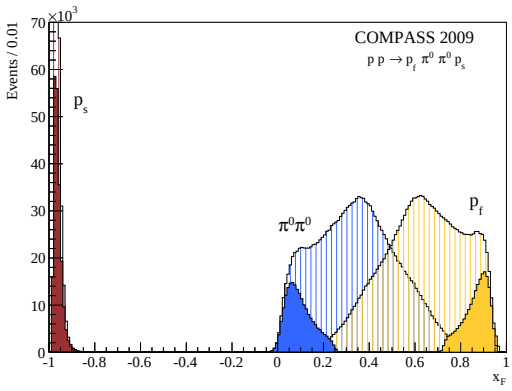

Figure 3.30: Feynman x_F distributions, $m(p\pi) > 1.5\,\mathrm{GeV}/c^2$ (filled).

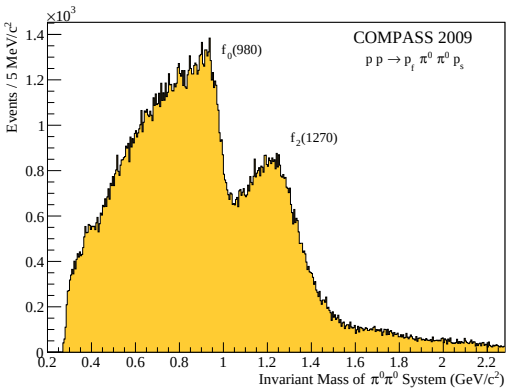

Figure 3.31: Invariant mass of $\pi^0\pi^0$ system with $m(p\pi) > 1.5\,\mathrm{GeV}/c^2$.

3.4.2 $pp \to p_f\,\eta\eta\,p_s$

An additional channel is accessible in COMPASS data if the selected $\gamma\gamma$ combinations form two η mesons. However, the total number of exclusive events recorded during the 2009 proton run is only roughly 4400. The low-momentum threshold for η reconstruction of about $7\,\mathrm{GeV}/c$ is the most important limiting factor. Consequently, a partial-wave analysis of this channel could not be carried out. On the other hand, the comparison to the data recorded with a negatively-charged pion beam (cf. Section 3.5) reveals important differences of the production process.

Even though single-η production with a proton beam in COMPASS reveals signs for resonances in the $p\eta$ system [104], the $p_f\eta$ invariant mass combination with the leading proton in this channel does not show any structures (cf. Figure 3.32). The η-pair is already kinematically confined to the central region without any additional selection cuts. The $\eta\eta$ mass spectrum in Figure 3.33 shows an enhancement at threshold and a broad structure around $1.5\,\mathrm{GeV}/c^2$. Previous experiments with a comparable data set [22] described the data with resonance parameters fixed to the values obtained by a coupled $\pi\pi$ and $K\bar{K}$ analysis [21]. A dominant contribution from $f_0(1500)$ and a shoulder from the $f_0(1710)$ resonance were reported, while the intensities of $f_2(1270)$ and $f_2(2150)$ play only a minor role. However, in the quoted publication only the partial-wave decomposed intensity distributions were fitted.

3.5 Beam-Particle Dependence

In addition to the data set with a positive hadron beam, the COMPASS experiment recorded a competitive data set with a negatively charged pion beam in 2008, which opens the possibility to study the dependence of the production mechanism on the beam particle species. Since the experimental setup including the trigger and a great fraction of the detectors did not change from 2008 to 2009, all final states can be directly compared on the level of kinematic distributions. Considerable differences can be observed, depending on the studied final-state.

For the following considerations, we use data sets which were selected for the analysis of diffractively produced $\pi^-\pi^+\pi^-$ [59], $\pi^-\pi^0\pi^0$ and $\pi^-\eta\eta$ [100] final-states.

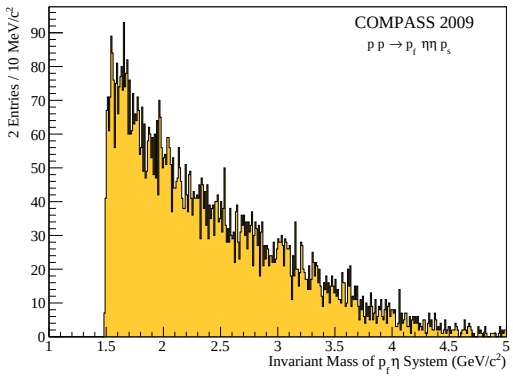

Figure 3.32: Invariant mass of $p_\mathrm{f}\eta$ systems.

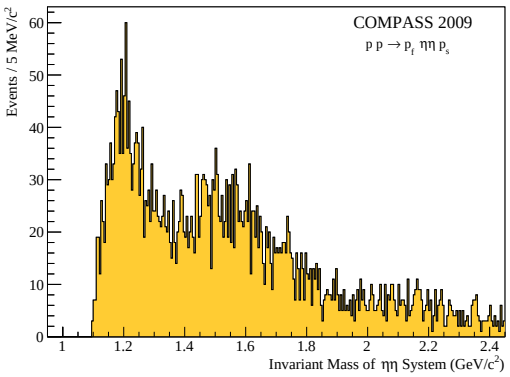

Figure 3.33: Invariant mass of $\eta\eta$ system.

3.5.1 $\pi^- p \to \pi_\mathrm{f}^- (\pi\pi)^0 p_\mathrm{s}$

In order to distinguish between the two negatively charged pions in the $\pi^-\pi^+\pi^-$ final state, we will call the pion with the larger absolute momentum in the laboratory system π_f^-. Nonetheless, a central-production topology is only present after a kinematic selection as introduced in Section 3.3. For reasons of consistency, we will require an invariant mass of the $\pi_\mathrm{f}^-\pi^+$ subsystem of at least $1.2\,\mathrm{GeV}/c^2$ as in [14] and a minimum momentum of $140\,\mathrm{GeV}/c$ for the fast pion. This suppresses a large fraction of diffractively produced resonances, similar to the reaction induced by a proton beam.

Without this requirement, the momentum distributions for the fastest final-state particle are already very different depending on the beam type. While the protons have a clear peak at momenta around $180\,\mathrm{GeV}/c$ (cf. Figure 3.3b), the fast pions in Figure 3.34 show a phase-space-like distribution which has a maximum at intermediate values and only a little enhancement around $180\,\mathrm{GeV}/c$. Consequently, the requirements for central production select only 10% of the total events, while more than 15% were selected with a proton beam.

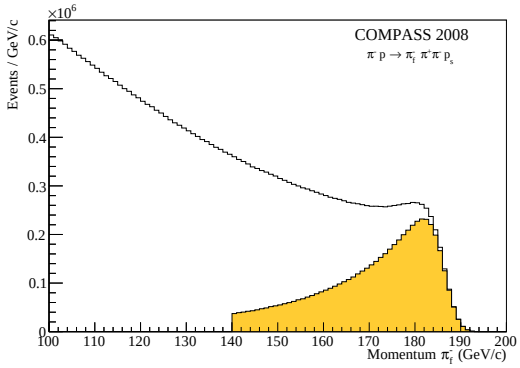

Figure 3.34: Momentum distribution π_f^-, $m(\pi_\mathrm{f}^-\pi^+) > 1.2\,\mathrm{GeV}/c^2$ (filled).

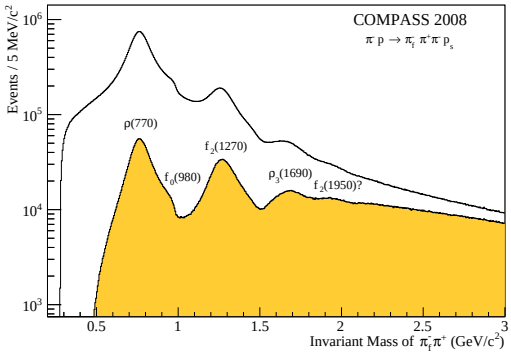

Figure 3.35: Invariant mass of $\pi_\mathrm{f}^-\pi^+$ system, $p(\pi_\mathrm{f}^-) > 140\,\mathrm{GeV}/c$ (filled).

Similar to $p_\mathrm{f}\pi^-$, the $\pi_\mathrm{f}^-\pi^+$ subsystem exhibits dominant resonant contributions as illustrated in Figure 3.35. As mentioned above, these resonant components can be emphasised with a momentum limit of $140\,\mathrm{GeV}/c$ for the fast particle. An additional enhancement emerg-

ing near $2\,\mathrm{GeV}/c^2$ may even be attributed to the $f_2(1950)$ meson. In contrast, the broad component at threshold is completely suppressed by this kinematic cut.

Finally, the central $\pi^+\pi^-$ system exhibits very similar features whether it is produced by a pion or a proton beam (cf. Figures 3.15 and 3.36), which strongly supports the hypothesis that the production mechanism is the same. The larger coupling to the $\rho(770)$ is expected in the 3π reaction and was also observed in earlier experiments [14]. The central-production reaction is an important background in the studies of meson spectroscopy through diffractive production [59].

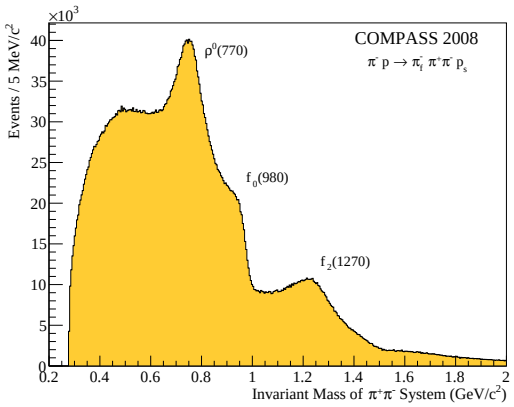

Figure 3.36: Invariant mass of $\pi^+\pi^-$ system with pion beam for $m(\pi_\mathrm{f}^-\pi^+) > 1.2\,\mathrm{GeV}/c^2$.

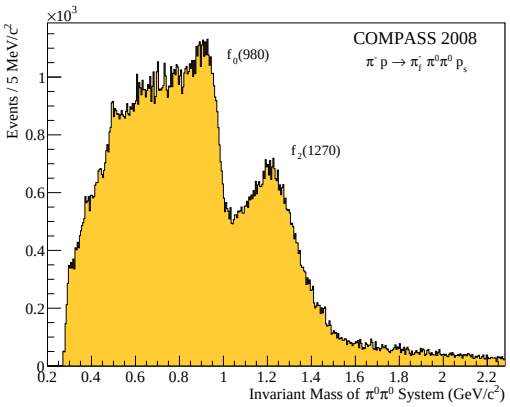

Figure 3.37: Invariant mass of $\pi^0\pi^0$ system with pion beam for $m(\pi_\mathrm{f}^-\pi^0) > 1.2\,\mathrm{GeV}/c^2$.

The production of two neutral pions with a pion beam shows equivalent kinematic characteristics. Here, the $\pi_\mathrm{f}^-\pi^0$ invariant mass is dominated by a $\rho(770)$ signal. After enriching the centrally produced events with a mass cut of $m(\pi_\mathrm{f}^-\pi^0) > 1.2\,\mathrm{GeV}/c^2$, the $\pi^0\pi^0$ spectrum in Figure 3.37 is almost congruent to the one produced with proton beam (cf. Figure 3.31). The lack of events in the low-mass region is attributed to the low photon acceptance in the kinematic region where the neutral pions propagate backwards in the $\pi^- p$ rest frame.

3.5.2 $\pi^- p \to \pi_\mathrm{f}^- \eta\eta\, p_\mathrm{s}$

A strong dependence on the beam particle can be observed in $\eta\eta$ production. While it was shown in Section 3.4.2 that a special central-production selection is not required for proton beams, the pion couples very strongly to the $\eta\eta$ system. In Figure 3.38, a dominant contribution from resonances in the $\pi_\mathrm{f}^-\eta$ subsystems can be discerned, e.g. the $a_0(980)$ and the $a_2(1320)$. Only if they are effectively removed by a minimum pion momentum of $140\,\mathrm{GeV}/c$, the $\eta\eta$ invariant mass distribution is reduced to a shape similar to the one reconstructed with a proton beam (cf. Figures 3.33 and 3.39). However, only about 6% of the data satisfy this requirement compared to more than 40% for an equivalent cut on the data recorded with a proton beam. The remaining sample of about 1000 events is too small to perform a dedicated partial-wave analysis. On the other hand, it illustrates nicely the invariance of the central-production reaction with respect to the beam particle species.

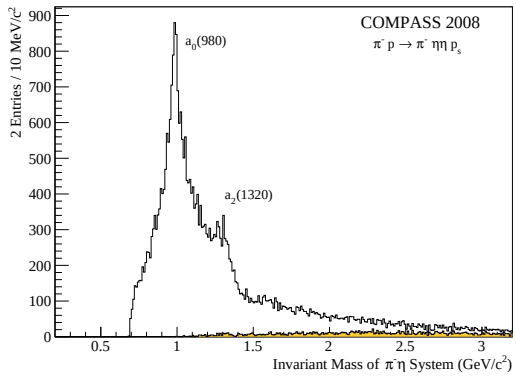

Figure 3.38: Invariant mass of the $\pi_f^-\eta$ system, central selection (filled).

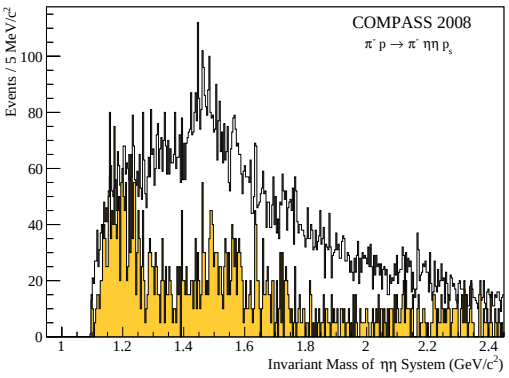

Figure 3.39: Invariant mass of $\eta\eta$ system, central selection (filled and scaled $\times 5$).

3.5.3 Deck Effect

An alternative production mechanism, the so-called Deck effect, was introduced in [42] in order to describe the dynamics of diffraction of a pion beam into three-pion final-states. The beam particle in this non-resonant reaction presumably dissociates into a di-pion resonance (e.g. $\rho(770)$, $f_0(980)$, $f_2(1270)$) and a pion which is almost on the mass shell. This pion scatters quasi-elastically off the target proton into a physical final-state pion (cf. Figure 3.40). A Monte-Carlo (MC) sample has been generated according to the amplitudes developed in [41] in order to study this background process for the diffractive dissociation of three-pion resonances [59].

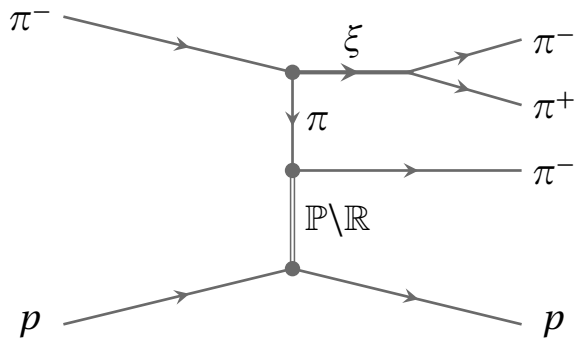

Figure 3.40: Illustration of the Deck process.

About 8% of the 10^8 generated events have a leading negative pion π_f^- with a momentum above 150 GeV/c. As a result, the kinematically allowed region for the remaining di-pion system lies within $|x_F| < 0.2$ and can therefore be mistaken as centrally produced. On the other hand, the fast pion seems to stem almost exclusively from the generated di-pion resonance, i.e. the four implemented resonances stand out nearly background-free in the $\pi_f^-\pi^+$ invariant mass spectrum (cf. Figure 3.41). In contrast, the combination of the π^+ with the slow π^- exhibits a threshold enhancement which is almost congruent with the central di-pion system observed with a pion beam (cf. Section 3.5). This appears to be a kinematic artifact of the wrong di-pion combination rather than a resonant contribution. Figure 3.42 overlays the threshold enhancement from the Deck MC sample onto the invariant mass distribution of the selected

sample from pion-beam data. The two curves nicely coincide below $0.6\,\mathrm{GeV}/c^2$. For higher masses, the resonant components in this di-pion system are not included in the model and can consequently not follow the data. Events with resonances in the central system can account for the large tail in the $\pi_\mathrm{f}^-\pi^+$ invariant mass distribution above $2\,\mathrm{GeV}/c^2$ in Figure 3.41.

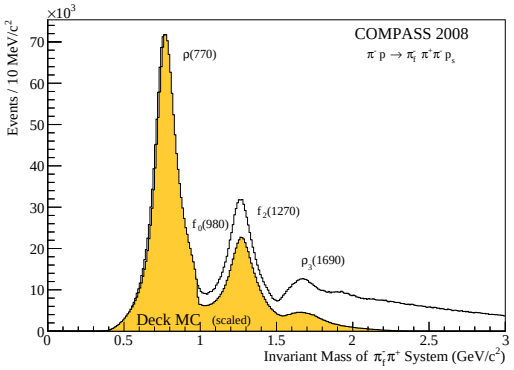

Figure 3.41: Invariant mass of $\pi_\mathrm{f}^-\pi^+$ system, data (open) and Deck MC (filled). Normalised to the maximum bin.

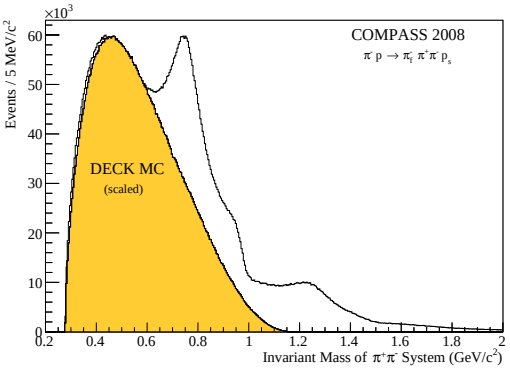

Figure 3.42: Invariant mass of central $\pi^+\pi^-$ system, data (open) and Deck MC (filled). Normalised to the maximum bin.

Quantitative conclusions from this observation are difficult to draw. Most notably, the selection of centrally produced events as introduced in Section 3.5.1 has only a small contribution from visible resonances above $1.5\,\mathrm{GeV}/c^2$ in the subsystems including the fast hadron (cf. Figure 3.35). As a consequence, the low-mass enhancement in the central di-pion system cannot be entirely a kinematic reflection of Deck-like processes. Small contributions may, however, be present.

This scenario is probably also applicable to the sample recorded with a proton beam, given the observed similarities in the central system. We have seen in Section 3.2 that baryon resonances decaying into $p_\mathrm{f}\pi^-$ can also be enhanced by the requirement of a minimal proton momentum in the laboratory frame. It might be necessary to study these Deck-like effects with intermediate baryon resonances in the future in order to understand the data entirely [74]. The COMPASS data set is unique for this task, as it was recorded with minimal kinematic bias.

Chapter 4

Acceptance Correction

A detailed Monte-Carlo (MC) simulation is needed in order to understand and correct for the effects of the experimental setup on the reaction under study. At first, the events with a centrally produced meson system are generated according to a physical model, taking into account the distributions of the beam momentum and the vertices in the target volume. These events are propagated through a detailed model of the COMPASS spectrometer, where all relevant secondary interactions and the responses of the detector planes are simulated. Finally, these simulated pseudo-data are reconstructed with the software chain used also for real data. All selection criteria introduced in Chapter 3 are applied in an analogous fashion.

Even though the acceptance correction for the partial-wave analysis is performed via normalisation integrals (cf. Chapter 5), we will present the acceptance projected onto selected kinematic variables in order to illustrate the effects of the apparatus on the measurement.

4.1 Event Generators

For the main part of this analysis, we use a phase-space generator for central production which can be integrated into the official COMPASS simulation software. In addition, alternative approaches that try to model the underlying physical process in more detail are compared to the data set. A phase-space generator for diffractive dissociation into multi-body final states is also used to study the impact of this background process on the analysis. The concept of these generators will be introduced in the following.

4.1.1 Central-Production Event Generator

An event generator for the kinematics of centrally produced systems was developed within the COMPASS collaboration in the preparation of the hadron run. A detailed description of it can be found in [101].

The physical process is generated in a two-step procedure. At first, the two squared four-momentum transfers t_1 from the beam proton and t_2 from the target proton are chosen randomly according to an exponential function. A single slope of $6\,(\mathrm{GeV}/c)^{-2}$ was used as an approximation for both distributions. Since the main component of the trigger, the recoil proton detector, is only sensitive starting from $t_2 > 0.07\,\mathrm{GeV}^2/c^2$, this threshold was implemented in the generator in order to maximise the efficiency of the computationally expensive simulation. The four-momentum transfers form an intermediate state X, which is generated uniformly in the rapidity interval $[-1, 1]$ (cf. Figure 4.1). As a result, the distribution of Feynman x_F of X is centred around zero and within $|x_\mathrm{F}| < 0.25$, which is illustrated in Figure 4.2. The invariant mass of this central system is uniformly distributed in the interval between the kinematic threshold and a specified maximum mass.

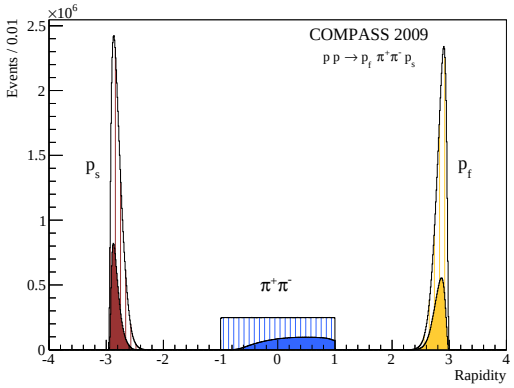

Figure 4.1: Generated (hatched) and accepted (filled) rapidity distributions.

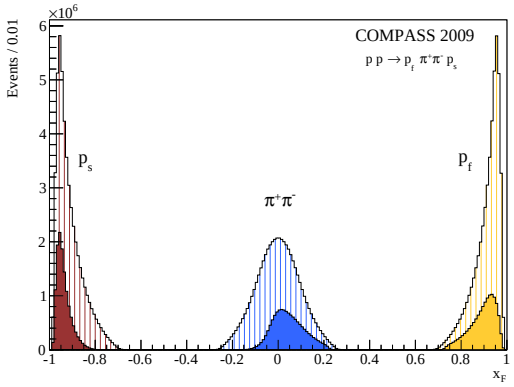

Figure 4.2: Generated (hatched) and accepted (filled) Feynman x_F distributions.

The generator acts in the proton-proton centre-of-mass frame. As a consequence, a flat distribution of the angle ϕ between the two proton scattering planes is generated in this frame. This does not agree with the measured distribution (cf. Figure 3.27), but since there are no correlations between the angular decay pattern of the central system and this angle, the partial-wave analysis is not biased.

In the second step, the decay of the intermediate state X into two pseudo-scalar mesons is simulated with an isotropic angular distribution in the X rest frame. $5 \cdot 10^7$ events of this type were generated in order to fill the entire available phase space in a sufficient manner. Depending on the strictness of the selection of centrally produced systems (cf. Section 3.3), this sample outnumbers the recorded data set at least by a factor of three.

4.1.2 Alternative Event Generator

An alternative approach for a central-production generator has been suggested in [89]. It is based on the invariant double-Pomeron cross section formula from [15]

$$\mathrm{d}\sigma_{pp\to p_1 X p_2} = \mathrm{e}^{-b_1 t_1} \left(\frac{s}{s_2}\right)^{2\alpha_\mathbb{P}(t_1)-1} \mathrm{e}^{-b_2 t_2} \left(\frac{s}{s_1}\right)^{2\alpha_\mathbb{P}(t_2)-1} \mathrm{d}\Gamma_3(\vec{p}_1, \vec{p}_2, \vec{p}_X)\ \sigma_{\mathbb{P}\mathbb{P}\to X}\ \mathrm{d}m_X^2\ . \quad (4.1)$$

The established parametrisation $\alpha_\mathbb{P}(t) = 1.2 + 0.25\,(\mathrm{GeV}/c)^{-2}\,t$ [43] is used for the Pomeron trajectory. If the integration variables $\vec{p}_{1,2}$ are changed into a longitudinal part expressed by Feynman $x_{1,2}$ and a transverse part $\vec{q}_{1,2}$, the two proton vertices can be factorised as long as m_X^2 is required to be positive:

$$\mathrm{d}\sigma_{pp\to p_1 X p_2} = \mathrm{e}^{-b_1 t_1}(1-x_1)^{1-2\alpha_\mathbb{P}(t_1)} \mathrm{e}^{-b_2 t_2}(1-x_2)^{1-2\alpha_\mathbb{P}(t_2)}\ \sigma_{\mathbb{P}\mathbb{P}\to X}\ \mathrm{d}x_1\ \mathrm{d}^2\vec{q}_1\ \mathrm{d}x_2\ \mathrm{d}^2\vec{q}_2 \quad (4.2)$$

The approximation $\frac{s_{2,1}}{s} \approx 1 - x_{1,2}$ is valid within about 10% for COMPASS centre-of-mass energies. The approximately chosen slopes for the squared four-momentum transfer distributions $b_{1,2}$ are re-weighted by this phenomenologically motivated formula. This effectively produces a slope around $8.5\,(\mathrm{GeV}/c)^{-2}$. An additional re-weighting step is needed in order to obtain a flat distribution for the invariant mass of the central system X. For the decay itself, a conventional isotropic phase-space generator is used.

In this approach, the azimuthal angle between the outgoing protons ϕ is simulated isotropically in the rest frame of X. After a boost to the proton-proton centre-of-mass system, a strong

asymmetry is obtained for di-pion masses below $1\,\mathrm{GeV}/c^2$ (cf. Figure 4.3.) This strongly contradicts the observed distribution (cf. Figure 3.27). Since this generator is in a preliminary stage and will have to be optimised in the future, we did not use it for the analysis presented in this work. It was, however, verified that the results of the partial-wave analysis of the decay process do not depend on the detailed simulation of the production variables. On the other hand, it will be important for an analysis that takes the production into account (cf. Chapter 8).

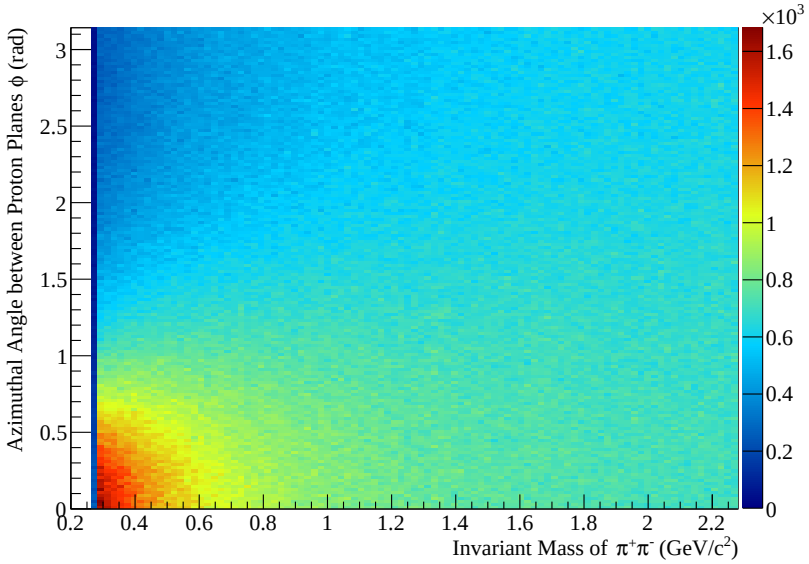

Figure 4.3: Azimuthal angle ϕ in pp centre-of-mass system for the alternative CP generator.

4.1.3 Dime MC

With the advent of the LHC, central exclusive production reactions in proton-proton collisions have regained interest in a larger community. Phenomenological predictions for cross sections and production characteristics are studied in detail. For example in [60, 62], perturbative approaches are combined with the tools of Regge theory, which play a dominant role for the creation of central systems with invariant masses below $2\,\mathrm{GeV}/c^2$. The probability for no additional proton-proton rescattering is implemented into a so-called eikonal survival factor S_{eik}, which modifies the central production amplitude in addition to other screening effects (cf. Figure 4.4).

We used the publicly available Dime Monte-Carlo generator [61] and compared the reconstructed events with our data sample, taking into account the full simulation of the experimental setup. The default definition of central exclusive production in this generator requires both pions to lie in the rapidity region $|y(\pi)| < 1.5$ and both outgoing protons to have $|x_{\mathrm{F}}| > 0.9$, which limits the accessible $\pi^+\pi^-$ mass range to below $1.8\,\mathrm{GeV}/c^2$. Similar to the comparison to ISR data in [62], the shape of the $\pi^+\pi^-$ invariant mass distribution can only be used to estimate the non-resonant contribution (cf. Figure 4.5). On the other hand, the distribution of t_1 in Figure 4.6 shows almost the same behaviour for data and this MC generator. The difference in the intermediate t_1 region between the two dominating slopes is probably an effect of the resonant contributions. Apart from trigger effects below $0.1\,\mathrm{GeV}^2/c^2$, this observation is equally valid for t_2. The distribution of ϕ shows an asymmetry for low $\pi^+\pi^-$ masses, while

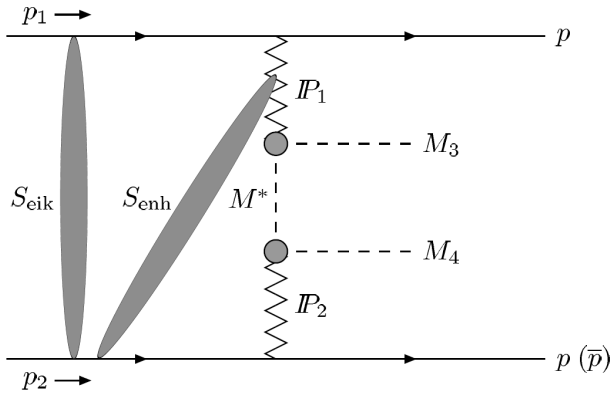

Figure 4.4: Non-perturbative central exclusive production of a meson pair (M_3, M_4) with an intermediate off-shell meson M^* [60]. Eikonal and (an example of) enhanced screening effects are indicated by the shaded areas.

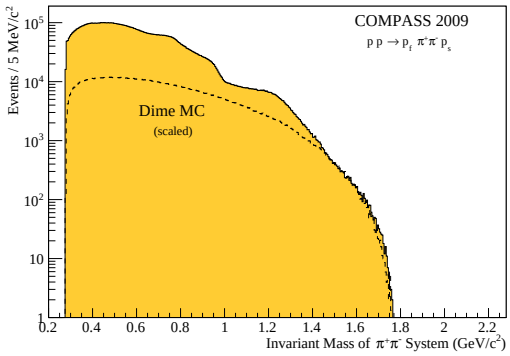

Figure 4.5: $\pi^+\pi^-$ invariant mass with $|y(\pi)| < 1.5$ and $|x_{\text{F}}(p_{\text{f,s}})| > 0.9$ compared to Dime MC generator (scaled to high mass).

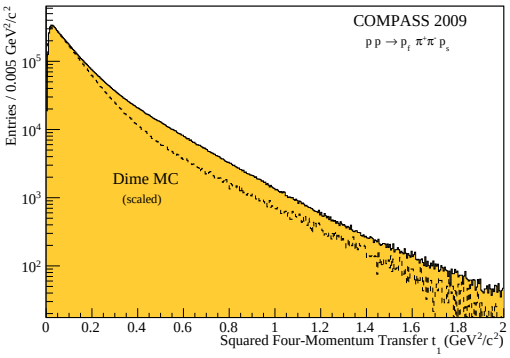

Figure 4.6: t_1 distribution for $\pi^+\pi^-$ with $|y(\pi)| < 1.5$ and $|x_{\text{F}}(p_{\text{f,s}})| > 0.9$ compared to Dime MC generator (scaled to maximum).

it becomes uniform above $1\,\text{GeV}/c^2$. It therefore follows the general trend of the data (cf. Figure 4.7). The angular distribution of the decay, which will be introduced in Chapter 5, is on the other hand highly non-uniform (cf. Figure 4.8). For this reason, the generator was not used for the acceptance correction of the partial-wave analysis presented later in this work.

4.1.4 Diffractive Phase-Space Generator

Diffractive dissociation of the beam particles, as introduced in Chapter 3, constitutes the dominant background process in the study of central-production reactions. In order to estimate the impact, the diffractive phase-space generator used in the analyses of multi-pion final states produced in $\pi^- p$ reactions (e.g. [80], [100]) was modified to simulate pp interactions where one proton dissociates into a $p_{\text{f}}\pi^+\pi^-$ final state. The squared four-momentum transfer t_2 to the target was generated according to a single-exponential slope, which approximates the measured distribution.

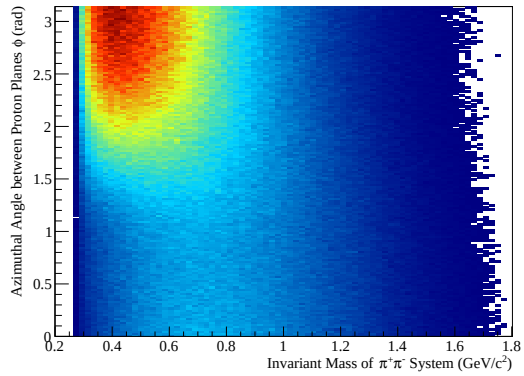

Figure 4.7: Azimuthal angle ϕ in pp centre-of-mass system for Dime MC generator.

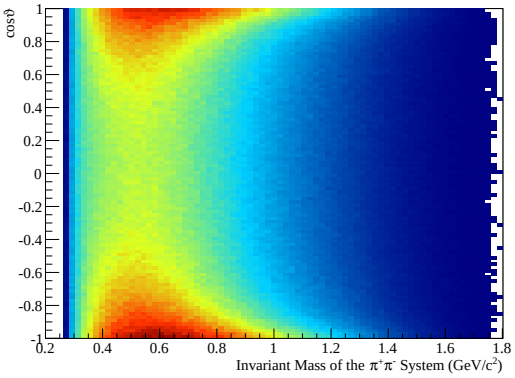

Figure 4.8: Polar angle of π^- in $\pi^+\pi^-$ centre-of-mass system for Dime MC generator.

First of all, the fraction of events which meet the requirements for central production can be estimated. As the decay of the $p_f\pi^+\pi^-$ system is generated without intermediate resonances, the minimal value for a $p_f\pi^\pm$ mass of $1.5\,\mathrm{GeV}/c^2$ lies below the most probable value of the distribution and does therefore not impose a strong limitation. More than 70% of the events pass this selection, even though they do not show any centrally produced characteristics. In contrast, the combination of this selection criterion with the requirement of a proton momentum above $140\,\mathrm{GeV}/c$ is only met by less than 10% of the events. Finally, only a negligible fraction of below 1% of the generated data features rapidity gaps of at least two units between the protons and the pions in the final state. The distribution of the four-momentum transfer t_1 from the beam proton to the central di-pion system exhibits only a very shallow slope for these events. The observed distribution of t_1 (cf. Figure 3.22a) can therefore not only be a kinematic consequence of the selection.

4.2 Reconstruction and Event Selection

In the next step, the generated events are processed by the official COMPASS simulation framework, where the final-state particles are propagated through the magnetic fields and the detector material. Monte-Carlo methods are used to simulate hard secondary scattering processes and soft interactions like energy loss and multiple scattering. The response of most detectors in the experimental setup is generated by the COMPASS reconstruction software, which is used for data and pseudo-data alike. Finally, the same requirements on the event topology have to be applied for both samples. A comparison with the generator output, the so-called Monte-Carlo truth, enables us to study and correct for geometrical and detector-related acceptance and resolution effects.

The key features of the simulation of the apparatus used for the hadron beam data-taking period in 2009 will be described in the following section.

4.2.1 Beam and Vertex Simulation

The magnet system which guides the beam from the production target to the COMPASS experiment produces strong correlations between energy, position and direction of the incident beam particles at the target position. In order to take these correlations into account, the reconstructed beam tracks and their vertex positions were taken directly from the selected

$p_f\pi^+\pi^-$ data set. A sample of 10^7 events, selected by the topological criteria introduced in Chapter 3, guaranteed a sufficiently dense coverage of the accepted beam phase space. An independent randomisation in the generator stage avoids event doubling for the generation of larger Monte-Carlo samples.

The reconstructed beam tracks fulfil all selection criteria. The divergence of the beam is therefore by definition limited to the geometrical acceptance and efficiency of the CEDAR detectors (cf. Section 3.1.3). A detailed simulation of the CEDAR detector response is not necessary.

4.2.2 RPD and Trigger Simulation

An important restriction on the acceptance is imposed by the trigger. All trigger and veto detector elements downstream of the target are implemented in the detailed geometrical model of the spectrometer. The largest restriction for centrally produced events is given by the geometrical acceptance of the spectrometer, which allows only scattering angles below 180 mrad with respect to the beam axis. Up to 50% of the generated events produce a signal in the sandwich veto detector, which translates into a vanishing acceptance for the backward hemisphere in the proton-proton centre-of-mass system. On the other hand, the veto on non-deflected proton tracks is only active for about 4% of the generated events. The beam counter condition is always fulfilled by the triggered beam track sample.

As introduced in Section 3.1.1, the target proton requires a minimal squared four-momentum transfer of $0.07\,\mathrm{GeV}^2/c^2$ in order to be able to penetrate the inner scintillator ring of the recoil proton detector. This sharp limit was already introduced on the generator level for reasons of efficiency. A detailed detector simulation provides the correct geometrical acceptance for the recoiling proton track as well as a realistic uncertainty for the reconstruction of its azimuthal angle.

4.2.3 RICH Matrices

A detailed simulation of the Cherenkov photon creation and propagation in the radiator vessel including the mirror system of the RICH detector can be arbitrarily complicated. In order to avoid this problem, the COMPASS analysis groups decided to evaluate the RICH performance with pure particle samples and tabulate the results as a function of particle momentum and polar angle θ with respect to the beam axis. A dedicated sample of events containing weak decays of K_S, Λ and $\overline{\Lambda}$ acts as a clean source for pions and (anti-)protons. The secondary decay is easily separated from the primary production vertex by a measurable flight path. The narrow $\phi(1020)$ resonance is used as a source for charged kaons. A detailed description of the selection can be found in [66].

These particle samples are analysed with the selection criteria motivated in Section 3.1.3 in order to determine the efficiency for particle identification. In addition, the probabilities for a wrongly attributed particle type play an important role. Figure 4.9 illustrates the relevant identification probabilities for positive pions and kaons used in this analysis. The square root of the polar angle θ was used to balance the available data to the spatial acceptance of the RICH detector. Especially the low misidentification probability for π^+ as K^+ in Figure 4.9b proves that the requirement for a 1.3-times larger kaon likelihood efficiently suppresses background from misidentified pions.

For centrally produced states decaying into charged kaons, the low-momentum threshold for $K^\pm$ identification at $9.5\,\mathrm{GeV}/c$ severely limits the accessible phase space. The kaon sample does, however, not allow for a fine granularity of the table in the low momentum region. We therefore introduced this cut explicitly into the simulation.

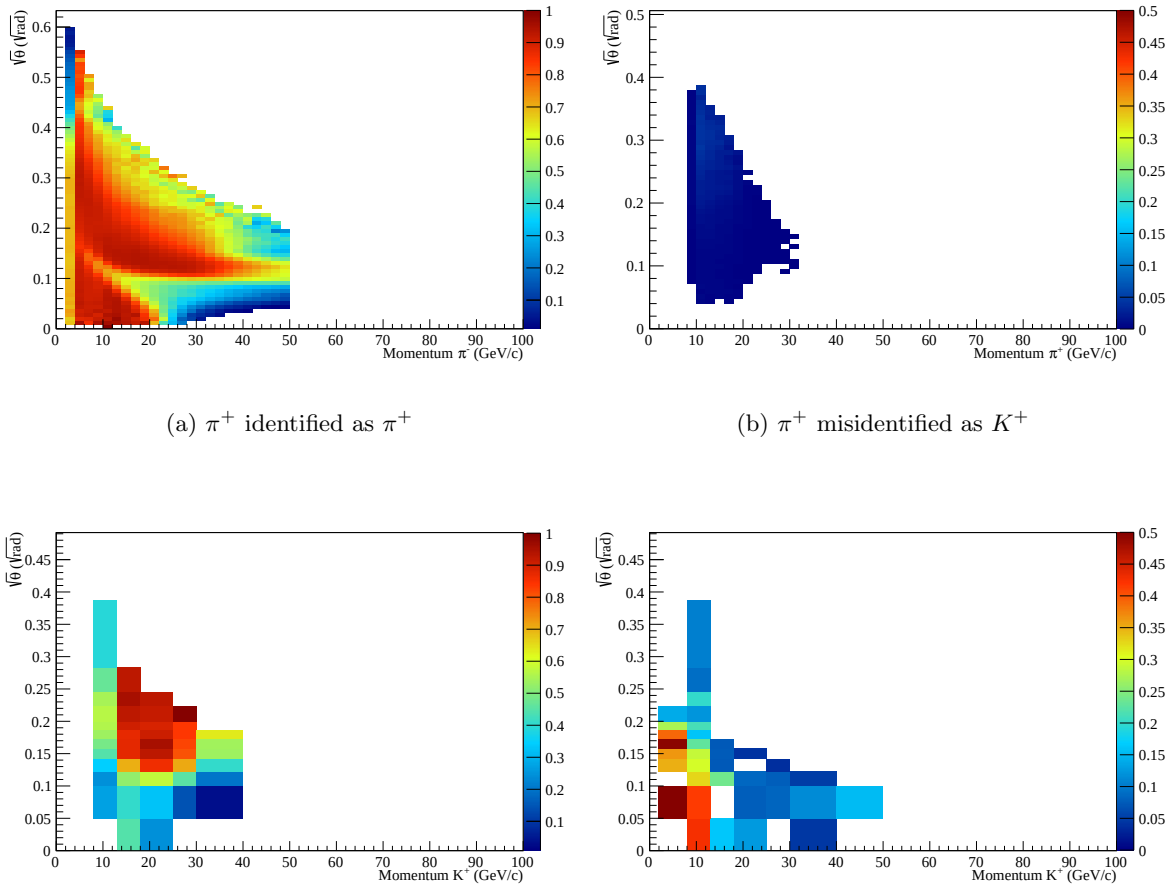

(a) π^+ identified as π^+

(b) π^+ misidentified as K^+

(c) K^+ identified as K^+

(d) K^+ misidentified as π^+

Figure 4.9: RICH probability tables used in this analysis.

4.3 Acceptance in Kinematic Variables

The acceptance is studied as a function of the relevant kinematic variables. All selection criteria are applied on pseudo-data reconstructed with the simulation of the experimental setup. The MC truth of these accepted events is filled into histograms and divided by the distributions of the generated sample. This neglects resolution effects, which are studied in Section 4.4. The homogeneous distribution of the kinematic properties in the available phase space avoids strong correlations between these quantities and allows to draw conclusions from one-dimensional projections. On the other hand, these correlations may be relevant in physical processes. Therefore, we include the multidimensional acceptance in the fit model for the partial-wave analysis (cf. Chapter 5).

The selection criteria for the central production reaction introduced in Section 3.3 strongly distort the generated sample. The $\pi^+\pi^-$ invariant mass distribution for events which fulfill the requirements $m(p\pi) > 1.5\,\mathrm{GeV}/c^2$ and $p(p_\mathrm{f}) > 140\,\mathrm{GeV}/c$ is, for example, shown in Figure 4.10, where the threshold is clearly emphasised. This effect dominates the acceptance as a function of the invariant mass of the centrally produced $\pi^+\pi^-$ system (cf. Figure 4.11). The average acceptance of approximately 30% is mainly due to the geometric acceptance of the

spectrometer, which covers only about 50% of the events completely. The vertex reconstruction with three outgoing charged tracks is another major source for deficiency. Apart from the enhancement towards the kinematic threshold, which is created by the selection of a central production topology, the acceptance is relatively flat as a function of the di-pion mass. Only for masses above $2\,\mathrm{GeV}/c^2$, the acceptance starts to diminish. This is one of the reasons, that the study of centrally produced charmonium states like the χ_{c0} with a mass of about $3.4\,\mathrm{GeV}/c^2$ is not feasible in COMPASS.

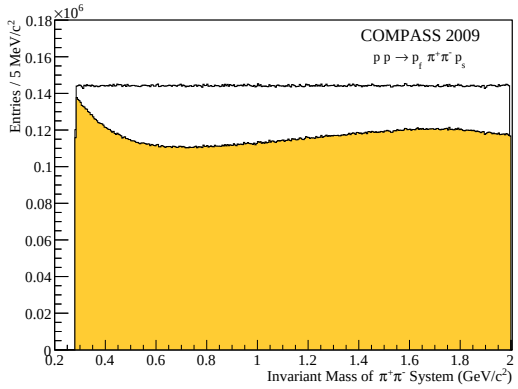

Figure 4.10: MC truth of $\pi^+\pi^-$ invariant mass, $m(p\pi) > 1.5\,\mathrm{GeV}/c^2$ and $p(p_\mathrm{f}) > 140\,\mathrm{GeV}/c$ (filled).

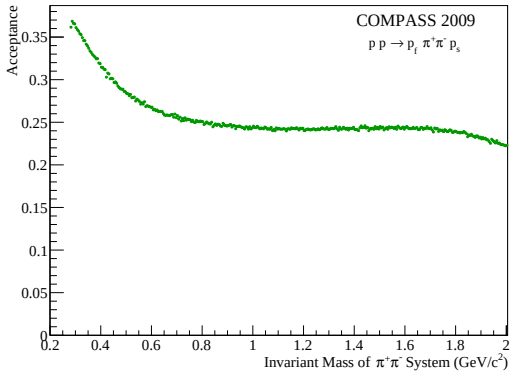

Figure 4.11: Acceptance as a function of the $\pi^+\pi^-$ invariant mass.

The rapidity distributions of the respective particle systems (cf. Figure 4.1) illustrate the effects of the geometrical acceptance. Starting from a uniform distribution in the rapidity interval $[-1, 1]$, the acceptance suppresses the events at negative rapidities. As a result, the initially symmetric Feynman x_F distribution in Figure 4.2 is also biased towards positive values.

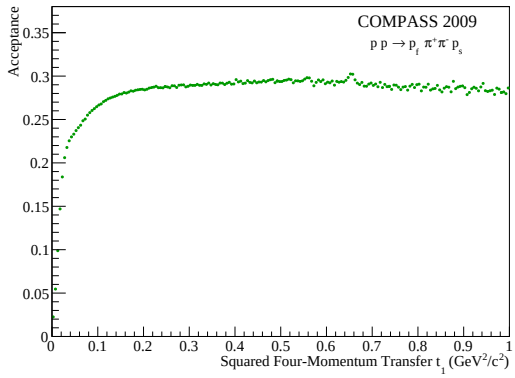

(a) $t_1 = -(p_\mathrm{beam} - p_\mathrm{f})^2$

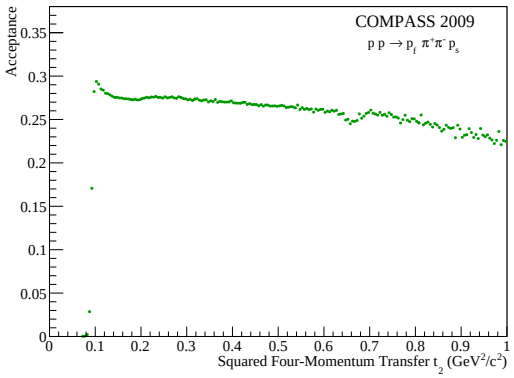

(b) $t_2 = -(p_\mathrm{target} - p_\mathrm{s})^2$

Figure 4.12: Acceptance as a function of the squared four-momentum transfer.

Figure 4.12 shows the dependence of the acceptance on the squared four-momentum transfer from the beam and the target proton to the central system, respectively. The trigger

threshold for t_2 is visible, but also the acceptance for t_1 decreases towards smaller values. Small discontinuities can further be observed around $t_2 = 0.7\,\mathrm{GeV}^2/c^2$, where the recoil proton momentum is no longer corrected for material effects in the barrels of the RPD [45].

The selection of centrally produced events by a minimal $p\pi$ invariant mass of $1.5\,\mathrm{GeV}/c^2$ has also a direct effect on the azimuthal angle ϕ between the proton scattering planes. While the acceptance is uniform for $\pi^+\pi^-$ masses above $1\,\mathrm{GeV}/c^2$, the correlation between ϕ and the di-pion mass can be clearly observed near threshold (cf. Figure 4.13), where an asymmetry is created by this kinematic requirement.

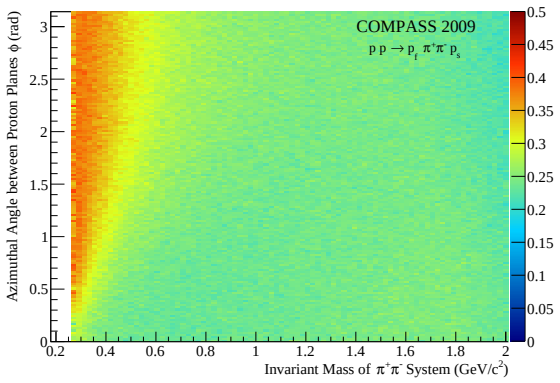

Figure 4.13: Acceptance as a function of the angle ϕ between the proton scattering planes and the $\pi^+\pi^-$ invariant mass.

4.4 Resolution

Monte-Carlo studies are also used to evaluate the reconstruction precision reachable with the experimental setup. For this purpose, the MC truth is compared to its reconstructed counterpart. The width of the residual distribution for a kinematic quantity is used as a measure for its resolution.

The partial-wave analysis is generally performed in bins of the invariant mass of the central system in order to guarantee a model-independent analysis without preconception of the resonant content. It is therefore useful to estimate the reachable mass resolution for the reconstruction of the studied $\pi^+\pi^-$ system, which can be estimated with the distribution of the relative residuum defined as

$$\Delta m = \frac{m_{\mathrm{truth}} - m_{\mathrm{reconstructed}}}{m_{\mathrm{truth}}} \,. \tag{4.3}$$

Figure 4.14a shows this relative residual distribution as a function of the $\pi^+\pi^-$ mass. Apart from the region at threshold which is dominated by kinematic constraints, the mass resolution is approximately constant as a function of the di-pion invariant mass. A Gaussian fit to the projection of the mass range between $0.4\,\mathrm{GeV}/c^2$ and $2.0\,\mathrm{GeV}/c^2$ has a width of about 1% (cf. Figure 4.14b), hence a mass binning smaller than $10\,\mathrm{MeV}/c^2$ is not reasonable for the analysis.

Since the experimental setup of the COMPASS experiment is not equipped to measure the incoming hadron beam momentum p_{beam}, it is important to estimate the resolution of the beam-momentum reconstruction via the final-state particles. The residual distribution, defined

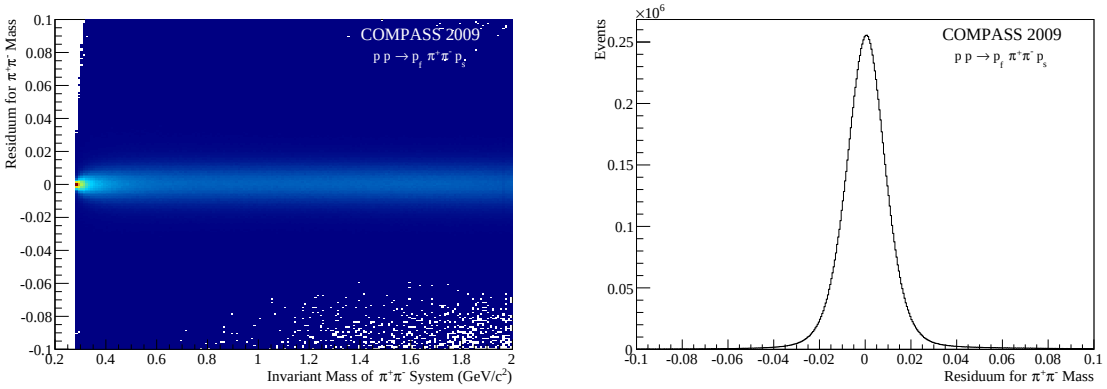

(a) Residuum for $\pi^+\pi^-$ mass

(b) Projection for $m_{\pi^+\pi^-} \in [0.4, 2]\,\mathrm{GeV}/c^2$

Figure 4.14: Mass resolution for the $\pi^+\pi^-$ system.

in analogy to Equation 4.3 for p_{beam}, is almost Gaussian, with a width below 0.4% (cf. Figure 4.15). The beam momentum of $191\,\mathrm{GeV}/c$ can thus be reconstructed with a precision of about $0.7\,\mathrm{GeV}/c$, which is much less than the intrinsic beam momentum spread of about $1.5\,\mathrm{GeV}/c$ (cf. Section 3.1.4).

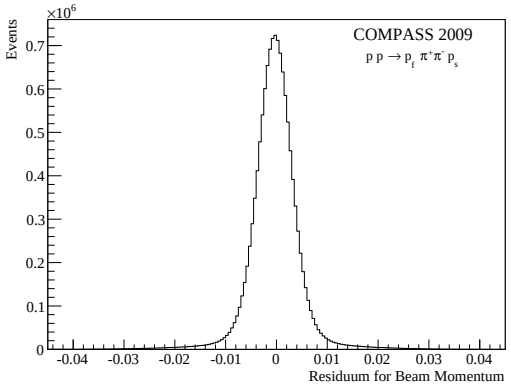

Figure 4.15: Resolution for beam momentum reconstruction.

The four-momentum transfers t_1 from the beam to the central system can be reconstructed within a resolution of about 3%. t_2 has a resolution of 5%, because it has to be reconstructed combining four-momentum conservation and the three particles measured by the spectrometer. The reconstruction capabilities of the RPD are considerably worse.

Chapter 5

Partial-Wave Decomposition

An invariant mass spectrum can show signs of resonances in the form of peaks, dips, or other structures. The properties of the resonances like mass, width, and quantum numbers can, however, only be determined by a multi-dimensional analysis of the decay process. The angular distribution of the daughter particles in two-body decays is directly related to the spin and parity quantum numbers of the system. Resonances that are produced with small cross sections can be traced back through their interference with known states. To this end, the data is decomposed into a sum of partial-wave amplitudes with complex-valued coefficients that describes the observed spatial distribution of the decay particles.

In this chapter, we will introduce the partial-wave analysis (PWA) method for centrally produced two-pseudoscalar meson systems on the example of $\pi^+\pi^-$ in the final state. At first, we will construct the decay amplitudes in term of angles with respect to the relevant coordinate system. These amplitudes are used for an extended maximum-likelihood fit to the data. The quality of the fit is evaluated by comparing differential distributions predicted by the model with those obtained with real data. Problems with the selection criteria for centrally produced events (cf. Section 3.3) will be discussed in this context. Finally, the partial-wave decomposition results in mathematical ambiguities, which are resolved by comparison with the $\pi^0\pi^0$ final state.

5.1 Partial-Wave Analysis Method

5.1.1 Coordinate System

The partial-wave analysis is performed assuming that the central $\pi^+\pi^-$ system is produced in the collision of two space-like particles emitted by the scattered protons [21]. These so-called exchange particles carry the squared four-momentum transfer t_1 from the beam proton and t_2 from the target proton to the central system, respectively. A Gottfried-Jackson frame [57] can be constructed if one of the space-like particles is treated as incoming beam.

In contrast to previous studies which chose the exchange with the greatest four-momentum transfer [21], we fixed the choice to t_1 in order to be able to correct for the different acceptances created by the trigger (cf. Chapter 4). In the centre-of-mass frame of the $\pi^+\pi^-$ system, the momentum vector of t_1 defines the z-axis for the reaction. The y-axis of the right-handed coordinate system is defined by the cross product of the two exchange particles in the pp centre-of-mass frame, which points along the production normal. The boost vector from the pp centre-of-mass frame to the $\pi^+\pi^-$ rest frame lies in the production plane and leaves the perpendicular axis unchanged.

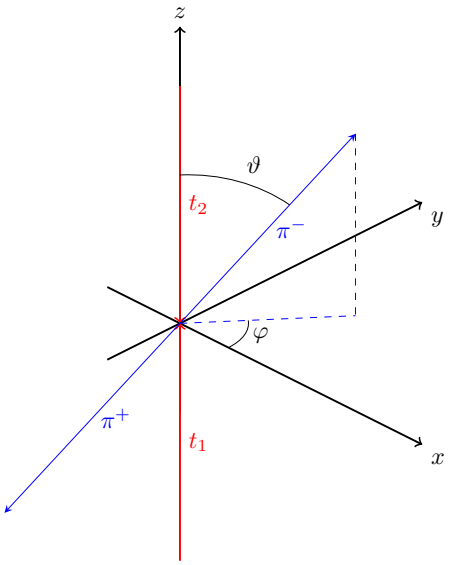

Figure 5.1: $\pi^+\pi^-$ Gottfried-Jackson rest system with definition of decay variables ϑ and φ.

Apart from the invariant mass of the $\pi^+\pi^-$ system, its decay is entirely characterised by two phase-space variables. A common choice [21] uses the polar angle ϑ and the azimuthal angle φ of the π^- in the di-pion rest frame relative to the Gottfried-Jackson coordinate system, specified above. Figure 5.1 illustrates the definition of these angles.

The distribution of the decay variables as a function of the di-pion mass is shown in Figure 5.2 for the selected centrally produced data sample. In $\cos\vartheta$, the data show a pronounced forward-backward symmetry, which is only slightly disturbed below $0.5\,\mathrm{GeV}/c^2$. A clearly distinguishable two-peak pattern can be observed in the mass regions around the $f_2(1270)$ resonance.

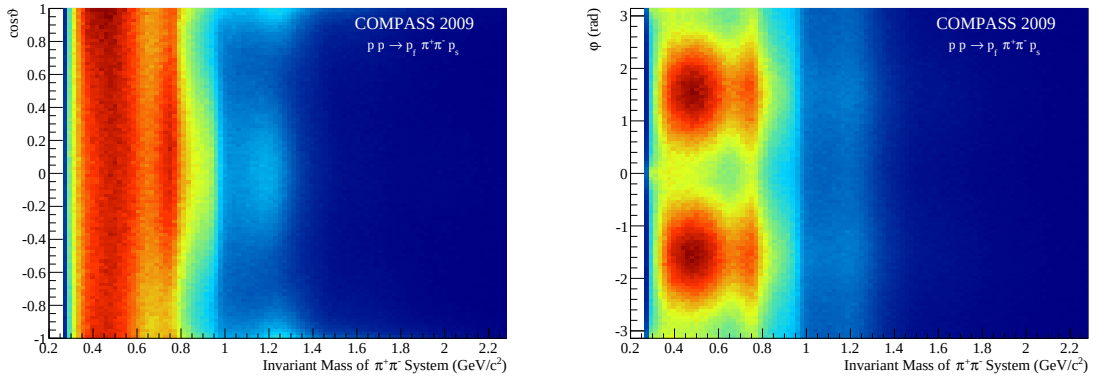

(a) $\cos\vartheta$ (b) φ

Figure 5.2: Decay variables as a function of the $\pi^+\pi^-$ mass.

Figure 5.3 shows the acceptance in the decay angles as it was evaluated with the Monte-Carlo simulation described in Chapter 4. It is mostly uniform, but poor above masses of $1\,\mathrm{GeV}/c^2$ for the cases where the central system decays along the z-axis, i.e. $\cos\vartheta \approx \pm 1$. The correction of this effect is indispensable for the partial-wave decomposition.

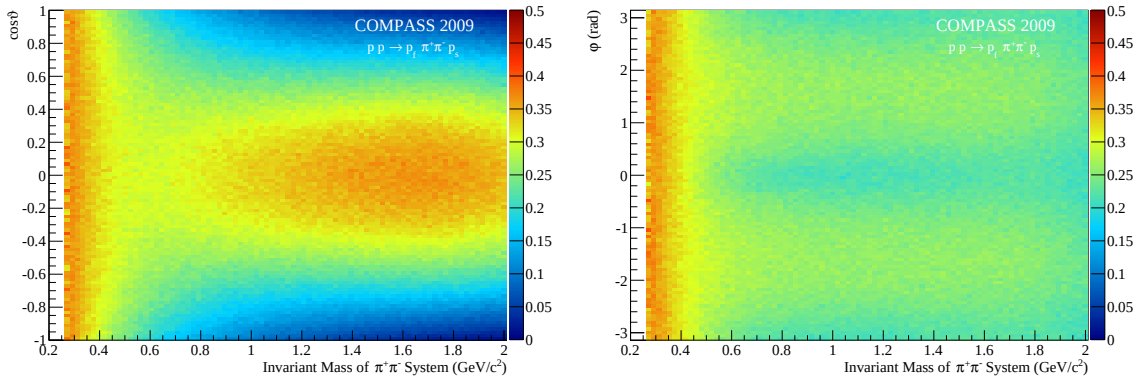

(a) $\cos\vartheta$ (b) φ

Figure 5.3: Acceptance in the decay angles and the $\pi^+\pi^-$ mass from phase-space MC.

5.1.2 Decay Amplitudes

The measured intensity distributions in ϑ, φ and the invariant mass m of the central system is decomposed into complex partial-wave amplitudes. The spherical harmonics $\mathcal{Y}_M^L(\vartheta,\varphi)$ are the natural choice for the decay amplitudes of a system of two spinless mesons with relative orbital angular momentum L and its projection M with respect to the quantisation axis. In order to avoid any assumptions on the mass-dependence of the amplitudes, we perform the decomposition independently in narrow mass bins of $10\,\mathrm{MeV}/c^2$. A finer segmentation is not beneficial due to the mass resolution evaluated in Chapter 4. However, this does not impose a disadvantage as most resonances in the light-quark sector have widths about an order of magnitude larger.

The fact that the strong interaction conserves parity is used to limit the number of fit parameters. We introduce the reflection operator as the parity operator followed by a rotation by 180° around the normal to the production plane [36]. This transformation preserves all relevant momenta. The parity is given by $(-1)^L$ for a system of two spinless particles. Therefore, the eigenstates of the reflection operator can be constructed as

$$\mathcal{Y}_M^{\varepsilon L}(\vartheta,\varphi) \equiv c_M \left[\mathcal{Y}_M^L(\vartheta,\varphi) - \varepsilon(-1)^M \mathcal{Y}_{-M}^L(\vartheta,\varphi)\right] \tag{5.1}$$

with the normalisation

$$c_M = \begin{cases} \frac{1}{2}, & \text{if } M > 0 \\ \frac{1}{\sqrt{2}}, & \text{if } M = 0 \\ 0, & \text{if } M < 0\ . \end{cases} \tag{5.2}$$

The so-called reflectivity quantum number ε can have the values ± 1. The two classes of eigenstates correspond to different production processes in the asymptotic limit of large s and low t and can therefore not interfere [57]. The magnetic quantum number M is restricted to

values between 0 and $+L$, and decays with $M = 0$ can only appear for negative reflectivities. In the original definition, the minus sign between the two terms in Formula 5.1 was chosen such that the reflectivity coincides with the exchanged naturality for diffractive reactions with a pion beam which has negative intrinsic parity. In the studied central-production reactions, only the product of the naturalities of both exchange particles can be identified with the reflectivity. The dominating process with two natural spin-parity transfers corresponds to the negative reflectivity $\varepsilon = -1$ and can produce a central system with $J^P = 0^+, 1^-, 2^+$ etc. Double-Pomeron exchange reactions are a special case in this field, where only even spins can be produced due to Bose symmetry. The positive-reflectivity domain is expected to be less important.

Using the properties of the spherical harmonics, the amplitudes can be brought into a simple form in terms of the associated Legendre polynomials $\mathcal{P}_M^L$:

$$\begin{aligned}\mathcal{Y}_M^{\varepsilon L}(\vartheta,\varphi) &= c_M \left[\mathcal{Y}_M^L(\vartheta,\varphi) - \varepsilon \mathcal{Y}_M^{L*}(\vartheta,\varphi)\right] \\ &= c_M \left[\mathcal{P}_M^L(\cos\vartheta) e^{iM\varphi} - \varepsilon \mathcal{P}_M^L(\cos\vartheta) e^{-iM\varphi}\right] \\ &= c_M \mathcal{P}_M^L(\cos\vartheta) \begin{cases} 2i\sin(M\varphi), & \text{if } \varepsilon = +1 \\ 2\cos(M\varphi), & \text{if } \varepsilon = -1 \end{cases}\end{aligned} \tag{5.3}$$

Since the reflectivity quantum number is conserved in strong interaction processes, the two reflectivity subsets are added incoherently. The imaginary factor i can thus be omitted as it does not affect the relative phases of waves with $\varepsilon = +1$. As a consequence, the decay amplitudes are real-valued functions in this special case. The complex-valued transition amplitudes $\mathcal{T}_{\varepsilon LM}$ represent the production dynamics. In narrow mass bins, they are approximated by constants, which are the parameters of the fit. All amplitudes, which have the same initial and final state, are allowed to quantum-mechanically interfere. Therefore, they have to be summed coherently. The intensity is expanded in terms of the partial-wave amplitudes as

$$\mathcal{I}(\vartheta,\varphi) = \sum_{\varepsilon=\pm1} \left| \sum_{L=0}^{\infty} \sum_{M=0}^{L} \mathcal{T}_{\varepsilon LM} \mathcal{Y}_M^{\varepsilon L}(\vartheta,\varphi) \right|^2 . \tag{5.4}$$

The infinite sum over the orbital angular momentum is truncated at $L = 2$, since contributions from higher spin states were not observed in previous experiments [21]. For the same reason, the magnetic quantum number is limited to $M \leq 1$. In the notation J_M^ε [21], where $J = L$ for the decay into pseudoscalar mesons, the general wave set is summarised as:

$$\{\boldsymbol{S_0^-}, P_0^-, P_1^-, D_0^-, D_1^-\}, \{\boldsymbol{P_1^+}, D_1^+\} \tag{5.5}$$

Since the global phase for each reflectivity is indeterminate, one transition amplitude in each class can be defined as purely real for the purposes of the fit. These so-called anchor waves are emphasised in bold font. The result does not dependent on this choice, which was adopted from [21].

Figure 5.4 shows the absolute value squared of the decay amplitudes as a function of the decay angles $\cos\vartheta$ and φ. These intensity distributions are symmetric with respect to the origin in both variables, hence the only possibility to produce an asymmetric distribution is through interference between partial waves with odd and even spin. As an example, this is demonstrated impressively in Figure 5.5 by varying the amplitude ratio between the S_0^-- and P_0^--waves. Even without relative phase, the interference terms produce a strong forward-backward asymmetry which is observed already with tiny admixtures. This illustrates the power of amplitude analysis.

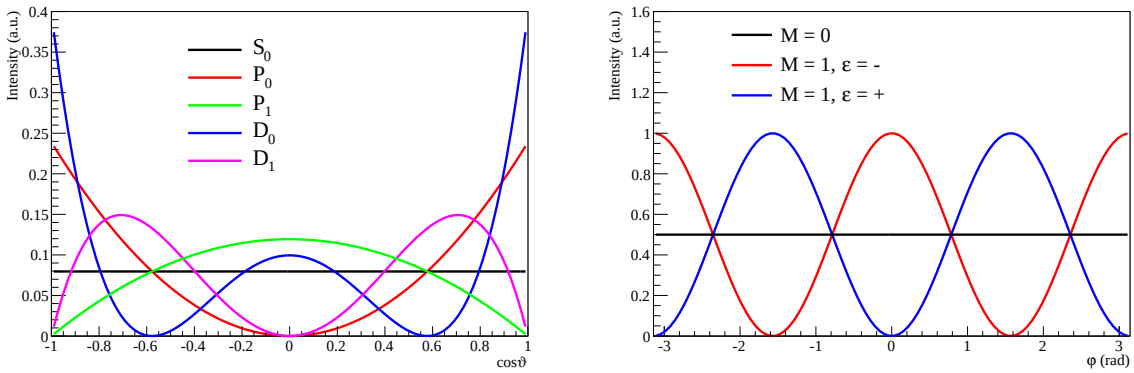

(a) $\cos\vartheta$ (b) φ

Figure 5.4: Intensity of lowest decay amplitudes as a function of the decay angles.

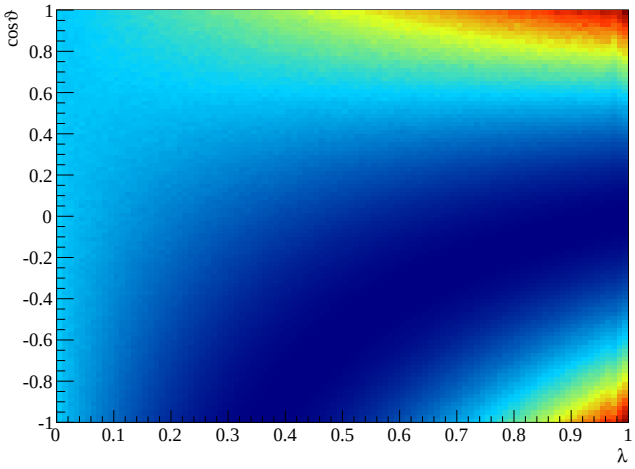

Figure 5.5: $\cos\vartheta$ distribution of intensity $\left|(1-\lambda)\,S_0^- + \lambda\,P_0^-\right|^2$ as a function of the ratio λ.

5.1.3 Extended Unbinned Maximum-Likelihood Fit

The agreement between measured data and the acceptance-corrected model is optimised by varying the complex transition amplitudes $\mathcal{T}_{\varepsilon LM}$ in each $\pi^+\pi^-$ mass bin independently. For this purpose, the extended likelihood function is maximised by a fitting algorithm. For the construction of this likelihood function, the probability for an event i characterised by ϑ_i and φ_i to be observed by the experiment with acceptance $\eta(\vartheta,\varphi)$ is defined by

$$P_i = \frac{\mathcal{I}(\vartheta_i,\varphi_i)\eta(\vartheta_i,\varphi_i)}{\int d\Omega\,\mathcal{I}(\vartheta,\varphi)\eta(\vartheta,\varphi)}\ . \tag{5.6}$$

The total number of observed events N in an experiment of fixed duration follows the Poisson distribution with an expectation value $\bar{N}$. The extended likelihood function

$$\mathcal{L} = \frac{e^{-\bar{N}}\bar{N}^N}{N!}\prod_{i=1}^{N} P_i \tag{5.7}$$

takes this variation into account. If we identify the expectation value $\bar{N}$ with the total number of measured events expressed by the integral in the denominator of Equation 5.6, the likelihood function simplifies to

$$\mathcal{L} = \frac{e^{-\bar{N}}}{N!}\prod_{i=1}^{N} \mathcal{I}(\vartheta_i, \varphi_i)\eta(\vartheta_i, \varphi_i) \ . \tag{5.8}$$

As sums are computationally easier to handle than products, the logarithm of the likelihood function is maximised in order to match the observed angular distribution $\mathcal{I}(\vartheta, \varphi)$.

$$\ln \mathcal{L} = \sum_{i=1}^{N} \ln \mathcal{I}(\vartheta_i, \varphi_i) + \sum_{i=1}^{N} \ln \eta(\vartheta_i, \varphi_i) - \ln N! - \int d\Omega\, \mathcal{I}(\vartheta, \varphi)\eta(\vartheta, \varphi) \ . \tag{5.9}$$

The constant terms $\Sigma \ln \eta$ and $\ln N!$ do not depend on the transition amplitudes $\mathcal{T}_{\varepsilon LM}$ and can therefore be omitted in the fit. The recorded events only enter in the first sum. The integral for the experimental acceptance is evaluated with the large phase-space Monte-Carlo sample introduced in Chapter 4. For this purpose, the sum of the absolute values squared for the intensity (cf. Equation 5.4) is written as a double sum:

$$\mathcal{I}(\vartheta, \varphi) = \sum_{\varepsilon} \sum_{L,L'} \sum_{M,M'} \mathcal{T}_{\varepsilon LM} \mathcal{T}^{*}_{\varepsilon L'M'} \mathcal{Y}^{\varepsilon L}_{M}(\vartheta, \varphi) \mathcal{Y}^{\varepsilon L'}_{M'}(\vartheta, \varphi) \tag{5.10}$$

This permits the separation of the fit parameters from the integral, so that it does not have to be computed in every iteration of the maximisation procedure.

$$\int d\Omega\, \mathcal{I}(\vartheta, \varphi)\eta(\vartheta, \varphi) = \sum_{\varepsilon} \sum_{L,L'} \sum_{M,M'} \mathcal{T}_{\varepsilon LM} \mathcal{T}^{*}_{\varepsilon L'M'} \underbrace{\int d\Omega\, \mathcal{Y}^{\varepsilon L}_{M}(\vartheta, \varphi) \mathcal{Y}^{\varepsilon L'}_{M'}(\vartheta, \varphi)\eta(\vartheta, \varphi)}_{\mathbb{I}^{\varepsilon}_{LML'M'}} \tag{5.11}$$

The so-called normalisation integral $\mathbb{I}^{\varepsilon}_{LML'M'}$ is approximated by the sum over all generated events $N^{\text{acc}}_{\text{MC}}$, which passed the reconstruction and selection criteria after the detector simulation:

$$\mathbb{I}^{\varepsilon}_{LML'M'} \approx \frac{4\pi}{N_{\text{MC}}} \sum_{j=1}^{N^{\text{acc}}_{\text{MC}}} \mathcal{Y}^{\varepsilon L}_{M}(\vartheta_j, \varphi_j) \mathcal{Y}^{\varepsilon L'}_{M'}(\vartheta_j, \varphi_j) \tag{5.12}$$

N_{MC} is the total number of generated Monte-Carlo events. The factor 4π is the integration volume and is important in order to obtain the correct normalisation for the transition amplitudes $\mathcal{T}_{\varepsilon LM}$ [94].

The extended likelihood function is maximised by choosing the parameters $\mathcal{T}_{\varepsilon LM}$ such that $\mathcal{I}(\vartheta, \varphi)$ matches the measured data best. This formalism was implemented in a stand-alone *C++* program, employing the Minuit minimiser [65] in the ROOT libraries [31]. A general description can be found in [94].

5.2 Evaluation of Fit Quality

If the fit converges, the expectation value $\bar{N}$ is very close to the measured number of events N. This can be used in order to evaluate the quality of the model. Using the numerical approximation of this integral by the sum over the accepted phase space Monte-Carlo events

$$\bar{N} = \int d\Omega\, \mathcal{I}(\vartheta, \varphi)\eta(\vartheta, \varphi) \approx \frac{4\pi}{N_{\mathrm{MC}}} \sum_{N_{\mathrm{acc}}} \mathcal{I}(\vartheta_{\mathrm{MC}}, \varphi_{\mathrm{MC}}) \ , \tag{5.13}$$

we can understand the amplitude for each MC event as a weight w_i for this particular phase-space element [94].

$$w_i = \frac{4\pi}{N_{\mathrm{MC}}} \sum_{\varepsilon} \left| \sum_{L} \sum_{M} \mathcal{T}_{\varepsilon LM} \mathcal{Y}_M^{\varepsilon L}(\vartheta_i, \varphi_i) \right|^2 \tag{5.14}$$

Events rejected by reconstruction and kinematic selection have zero weight. The acceptance of the apparatus is therefore taken into account by definition. We can use these weights to compare any kinematic distribution of the fitted model with the data. An agreement within statistical errors in the angles that enter the decay amplitudes is a confirmation that the truncated wave set is sufficient to describe the data. The distributions in other kinematic variables can be used to assess the quality of the simulation.

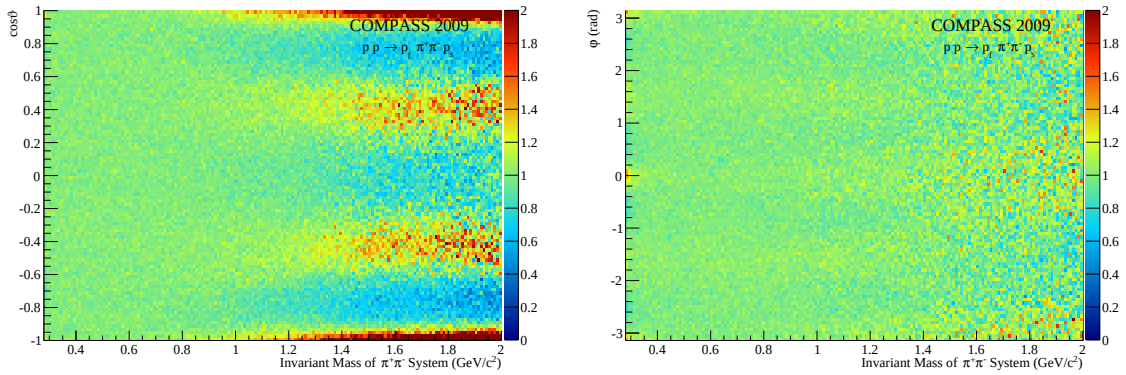

(a) $\cos\vartheta$ (b) φ

Figure 5.6: Ratio between data and weighted phase space Monte-Carlo sample.

After a successful fit, the angular distributions show a reasonable agreement. However, the ratio between data and the weighted Monte-Carlo sample (cf. Figure 5.6) reveals deviations of the model in the $\cos\vartheta$ distributions for $\pi^+\pi^-$ masses above $1\,\mathrm{GeV}/c^2$, in particular in the regions around $\cos\vartheta = \pm 1$. As an illustration for this, we compare the $\cos\vartheta$ and φ distributions in selected $100\,\mathrm{MeV}/c^2$ wide $\pi^+\pi^-$ mass slices in Figure 5.7. The tendency of the data to peak at forward and backward angles of the pions for high di-pion masses cannot be reproduced by the limited wave set. The sharp structures would require contributions from higher spins. In addition, this effect biases the fit also for intermediate polar angles.

In order to prove that the origin for this artifact is only restricted to the kinematic region near $\cos\vartheta = \pm 1$, we performed a partial-wave analysis disregarding the data with $|\cos\vartheta| > 0.8$, which is about 20% of the total sample. The improvement can be directly observed in Figure 5.8, where the fitted region is nicely reproduced up to $2\,\mathrm{GeV}/c^2$. Qualitatively, this additional cut does not influence the results of the analysis.

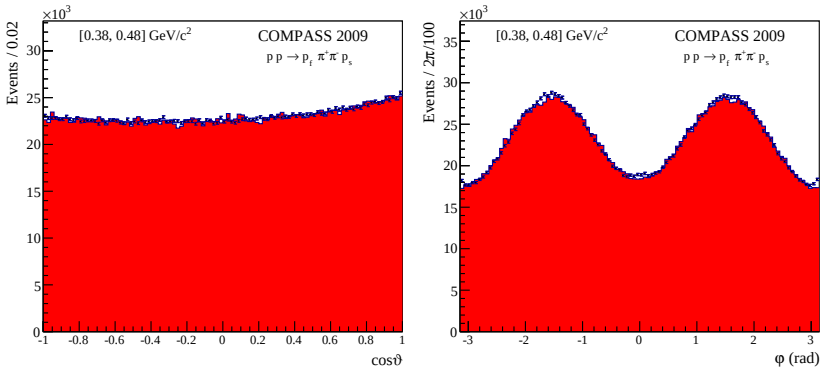

(a) $m_{\pi^+\pi^-} = [0.38, 0.48]\,\mathrm{GeV}/c^2$

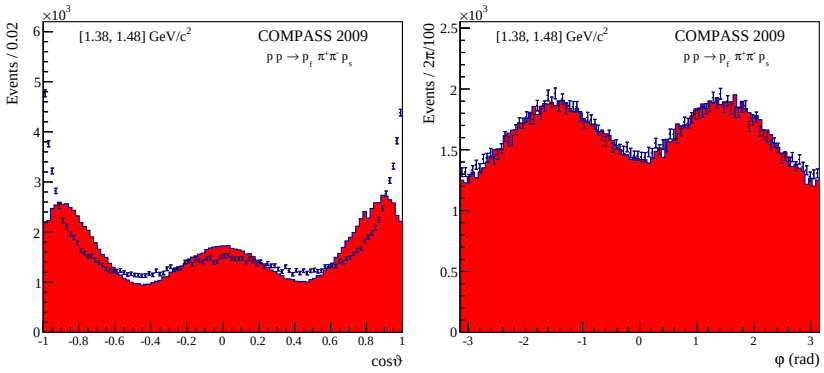

(b) $m_{\pi^+\pi^-} = [1.38, 1.48]\,\mathrm{GeV}/c^2$

Figure 5.7: Real data (blue) and weighted Monte-Carlo (red) for two di-pion mass ranges.

An alternative production process competing with central production can explain this $\cos\vartheta$ behaviour. If a baryon resonance and a slow pion are produced via Regge-exchange in analogy to the Deck process (cf. Figure 3.40), and the resonance subsequently decays into $p_\mathrm{f}\pi$, the two pions will be kinematically separated. Consequently, their invariant mass is rather high and the polar angle in the $\pi\pi$ rest frame is close to zero or 180°, which is exactly the observed signature. As it was discussed in Section 3.3.1, there is indeed considerable evidence for baryon resonances above the central production selection criterion $m(p\pi) > 1.5\,\mathrm{GeV}/c^2$.

As a consequence, we decided to abandon the $p\pi$ invariant-mass cut suggested by a previous analysis [21] for this work. In Section 3.3.2, we introduced the central di-pion system, for which a minimal rapidity gap between the protons and the pions of at least two units is required. This theoretically motivated selection [43] effectively suppresses the background from baryon resonance production (cf. Figure 3.19). In fact, the acceptance for the centrally produced di-pion system imposes a restriction similar to the $\cos\vartheta$ cut on the regions of phase space with forward or backward angles (cf. Figure 5.9). The occurrence of rapidity gaps is, however, only indirectly related to the invariant mass of the $p\pi$ systems. A cleaner separation of the centrally produced sample is achieved in rapidity space.

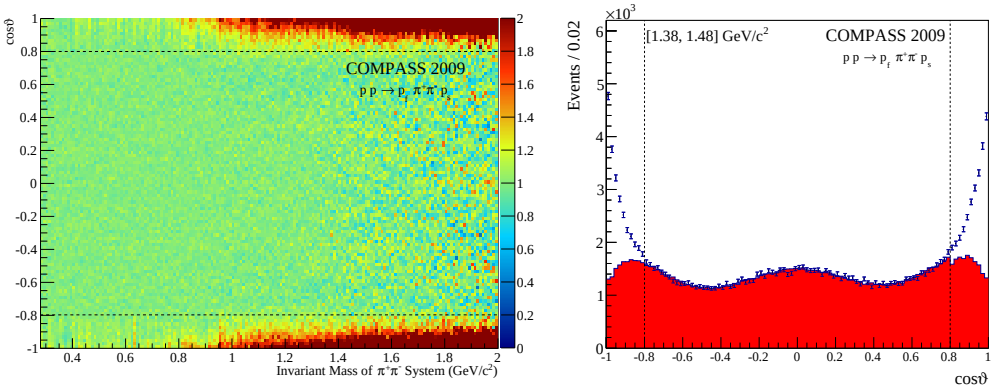

(a) Ratio (b) $m_{\pi^+\pi^-} = [1.38, 1.48]\,\mathrm{GeV}/c^2$

Figure 5.8: Data and weighted Monte-Carlo for fit restricted to $|\cos\vartheta| < 0.8$ (dashed lines).

For a fit to the data sample selected with the requirement for rapidity gaps larger than two units, the angular distributions are reproduced in the entire available phase space without additional restrictions. Figure 5.10 shows the corresponding ratio between the data and the Monte-Carlo sample weighted with the fit results. In comparison with Figure 5.8, the difference for the mass slice from $1.38\,\mathrm{GeV}/c^2$ to $1.48\,\mathrm{GeV}/c^2$ is striking. Nevertheless, the results for the transition amplitudes are not substantially different, which proves that the acceptance effects are properly corrected for.

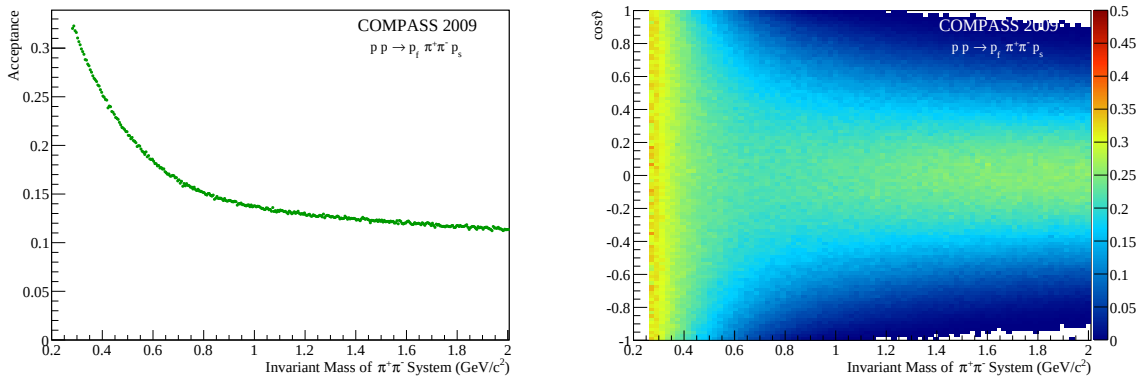

(a) (b)

Figure 5.9: Acceptance in $\cos\vartheta$ with $|y(p) - y(\pi)| > 2$.

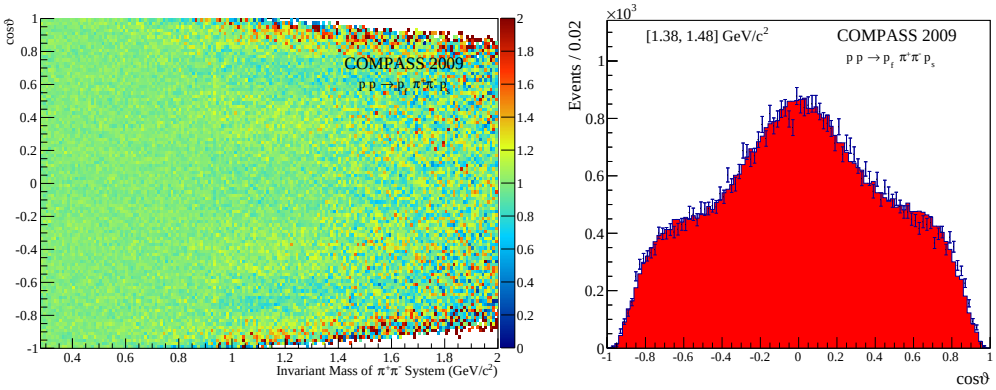

(a) Ratio

(b) $m_{\pi^+\pi^-} = [1.38, 1.48]\,\mathrm{GeV}/c^2$

Figure 5.10: Data and weighted Monte-Carlo for sample selected with $|y(p) - y(\pi)| > 2$.

5.3 Ambiguities in the PWA of Two-Pseudoscalar Final States

The fitted transition amplitudes $\mathcal{T}_{\varepsilon LM}$ include a phase difference with respect to the anchor wave, whose choice is essentially arbitrary. Only the products $\mathcal{T}_{\varepsilon LM}\mathcal{T}^*_{\varepsilon L'M'}$ correspond to physical observables, the components of the so-called spin-density matrix [36]. The diagonal elements are the real-valued partial-wave intensities, while the off-diagonal elements are complex-valued interference terms. It is customary to quote the argument of these terms, which specifies the respective phase difference between the two partial waves.

In the case of a two-pseudoscalar final state, the decomposition of the intensity in Equation 5.4 is not unique. We will introduce the reasons for this ambiguity in the following section, before discussing the physically meaningful solution.

5.3.1 Mathematical Basis

In general, the truncated $\pi\pi$ scattering amplitude $A(s,t)$ can be expanded in terms of Legendre polynomials $\mathcal{P}_\ell$ with a maximal orbital angular momentum L,

$$A(s,t) = \sum_{\ell=1}^{L} (2\ell+1)\, a_\ell(s)\, \mathcal{P}_\ell(\cos\vartheta)\ . \tag{5.15}$$

The fundamental theorem of algebra states that this degree-L polynomial in $z \equiv \cos\vartheta$ has exactly L complex roots z_i. The amplitude can therefore be expressed as a function of the so-called Barrelet-zeros z_i[23]

$$A(s,t) \propto \prod_{i=1}^{L} (z - z_i)\ . \tag{5.16}$$

The measurable intensity is proportional to the absolute square of this term

$$I(s,t) = |A(s,t)|^2 \propto \prod_{i=1}^{L} (z - z_i)(z - z_i^*)\ . \tag{5.17}$$

This expression is invariant under complex conjugation of any number of the Barrelet zeros z_i. Hence, the measurement has an intrinsic mathematical ambiguity. The decomposition into angular momentum states can be done in 2^L ways, characterised by the signs of the imaginary parts of the roots. All solutions reproduce exactly the same angular distribution.

The authors of [56, 90] have extended this method for the case of two-pseudoscalar final states in scattering experiments. The two incoherent naturalities and the additional magnetic quantum number M require a rather complicated approach. The Weierstrass substitution $u \equiv \tan\frac{\vartheta}{2}$ is a key ingredient for the analogous construction of the polynomials. The direct transformation between the coefficients, the partial-wave amplitudes and the roots u_i are explicitly worked out for a number of examples in [35].

5.3.2 Application to Data

For the wave-set used in this analysis, it is shown that only the waves with negative reflectivity can give rise to ambiguities. In a system of S-, P- and D-waves with $M \leq 1$, eight mathematically ambiguous solutions are obtained. Experimentally, this can be illustrated by using different random starting values in every mass bin for several fits. Figure 5.11 shows the intensities of 30 fit attempts as a function of the $\pi^+\pi^-$ mass, where several different solutions can be discerned. It is, however, difficult to achieve a separation over the full mass range if the solutions overlap, and the necessity for a large number of fit attempts is impractical. A procedure to perform the decomposition mathematically is therefore essential.

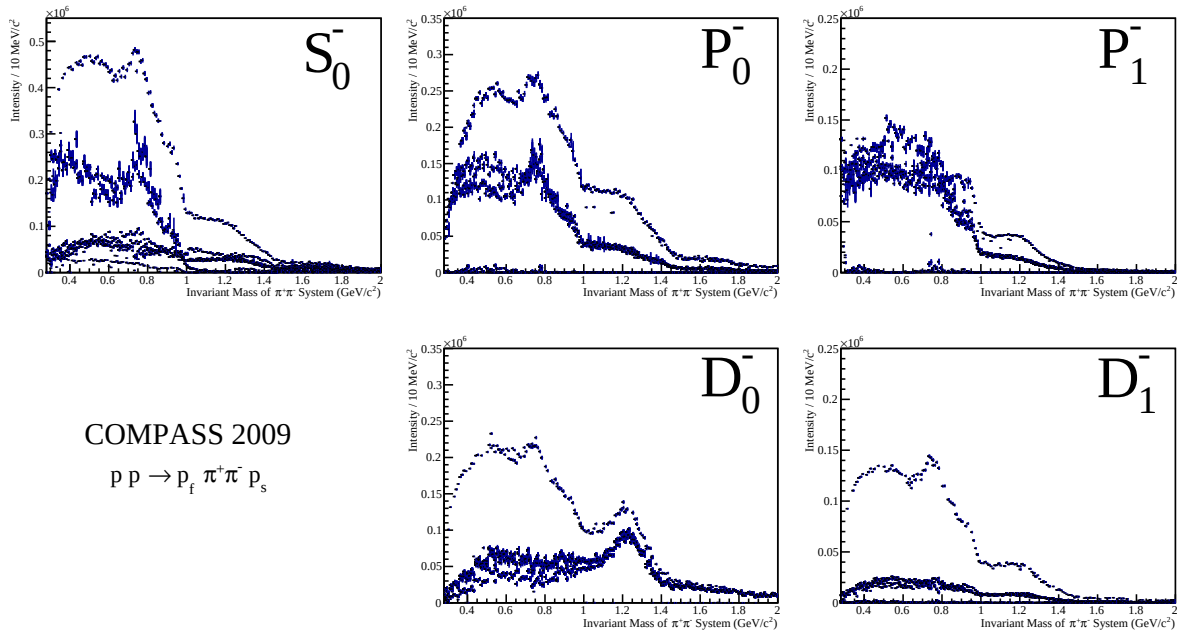

Figure 5.11: Partial-wave intensities for 30 fit attempts with random starting values.

With the method described in [35], the transition amplitudes $\mathcal{T}_{\varepsilon LM}$ obtained by one single fit attempt can be used to calculate all eight solutions analytically. The formulae for the coefficients of the forth-order polynomial in terms of the amplitudes can be found in Appendix A.1. The inverse transformation from Barrelet zeros to partial-wave amplitudes is given as well.

Laguerre's method [86] is used to find the complex polynomial roots numerically. It starts from an initial guess and iteratively converges to the polynomial roots. Figure 5.12 shows the

real and imaginary parts of these four roots for all $\pi^+\pi^-$ mass bins. A sorting depending on the magnitude of the real part has been performed, where the solutions are well separated from each other and can be easily linked from mass bin to mass bin. Since the sign of the imaginary part of the roots can be chosen, we plotted only the positive branches. The imaginary parts do not approach zero, hence bifurcation of the solutions in the complex plane does not pose a problem and they can be uniquely identified.

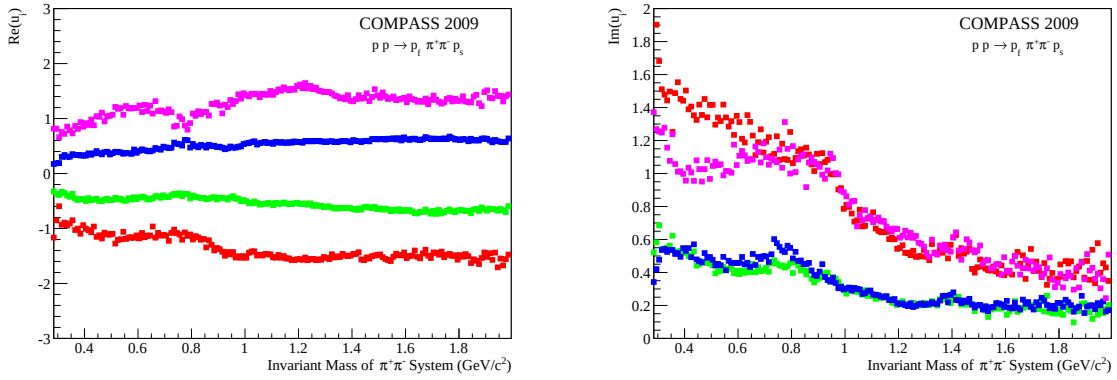

(a) Real part

(b) Imaginary part

Figure 5.12: Barrelet zeros as a function of the $\pi^+\pi^-$ mass.

The entire set of eight ambiguous solutions is computed using the transformation in Appendix A.1. The intensity distributions resulting from one single fit attempt are depicted as a function of the $\pi^+\pi^-$ mass in Figure 5.13. The solutions exactly reproduce the picture in Figure 5.11, which was obtained with random starting variables, proving the correct implementation of the procedure.

As a last step, the calculated transition amplitudes are introduced as starting values to the extended maximum-likelihood fit. Its convergence proves the equivalence of the solutions. In addition, the fit routine provides error estimates that cannot be calculated with the method of the Barrelet zeros.

5.3.3 Choice of Physical Solution

The choice of the physical amplitudes requires additional input. In previous analyses, e.g. [21], the behaviour at threshold or towards expected resonances was quoted as a justification for this choice. In contrast, we can use the associated production of a central $\pi^0\pi^0$ system as a reference, since only even partial waves are allowed for a decay into these two equal particles. This reduces the number of mathematical ambiguities to two solutions, the choice is facilitated. The analogy to the partial-wave decomposition in the case of charged final-state pions can be used to support the physical solution.

For the analysis, we used the $\pi^0\pi^0$ sample introduced in Section 3.4. Since the acceptance for the successful reconstruction of the centrally produced four-photon final state is only about 2%, another sample of $5 \cdot 10^7$ Monte-Carlo events was generated for this channel with the framework described in Chapter 4. The wave set is reduced to only four waves by the restrictions from Bose symmetry:

$$\{\boldsymbol{S_0^-}, D_0^-, D_1^-\}, \{\boldsymbol{D_1^+}\} \tag{5.18}$$

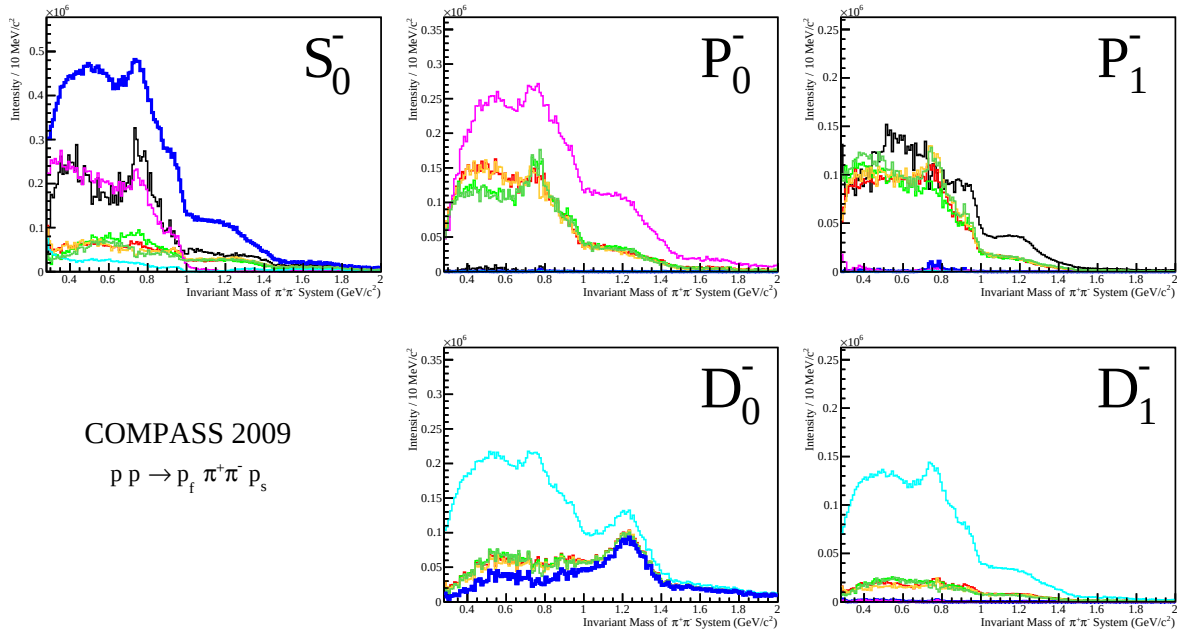

Figure 5.13: Partial-wave intensities of eight ambiguous solutions, computed with the results of one single fit.

Due to the limited data sample, we perform the partial-wave analysis in $\pi^0\pi^0$ mass bins of $30\,\mathrm{MeV}/c^2$ width. The intensity distribution can now be expressed in a second-order polynomial, which yields only two independent ambiguous solutions. The detailed mathematical treatment is described in [35], the applied formulae are summarised in Appendix A.2. Figure 5.14 shows the roots obtained by one fit to the data. A unique identification along all bins is possible by the sign of the real part, even though the fluctuations are large.

After expressing the transition amplitudes in terms of the obtained Barrelet zeros, we obtain two different intensity distributions which are shown in Figure 5.15. The most dominant feature is the peak in the D_0^--wave at the mass of the $f_2(1270)$. In one solution, however, the peak lies on top of another large signal, which describes the majority of the entire intensity by its interference with the D_1^--wave. The scalar component is comparably small for this solution (red), an effect that is not physical especially near threshold due to the angular momentum barrier of the breakup.

In contrast, a clean $f_2(1270)$ peak can be discerned in the blue histogram, which represents the second solution. The S_0^--wave is dominant at threshold, and exhibits the characteristic shoulder near the $f_0(980)$ meson. In addition, the strong suppression of the $M = 1$ component is a clear sign for Pomeron-exchange processes. For these reasons, we will call this one the physical solution from now on.

Figure 5.16 shows the intensities and phases of the physical solution, as they are obtained after a refit with the calculated starting values. The results are presented in a block-diagonal matrix form, corresponding to the spin-density matrix according to Chung and Truman [36]. The plots on the diagonal show the intensities of the partial waves, the off-diagonal entries depict the relative phases between the waves in the rows and columns, respectively. Since the spin-density matrix is hermitian, it is sufficient to show only the upper triangle. The 3×3 matrix represents the negative-reflectivity part, the single field in the bottom left corresponds to the incoherent positive-reflectivity wave.

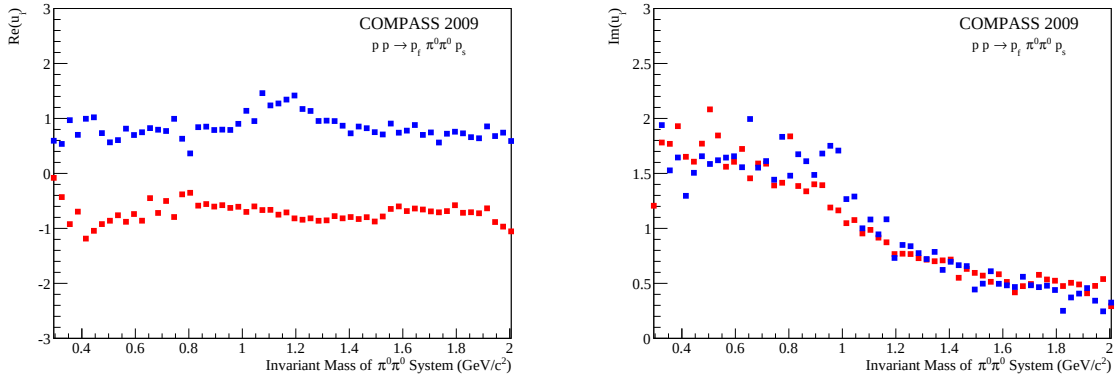

(a) Real part

(b) Imaginary part

Figure 5.14: Barrelet zeros as a function of the $\pi^0\pi^0$ mass.

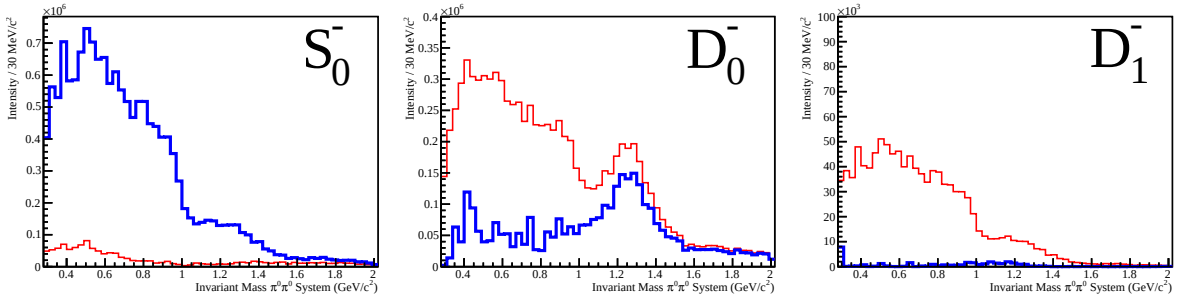

Figure 5.15: Two ambiguous solutions for the $\pi^0\pi^0$ system, computed with the results of one single fit.

In addition to the intensity distributions, we can now observe a distinct phase motion of about 40° near the $f_2(1270)$ resonance with respect to the S-wave. For a part of the mass range, the phases with respect to the D_1^--wave are not well-defined due to its low intensity. No indication for a resonant behaviour can be observed in this wave.

The insights gained with the $\pi^0\pi^0$ sample are used to justify the choice of the solution for the more complicated case with two distinguishable pions. Disregarding the $\rho(770)$ mass region, the blue curve in Figure 5.13 turns out to be almost congruent with the physical solution of the neutral pion case. Also here, the largest part of the intensity is in the S-wave, and a prominent peak for the $f_2(1270)$ can be observed in D_0^-. The biggest difference is the peak near $0.8\,\mathrm{GeV}/c^2$ in the S-wave, a sign for the production of the $\rho(770)$ resonance. Since there is no solution where the $\rho(770)$ meson is isolated in the correct P-waves, a different production mechanism has to be responsible for it. Candidates for this behaviour are the diffractive dissociation of the proton into $p\rho(770)$ or Deck-like processes (cf. Section 3.5.3).

We provide the physical solution as starting values for the fit and present the results in the symmetric, block-diagonal matrix-form in Figure 5.17. The complicated structure of the phase difference between S_0^-- and D_0^--wave is revealed in the fine binning, permitted

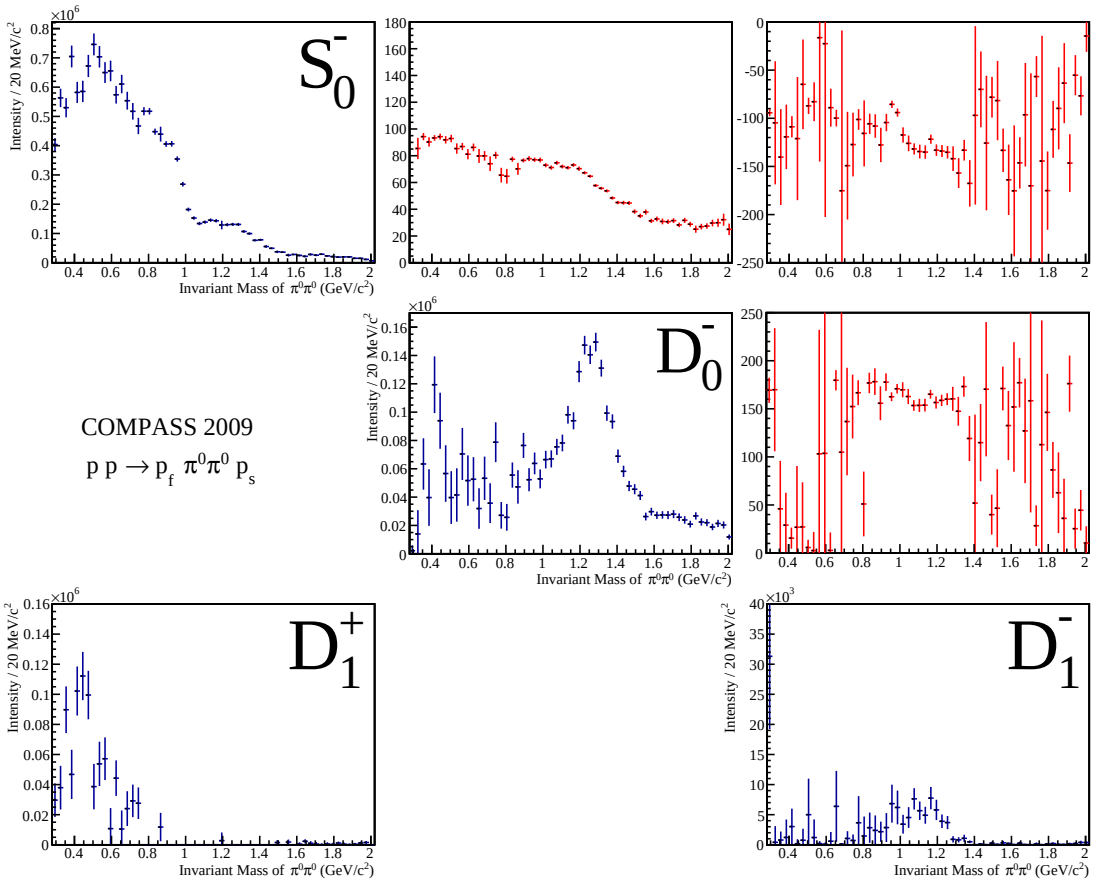

Figure 5.16: Physical solution for $\pi^0\pi^0$, intensities (blue) and relative phases in degrees (red).

by the large data set. The P^--waves exhibit very little intensity, the phase with respect to these waves consequently carries no information. Only in P_1^-, hints for the $\rho(770)$ can be discerned. The suppression of odd waves in central production supports the notion of a dominant contribution from the symmetric double-Pomeron exchange process. Only the P_1^+-wave seems to be especially important for the description of the angular distributions below $0.6\,\mathrm{GeV}/c^2$, where the intensity is even larger than that of the $f_2(1270)$ resonance in the D_0^--wave. We attribute this effect to non-resonant components. An incoherently added, uniform amplitude was tried to take this component into account. However, it created an instability due to its similarity to the S-wave.

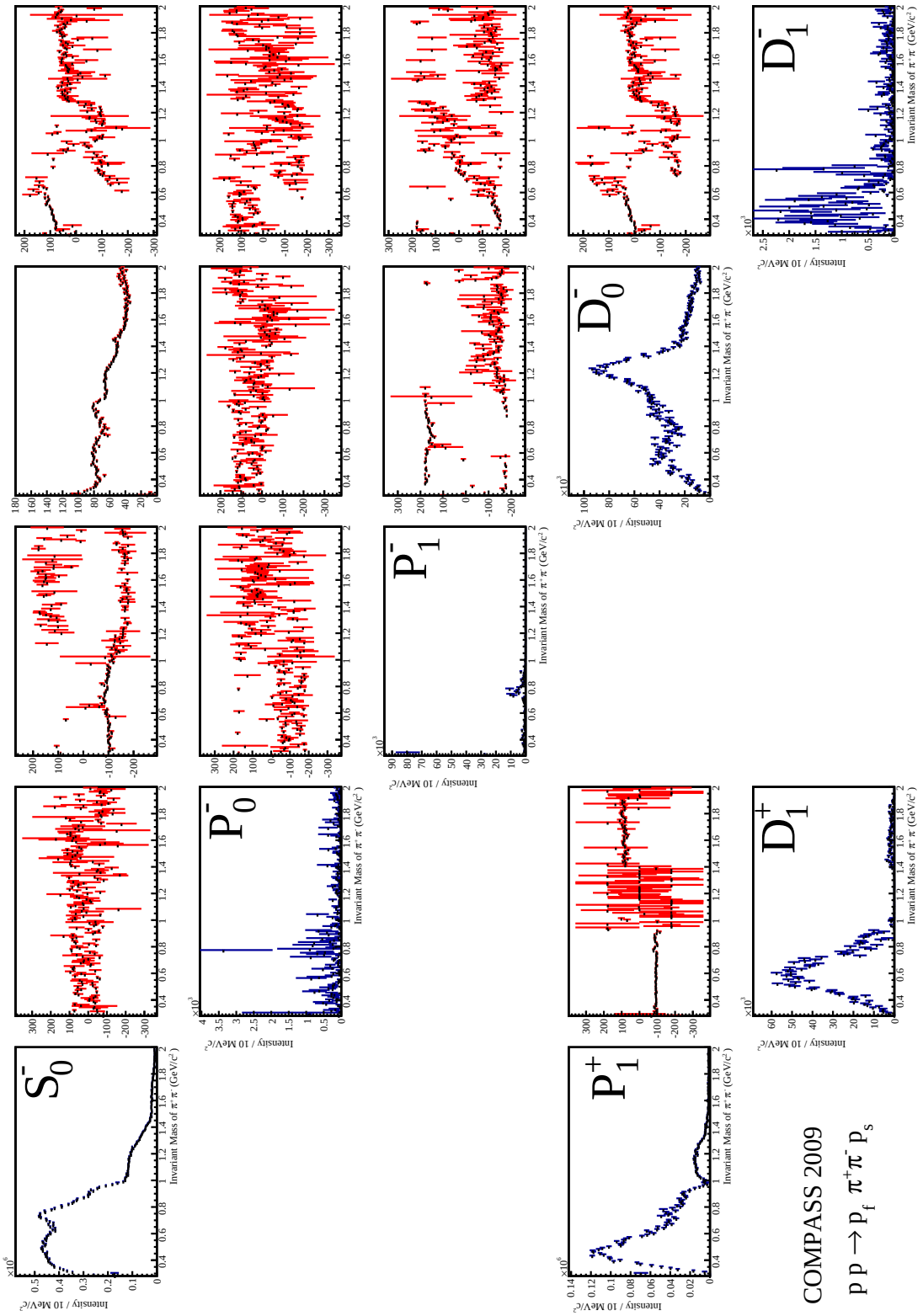

Figure 5.17: Physical solution for $\pi^+\pi^-$, intensities (blue) and relative phases in degrees (red).

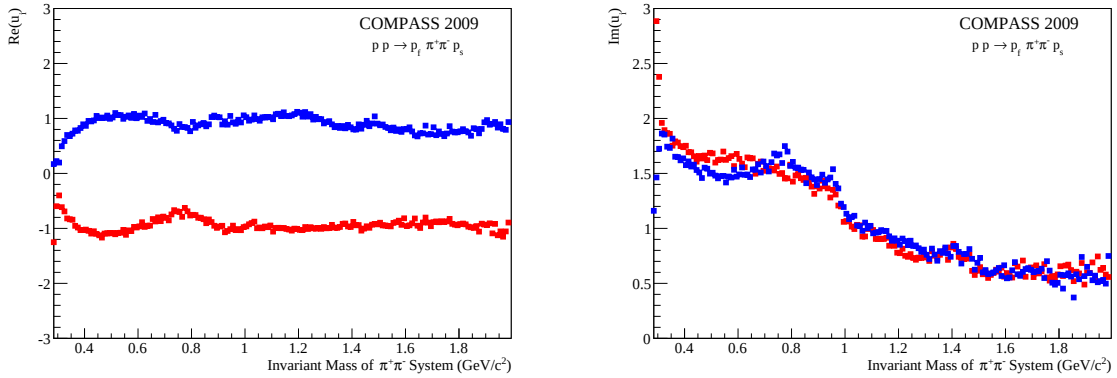

(a) Real part

(b) Imaginary part

Figure 5.18: Barrelet zeros as a function of the $\pi^+\pi^-$ mass.

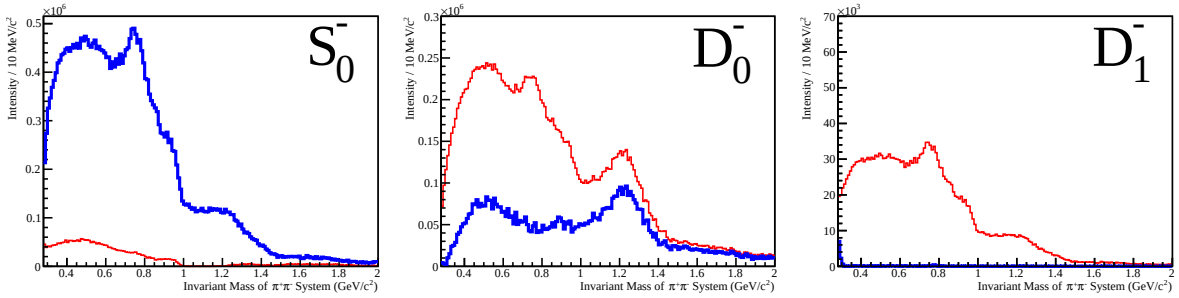

Figure 5.19: Two ambiguous solutions, computed with the results of one single fit.

If we perform the partial-wave analysis also for the $\pi^+\pi^-$ system with even waves only, we find almost exactly the same picture as for the $\pi^0\pi^0$ system (cf. Figure 5.16). The comparison with weighted Monte-Carlo distributions shows, that the angular distributions can be described already with this limited wave set. The Barrelet zeros can be unmistakably distinguished by the sign of their real part (cf. Figure 5.18). The physical solution has a dominating S-wave contribution, while the D_0^--wave has a clear $f_2(1270)$ peak (cf. Figure 5.19). However, the unphysical enhancement below $0.6\,\mathrm{GeV}/c^2$ in this wave is a direct consequence of the omitted but apparently important P_1^+-wave, which is shown in Figure 5.20.

Since we are mainly interested in the scalar component and its interference with the D-wave, we decided to restrict the decomposition into the following wave-set for this analysis:

$$\{\boldsymbol{S_0^-}, D_0^-, D_1^-\}, \{\boldsymbol{P_1^+}, D_1^+\} \tag{5.19}$$

The final result for the partial-wave analysis of the centrally produced $\pi^+\pi^-$ system is depicted in Figure 5.21.This decomposition into partial waves in narrow mass bins will serve as a starting point for the studies concerning the dependence on the squared four-momentum transfer to the central system in the next section and the parametrisation of the mass-dependence in Chapter 6.

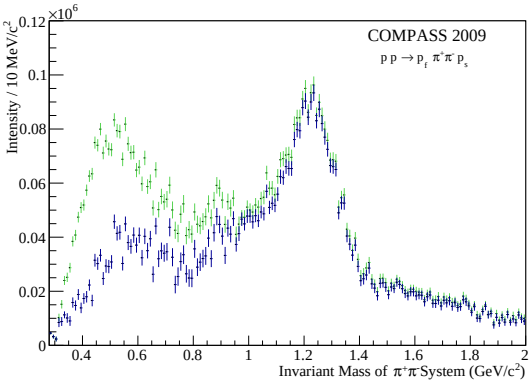

Figure 5.20: D_0^- intensity in the $\pi^+\pi^-$ data with (blue) and without (green) P_1^+-wave.

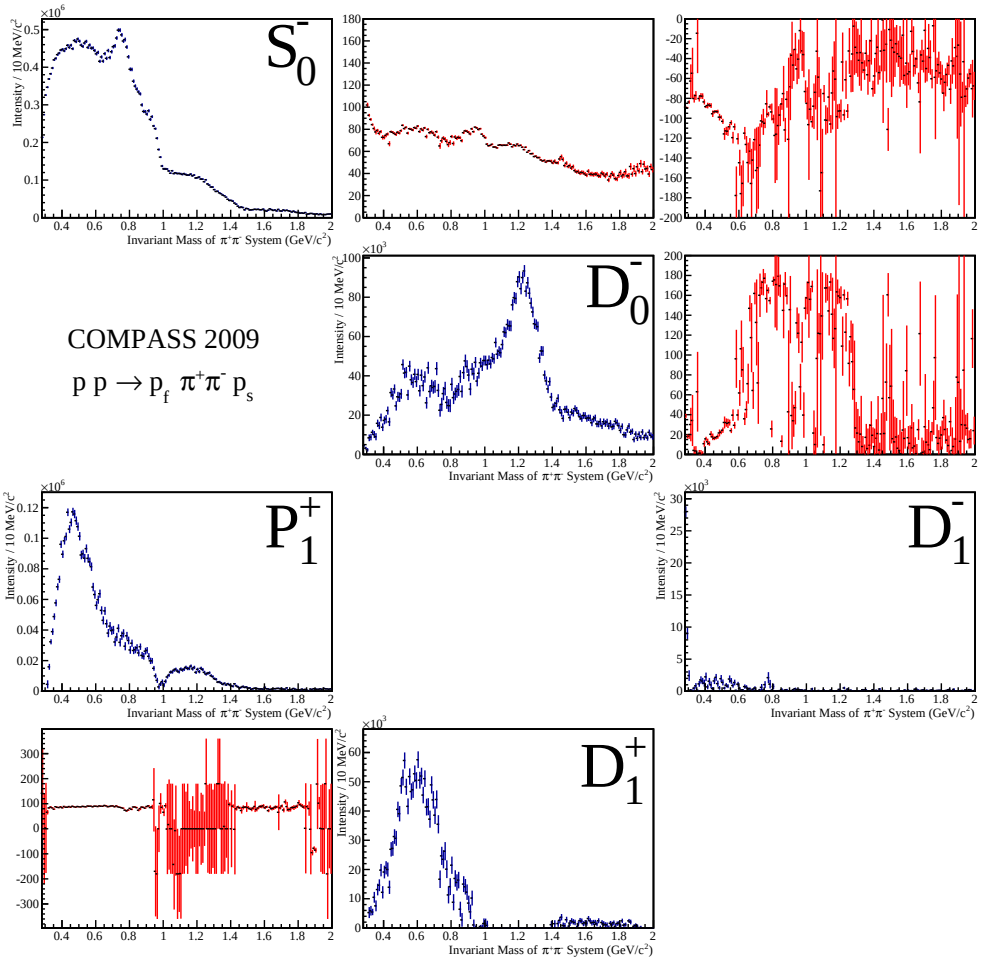

Figure 5.21: Physical solution for the $\pi^+\pi^-$ system, intensities (blue) and relative phases in degrees (red).

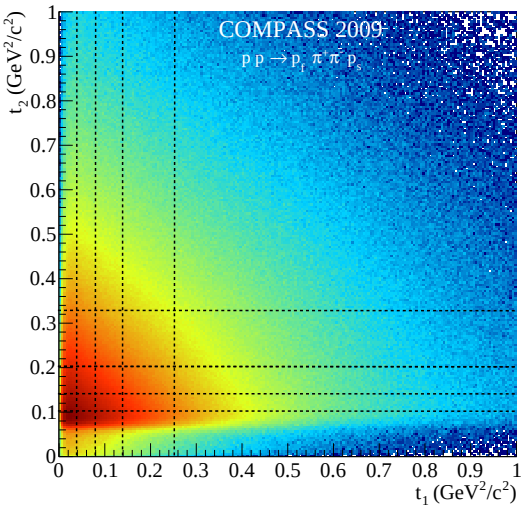

Bins in t_1 (GeV$^2/c^2$)	Bins in t_2 (GeV$^2/c^2$)
$[0.000, 0.040[$	$[0.000, 0.100[$
$[0.040, 0.080[$	$[0.100, 0.140[$
$[0.080, 0.140[$	$[0.140, 0.200[$
$[0.140, 0.255[$	$[0.200, 0.325[$
$[0.255, 2.000[$	$[0.325, 2.000[$

Figure 5.22: Squared four-momentum transfers to the $\pi^+\pi^-$ system t_1 vs. t_2 with logarithmic colour-scale and two-dimensional binning (dashed lines).

5.4 Dependence on Squared Four-Momentum Transfers

The central-production reaction is characterised by the two squared four-momentum transfers t_1 from the beam proton and t_2 from the target proton to the central di-pion system, respectively. So far, this information was neglected for the decomposition into partial-wave amplitudes. In this section, we will present observations obtained by binning the data set in these two dimensions.

In studies by previous experiments, restrictions on the absolute value of the sum $|t_1+t_2|$ [14] or the difference in transverse momentum dP_T [37] (cf. Section 3.3.3) were claimed to enhance the DPE component in the analysed sample. In contrast, the size of our data set allows a differential analysis in two-dimensional bins of the Lorentz-invariant variables t_1 and t_2. This way, the experimental acceptance for t_2 in COMPASS, which vanishes below $0.7\,\mathrm{GeV}^2/c^2$, and could bias the conclusions obtained in a one-dimensional analysis, is taken into account.

In order to balance the number of events in the bins, we split the ranges asymmetrically in five regions for t_1 and t_2 between 0 and $2\,\mathrm{GeV}^2/c^2$. No apparent correlations between the kinematic variables can be discerned (cf. Figure 5.22), which was quoted as a confirmation of the factorisation into two proton vertices [46]. The obtained boundaries can be found in the accompanying table.

Figure 5.23 shows the $\pi^+\pi^-$ invariant mass distribution for all bins. The spectra for the lowest two bins of t_1 and t_2 (left top) are dominated by the enhancement at threshold, which is slightly modulated by the $f_0(980)$ resonance near $1\,\mathrm{GeV}/c$. No signs for $\rho(770)$ and $f_2(1270)$ production can be observed for low squared four-momentum transfers to the central system. By increasing t_1 or t_2, the peaks for both resonances gradually emerge from the spectrum. Also the steep drop near the $f_0(980)$ mass is becoming more pronounced, especially in the highest bin in both variables (right bottom).

These qualitative statements are confirmed by a decomposition of the binned samples into partial-wave amplitudes. About $3 \cdot 10^5$ events in each two-dimensional bin are sufficient to perform the full partial-wave analysis in mass bins as described in Section 5.3, including the identification of the physical solution via the Barrelet zeros. Only the width of the mass bins

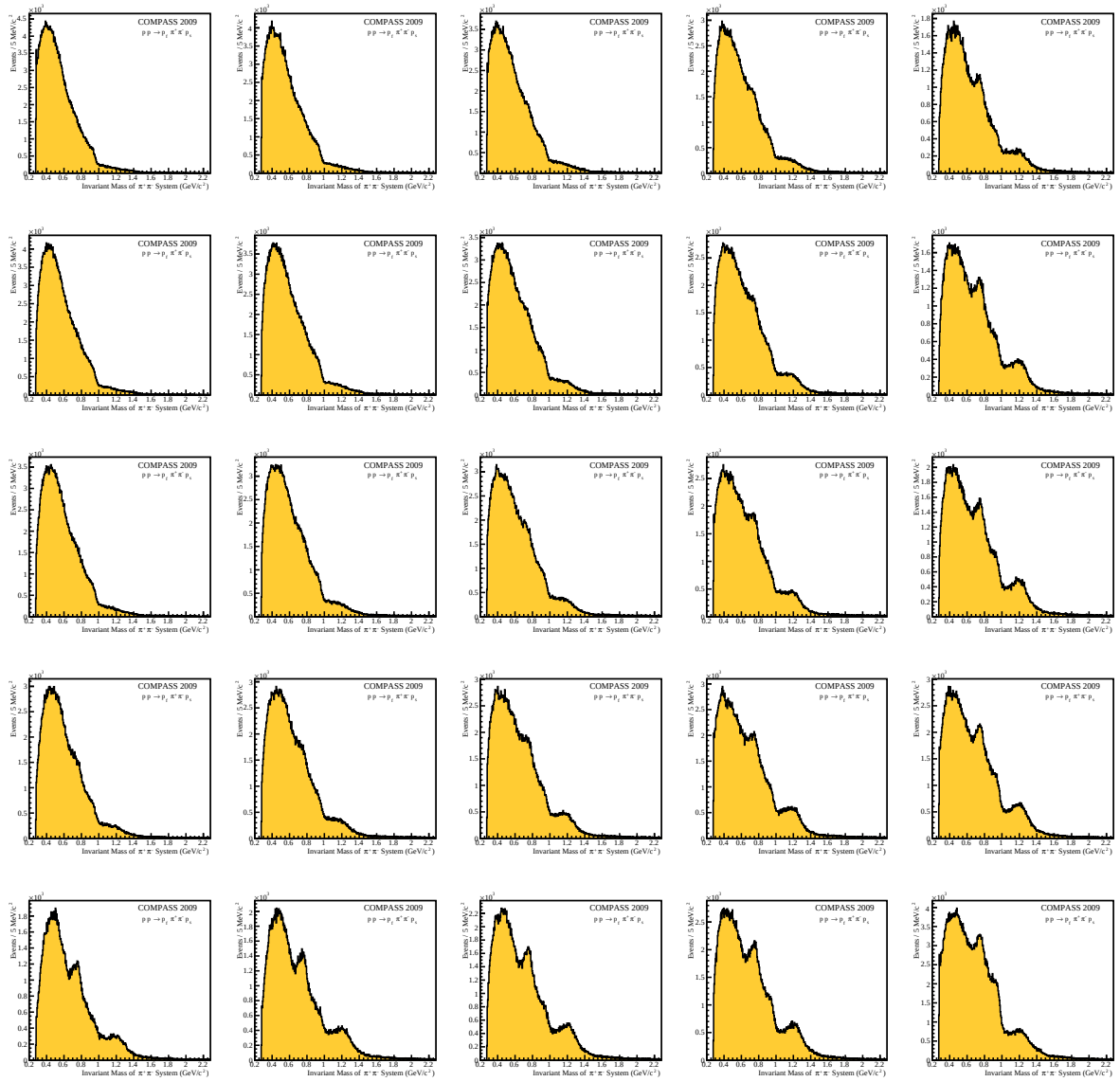

Figure 5.23: Invariant Mass of the $\pi^+\pi^-$ System in bins (cf. text) of t_1 (horizontal, increasing from left to right) and t_2 (vertical, increasing from top to bottom)

had to be enlarged to $20\,\mathrm{MeV}/c^2$. The intensity distributions of the S_0^-- and D_0^--waves as well as their relative phases for all bins can be found in Appendix B.1.

The analysis of the sample with a squared four-momentum transfer t_2 from the target to the central system below $0.1\,\mathrm{GeV}^2/c^2$ is difficult due to the threshold imposed by the recoil proton detector. Especially the Monte-Carlo description of this threshold is not realistic enough at the present stage for a reliable acceptance correction, which results in a wrong absolute normalisation of the partial-wave amplitudes. For this reason, we discuss the intensity distributions of the S_0^-- and D_0^--wave for the lowest bin in t_1 and the second lowest bin in t_2 (cf. Figure 5.24). In this bin, the S_0^--wave is largely dominated by the enhancement at threshold, with the $f_0(980)$ resonance as a shoulder near the $\pi^+\pi^-$ mass of $1\,\mathrm{GeV}/c^2$. The $\rho(770)$ peak is completely removed from the sample. However, no clear signal for the $f_2(1270)$ meson

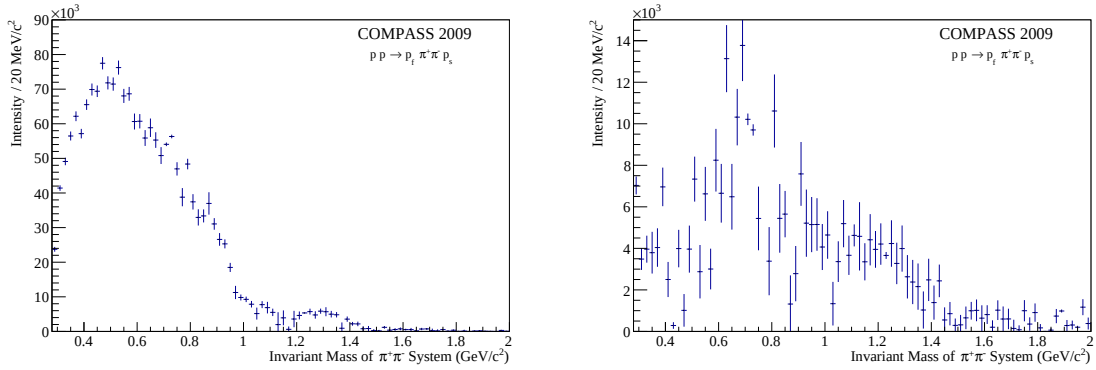

(a) S_0^--wave (b) D_0^--wave

Figure 5.24: Intensities from the partial-wave analysis in the region $t_1 \in [0.000, 0.040[\,\mathrm{GeV}^2/c^2$ and $t_2 \in [0.100, 0.140[\,\mathrm{GeV}^2/c^2$.

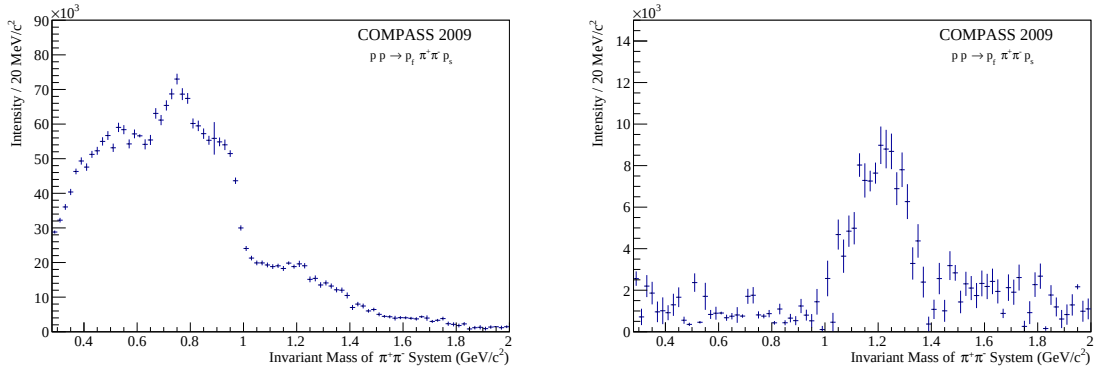

(a) S_0^--wave (b) D_0^--wave

Figure 5.25: Intensities from the partial-wave analysis in the region $t_1 \in [0.255, 2.000[\,\mathrm{GeV}^2/c^2$ and $t_2 \in [0.325, 2.000[\,\mathrm{GeV}^2/c^2$.

can be observed either in the D_0^--wave, which is relatively unstable below $1\,\mathrm{GeV}/c^2$. As a consequence, the $f_2(1270)$ cannot be used to interpret the interference with the S_0^--wave.

The partial-wave analysis of the highest bin in both t_1 and t_2 results in very different intensity distributions (cf. Figure 5.25). The peak of the $f_2(1270)$ meson in the D_0^--wave is separated almost background-free. The S_0^--wave exhibits a pronounced structure at the $f_0(980)$ mass, and also the intensity caused by the wrongly attributed $\rho(770)$ meson can be clearly discerned.

In summary, the scalar component of the $\pi^+\pi^-$ spectrum can be selected by restricting the squared four-momentum transfers to the central system to a minimum. The $\rho(770)$ meson is suppressed since it cannot be produced via double-Pomeron exchange mechanisms. The $f_2(1270)$ resonance is suppressed in a similar fashion. This can be explained by a dependence

of the relative contributions from different production mechanisms on t_1 and t_2 [74]. Since we want to profit from the phase information with respect to the well-studied D_0^--wave in order to study the resonant content of the S_0^--wave, we will continue the analysis on the unbinned sample. However, full coherence between the different production mechanism has to be assumed.

Chapter 6

Parametrisation of Mass Dependence

So far, the sample of centrally produced di-pion systems was decomposed into partial-wave amplitudes, which are assumed to be constant as a function of the $\pi^+\pi^-$ mass across narrow bins of $10\,\mathrm{MeV}/c^2$ width. Since every mass bin is fitted independently, this so-called mass-independent analysis does not require any assumption on the resonant behaviour in the di-meson system. Nevertheless, we observe continuous behaviour of intensity distributions and phase differences as a function of mass. Especially the peak in the D-wave can be unmistakably identified with the $f_2(1270)$ meson. This resonance can be used as a reference for the complicated scalar contribution.

In this chapter we introduce the components of a model for the mass dependence of the spin-density matrix elements extracted by the bin-wise decomposition into partial-wave amplitudes. We will briefly summarise the possibilities for a χ^2-minimisation to determine the parameters, before we focus on the application of this model to the S_0^--wave and its interference with the D_0^--wave for the centrally produced $\pi^+\pi^-$ system.

6.1 Components

The mass-dependence of the partial-wave amplitudes are parametrised using a coherent sum of resonant terms and contributions with a constant phase, which account for the non-resonant production of the central $\pi^+\pi^-$ system.

In its rest frame, the kinematic properties of the two-body decay are given by the invariant mass m of the central system. The breakup momentum q is often used as the kinematic variable for the parametrisation of the mass dependence. Its functional form [26] is simplified due to the decay into pions with equal mass:

$$q = \frac{\sqrt{\left[m^2 - (m_1 + m_2)^2\right]\left[m^2 - (m_1 - m_2)^2\right]}}{2m} \quad \overset{m_1 = m_2 = m_\pi}{=} \quad \frac{1}{2}\sqrt{m^2 - 4m_\pi^2}\,. \tag{6.1}$$

Without the constant factor for the angular integral, the Lorentz-invariant phase space element ρ_π is defined as

$$\rho_\pi = \frac{2q}{m} = \sqrt{1 - \frac{4m_\pi^2}{m^2}}\,. \tag{6.2}$$

Figure 6.1 illustrates the behaviour of the breakup momentum q and the density of final states ρ_π as a function of the two-body invariant mass m.

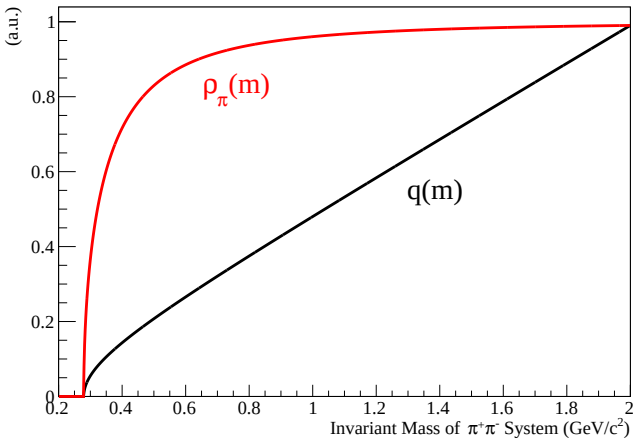

Figure 6.1: Breakup momentum q and Lorentz-invariant phase space element ρ_π as a function of the di-pion mass.

6.1.1 Breit-Wigner Resonance

The amplitude for a narrow, isolated resonance in high-energy physics is described by a relativistic Breit-Wigner function [30].

$$\mathcal{R}(m) = \frac{m_0\Gamma_0}{m_0^2 - m^2 - im_0\Gamma_0} \tag{6.3}$$

The nominal mass of the resonance is specified by m_0, its nominal total width by Γ_0. In the complex plane, the amplitude follows a circle with radius 0.5 around $0.5i$ in the anti-clockwise direction. Figure 6.2a shows this so-called Argand diagram of the complex plane. At the mass of the resonance, the amplitude is purely imaginary and the intensity, which is defined as the absolute value squared of the amplitude, is maximal (cf. Figure 6.2b). Going across the resonance, the phase of the amplitude varies by 180° and is 90° at m_0 (cf. Figure 6.2c).

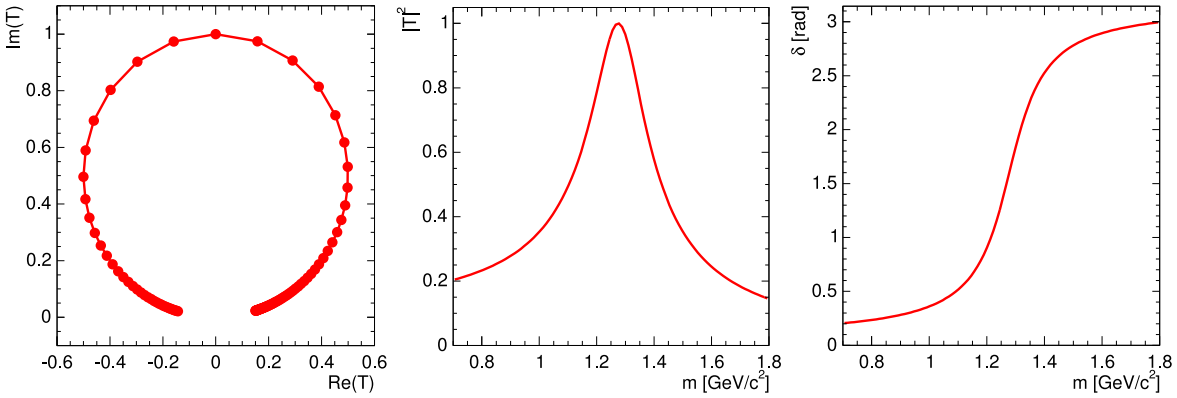

(a) Argand Diagram (b) Intensity (c) Phase

Figure 6.2: Relativistic Breit-Wigner function [85].

In order to incorporate the mass dependence of the two-body decay phase space [26], we introduce the dynamic width as

$$\Gamma(m;L) = \Gamma_0 \frac{q}{m} \frac{m_0}{q_0} \left[\frac{B_L((qR)^2)}{B_L((q_0R)^2)} \right]^2 , \tag{6.4}$$

with the breakup momentum q_0 at the resonance point. The asymptotic behaviour caused by the orbital angular momentum L of the decay is taken into account by the Blatt-Weisskopf barrier factors B_L [102]. The empirical interaction radius R is usually set to 1 fm. The Breit-Wigner amplitude is therefore modified to

$$\mathcal{R}_{\mathrm{dyn}}(m) = \frac{m_0 \sqrt{\Gamma_0} \sqrt{\Gamma(m)}}{m_0^2 - m^2 - i m_0 \Gamma(m)} . \tag{6.5}$$

If several decay channels contribute to the same resonance, the width in the numerator has to be replaced by the total width Γ_{tot}. It is defined as the sum over all partial widths weighted by their respective branching fractions. As a consequence, the leading channel determines the behaviour of the function. Since the decay into $\pi\pi$ is the dominant channel for all resonances discussed in this chapter, additional partial widths can safely be ignored.

Besides the fit parameters m_0 and Γ_0, we allow for a free complex coefficient for every Breit-Wigner function, which are summed up coherently for each partial wave.

6.1.2 Flatté Parametrisation

Unitarity, i.e. the preservation of probability, leads to observable modifications of the resonance shape if the mass is near the threshold of a second decay channel. Flatté [52] has proposed a parametrisation to explain the behaviour of the $\pi\eta$ and $K\bar{K}$ systems by a coupled-channel resonance, which was later called $a_0(980)$. Through analytic continuation of the amplitude in the complex plane, the $K\bar{K}$ channel affects the mass region even below the $K\bar{K}$ threshold, resulting in a very narrow peak, a so-called cusp phenomenon, in the $\pi\eta$ mass distribution.

In the case of isospin $I = 0$, a similar effect has to be taken into account when parametrising the $f_0(980)$ meson, which is also heavily deformed by the opening of the $K\bar{K}$ channel. The amplitude is expressed in the form

$$\mathcal{F}_j(m) = \frac{m_0 \sqrt{\Gamma_0} \sqrt{\Gamma_j}}{m_0^2 - m^2 - i m_0 (\Gamma_\pi + \Gamma_K)} , \quad j \in \{\pi, K\}. \tag{6.6}$$

The partial decay widths are functions of the breakup momentum

$$\Gamma_j = g_j q_j(m) = \frac{g_j}{2} \sqrt{m^2 - 4m_j^2} , \tag{6.7}$$

$$\Gamma_0 = g_j q_j(m_0) . \tag{6.8}$$

Below the $K\bar{K}$ threshold, Γ_K is analytically continued to

$$\Gamma_K = i \frac{g_K}{2} \sqrt{4m_K^2 - m^2} , \tag{6.9}$$

which modifies the line shape drastically. In Figure 6.3, the Argand diagram is shown together with the intensity and the phase for parameters determined by the BES collaboration [4] in J/ψ decays ($m_0 = 965\,\mathrm{MeV}/c^2$, $g_\pi = 0.165$, $g_K/g_\pi = 4.21$). A review of several experimental results can be found in [24], where it is argued that the large discrepancies in the published parameter values for the $f_0(980)$ can be explained by scaling the ratio g_π/g_K of the coupling constants. For a fit to experimental data, this ratio is therefore better suited as a parameter than the individual values.

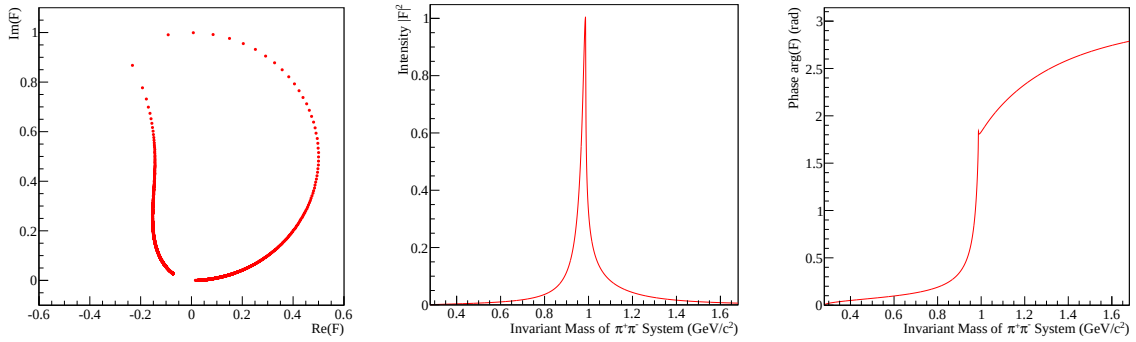

(a) Argand Diagram (b) Intensity (c) Phase

Figure 6.3: Flatté parametrisation of the $f_0(980) \to \pi^+\pi^-$ decay with constants from [4].

6.1.3 AMP Parametrisations

The Watson theorem [103] relates the phase of the elastic scattering amplitudes for $\pi\pi \to \pi\pi$ and for $\pi\pi \to K\bar{K}$ to the amplitude of the central production process. Data from both scattering processes were combined in a multi-channel unitary analysis by Au, Morgan and Pennington (AMP) [16]. The amplitudes for the different channels are arranged as elements of the $\mathbb{T}$-matrix

$$\mathbb{T} = \begin{pmatrix} \mathcal{T}_{\pi\pi\to\pi\pi} & \mathcal{T}_{\pi\pi\to K\bar{K}} \\ \mathcal{T}_{K\bar{K}\to\pi\pi} & \mathcal{T}_{K\bar{K}\to K\bar{K}} \end{pmatrix} , \tag{6.10}$$

which is parametrised as

$$\mathbb{T} = \mathbb{K}(\mathbb{I} - i\boldsymbol{\rho}\mathbb{K})^{-1} \quad \text{or} \quad \mathbb{T} = (\mathbb{M} - i\boldsymbol{\rho})^{-1} \quad \text{with} \quad \boldsymbol{\rho} = \text{diag}(\rho_\pi, \rho_K) , \tag{6.11}$$

where ρ_K is defined in analogy to Equation 6.2. As described in Section 1.2.3, data from elastic scattering experiments were combined with those from central production of $\pi^+\pi^-$ in order to determine the parameters in the matrices $\mathbb{K}$ or $\mathbb{M}$, respectively, by a fit. The resulting intensity has a pronounced dip at the position of the $f_0(980)$, which is shown in Figure 6.4b. The jump in the phase around $1\,\text{GeV}/c^2$ (cf. Figure 6.4c) is an effect of the parametrisation of the amplitude, which has to leave the unitary circle after the opening of the $K\bar{K}$ channel (cf. Figure 6.4a). As a consequence, the angle with respect to the real axis does not reach the origin and can therefore not be analytically continued through 180°, even though it is still rising. The falling phase above $1.5\,\text{GeV}/c^2$, however, is unphysical [85]. Due to the lack of precise data from elastic scattering and central production experiments at that time, the behaviour of the amplitude is not well defined in this region.

The so-called $\mathbb{M}$-solution for the $\mathcal{T}_{\pi\pi\,\to\pi\pi}$ amplitude is used in a modified version as a description of the intermediate $\pi\pi$ S-wave in pion diffraction analyses [59, 100]. In order to be able to implement the $f_0(980)$ as a separate resonance, all coefficients in the amplitude which are responsible for it are artificially set to zero, as well as the off-diagonal terms. This results in the simplified mass dependence shown in Figure 6.4.

The elastic scattering amplitude is required to be vanishing close to threshold by the Adler condition [5]. In the central production process on the other hand, the duality with a one-pion exchange (cf. Figure 6.5) avoids the Adler zero [16]. In order to remove this process dependence, the amplitudes are divided by the pole of the elastic channel at s_0, which is very

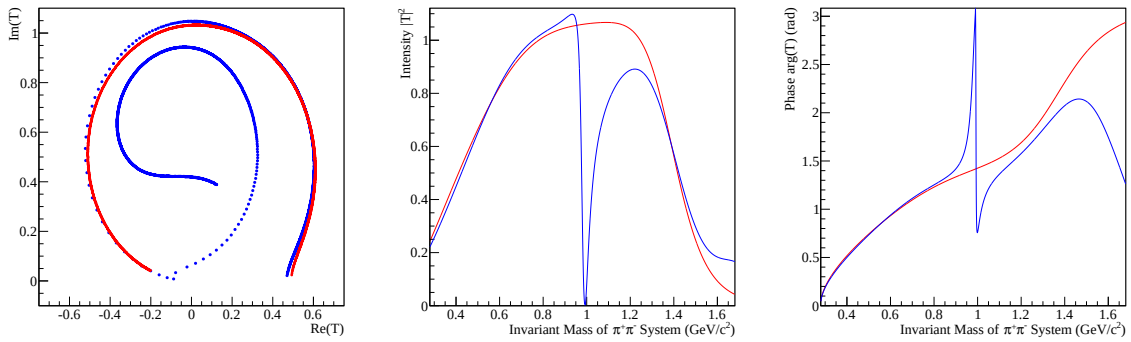

(a) Argand diagram (b) Intensity (c) Phase

Figure 6.4: AMP $\mathbb{M}$ solution for the $\pi\pi \to \pi\pi$ S-wave, original (blue) and simplified (red).

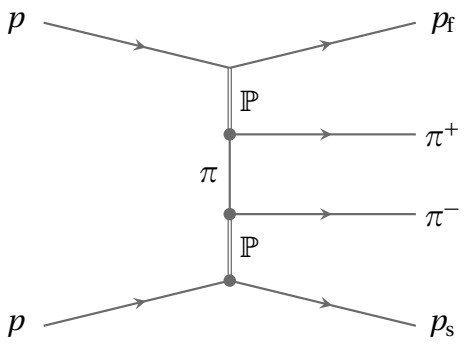

Figure 6.5: Illustration of central production as one-pion exchange

close to the origin.

$$\mathbb{T}_{\text{reduced}} = \frac{\mathbb{T}}{s - s_0} \ . \tag{6.12}$$

It is shown that this approximate factor of $1/m^4$ multiplied to the intensity distribution describes the general trend of the data [16]. An updated $\mathbb{K}$-matrix parametrisation without the Adler zero was provided by [84]. This so-called reduced $\mathbb{K}$ solution is illustrated in Figure 6.6. Here, we show also the components of the $\mathbb{T}$-matrix which involve kaons since they will be important in Chapter 7.

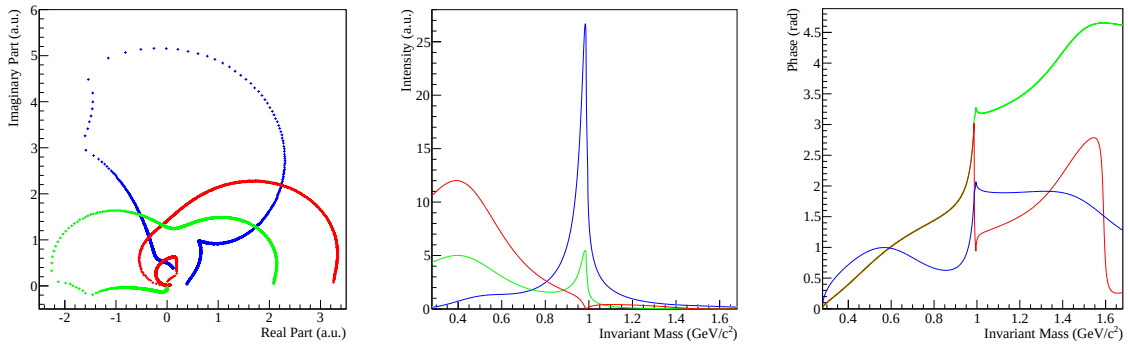

(a) Argand Diagram (b) Intensity (c) Phase

Figure 6.6: Reduced AMP amplitude for $\pi\pi \to \pi\pi$ (red), $K\bar{K} \to K\bar{K}$ (blue) and $K\bar{K} \to \pi\pi$ (green) as a function of the two-body mass of the final state [84].

6.1.4 Parametrisation of the Non-Resonant Component

An additional coherent, but non-resonant component has to be introduced in each partial wave in order to account for the contribution from other production processes which translate through their angular characteristics into intensity in the S- and D-waves (cf. Section 5.2). We parametrise the non-resonant terms $\mathcal{N}$ by

$$\mathcal{N}(m; L) = \left(\frac{q}{m}\right)^L \cdot \sqrt{\frac{q}{m}} \cdot \exp(-\alpha q^2) \tag{6.13}$$

with the breakup momentum q and the real-valued fit parameter α. The factor q^L provides the correct asymptotic behaviour for the angular-momentum barrier. The two-body phase space is represented by the square root term [26] and is damped towards large m by the exponential function.

Alternative parametrisation were tried for this analysis, including the model used in [21], but the presented results showed no significant dependence on the functional form of the non-resonant term. These studies are, however, important for the estimation of systematic errors.

6.2 Definition of χ^2

For each wave i, the model $\mathcal{M}_i$ includes a coherent sum of resonant and non-resonant terms as introduced in the previous section. In addition to the parameters for mass m_0 and width Γ_0, every resonant contribution $\mathcal{R}_r$ has a complex-valued coefficient c_r as fit parameter, which determines its strength and phase. For the same purpose, the non-resonant component $\mathcal{N}$ has a fitted complex coefficient c_n. The number of Breit-Wigner functions r is kept to the minimum required to describe the data reasonably.

$$\mathcal{M}_i = \sum_r c_r \mathcal{R}_r(m_{0,r}, \Gamma_{0,r}) + c_n \mathcal{N}(\alpha) \tag{6.14}$$

All parameters are varied in order to fit the distributions obtained by the decomposition into partial-wave amplitudes in individual mass bins (cf. Chapter 5). The residual vector $\vec{\Delta}$ of the model with respect to the results of the mass-independent partial-wave analysis $\mathcal{T}_i$ in each mass bin has one component for the real part and one for the imaginary part of each used partial wave i.

$$\vec{\Delta} = \begin{pmatrix} \vdots \\ \operatorname{Re}\mathcal{T}_i - \operatorname{Re}\mathcal{M}_i \\ \operatorname{Im}\mathcal{T}_i - \operatorname{Im}\mathcal{M}_i \\ \vdots \end{pmatrix} \tag{6.15}$$

As fit criterion, we use the weighted sum χ^2 of the squared errors. The χ^2 is computed using the definition

$$\chi^2 = \sum_m^{\text{bins}} \vec{\Delta}^{\mathrm{T}}\, \mathbb{C}^{-1}\, \vec{\Delta}\ , \tag{6.16}$$

with the covariance matrix $\mathbb{C}$, obtained by the maximum-likelihood fit. It is composed of two columns and two rows for each wave describing the uncertainties of the real and the imaginary parts of the transition amplitudes, respectively. This method has the advantage, that all covariances provided by the fit in mass bins are used directly.

A second definition has been used in the past (e.g. in [80]), which rather parametrises the elements of the spin-density matrix [36]. The residual vector is calculated separately for each of the products $\mathcal{T}_i\mathcal{T}_j^*$, which correspond to the relevant physical properties intensity and phase difference. In this formalism, the residual vectors have only two components, the real and the imaginary part of the product $\mathcal{T}_i\mathcal{T}_j^*$.

$$\vec{\Delta}_{ij} = \begin{pmatrix} \operatorname{Re}\mathcal{T}_i\mathcal{T}_j^* - \operatorname{Re}\mathcal{M}_i\mathcal{M}_j^* \\ \operatorname{Im}\mathcal{T}_i\mathcal{T}_j^* - \operatorname{Im}\mathcal{M}_i\mathcal{M}_j^* \end{pmatrix} \tag{6.17}$$

The χ^2 for the fit is summed over all possible combinations of the waves:

$$\chi^2 = \sum_m^{\text{bins}} \sum_{ij}^{\text{waves}} \vec{\Delta}_{ij}^{\mathrm{T}}\, \mathbb{C}_{ij}^{-1}\, \vec{\Delta}_{ij}\ . \tag{6.18}$$

The covariance matrices $\mathbb{C}_{ij}$ have to be constructed using error propagation from the submatrices of $\mathbb{C}$ which correspond to the waves i and j via

$$\mathbb{C}_{ij} = \mathbb{J} \cdot \operatorname{cov}(\mathbb{C}_i \times \mathbb{C}_j) \cdot \mathbb{J}^{\mathrm{T}}\ . \tag{6.19}$$

$\mathbb{J}$ is the Jacobian matrix for this transformation. For a growing number of waves N, this method puts an increasing weight on the mixed terms. Instead of the $2N$ variables which are the result of the partial-wave decomposition in mass bins, N^2 distributions are fitted. Nevertheless, both methods converge to the same results within the statistical uncertainties.

6.3 Results for the $\pi^+\pi^-$ System

6.3.1 Fit to the *S*-Wave Intensity

At first, we tried to fit only the S-wave intensity distribution with a model similar to the analysis of ISR data published in [77], but ignoring the mass range between 0.65 and 0.82 GeV/c^2 which is contaminated by the $\rho(770)$. The interference between a dominant, non-resonant component and two Breit-Wigner functions is able to describe the distribution. The first resonant contribution has a mass of about 0.99 GeV/c^2 and matches the $f_0(980)$ meson. Its width of about 0.1 GeV/c^2 is also in agreement with the range given in [26]. The second component can be identified with the $f_0(1500)$ resonance with a mass of precisely 1.5 GeV/c^2, even though the value for the width is exceeded by more than a factor of two. The obtained Breit-Wigner parameters are summarised and compared to the literature values in Table 6.1.

Resonance	Fit result		PDG values [26]	
	Mass (MeV/c^2)	Width (MeV/c^2)	Mass (MeV/c^2)	Width (MeV/c^2)
$f_0(980)$	989 ± 1	102 ± 1	990 ± 20	$40 - 100$
$f_0(1500)$	1542 ± 3	225 ± 6	1505 ± 6	109 ± 7

Table 6.1: Parameters for fit with two Breit-Wigner functions and non-resonant contribution (10 parameters, $\chi^2/\mathrm{NDF} = 128$). Only statistical errors are given for the fit results.

In addition to the four Breit-Wigner parameters, three complex amplitudes and the damping factor α are varied in the fit to about 150 data points. Since the overall phase is arbitrary, one coefficient is chosen to be real-valued. The final model with ten parameters roughly describes the one-dimensional mass distribution, which is illustrated in Figure 6.7. The large value of χ^2 divided by the number of degrees of freedom reflects the tiny statistical errors for each data point, owing to the size of the analysed data set. The simplistic model is not able to describe the observed distribution entirely. Therefore, the reduced χ^2 does not allow an interpretation in terms of the probability. Nevertheless, it is quoted as a relative goodness of fit criterion for all results in the following.

The slight deviation in the mass range between the two resonances led to the introduction of a broad $f_0(1370)$ in the past [19]. We could, however, not achieve a stable fit with an additional Breit-Wigner function at this stage. An asymmetric distribution for the $f_0(980)$, e.g. the Flatté parametrisation introduced above, can also account for this effect. The interference of the S-wave with the well-known $f_2(1270)$ meson in the D-wave enables a more detailed analysis of the resonant content. We will focus on this technique in the following.

6.3.2 Mass-Dependent Fit to the *S*- and *D*-Wave Interference

The simplest extension to the model introduced in the previous section requires only one Breit-Wigner term for the $f_2(1270)$ meson on top of a non-resonant contribution in the D-wave. With two additional complex coefficients, this results in seven additional fit parameters for the simultaneous χ^2-fit to the S- and D-wave intensity distributions and their relative

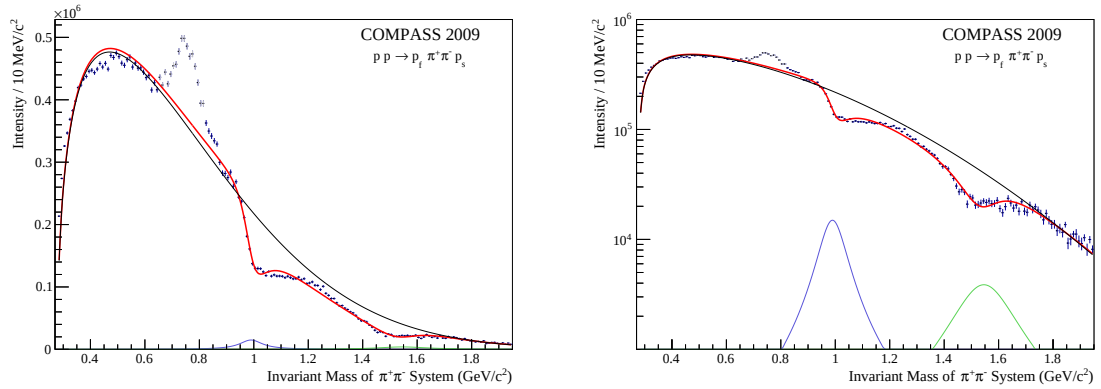

(a) Linear Scale

(b) Logarithmic Scale

Figure 6.7: Fit to S-wave intensity (red) with Breit-Wigner functions for $f_0(980)$ (blue) and $f_0(1500)$ (green). The non-resonant component is drawn in black, the ignored mass range of $[0.65, 0.82]\,\mathrm{GeV}/c^2$ in grey.

phase. In the fit, the D-wave is ignored below the mass of $0.83\,\mathrm{GeV}/c^2$. No resonant behaviour is expected in this region, which was shown to be prone to fit instabilities in Figure 5.20.

The data are shown together with the fit result in Figure 6.8. The complicated phase motion is well reproduced by the three resonant components, which are shifted separately to the interval between 0° and 180° for illustration. Especially the phase information enlarges the discrepancy of the intensity distribution in the $f_0(980)$ mass region compared to the one-dimensional approach (cf. Figure 6.7). The Breit-Wigner parameters of the fit result are presented in Table 6.2. The mass and width of the $f_2(1270)$ meson approximately reproduce the precisely known literature values [26], even though the peak in the intensity distribution is not fitted correctly. More freedom in the model for the non-resonant component is required to match the interference with the resonance in the D_0^--wave. The mass parameters of the scalar resonances $f_0(980)$ and $f_0(1500)$ are also compatible with previous measurements [21], while the width of the latter is still estimated to large.

Resonance	Fit result		PDG values [26]	
	Mass (MeV/c^2)	Width (MeV/c^2)	Mass (MeV/c^2)	Width (MeV/c^2)
$f_0(980)$	993 ± 1	110 ± 1	990 ± 20	$40 - 100$
$f_0(1500)$	1489 ± 3	247 ± 5	1505 ± 6	109 ± 7
$f_2(1270)$	1300 ± 2	171 ± 2	1275 ± 1	185 ± 3

Table 6.2: Parameters for fit with three Breit-Wigner functions and non-resonant contributions (17 parameters, $\chi^2/\mathrm{NDF} = 58$). Only statistical errors are given for the fit results.

In the next step, the Breit-Wigner function for the $f_0(980)$ is replaced with the asymmetric Flatté parametrisation introduced in Section 6.1.2. The precision of the data in this mass region does not allow a stable fit of the nominal mass m_0 and the coupling parameters g_1 and g_2, they are thus fixed to the parameters quoted by the BES collaboration [4]. Only the complex coefficient is able to vary the magnitude and phase. Figure 6.9 shows this fit, which is not substantially different from the previous one. Nevertheless, the slowly rising phase of the

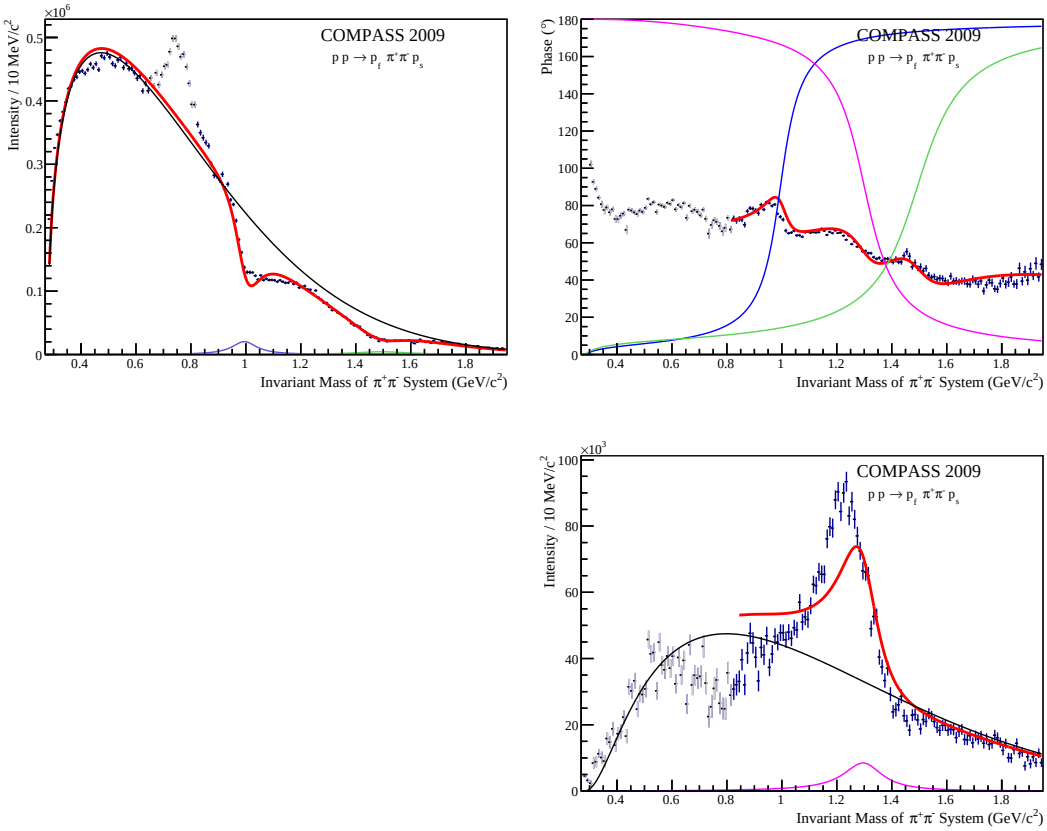

Figure 6.8: Fit to S- and D-wave (red) with Breit-Wigner functions for $f_0(980)$ (blue), $f_0(1500)$ (green) and $f_2(1270)$ (magenta). Non-resonant components are drawn in black.

Flatté function above the $K\bar{K}$ threshold produces a width of the $f_0(1500)$ closer to the value given in the PDF (cf. Table 6.3).

Resonance	Fit result		PDG values [26]	
	Mass (MeV/c^2)	Width (MeV/c^2)	Mass (MeV/c^2)	Width (MeV/c^2)
$f_0(1500)$	1478 ± 2	182 ± 3	1505 ± 6	109 ± 7
$f_2(1270)$	1301 ± 1	165 ± 2	1275 ± 1	185 ± 3

Table 6.3: Parameters for fit with two Breit-Wigner functions, the fixed Flatté parametrisation for the $f_0(980)$ and non-resonant contributions (15 parameters, $\chi^2/\text{NDF} = 72$). Only statistical errors are given for the fit results.

The reduced χ^2 of both fits can be improved by the implementation of a broad Breit-Wigner component for the $f_0(1370)$ in the S-wave, overlapping with the $f_0(980)$ and the $f_0(1500)$ states. However, the small visible improvements in the distributions do not necessarily justify four additional fit parameters. The fit becomes unstable and only converges if the mass parameters of the Breit-Wigner functions in the scalar sector are restricted to narrow ranges around the minimum. An objective result is difficult to achieve in this case.

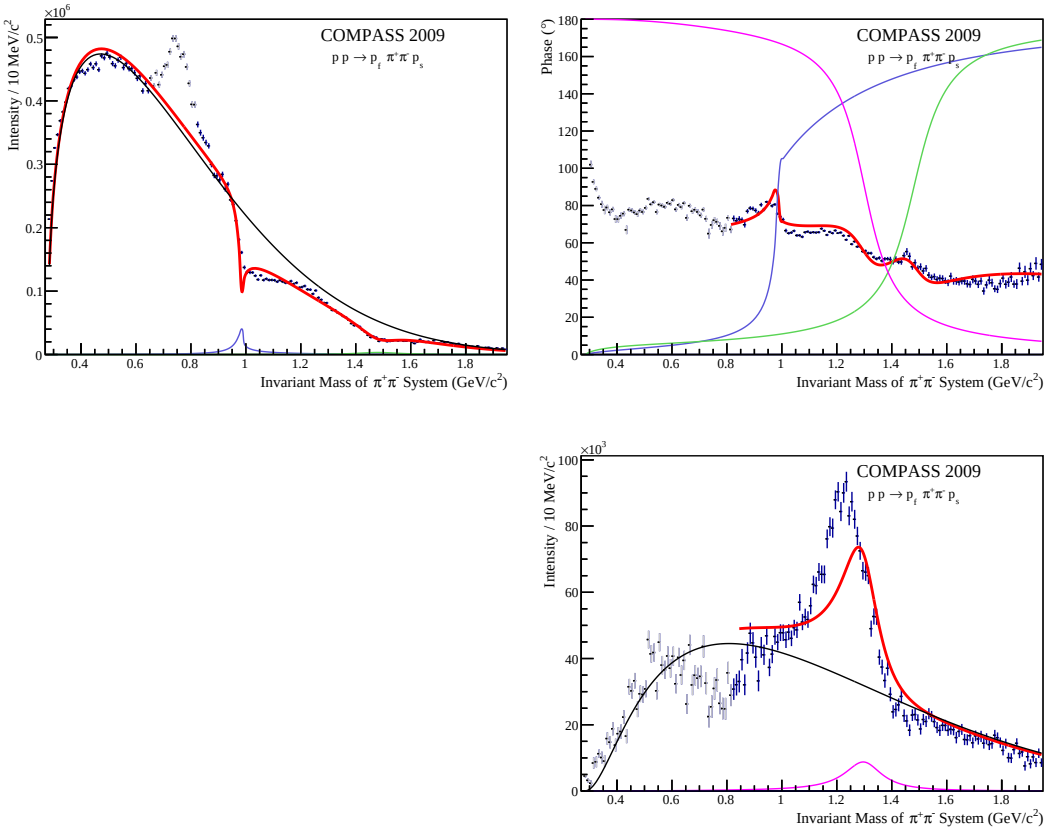

Figure 6.9: Fit to S- and D-wave (red) with fixed Flatté parametrisation for $f_0(980)$ (blue), and Breit-Wigner functions for $f_0(1500)$ (green) and $f_2(1270)$ (magenta). Non-resonant components are drawn in black.

6.3.3 Fixed Parametrisation

The sum of overlapping Breit-Wigner functions can only serve as an approximation to the scattering amplitude. As it is impressively demonstrated by K. Peters [85], the intensity distribution as well as the phase can be considerably altered by this simplification.

The $\pi\pi$ scattering amplitude was extensively studied in the past. As a prominent example, we apply the widely-used $\mathbb{M}$-matrix parametrisation from Au, Morgan and Pennington [16] in this analysis. Even though the amplitude was mostly determined by elastic $\pi\pi$ scattering, the Watson theorem [103] relates its phase to other hadronic processes. The $\pi\pi$ amplitude is divided by the Adler zero (cf. Equation 6.12) in order to accommodate the characteristics of central production. Since knowledge of the exact nature of the production mechanism is inessential [16], we multiply the amplitude with a second-order polynomial in the breakup momentum in order to match the kinematic dependence.

With only three real-valued polynomial coefficients, a fit to the S-wave intensity distribution below $0.65\,\mathrm{GeV}/c^2$ yields a remarkably close match far beyond the fitted mass range (cf. Figure 6.10). Particularly, the original amplitude describes the sharp drop at the position of the $f_0(980)$ meson as well as the kink near the $f_0(1500)$ mass. The fact that the measured distribution does not vanish completely at the $f_0(980)$ resonance is a definite sign that the pure $\pi\pi$ scattering amplitude is not enough to describe the dynamics of the central-production reaction.

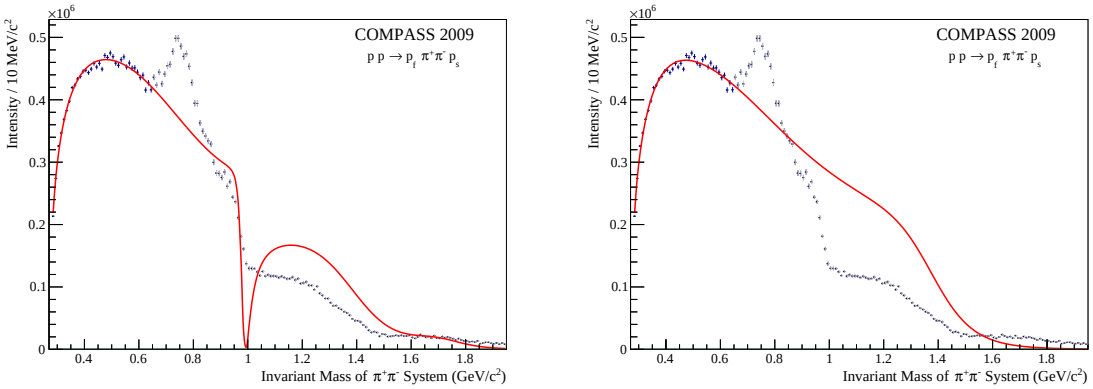

(a) original (b) simplified

Figure 6.10: Fit to S-wave intensity below $0.65\,\mathrm{GeV}/c^2$ with AMP $\mathbb{M}$ solution.

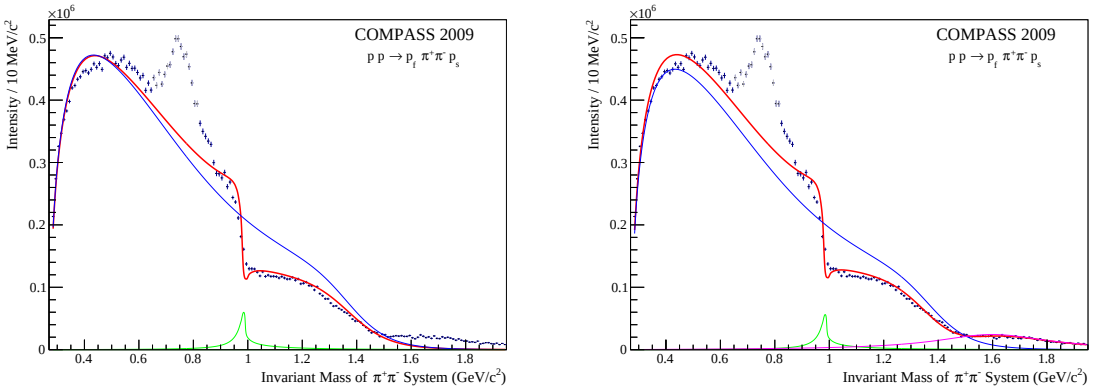

(a) AMP $\mathbb{M}$ + Flatté (b) AMP $\mathbb{M}$ + Flatté + Breit-Wigner

Figure 6.11: Fit to S-wave intensity with Flatté parametrisation (green) added to simplified AMP $\mathbb{M}$ solution (blue).

In order to describe production reactions, it might be necessary to vary the phase of the $f_0(980)$ meson with respect to the broad $f_0(500)$ resonance, such that the interference is no longer completely destructive as it was observed in elastic scattering experiments [64]. In the two-pion subsystem of a diffractively produced three-pion system [59], the $f_0(980)$ can be even observed as a peaking structure. A model with a Flatté function for the $f_0(980)$ state added coherently to the simplified AMP $\mathbb{M}$ parametrisation provides this freedom. Figure 6.11a illustrates a fit to the intensity spectrum of the S_0^--wave with this model. The shape of the distribution is reproduced up to $\pi^+\pi^-$ masses of $1.5\,\mathrm{GeV}/c^2$. For Figure 6.11b, an effective Breit-Wigner function is added in order to accommodate the observed intensity at higher masses. It has an unphysical width of more than $0.5\,\mathrm{GeV}/c^2$ and should not be associated with an actual state.

This approach is also applied to a simultaneous fit of S- and D-wave intensities and their relative phase. The D-wave is modelled with a Breit-Wigner function for the $f_2(1270)$ and

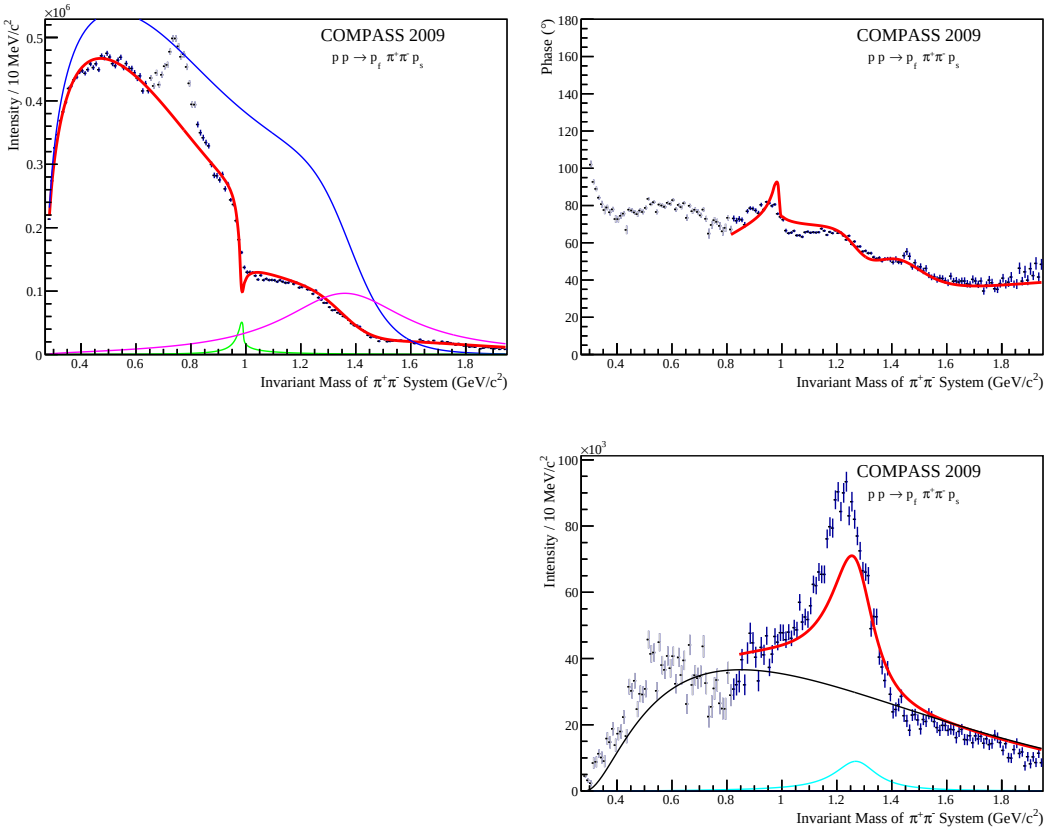

Figure 6.12: Fit to S- and D-wave (red) with simplified AMP $\mathbb{M}$ solution (blue), Flatté parametrisation for the $f_0(980)$ (green) and an effective Breit-Wigner function (magenta) in the S-wave, $f_2(1270)$ (cyan) and non-resonant component (black) in the D-wave.

a non-resonant component. The result is depicted in Figure 6.12. Similar to the fit with a non-resonant component in the S-wave (cf. Figure 6.9), all features of the distributions are described. The effective Breit-Wigner function is obtained with a large magnitude in order to fit the relative phase with respect to the D-wave.

Interference of the $\pi\pi \to \pi\pi$ scattering amplitude with the coherent process $K\bar{K} \to \pi\pi$ can also change the appearance of the observed intensity. In order to take the $K\bar{K} \to \pi\pi$ amplitude correctly into account, we used the reduced $\mathbb{K}$-matrix parametrisation [84] as introduced in Section 6.1.3. The coherent sum of the relevant components is multiplied with the fitted second-order polynomial in the breakup momentum. The result of the fit to the intensity distribution is illustrated in Figure 6.13, where the characteristic shape near the $f_0(980)$ meson is qualitatively reproduced. The amplitude vanishes at a mass of $1.6\,\mathrm{GeV}/c^2$, an additional component is required to describe this region.

With an effective Breit-Wigner function in the mass region of $1.5\,\mathrm{GeV}/c^2$, we can use these results to fit the interference with the D-wave. The unphysical behaviour of the parametrised amplitude for high masses, however, prevents quantitative statements about the resonant content in this interesting region. We show one exemplary fit in Figure 6.14, which follows the intensity distribution of both waves. The general trend of the phase difference is reproduced as well, even though the $f_0(980)$ meson is observed with a larger width.

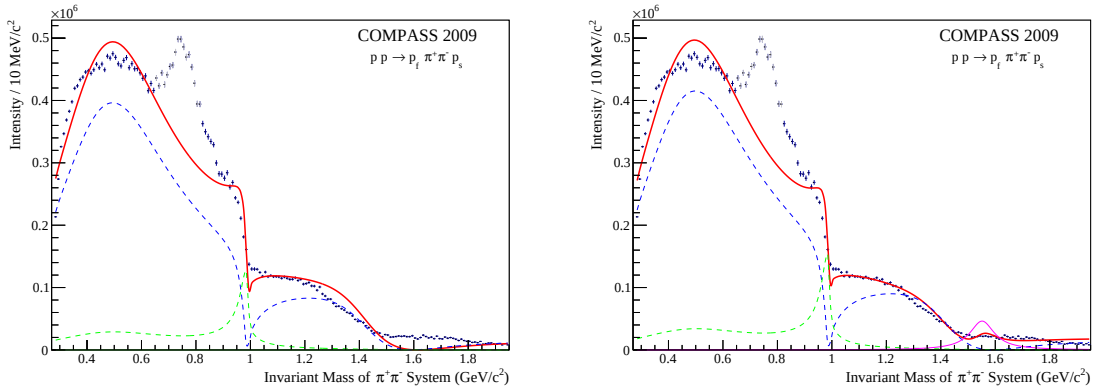

(a) $\mathbb{K}_{\text{red}}$ (b) $\mathbb{K}_{\text{red}} + f_0(1500)$

Figure 6.13: Fit to S-wave intensity with coherent sum (red) of the $\pi\pi \to \pi\pi$ (blue) and $K\bar{K} \to \pi\pi$ (green) components of the $\mathbb{K}_{\text{red}}$ amplitudes.

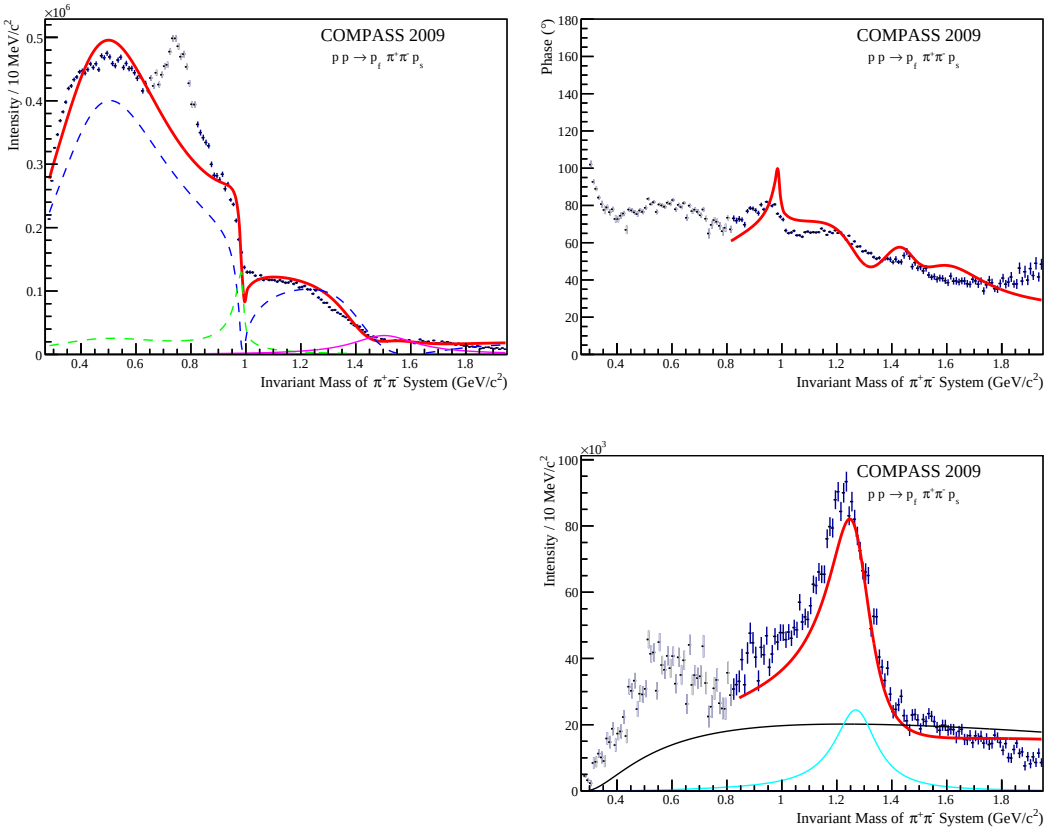

Figure 6.14: Fit to S- and D-wave (red) with $\mathbb{K}_{\text{red}}$ (dashed) and $f_0(1500)$ (magenta) in the S-wave, $f_2(1270)$ (cyan) and non-resonant component (black) in the D-wave.

6.3.4 Discussion

We fitted the S- and D-wave amplitudes obtained by a partial-wave decomposition in narrow mass bins with a series of models. Even though it can violate unitarity constraints, the coherent sum of Breit-Wigner functions and non-resonant terms is able to describe the mass-dependence qualitatively. The results for mass and width parameters of the states $f_0(980)$, $f_0(1500)$ and $f_2(1270)$ are roughly consistent with the summary tables provided by the Particle Data Group [26].

A published parametrisation [16] of the scattering amplitude which satisfies the physical boundaries from unitarity and analyticity is able to fit the gross features of the S-wave intensity distribution with only few parameters. However, the amplitudes are not well defined for di-pion masses above $1.5\,\mathrm{GeV}/c^2$ and do not follow the data. On the other hand, the coherent sum with additional components loses the physical properties.

The internal parameters of such a parametrisation should rather be released in a fit. This can, however, not be done with our analysis alone. Elastic scattering and especially semi-leptonic kaon decays provide very precise information of the hadronic amplitude of the $\pi\pi$ system for masses near the $f_0(980)$. In contrast, fewer information is available about the amplitudes above $1.5\,\mathrm{GeV}/c^2$. A combined fit of the different production processes including the large data set measured by COMPASS may improve the understanding of the super-numerous scalar $\pi\pi$ resonances. We are not able to continue the analytic function in a reasonable way without knowledge of the inherent uncertainties.

Chapter 7

Partial-Wave Analysis of the $K\bar{K}$ System

Due to its good particle identification capabilities, the COMPASS experiment is able to measure the decay of centrally produced systems into charged kaons. The reconstruction of neutral kaon decays is also possible, the efficiency for their identification by a displaced vertex is, however, about one order of magnitude worse [94]. We will therefore focus on the K^+K^- system in this chapter.

At first, we will revisit the kinematic selection of the centrally produced sample. The momentum limits for particle identification as well as the nature of the production process allow an easier separation from diffractive dissociation reactions. We will then perform the model-independent decomposition into partial waves in narrow K^+K^- mass bins completely equivalent to the analysis of the $\pi\pi$ systems in Chapter 5. Finally, the mass-dependence of the intensities of S- and D-waves and the interference between them will be fitted with different models.

7.1 Selection of a Centrally Produced K^+K^- Sample

The production of a kaon pair with a proton beam at COMPASS was already introduced in Section 3.2.2. A narrow peak corresponding to the $\Lambda^0(1520)\,3/2^+$ state and other baryon resonances with masses around $1.7\,\mathrm{GeV}/c^2$ are an unmistakable sign for a diffractive component besides the centrally produced sample. The magnitude of this contamination seems to be considerably smaller than for the $\pi\pi$ case, owing to the negligible strangeness content of the initial state. In addition, the RICH particle identification system is limited to momenta below $50\,\mathrm{GeV}/c$, which favours the central production topology with a fast outgoing proton.

If we require the proton to have a momentum larger than $140\,\mathrm{GeV}/c$, both other particles must be slower than $50\,\mathrm{GeV}/c$ and are hence able to leave a signal in the RICH detector. For these event, the identification of either one of the particles as a kaon is sufficient, which increases the number of events by about 50% compared to the method introduced in 3.2.2. A minimal proton momentum is, however, not sufficient to suppress the diffractive background completely, as established in Section 3.3.1. Small signs of baryon resonances around $1.8\,\mathrm{GeV}/c^2$ in the invariant mass spectrum of the $p_\mathrm{f}K^-$ subsystem remain (cf. Figure 7.1).

In order to justify the final choice of the kinematic selection criteria for the centrally produced K^+K^- system, we applied the decomposition into partial waves and compared the angular distributions from the measured data with weighted Monte-Carlo events as explained in Section 5.2. For this study, we used the most general wave set with $L \leq 2$ and

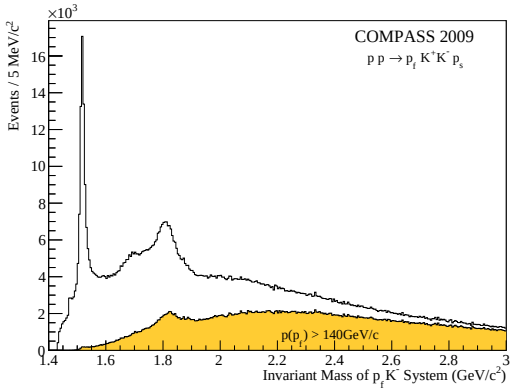

Figure 7.1: Invariant mass of $p_\mathrm{f}K^-$ system, $p(p_\mathrm{f}) > 140\,\mathrm{GeV}/c$ (filled).

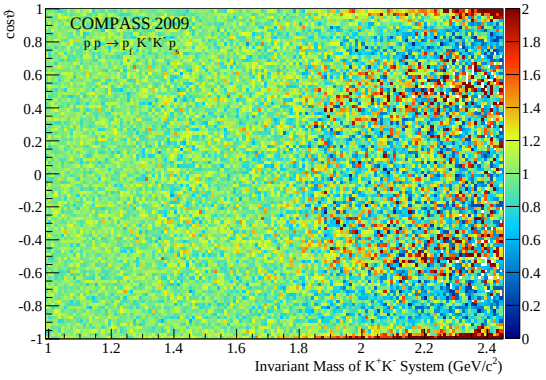

Figure 7.2: Ratio between data and weighted MC with $p(p_\mathrm{f}) > 140\,\mathrm{GeV}/c$.

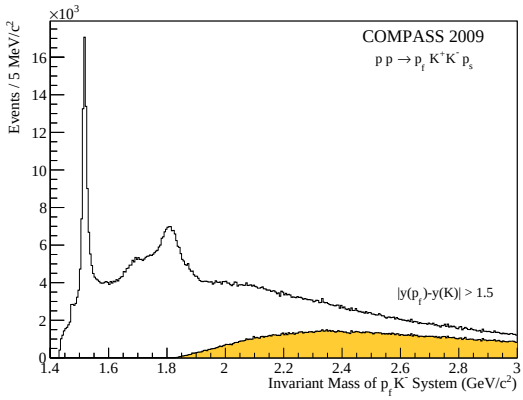

(a) $p_\mathrm{f}K^-$

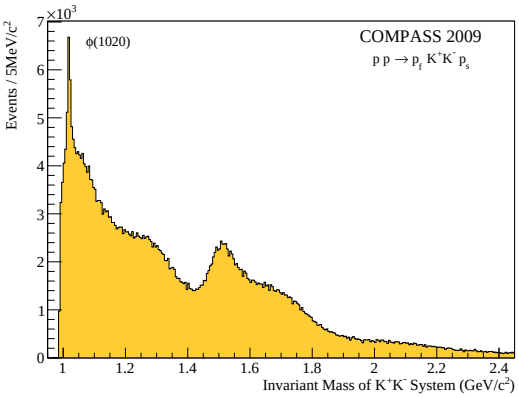

(b) K^+K^-

Figure 7.3: Invariant mass of subsystems, $|y(p) - y(K)| > 1.5$ (filled).

$M \leq 1$ (cf. Equation 5.5). Figure 7.2 illustrates the obtained ratio of real data over weighted MC for the events selected by requiring a minimal proton momentum of $140\,\mathrm{GeV}/c$. The peaks near $\cos\vartheta = \pm 1$ which are characteristic for a diffractive contribution can be discerned for K^+K^- masses above $1.8\,\mathrm{GeV}/c^2$. This artifact also influences the fit result for lower values of $|\cos\vartheta|$, which may alter the conclusions from the analysis significantly. For this reason, we decided to apply different selection criteria.

In contrast, the requirement of a rapidity gap between protons and kaons of at least 1.5 units suppresses any signs of diffractively produced baryon resonances with strangeness. The threshold for the invariant mass of the $p_\mathrm{f}K^-$ subsystem in Figure 7.3a is above $1.8\,\mathrm{GeV}/c^2$, and the remaining $p_\mathrm{f}K^-$ mass spectrum is compatible with a pure phase-space distribution. The prominent peak of the $\phi(1020)$ resonance in the selected K^+K^- sample, which is not expected for double-Pomeron exchange processes, is also considerably reduced (cf. Figure 3.11b and Figure 7.3b). The comparison of data with a Monte-Carlo sample weighted by the final fit result will be discussed in Section 7.2.1.

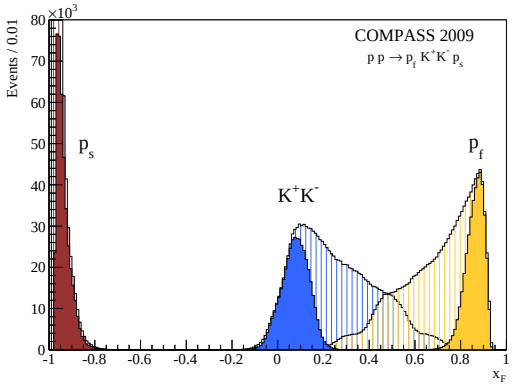

Figure 7.4: Feynman x_F distributions, $|y(p) - y(K)| > 1.5$ (filled).

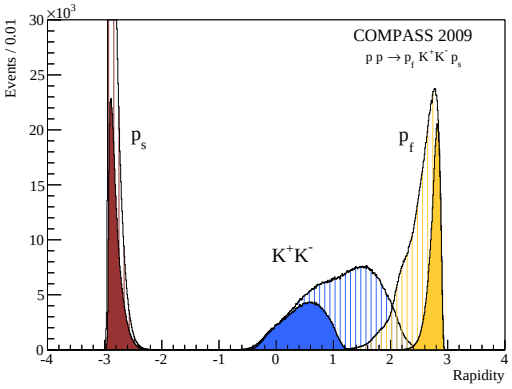

Figure 7.5: Rapidity distributions, $|y(p) - y(K)| > 1.5$ (filled).

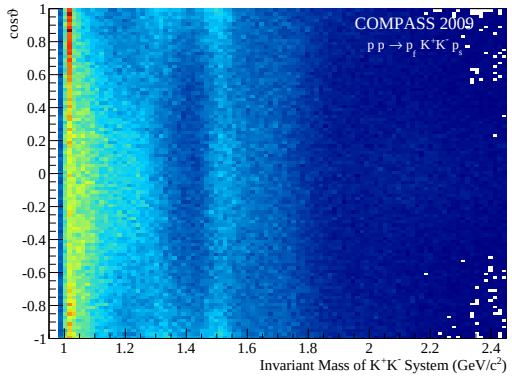

(a) $\cos\vartheta$

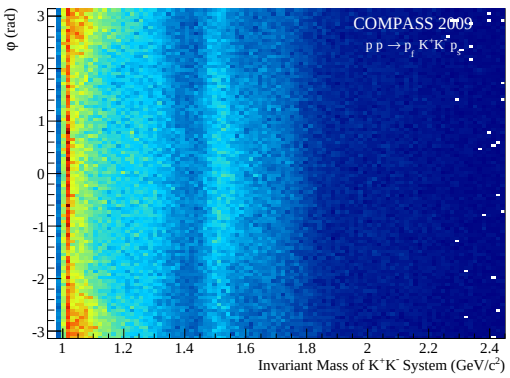

(b) φ

Figure 7.6: Decay variables as a function of the K^+K^- mass.

About $4 \cdot 10^5$ events are selected by this rapidity gap requirement, at least one order of magnitude more than available at previous experiments [20]. The x_F distribution (cf. Figure 7.4) shows the expected behaviour, with the central system concentrated in the x_F region below 0.2. Analogous to the $\pi\pi$ decay, the experimental setup has a poor acceptance for central systems produced in the backward hemisphere in the pp centre-of-mass frame. For the majority of the events, the rapidity of the K^+K^- system lies between zero and one (cf. Figure 7.5).

The partial-wave analysis is performed in the angles ϑ and φ of the K^- with respect to the reference frame defined in Section 5.1.1. Figure 7.6 shows the angular distributions as a function of the invariant mass of the central K^+K^- system. Except near the mass of the vector meson $\phi(1020)$, the distribution of the polar angle $\cos\vartheta$ is symmetric. This effect is characteristic for the likewise symmetric central-production process, and limits the required partial-wave contributions to even spins. In order to prove this, we start the analysis with the general wave set (cf. Equation 5.5).

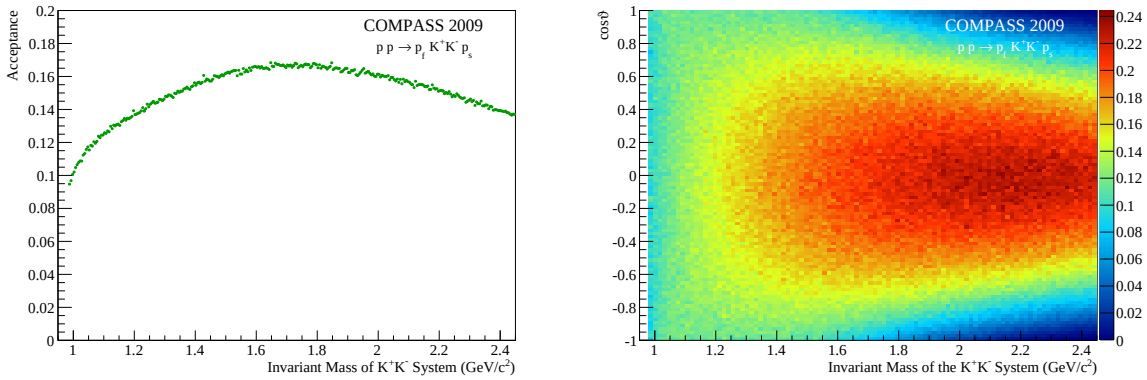

(a) Acceptance in $m_{K^+K^-}$

(b) Acceptance in $\cos\vartheta$

Figure 7.7: Acceptance for the central K^+K^- system with $|y(p) - y(K)| > 1.5$.

7.2 Mass-Independent Partial-Wave Analysis

The partial-wave decomposition in K^+K^- mass bins was performed in a fashion completely equivalent to the analysis of the central di-pion system as explained in Chapter 5. The data set allowed to use $10\,\mathrm{MeV}/c^2$ mass bins, which is four times finer than a previous analysis [20]. A Monte-Carlo data sample of $5 \cdot 10^7$ events was generated and reconstructed, using the efficiency tables for particle identification that were introduced in Section 4.2.3. The average acceptance for the fully reconstructed central production of a charged kaon pair with rapidity gaps larger than 1.5 units is about 15%, if one kaon is required to be identified by the RICH detector. Figure 7.7a depicts the acceptance as a function of the invariant mass of the central system. The decrease towards low K^+K^- masses is a direct consequence of the low-momentum threshold of $9.5\,\mathrm{GeV}/c$ for particle identification with the RICH detector. The effect of the requirement of a large rapidity gap between protons and kaons can be observed in Figure 7.7b, where the regions of $\cos\vartheta = \pm 1$ are suppressed for K^+K^- masses above $2\,\mathrm{GeV}/c^2$.

7.2.1 Evaluation of Goodness of Fit with Weighted MC

As a first step, we evaluate the fitting model by comparing the angular distributions of a weighted Monte-Carlo sample with the measured ones. For this purpose, we use all allowed partial waves up to the orbital angular momentum $L = 2$ with $M \leq 1$. They are grouped into two independent blocks by their reflectivity quantum number and the phase of the lowest-spin wave is fixed to zero in each block. These anchor waves are highlighted in bold font:

$$\{\boldsymbol{S_0^-}, P_0^-, P_1^-, D_0^-, D_1^-\}, \{\boldsymbol{P_1^+}, D_1^+\} \tag{7.1}$$

The result of a fit in mass bins is used to weight the phase-space Monte-Carlo sample, and the obtained angular distributions are compared with the measured ones. Figure 7.8 shows the ratio of real data over weighted MC, which is uniform in both decay angles as a function of the K^+K^- invariant mass. The decay can be perfectly described by the employed wave set, which confirms the suppression of diffractively produced events. Projections onto $100\,\mathrm{MeV}/c^2$ wide mass ranges illustrate the correctly found variations of the angular distributions with mass (cf. Figure 7.9).

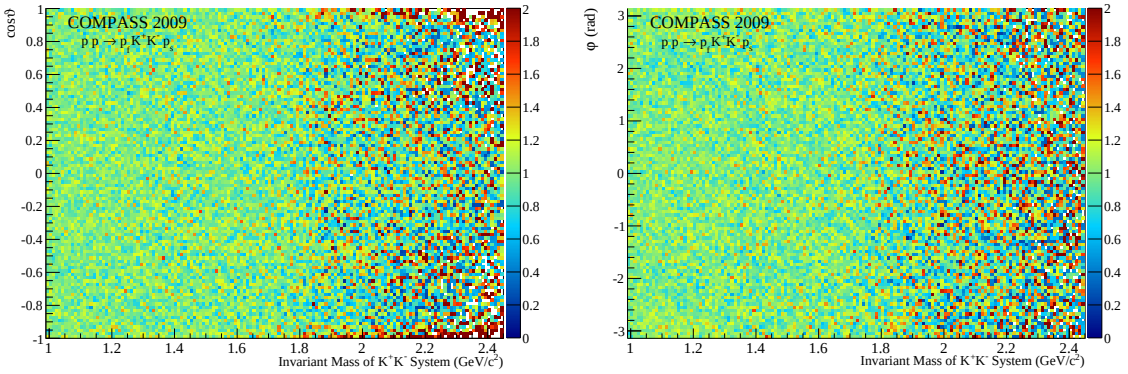

(a) $\cos\vartheta$ (b) φ

Figure 7.8: Ratio between data and weighted phase-space Monte-Carlo sample.

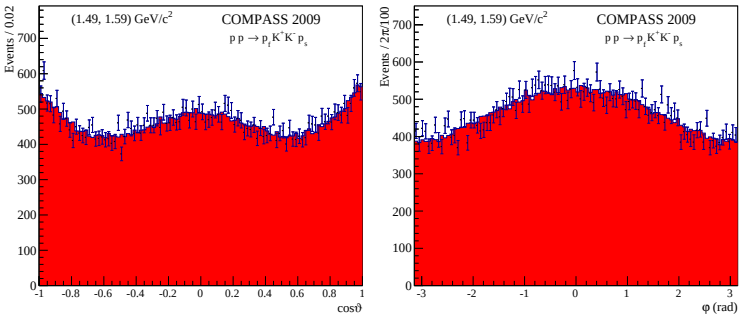

(a) $m_{K^+K^-} = [1.49, 1.59]\,\mathrm{GeV}/c^2$

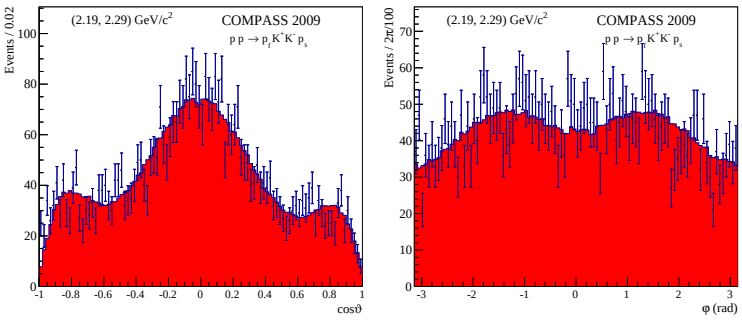

(b) $m_{K^+K^-} = [2.19, 2.29]\,\mathrm{GeV}/c^2$

Figure 7.9: Real data (blue) and weighted Monte-Carlo (red) for two K^+K^- mass ranges.

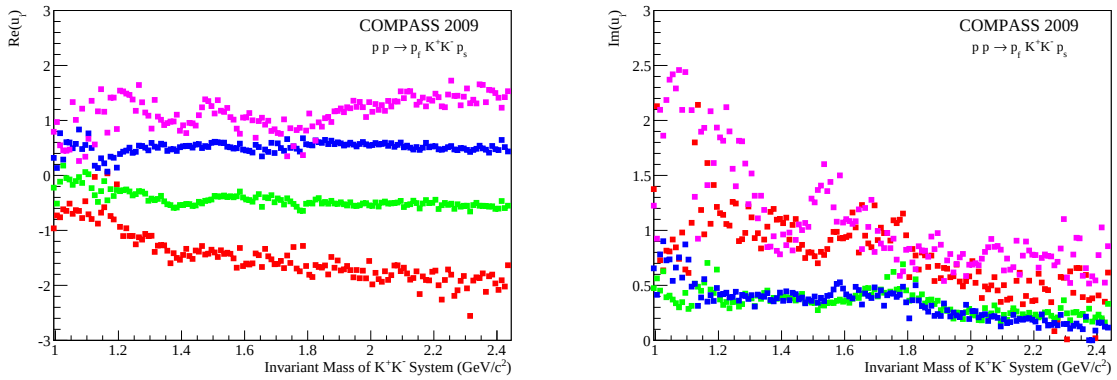

(a) Real part

(b) Imaginary part

Figure 7.10: Barrelet-zeros as a function of the K^+K^- mass.

7.2.2 Ambiguities

Eight mathematically equivalent sets of production amplitudes can be derived from the fitted amplitudes when considering the angular momentum $L \leq 2$ and its projections on the quantisation axis $M \leq 1$ [35]. As explained in Section 5.3, they can be calculated analytically from the complex roots of a forth-order polynomial in the angular variable $u = \tan\frac{\vartheta}{2}$. Figure 7.10 illustrates these so-called Barrelet-zeros [23] as they are obtained from the results of one fit. A clean separation of the roots and therefore a continuous identification of the eight solutions is possible by sorting them by their real part. Only in the region below $1.2\,\mathrm{GeV}/c^2$ and near $1.8\,\mathrm{GeV}/c^2$, the imaginary part has to be used to distinguish the cases for a few mass bins.

The eight complex-valued amplitudes for each wave can be directly derived from these four Barrelet zeros. Figure 7.11 shows the intensities for all waves with negative reflectivity. Analogous to the analysis of the $\pi\pi$ system (cf. Chapter 5), one particular solution is dominated by the S_0^--wave intensity. This solution also exhibits a clean peak in the D_0^--wave at the mass of the $f_2'(1525)$, and the P-waves are almost completely suppressed for masses above $1.1\,\mathrm{GeV}/c^2$. This supports the assumption of a symmetric production process.

Using the calculated physical solution as starting values for the transition amplitudes, the partial-wave fit in mass bins gives Figure 7.12. The peak in the D_0^- wave can be unmistakably identified as the $f_2'(1525)$ resonance. The $f_2(1270)$ plays a role as well. Traces for both mesons can also be identified in the D_1^--wave with magnetic quantum number $M = 1$. However, the enhancement at threshold in the latter wave is not physical due to the angular momentum barrier. The broad structures in the S_0^--wave remain difficult to interpret at this stage, but the distinct phase motion with respect to the D-wave provides an important constraint.

The $\phi(1020)$ can be found in both P_0^-- and P_1^--waves, but the identification of the physical solution is very unstable in this region. Above masses of $1.1\,\mathrm{GeV}/c^2$, the P-waves do not contribute to the intensity. Hence, the relative phases with respect to these waves are not well-defined. In the positive-reflectivity sector, a signal for the $a_2(1320)$ meson may even be discernible in the D_1^+-wave. However, the phase against the P_1^+ wave does not allow a definite statement.

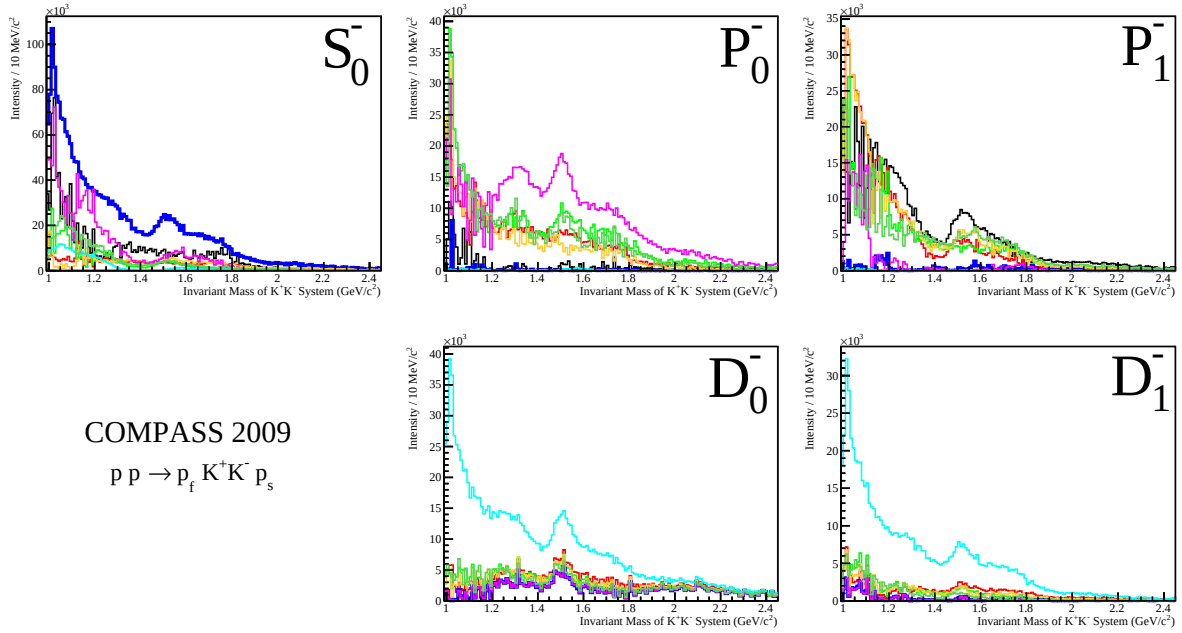

Figure 7.11: Intensities for the mathematically ambiguous solutions, calculated from the results of one fit. The physical solution (dark blue) was chosen as explained in the text.

7.2.3 Reduction of the Wave Set

Since the P-wave amplitudes are not necessary to describe the data apart from the narrow mass region near the $\phi(1020)$ meson, we studied the decomposition into scalar and tensor contributions only. For this simplified case, the mathematical ambiguities are decreased, as described in Section 5.3. The problem is reduced to a second-order polynomial, which yields only two independent solutions. Figure 7.13 illustrates the roots obtained by one fit to the data. Combining the information from the real parts for masses above $1.2\,\mathrm{GeV}/c^2$ with the imaginary parts below, a unique identification along all bins is achieved. Recalculating the intensity distributions for the two solutions (cf. Figure 7.14), one of the cases yields the expected dominance of the S-wave at threshold similar to Figure 7.11. The intensity distributions generally have the same appearance as the physical solution for the full wave set (cf. Figure 7.12). Only the peak of the $\phi(1020)$ resonance is wrongly attributed to the S-wave.

Figure 7.15 shows the final result for the acceptance-corrected partial-wave analysis of the centrally produced K^+K^- system in $10\,\mathrm{MeV}/c^2$ mass bins. The intensity distributions show all features observed already in the analysis with the P-waves included, while the fit seems to be much more stable. The intensities form smooth curves as a function of mass. A clear phase motion is visible between the S_0^-- and D_0^--wave, which will be an important ingredient for the interpretation in terms of resonant contributions in the Section 7.4. Before that, we will study the dependence of the observed spectra on the squared four-momentum transfer to the central K^+K^- system.

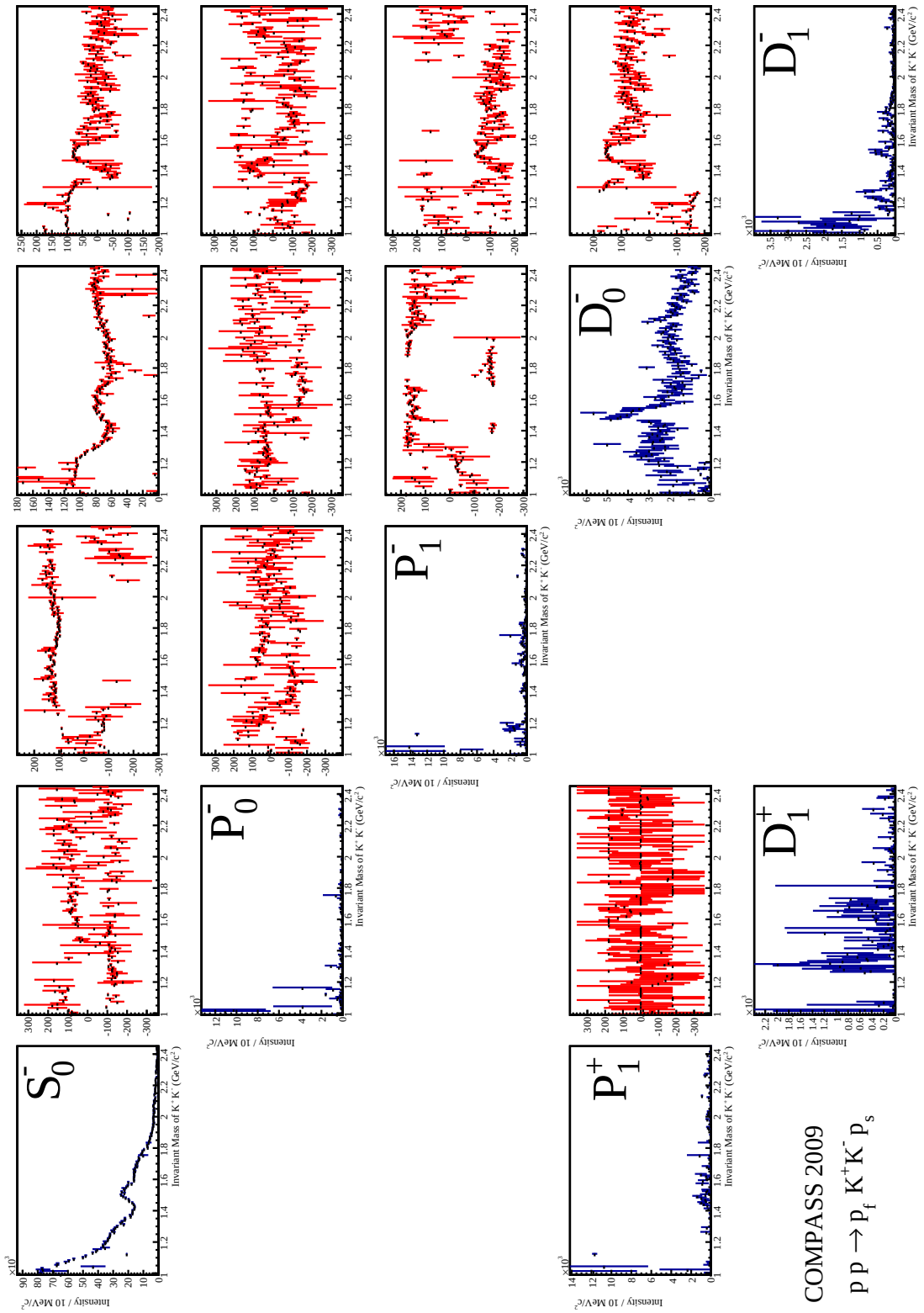

Figure 7.12: Physical solution, intensities (blue) and relative phases (red).

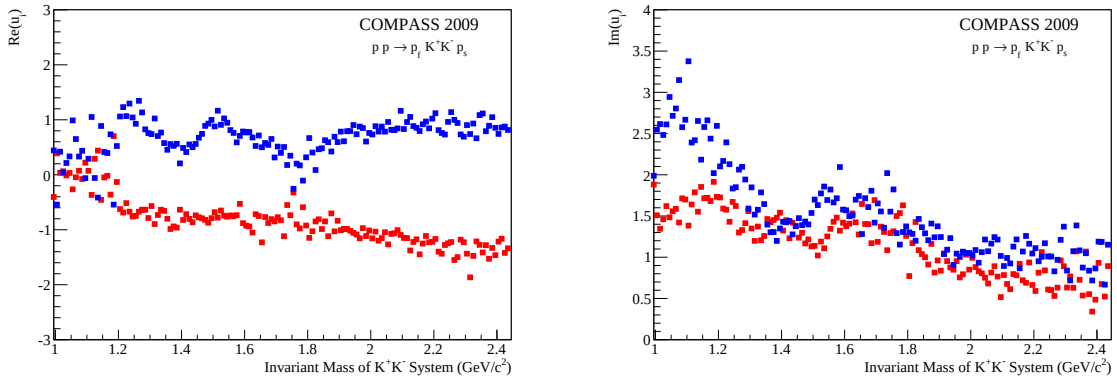

(a) Real part (b) Imaginary part

Figure 7.13: Barrelet-zeros as a function of the K^+K^- mass.

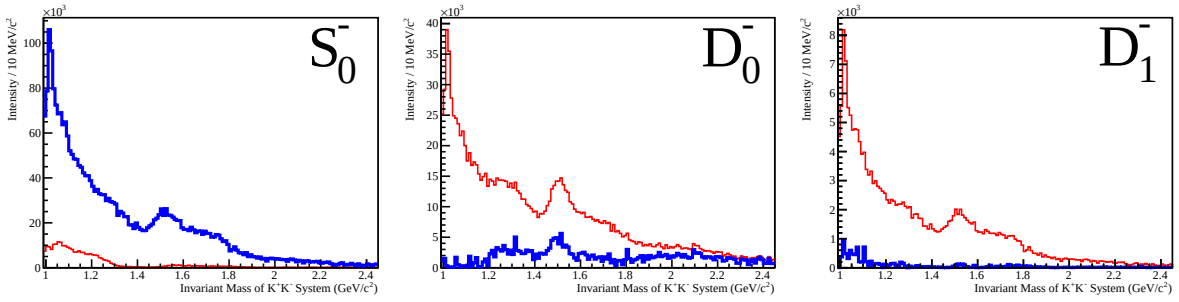

Figure 7.14: Two mathematically ambiguous intensity distributions, computed from the results of one fit. The physical solution (blue) was chosen for its S-wave dominance.

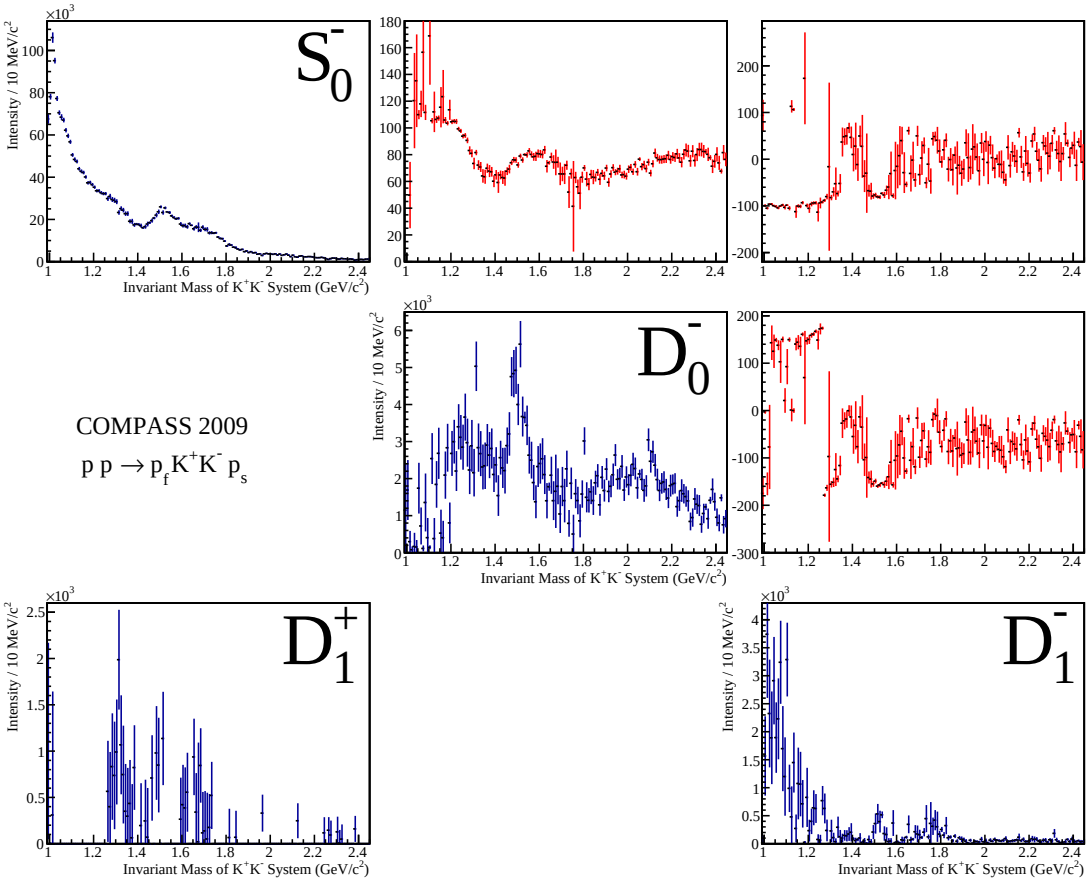

Figure 7.15: Physical solution for the reduced wave set without P-waves; intensities (blue) and phases (red).

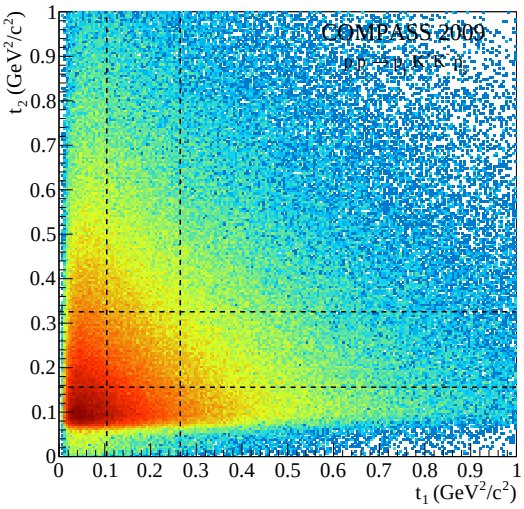

Bins in t_1 (GeV$^2/c^2$)	Bins in t_2 (GeV$^2/c^2$)
$[0.000, 0.105[$	$[0.000, 0.155[$
$[0.105, 0.265[$	$[0.155, 0.325[$
$[0.265, 2.000[$	$[0.325, 2.000[$

Figure 7.16: Squared four-momentum transfers t_1 vs. t_2 to the K^+K^- system with logarithmic colour-scale and two-dimensional binning (dashed lines).

7.3 Momentum-Transfer Dependence

In analogy to the analysis in two-dimensional bins of the squared four-momentum transfers t_1 and t_2 to the $\pi^+\pi^-$ system in Section 5.4, we split the data sample of about $4 \cdot 10^5$ centrally produced K^+K^- events into regions with approximately the same number of events. The division into nine sets allows a partial-wave analysis in $20\,\mathrm{MeV}/c^2$ wide mass bins. The boundaries for t_1 and t_2 are displayed in Figure 7.16.

Variations can already be discerned when comparing the invariant mass distributions for individual bins (cf. Figure 7.17). For the set with the lowest t_1 and t_2, the spectrum appears almost congruent with the S_0^- intensity extracted from the full sample (cf. Figure 7.12). Apart from the expected shift of the weight towards higher K^+K^- masses for increasing t_1 and t_2, the structures near $1.5\,\mathrm{GeV}/c^2$ and $1.7\,\mathrm{GeV}/c^2$ remain approximately stable. The narrow peak at the $\phi(1020)$ mass is becoming more pronounced, which is a sign for the onset of contributions from single- or double-Regge exchange processes. The broad enhancement below the $\phi(1020)$ peak, which turns out to be partly caused by the $f_0(980)$ in the next section, is suppressed relative to the other peaks for large $t_{1,2}$.

The partial-wave analysis of the nine data sets confirms the results obtained with the $\pi^+\pi^-$ system in Section 5.4. The obtained intensity distributions of the S_0^-- and D_0^--waves as well as their relative phases for all bins can be found in Appendix B.2. An almost background-free peak in the D_0^--wave at the mass of the $f_2'(1525)$ meson can be observed only for large $t_{1,2}$. However, the majority of the centrally produced K^+K^- events seems to be produced in a relative S_0^--wave. The results of all nine bins exhibit a clear phase motion between the S_0^-- and D_0^--waves, which is slightly modified from bin to bin. Full coherence between the different kinematic regions can therefore be safely assumed for the following analysis of the mass dependence.

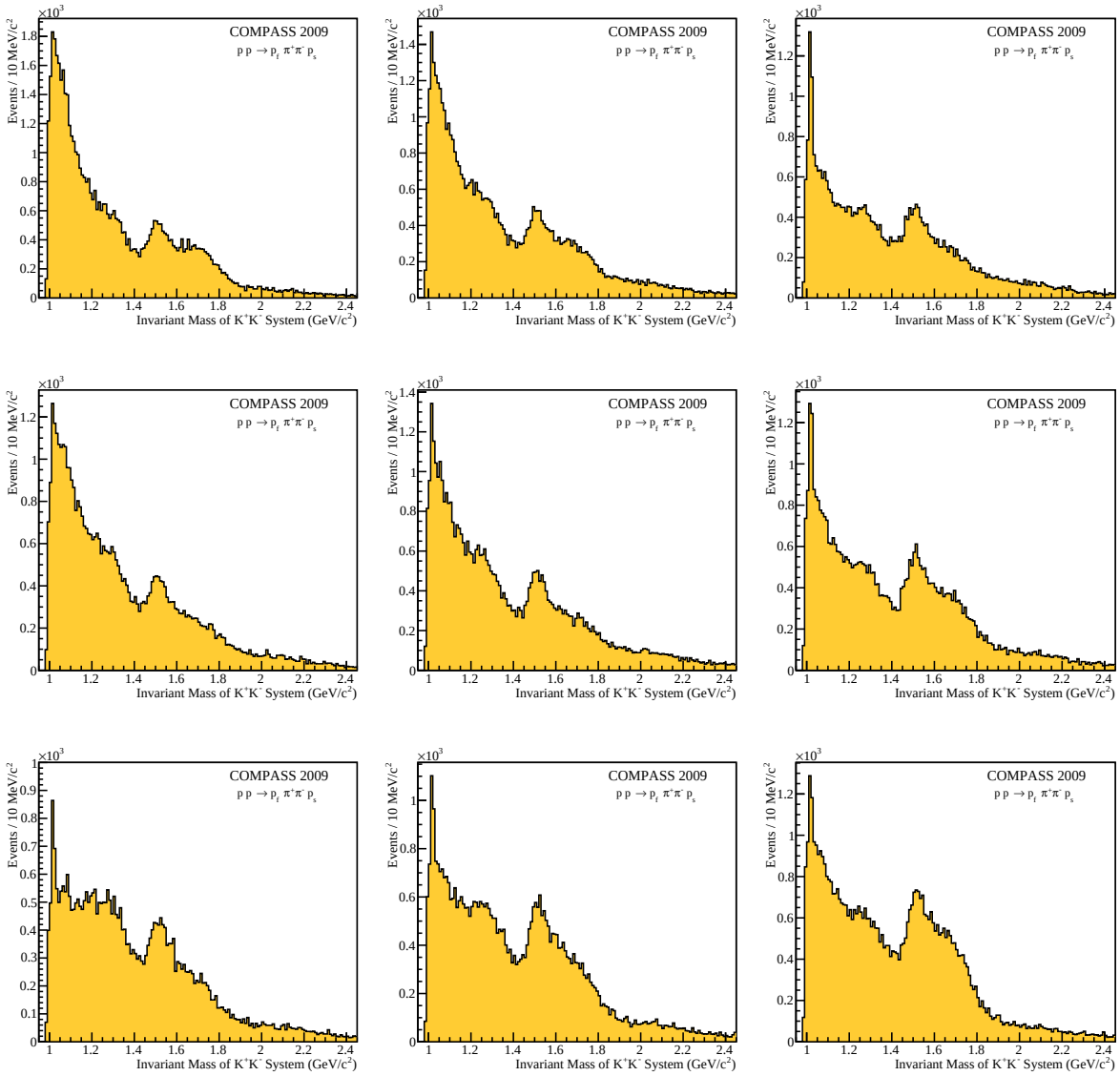

Figure 7.17: Invariant Mass of the K^+K^- System in bins (cf. text) of t_1 (horizontal, increasing from left to right) and t_2 (vertical, increasing from top to bottom)

7.4 Parametrisation of the Mass Dependence

The mass dependence of the S_0^--wave of the centrally produced K^+K^- system has to be described by a model in order to extract the resonant content. The basic ingredients for this model are Breit-Wigner functions and non-resonant contributions as introduced in Section 6.1, which are added coherently. The parameters are determined with a χ^2-fit to the results of the partial-wave decomposition in mass bins.

The mass of the $f_0(980)$ meson lies below threshold in the K^+K^- final-state, but it can have considerable influence on this channel through unitarity constraints. We will therefore demonstrate the effect of various parametrisations on the final result.

7.4.1 Fit to the *S*-Wave Intensity

Owing to their limited data sets, previous experiments (e.g. [20]) were only able to perform a fit to the intensity distributions, neglecting the interference between S- and D-wave amplitudes. Figure 7.18 illustrates such a χ^2-fit to the obtained S_0^--wave intensity with a simple model, adding three Breit-Wigner functions for the $f_0(1370)$, the $f_0(1500)$ and the $f_0(1710)$ coherently to a non-resonant component. The curve matches the data points accurately with the parameters specified in Table 7.1. We herein quote only the statistical errors provided by Minuit [65] and the weighted sum of squared errors divided by the number of degrees of freedom (χ^2/NDF) as the relative fit criterion. Analogous to the results on the central $\pi^+\pi^-$ system, the reduced χ^2 should not be interpreted as an absolute probability for the model.

The mass and width parameters of the established states $f_0(1500)$ and $f_0(1710)$ are in fairly good agreement with the precisely measured resonance parameters provided by the Particle Data Group [26]. For the $f_0(1370)$, only wide ranges are available for mass and width due to many contradicting analyses and the dispute about its existence [83, 81]. Nevertheless, our presented results are consistent with previous determinations with a similar analysis technique [20].

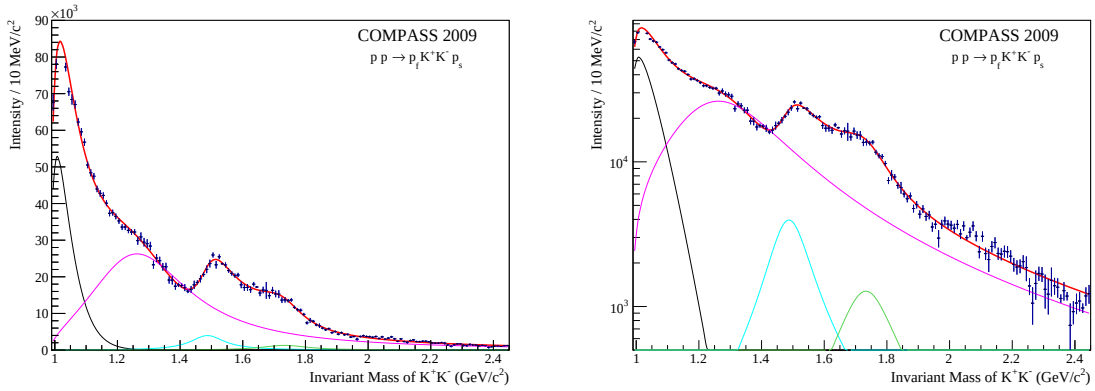

(a) Linear scale

(b) Logarithmic scale

Figure 7.18: Fit to S-wave intensity (red) with a non-resonant component (black) and three Breit-Wigner functions (other colours).

In order to illustrate the dependence of the Breit-Wigner parameters and especially of their relative magnitudes on the composition of the model, Figure 7.19 shows the results of a fit

Resonance	Fit result		PDG values [26]	
	Mass (MeV/c^2)	Width (MeV/c^2)	Mass (MeV/c^2)	Width (MeV/c^2)
$f_0(1370)$	1271 ± 7	385 ± 8	$1200 - 1500$	$200 - 500$
$f_0(1500)$	1487 ± 5	132 ± 5	1505 ± 6	109 ± 7
$f_0(1710)$	1737 ± 5	180 ± 7	1720 ± 6	135 ± 8

Table 7.1: Parameters for the fit with three Breit-Wigner functions and a non-resonant contribution (χ^2/NDF = 5.45). Only statistical errors are given for the fit result.

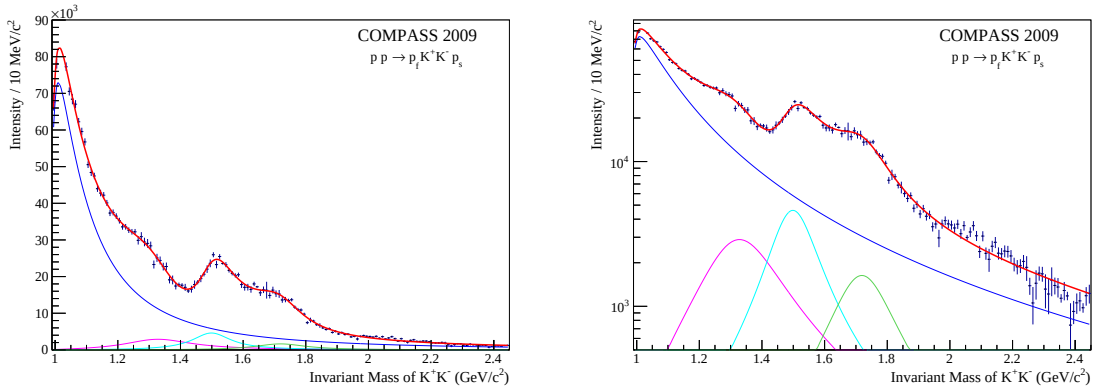

(a) Linear scale

(b) Logarithmic scale

Figure 7.19: Fit to S-wave intensity (red) with four Breit-Wigner functions (other colours).

Resonance	Fit result		PDG values [26]	
	Mass (MeV/c^2)	Width (MeV/c^2)	Mass (MeV/c^2)	Width (MeV/c^2)
$f_0(980)$	1044 ± 2	204 ± 8	990 ± 20	$40 - 100$
$f_0(1370)$	1330 ± 10	257 ± 26	$1200 - 1500$	$200 - 500$
$f_0(1500)$	1498 ± 5	105 ± 9	1505 ± 6	109 ± 7
$f_0(1710)$	1718 ± 5	199 ± 11	1720 ± 6	135 ± 8

Table 7.2: Parameters for the fit with four Breit-Wigner functions and no non-resonant component (χ^2/NDF = 4.96). Only statistical errors are given for the fit result.

where the non-resonant component was replaced by an additional Breit-Wigner for the $f_0(980)$ meson. With one additional parameter, the minimised χ^2 is decreased and the contributions of the resonant components fundamentally altered. The magnitude of the previously dominant $f_0(1370)$ is substantially reduced, and its Breit-Wigner parameters changed far beyond the statistical errors. On the other hand, the parameters of the $f_0(1500)$ and $f_0(1710)$ states are relatively stable and in even better agreement with the literature (cf. Table 7.2).

The mass and width of the Breit-Wigner function for the $f_0(980)$ at threshold are not well reproduced, possibly requiring an additional non-resonant contribution. However, the fit is not able to distinguish between both components on the basis of the one-dimensional intensities alone. Replacing the Breit-Wigner function for the $f_0(980)$ with the Flatté parametrisation

introduced in Section 6.1.2 does not substantially change these conclusions.

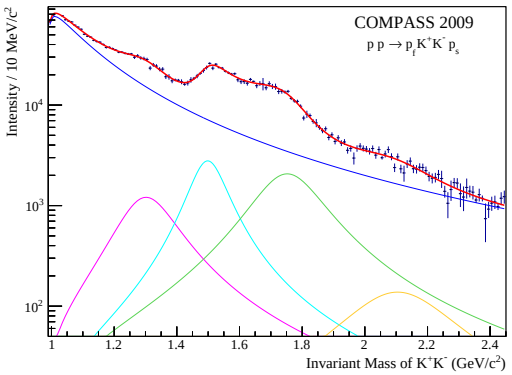

Figure 7.20: Fit to the S-wave intensity (red) with five Breit-Wigner functions (other colours).

Resonance	Fit result		PDG values [26]	
	Mass (MeV/c^2)	Width (MeV/c^2)	Mass (MeV/c^2)	Width (MeV/c^2)
$f_0(980)$	1049 ± 3	226 ± 13	990 ± 20	$40 - 100$
$f_0(1370)$	1303 ± 13	193 ± 18	$1200 - 1500$	$200 - 500$
$f_0(1500)$	1498 ± 4	122 ± 7	1505 ± 6	109 ± 7
$f_0(1710)$	1750 ± 7	229 ± 18	1720 ± 6	135 ± 8
$f_0(2100)$	2099 ± 43	358 ± 59	2103 ± 8	209 ± 19

Table 7.3: Parameters for a fit with five Breit-Wigner functions ($\chi^2/\text{NDF} = 3.74$). Only statistical errors are given for the fit result.

The χ^2 can be further improved by adding an additional Breit-Wigner function in order to describe the mass region above 2 GeV more accurately (cf. Figure 7.20). Mass and width of this additional state are listed in Table 7.3 and match the properties of the $f_0(2100)$ resonance within the large statistical uncertainties. This state needs further confirmation and is therefore omitted in the summary table of the Review of Particle Physics [26]. It was last reported in a combined analysis of $\pi\pi$ and $\eta\eta$ final states in $p\bar{p}$ annihilation [12], but has never been observed in $K\bar{K}$ systems.

All extracted resonance parameters bear systematic uncertainties, caused by the large model dependence. Especially since the fit to the intensity distribution neglects the phase information of the partial-wave amplitudes, both resonant and non-resonant components can be used to model the one-dimensional shape. The interference with the well defined states in the D-wave is used in the next section in order to reduce these ambiguities.

7.4.2 Simultaneous Fit to the *S*- and *D*-Wave

The visible peak in the D_0^--wave is formed by the narrow $f_2'(1525)$ resonance, which has a branching fraction of 88.7% for the decay into $K\bar{K}$ [26]. The decay probability of the $f_2(1270)$ into this final state is much lower (4.6%), but may also play a role for the enhancement near 1.3 GeV/c^2 in the D_0^--wave of Figure 7.15. Furthermore, a previous analysis of the same final state recorded at the OMEGA spectrometer [20] suggested a $f_2(2150)$ meson in this wave in

order to account for the broad peak at masses near $2\,\mathrm{GeV}/c^2$. On the other hand, only an incoherent sum of Breit-Wigner functions was fitted to the D_0^--wave intensity distribution in their analysis. The obtained parameters are therefore ignored for the official averages in the Review of Particle Physics [26], and the state is omitted from the summary table.

The simplest mass-dependent fit which describes the intensity distributions of the S_0^-- and D_0^--wave as well as the relative phase between them reasonably well requires five states. Similar to the fit of the S_0^- intensity alone (cf. Figure 7.18), at least three Breit-Wigner functions and a non-resonant component at threshold are needed in the S-wave. Two spin-two Breit-Wigner functions are used in the D-wave for the $f_2(1270)$ and the $f_2'(1525)$, which are added coherently to a non-resonant component. For this, we had to extend the parametrisation introduced in Section 6.1.4 with one additional parameter β in order to allow for more freedom in the shape. The non-resonant component in the D_0^--wave is parametrised by

$$\mathcal{N}'(m, L) = \left(\frac{q}{m}\right)^L \cdot \sqrt{\frac{q}{m}} \cdot \exp(-\alpha q^2 - \beta q) \; . \tag{7.2}$$

Since the χ^2-minimisation is susceptible to local minima, the fit had to be performed in several steps. At first, only the complex amplitude coefficients and the parameters of the non-resonant components were determined, leaving the masses and widths at the literature values [26]. In a second step, the mass parameters of the scalar resonances were released using the set of previously determined complex coefficients as the starting point. As the masses of the spin-two states $f_2(1270)$ and $f_2'(1525)$ are extremely well known, they are kept fixed to the literature values in order to stabilise the procedure. Finally, also the width parameters of all Breit-Wigner functions were determined by the fit. During all steps, the parameters m_0 and Γ_0 were limited to large but non-overlapping ranges of the order of several hundred MeV/c^2. An illustration of the final result expressed in intensities and relative phase is displayed in Figure 7.21. The estimated Breit-Wigner parameters are summarised in Table 7.4.

Resonance	Fit result		PDG values [26]	
	Mass (MeV/c^2)	Width (MeV/c^2)	Mass (MeV/c^2)	Width (MeV/c^2)
$f_2(1270)$	1275 (fixed)	311 ± 13	1275 ± 1	185 ± 3
$f_2'(1525)$	1525 (fixed)	102 ± 7	1525 ± 5	73 ± 6
$f_0(1370)$	1269 ± 2	259 ± 5	$1200 - 1500$	$200 - 500$
$f_0(1500)$	1500 ± 2	141 ± 6	1505 ± 6	109 ± 7
$f_0(1710)$	1734 ± 5	190 ± 7	1720 ± 6	135 ± 8

Table 7.4: Parameters for a simultaneous fit of the S_0^-- and D_0^--amplitudes with five Breit-Wigner functions and two non-resonant contributions ($\chi^2/\mathrm{NDF} = 4.90$). Only statistical errors are given for the fit result.

Even though this solution describes both intensity distributions and the relative phase between the waves quite well, its interpretation is difficult. The large contribution from the $f_0(1370)$ is not expected from the results of previous experiments. Analogous to the one-dimensional fit in the previous section, the relative intensities of the contributions change drastically if the influence of the $f_0(980)$ meson is taken into account. In addition, the parameters of the $f_0(1370)$ and the $f_2(1270)$ Breit-Wigner functions are strongly correlated. Consequently, the $f_2(1270)$ is reproduced far too broad. If the width is fixed to the nominal value [26], the model cannot reproduce the phase between the S_0^-- and the D_0^--wave.

As an illustration of this problem, we present a fit with the similar number of free parameters and a comparable χ^2/NDF in Figure 7.22. In this model, we use a Breit-Wigner function

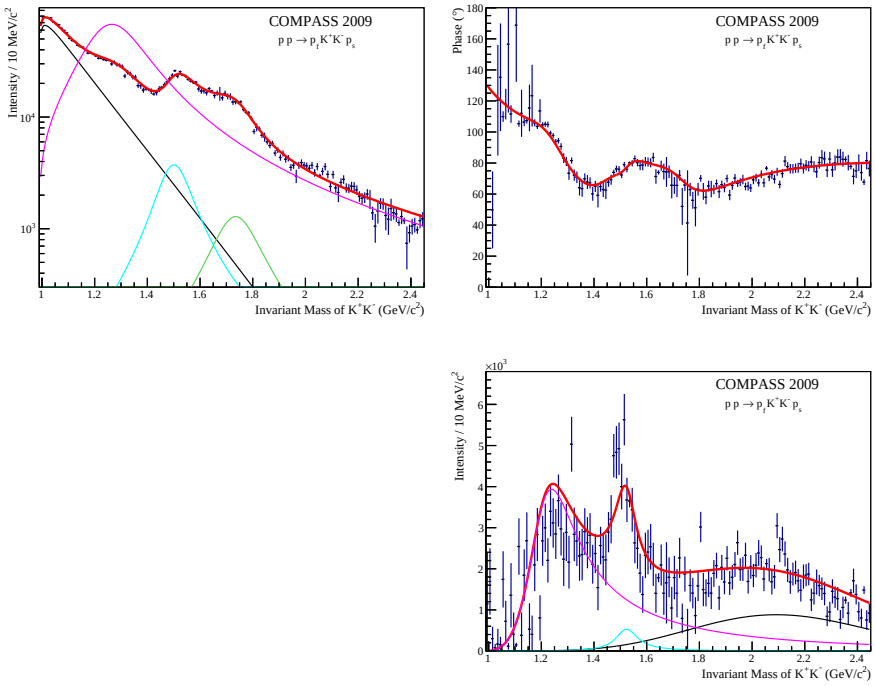

Figure 7.21: Mass-dependent parametrisation of intensities and phases (red) with non-resonant components (black) and Breit-Wigner functions (other colours)

for the $f_0(980)$ contribution at threshold in the S-wave. Two additional resonant terms are used for the $f_0(1500)$ and the $f_0(1710)$ mesons in the S-wave. A non-resonant component of the standard form (cf. Section 6.1.4) is added coherently. In the D-wave, two different non-resonant components describe the intensity distribution phenomenologically. The first one follows the shape of the angular momentum barrier (cf. Equation 6.13) and is responsible for the enhancement at threshold. For the term describing the broad peak above $2\,\mathrm{GeV}/c^2$, an additional parameter allows for more freedom (cf. Equation 7.2).

The Breit-Wigner parameters of this fit and their statistical errors are presented in Table 7.5. The masses and widths match the literature values reasonably well [26]. In particular, the relative phase between the S- and the D-wave is reproduced without the disputed $f_0(1370)$ resonance in this model (cf. Figure 7.22), even though a small overshoot of the data can be observed in the intensity distribution of the S-wave near $1.3\,\mathrm{GeV}/c^2$. The origin of this excess has to be studied in detail before a definite statement can be made. Leakage from the D-wave due to an insufficient description of the apparatus effects may be responsible for it. The relative phase with respect to the D-wave does not require the introduction of a Breit-Wigner term for the $f_0(2100)$ resonance. On the other hand, detailed knowledge about the resonant contributions in the D-wave above $2\,\mathrm{GeV}/c^2$ are indispensable for this claim.

In principle, the phase information between the S- and D-waves is a powerful tool to study the resonant content of the produced meson systems. However, the D-wave has to be exactly understood before it can be used as a reference. Moreover, systematic studies are needed in order to be able to judge the model dependence. Especially the dependence of the fit convergence on the choice of the starting values complicates an objective result.

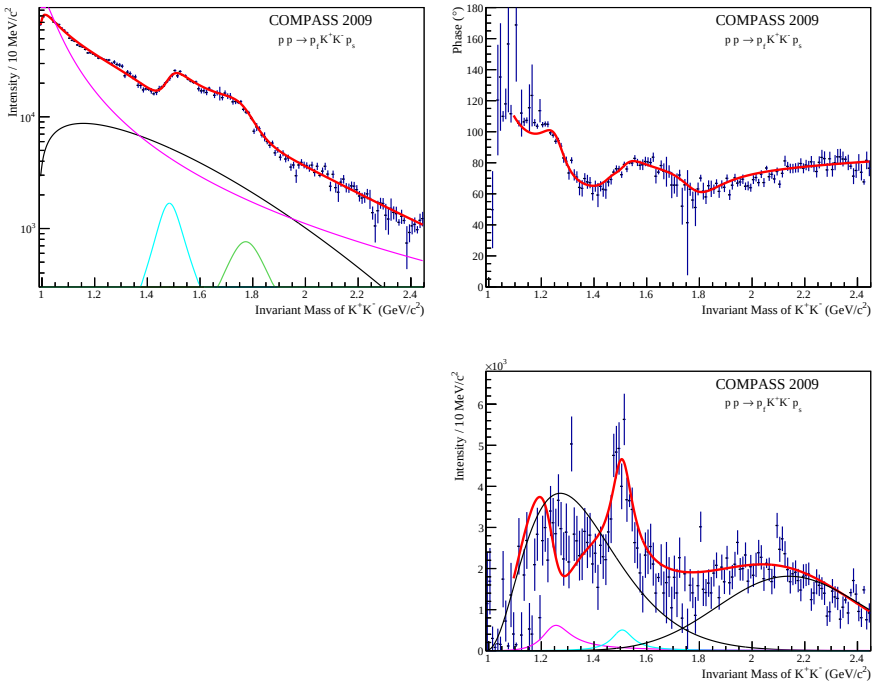

Figure 7.22: Mass-dependent parametrisation of intensities and phases (red) with non-resonant components (black) and Breit-Wigner functions (other colours)

Resonance	Fit result		PDG values [26]	
	Mass (MeV/c^2)	Width (MeV/c^2)	Mass (MeV/c^2)	Width (MeV/c^2)
$f_2(1270)$	1265 ± 4	140 ± 12	1275 ± 1	185 ± 3
$f_2'(1525)$	1508 ± 5	99 ± 7	1525 ± 5	73 ± 6
$f_0(980)$	1020 ± 1	126 ± 6	990 ± 20	$40 - 100$
$f_0(1500)$	1483 ± 4	106 ± 4	1505 ± 6	109 ± 7
$f_0(1710)$	1772 ± 5	173 ± 8	1720 ± 6	135 ± 8

Table 7.5: Parameters for a simultaneous fit of the S_0^-- and D_0^--amplitudes with five Breit-Wigner functions and three non-resonant contributions (χ^2/NDF = 4.92). Only statistical errors are given for the fit result.

Chapter 8

Discussion and Conclusions

We have studied the central production of systems decaying into two pseudoscalar mesons with the data set recorded with a 190 GeV/c proton beam at COMPASS in 2009. In this chapter, we will summarise the different steps of the analysis and discuss the results in a broader context. We will also present suggestions for further studies with this unique data set. Finally, an outlook on first results of a partial-wave analysis using a novel representation of the process amplitudes will be given, taking into account the relative orientation of both proton scattering planes.

8.1 Conclusions from the Data Selection

Nearly 10^8 exclusive events with three charged tracks leaving a primary vertex located in the liquid hydrogen target were successfully reconstructed from the COMPASS data recorded with a 190 GeV/c proton beam. Prominent structures in the $p_\mathrm{f}\pi^+\pi^-$ invariant mass distributions indicate that the diffractive dissociation of the beam proton is the dominating reaction in the triggered data sample. A number of known baryon resonances are also observed in the decay of the diffractively produced system. A partial-wave analysis of the data in terms of baryonic amplitudes may provide access to high-mass and high-angular momentum states that are not reachable for traditional baryon spectroscopy experiments [73].

We studied various kinematic criteria in order to enrich central-production reactions in the data. Only the theoretically motivated requirement for rapidity gaps larger than two units between all possible proton-pion combinations successfully suppresses evidence for baryon resonances in the remaining sample. This selection condition is fulfilled by approximately $7.5 \cdot 10^6$ $\pi^+\pi^-$ events in the mass range between threshold and 2 GeV/c^2, which is about a factor of three more than the samples available in any previous experiment [21]. Even though double-Pomeron exchange is considerably enhanced by this cut, the remaining $\rho(770)$ peak in the $\pi^+\pi^-$ mass spectrum is a sign for contamination by single- or double-Regge exchange processes, which cannot be discriminated at the centre-of-mass energy of $\sqrt{s} = 18.9$ GeV.

Baryons with strangeness can also be observed when kaons are identified in the final state. These baryon resonances are already efficiently suppressed by requiring a rapidity gap larger than 1.5 units between outgoing protons and kaons. With $4 \cdot 10^5$ centrally produced K^+K^- events, the COMPASS data set surpasses those acquired by previous experiments even by one order of magnitude [20].

A comparison with the data recorded with a pion beam may provide additional information about the production process. We showed in Section 3.5.3, that non-resonant contributions like the Deck effect can be responsible for parts of the enhancement at low masses in the

$\pi^+\pi^-$ invariant mass spectrum. Partial-wave amplitudes which include these processes may be formulated and applied in the analysis in the future.

In the hadron spectroscopy data recorded by the COMPASS experiment in 2008 and 2009, nearly all light two-pseudoscalar final states are reconstructed. The combination of $(\pi\pi)^0$, $(K\bar{K})^0$ and $\eta\eta$ systems will allow to draw conclusions on the quark content of the observed scalar mesons. This work describes an analysis method which is applicable to all these final states and provides the foundation for such a combined analysis.

8.2 Conclusions from the Partial-Wave Analysis in Mass Bins

Using conservative assumptions on the production process, the angular distribution of the pseudoscalar decay products of the central systems is described by partial-wave amplitudes estimated by independent fits to the data in $10\,\mathrm{MeV}/c^2$ wide mass bins. The inherent mathematical ambiguities of the decomposition of the measured intensity distribution into complex-valued amplitudes are determined with the help of the Barrelet zeros. The comparison of the $\pi^+\pi^-$ system with the analysis of the decays into $\pi^0\pi^0$ supports the choice of the physical solution.

For the case of the $\pi^+\pi^-$ final state, the partial-wave analysis isolates the $f_2(1270)$ meson in the D_0^--wave. A continuous phase motion with respect to the S_0^--wave is also observed with unprecedented precision. Apart from the dominant enhancement at threshold in the S_0^--wave which is characteristic for centrally produced systems [16], the $f_0(980)$ resonance can be discerned as a shoulder near $1\,\mathrm{GeV}/c^2$. On the other hand, the single- or double-Regge exchange production of the $\rho(770)$ meson cannot be cleanly separated with these amplitudes. A large fraction of the $\rho(770)$ intensity is wrongly attributed to the S_0^- wave, but the phase behaviour is not disturbed by this leakage effect. Since we are focusing on the resonant content of the scalar sector above $1\,\mathrm{GeV}/c^2$, the affected mass region is omitted from attempts to interpret the spectrum. Odd partial waves play only a subordinate role, as they are not allowed for double-Pomeron exchange reactions due to Bose symmetry constraints.

Despite the apparent shortcomings of the model to describe the entire data set, the partial-wave analyses of the centrally produced $\pi^+\pi^-$ and K^+K^- systems are more precise than any previous experimental result obtained with similar methods. The observed intensity distributions are consistent with established results [21, 20]. However, an interpretation including the relative phase between S_0^-- and D_0^--wave amplitudes allows a more differentiated interpretation of the centrally produced scalar resonances. In addition, the analysis in two-dimensional bins of the four-momentum transfers to the central system reveals dynamic dependencies which were previously neglected.

The evaluation of the fit quality with weighted Monte-Carlo data allows systematic studies about the dependence of the result on different kinematic selection criteria and Monte-Carlo generators for centrally produced systems. As an example, the simple cut on the invariant mass of the $p\pi$ combinations, as it was used in the past [21, 20], is found to produce considerable bias especially for $\pi^+\pi^-$ (K^+K^-) masses above $1.5\,\mathrm{GeV}/c^2$ ($2.0\,\mathrm{GeV}/c^2$). The cut is therefore not sufficient to select centrally produced systems efficiently.

8.3 Conclusions from Studies of the Mass Dependence

In order to extract the resonant content, physically motivated models with Breit-Wigner functions and non-resonant terms are fitted to the results of the amplitude analysis in mass bins. The intensity distribution of the S_0^--wave alone, which was mainly studied in the past, can be

described by substantially different models with arguable justification. We present a selection of different fits of mass-dependent amplitudes to the one-dimensional spectra, which illustrate this lack of uniqueness.

Since the phase of the S_0^--wave with respect to the D_0^--wave is determined with high precision in the partial-wave decomposition in mass bins, we exploit the interference with the well-known resonances $f_2(1270)$ and $f_2'(1525)$ in order to better pin down the resonant content in the scalar sector. For the $\pi^+\pi^-$ final state, the interpretation is, however, strongly dependent on the parametrisation of the $f_0(500)$, which cannot be modelled with a Breit-Wigner function. Due to its slow phase motion, it can be approximated by a non-resonant component for a rough estimate. A combined fit to the results of the partial-wave analysis in bins of t_1 and t_2 with stable Breit-Wigner parameters, but freedom in the non-resonant contributions and the relative phase between the components will provide an additional handle on the reaction dynamics.

The fit of the centrally produced K^+K^- system is also strongly dependent on the parametrisation of the enhancement at threshold, which may be formed by the tail of the $f_0(980)$, a non-resonant contribution or the combination of both. Since the D_0^--wave is suppressed by the angular-momentum barrier at threshold, we cannot use the relative phase to resolve this ambiguity. Consequently, we can neither prove nor disprove the existence of the disputed $f_0(1370)$ [81] in this work.

Simple parametrisations, that use the sum of Breit-Wigner functions and additional phenomenological backgrounds, are often met with criticism [83]. Especially if the states are broad and overlapping, the approximation with a Breit-Wigner function is no longer valid in order to determine the pole positions of physical resonances in the complex scattering plane. Models starting from the fundamental properties of analyticity and unitarity of the scattering amplitude are better suited to extract the resonance properties in this case (cf. D. Asner et al. in [26]).

A well-established parametrisation of this kind, which was determined by the combination of elastic scattering events, semi-leptonic kaon decays and data from production experiments [16], is fitted to our mass-independent results with only limited success. The interplay between $\pi\pi \to \pi\pi$ and $K\bar{K} \to \pi\pi$ amplitudes reproduces the gross features of the intensity and phase distributions. However, the parametrisation is only well-defined below $1.5\,\mathrm{GeV}/c^2$ and cannot easily be extended towards higher di-pion masses. In addition, it does not provide enough freedom to describe non-resonant contributions or resolution effects in the $f_0(980)$ mass region. On the other hand, the analysed COMPASS data may provide a valuable input for a combined fit to the results of various experiments with a dispersive approach, as it was recently summarised by J. R. Pelaez in [83]. Only the combination of rigorous theoretical models with new precision data can clarify the reigning confusion in the scalar meson spectrum. Otherwise, a satisfying answer to the question whether glueballs have a manifestation in nature cannot be achieved.

8.4 Outlook: Alternative Amplitude Representation

A different amplitude representation for the central-production reaction was proposed by D. Ryabchikov [89], following the works of F. E. Close et al. [38] and Kaidalov et al. [68]. It only assumes parity conservation in the production and decay processes, while all other physical properties are deduced from symmetry considerations. The amplitudes are constructed using the z-axis $\vec{n}_z$, defined by the two exchanged Reggeons in the rest frame of the central system, and the momentum vector $\vec{p}$ of one of the decay products of the central system. In contrast to the decay amplitudes introduced in Chapter 5, the normals $\vec{n}_1$ and $\vec{n}_2$ of the proton scattering planes defined in the rest frame of the central system are taken into account in this

approach as well. Formulated using non-relativistic Zemach tensors [85], the amplitudes for the lowest spin states are proportional to the expressions in Table 8.1. η specifies the product of the naturalities of the spin-parity transfers to the central system in the reaction.

Symbol	$J^{PC}M^{\eta}$	Zemach tensor
S_0	$0^{++}0^{+}$	1
S_0'	$0^{++}0^{+}$	$\vec{n}_1 \cdot \vec{n}_2$
P_0	$1^{--}0^{+}$	$\vec{p} \cdot \vec{n}_z$
P_1	$1^{--}1^{+}$	$\vec{p} \cdot (\vec{n}_1 + \vec{n}_2)$
D_0	$2^{++}0^{+}$	$(p_i p_j - \frac{1}{3}p^2\delta_{ij})\ n_{z,i}\ n_{z,j}$
D_0'	$2^{++}0^{+}$	$(p_i p_j - \frac{1}{3}p^2\delta_{ij})\ n_{z,i}\ n_{z,j}\ (\vec{n}_1 \cdot \vec{n}_2)$
D_1	$2^{++}1^{+}$	$(p_i p_j - \frac{1}{3}p^2\delta_{ij})\ (n_{1,i}\ n_{z,j} - n_{2,i}\ n_{z,j})$
D_2	$2^{++}2^{+}$	$(p_i p_j - \frac{1}{3}p^2\delta_{ij})\ \vec{n}_1 \cdot \vec{n}_2$
D_2'	$2^{++}2^{+}$	$(p_i p_j - \frac{1}{3}p^2\delta_{ij})\ (n_{1,i}\ n_{1,j} + n_{2,i}\ n_{2,j})$
	$0^{++}0^{-}$	$(\vec{n}_1 \times \vec{n}_2) \cdot \vec{n}_z$
	$1^{--}1^{-}$	$[(\vec{n}_1 \times \vec{n}_z) - (\vec{n}_2 \times \vec{n}_z)] \cdot \vec{p}$

Table 8.1: Alterative process amplitudes in Zemach tensor formalism [89].

These amplitudes were implemented in the COMPASSPWA framework also used for the analysis of diffractively produced three-pion systems [59]. An extended likelihood fit in $10\,\mathrm{MeV}/c^2$ mass bins was performed on the centrally-produced $\pi^+\pi^-$ data, selected by a rapidity gap of at least two units between all proton-pion combinations. For the correction of acceptance effects, the Monte-Carlo data sample that was generated for the main analysis was used, even though the generator did not produce a uniform distribution of the angle ϕ between the proton scattering planes in the $\pi^+\pi^-$ centre-of-mass frame (cf. Section 4.1.1).

A stable fit could only be achieved by excluding the waves with $\eta = -1$. On the other hand, the inherent ambiguities of the two-pseudoscalar system are apparently resolved by the additional dependence on the normals to the proton scattering planes. The different solutions can still be seen as local maxima with several fit attempts with random starting values, but the solution with the highest likelihood is unique and continuous from mass bin to mass bin. Figure 8.1 shows the intensities of the best fit for all partial-wave amplitudes with $\eta = +1$. Compared to the physical solution of the fit described in Chapter 5, the S-wave is split into a part S_0 which is uniform in all angles, and a part S_0' which can describe the observed modulation of the angle ϕ for low values of the $\pi^+\pi^-$ mass (cf. Figure 3.27). As a consequence, this partial-wave exhibits only intensity for di-pion masses below $1\,\mathrm{GeV}/c^2$. Above this mass, the S_0-wave in this approach is very similar to the physical solution presented in Figure 5.17.

A clear peak at the mass of the $f_2(1270)$ meson is seen in the D_0-wave, which is independent of the angle between the two proton scattering planes ϕ. Signs for the resonance can also be seen in the D_0'-wave which is modulated by ϕ, and both partial-wave amplitudes with $M = 2$. The P_1-wave with the quantum numbers $1^{--}1^{+}$ exhibits a peak consistent with the $\rho(770)$ meson. However, a similar peak is also found in the S_0-wave, while no intensity is attributed to the P_0-wave. Analogous to the analysis described in Chapter 5, also these amplitudes are not able to separate the $\rho(770)$ entirely. This is an independent confirmation that a different production is probably responsible for it.

Even though this novel method was not yet studied in detail, the obtained results seem very promising. Especially the central-production generator has to be tuned in order to obtain the correct behaviour of the angle ϕ in the rest frame of the central system.

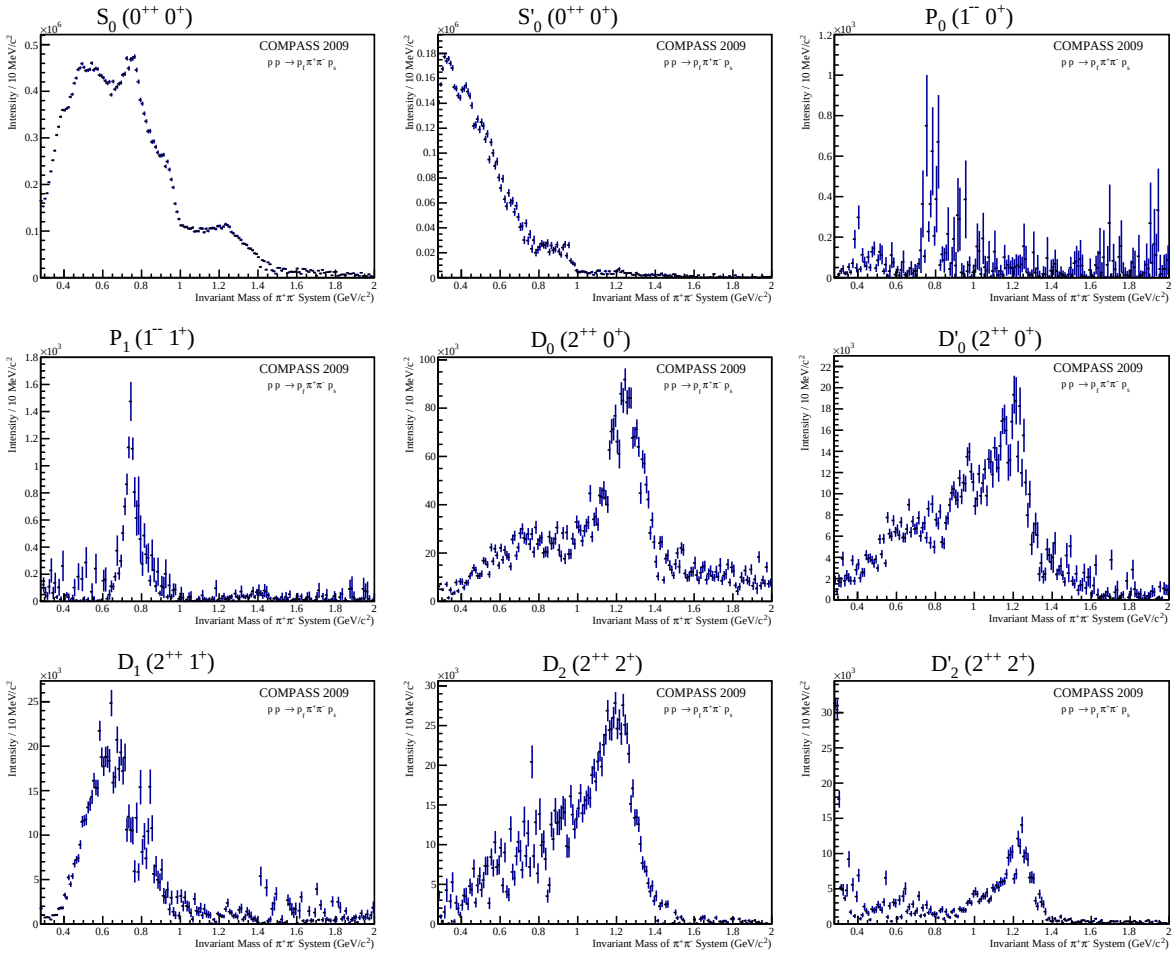

Figure 8.1: Partial-wave intensities obtained by a fit with the tensor amplitudes of Table 8.1. The best fit out of 20 attempts is shown. The data sample was selected requiring $|y(p) - y(\pi)| > 2$.

Bibliography

[1] G. Aad et al. Observation of a new particle in the search for the Standard Model Higgs boson with the ATLAS detector at the LHC. *Phys. Lett. B*, 716:1, 2012.
Cited on page(s): 1

[2] D. Abbaneo et al. Observation of a new boson at a mass of 125 GeV with the CMS experiment at the LHC. *Phys. Lett. B*, 716:30, 2012.
Cited on page(s): 1

[3] P. Abbon et al. The COMPASS experiment at CERN. *Nucl. Instr. and Meth. A*, 577:455, 2007.
Cited on page(s): 14

[4] M. Ablikim et al. Resonances in $J/\psi \to \phi\pi^+\pi^-$ and ϕK^+K^-. *Phys. Lett. B*, 607:243, 2005.
Cited on page(s): 83, 84, 89

[5] S. L. Adler. Consistency conditions on the strong interactions implied by a partially conserved axial-vector current. *Phys. Rev. B*, 137:1022, 1965.
Cited on page(s): 13, 84

[6] C. Adolph et al. The COMPASS setup for physics with hadron beams. to be submitted to *Nucl. Instr. and Meth. A*, 2014.
Cited on page(s): 14, 15, 16, 17, 21, 22, 24, 27, 43

[7] C. Adolph et al. Measurment of the charged–pion polarisability. submitted to *Phys. Rev. Lett.*, 2014.
Cited on page(s): 14, 23

[8] C. Adolph et al. Spin alignment and violation of the OZI rule in exclusive ω and ϕ production in pp collisions. accepted to *Nucl. Phys. B*, 2014.
Cited on page(s): 25, 33, 144

[9] A. Alekseev et al. Observation of a $J^{PC} = 1^{-+}$ exotic resonance in diffractive dissociation of 190 GeV/c π^- into $\pi^-\pi^-\pi^+$. *Phys. Rev. Lett.*, 104:241803, 2010.
Cited on page(s): 9

[10] C. Amsler. Antiproton-proton annihilation at rest into two-body final states. *Z. Phys. C*, 58:175, 1993.
Cited on page(s): 12

[11] C. Amsler. High-statistics study of $f_0(1500)$ decay into $\pi^0\pi^0$. *Phys. Lett. B*, 342:433, 1995.
Cited on page(s): 12

[12] A. V. Anisovich et al. $I = 0$ $C = +1$ mesons from 1920 to 2410 MeV. *Phys. Lett. B*, 491:47, 2000.
Cited on page(s): 110

[13] M. Antinucci et al. Multiplicities of charged particles up to ISR energies. *Lett. Nuovo Cim.*, 6:121, 1973.
Cited on page(s): 27

[14] T. A. Armstrong et al. Study of the centrally produced $\pi\pi$ and $K\bar{K}$ systems at 85 and 300 GeV/c. *Z. Phys. C*, 51:351, 1991.
Cited on page(s): 10, 45, 46, 77

[15] M. R. Atayan et al. A study of double pomeron exchange in $\pi^+ p$ and $K^+ p$ interactions at 250 GeV/c. *Z. Phys. C*, 50:353, 1991.
Cited on page(s): 50

[16] K. L. Au, D. Morgan, and M. R. Pennington. Meson dynamics beyond the quark model: Study of final-state interactions. *Phys. Rev. D*, 35:1633, 1987.
Cited on page(s): 8, 9, 84, 85, 91, 95, 115, 116

[17] A. Austregesilo. Baryon spectroscopy at COMPASS. *Proceedings of XIV International Conference on Hadron Spectroscopy*, 2011, hep-ex/1109.0230.
Cited on page(s): 30

[18] A. Austregesilo et al. First results of the PixelGEM central tracking system for COMPASS. *Nucl. Phys. B (Proc. Suppl)*, 197:113, 2009.
Cited on page(s): 17

[19] D. Barberis et al. A coupled channel analysis of the centrally produced K^+K^- and $\pi^+\pi^-$ final states in pp interactions at 450 GeV/c. *Phys. Lett. B*, 462:462, 1999.
Cited on page(s): 10, 88

[20] D. Barberis et al. A partial wave analysis of the centrally produced K^+K^- and $K^0_s K^0_s$ systems in pp interactions at 450 GeV/c and new information on the spin of the $f_J(1710)$. *Phys. Lett. B*, 453:305, 1999.
Cited on page(s): 98, 99, 108, 110, 114, 115

[21] D. Barberis et al. A partial wave analysis of the centrally produced $\pi^+\pi^-$ system in pp interactions at 450 GeV/c. *Phys. Lett. B*, 453:316, 1999.
Cited on page(s): 10, 34, 36, 44, 59, 60, 62, 66, 70, 86, 89, 114, 115

[22] D. Barberis et al. A study of the $\eta\eta$ channel produced in central pp interactions at 450 GeV. *Phys. Lett. B*, 479:59, 2000.
Cited on page(s): 44

[23] E. Barrelet. A new point of view in the analysis of two-body reactions. *Nuovo Cim. A*, 8:331, 1972.
Cited on page(s): 68, 101

[24] V. Baru et al. Flatté-like distributions in the $a_0(980)/f_0(980)$ mesons. *Eur. Phys. J. A*, 23:523, 2005.
Cited on page(s): 83

[25] G. Baum et al. COMPASS: A proposal for a COmmon Muon and Proton Apparatus for Structure and Spectroscopy. CERN/SPSLC 96-14, SPSC/P 297, March 1996.
Cited on page(s): 14

[26] J. Behringer et al. Review of particle physics. *Phys. Rev. D*, 86:010001, 2012.
Cited on page(s): 3, 30, 81, 83, 86, 88, 89, 90, 95, 108, 109, 110, 111, 112, 113, 116

[27] S. Betke. Experimental tests of asymptotic freedom. *Progress in Particle and Nuclear Physics*, 58:351, 2007.
Cited on page(s): 1

[28] V. Blobel and C. Kleinwort. A new method for the high-precision alignment of track detectors. *Conference on Advanced Statistical Techniques in Particle Physics*, 2002, hep-ex/0208021.
Cited on page(s): 22

[29] A. Brandt et al. A study of inclusive double-Pomeron-exchange $p\bar{p} \to pX\bar{p}$ at $\sqrt{s} = 630\,\text{GeV}$. *Eur. Phys. J. C*, 25:361, 2002.
Cited on page(s): 9

[30] G. Breit and E. Wigner. Capture of slow neutrons. *Phys. Rev.*, 49:519, 1936.
Cited on page(s): 82

[31] R. Brun and F. Rademakers. ROOT - an object oriented data analysis framework. *Nucl. Instr. and Meth. A*, 389:81, 1997.
Cited on page(s): 64

[32] M. Capeans. Aging and materials: lessons for detectors and gas systems. *Nucl. Instr. and Meth. A*, 515:73, 2003.
Cited on page(s): 19, 21

[33] D. M. Chew. Search for experimental evidence on exclusive double-pomeron exchange. *Nucl. Phys. B*, 82:422, 1974.
Cited on page(s): 38, 39

[34] S.-U. Chung. Introduction to partial-wave analyses II. presented at TUM Workshop, March 17^{th} 2008.
Cited on page(s): 6

[35] S.-U. Chung. Techniques of amplitude analysis for two-pseudoscalar systems. *Phys. Rev. D*, 56:7299, 1997.
Cited on page(s): 69, 71, 101, 132, 133

[36] S.-U. Chung and T. L. Trueman. Positivity conditions on the spin density matrix: A simple parametrization. *Phys. Rev. D*, 11:633, 1975.
Cited on page(s): 61, 68, 71, 87

[37] F. E. Close and A. Kirk. A glueball-$q\bar{q}$ filter in central hadron production. *Phys. Lett. B*, 397:333, 1997.
Cited on page(s): 11, 41, 77

[38] F. E. Close, K. Kirk, and G. Schuler. Dynamics of glueball and $q\bar{q}$ production in the central region of pp collisions. *Phys. Lett. B*, 477:13, 2000.
Cited on page(s): 116

[39] F. E. Close and G. A. Schuler. Evidence that the Pomeron transforms as a non-conserved vector current. *Phys. Lett. B*, 464:279, 1999.
Cited on page(s): 11

[40] J. C. Collins. Light-cone variables, rapidity and all that. 1997, hep-ph/9705393.
Cited on page(s): 7

[41] C. Daum et al. Diffractive production of 3π states at 63 GeV and 94 GeV. *Nucl. Phys. B*, 182:269, 1981.
Cited on page(s): 47

[42] R. T. Deck. Kinematical interpretation of the first π - ρ resonance. *Phys. Rev. Lett.*, 13:169, 1964.
Cited on page(s): 47

[43] S. Donnachie, G. Dosch, P. Landshoff, and O. Nachtmann. *Pomeron Physics and QCD.* Cambridge University Press, 2002.
Cited on page(s): 5, 6, 7, 30, 38, 50, 66

[44] C. Dreisbach. Investigation of aging effects in GEM detectors. Bachelor thesis, Technische Universität München, 2012.
Cited on page(s): 20

[45] C. Dreisbach. Master thesis in preparation, Technische Universität München, 2014.
Cited on page(s): 57

[46] D. Drijard et al. Double pomeron exchange in the reaction $pp \to pp\pi^+\pi^-$ at ISR energies. *Nucl. Phys. B*, 143:61, 1978.
Cited on page(s): 8, 77

[47] J. J. Dudek. The lightest hybrid meson supermultiplet in QCD. *Phys. Rev. D*, 84:074023, 2011.
Cited on page(s): 4

[48] J. J. Dudek, R. G. Edwards, P. Guo, and C. E. Thomas. Toward the excited isoscalar meson spectrum from lattice QCD. *Phys. Rev. D*, 88:094505, 2013.
Cited on page(s): 4

[49] J. J. Dudek, R. G. Edwards, and C. E. Thomas. Energy dependence of the ρ resonance in $\pi\pi$ elastic scattering fromm lattice QCD. *Phys. Rev. D*, 87:034505, 2013.
Cited on page(s): 4

[50] W. Erni et al. Physics performance report for $\overline{\mathrm{P}}$ANDA: Strong interaction studies with antiprotons. 2009, hep-ex/0903.3905.
Cited on page(s): 12

[51] R. P. Feynman. Very high-energy collision of hadrons. *Phys. Rev. Lett.*, 23:1415, 1969.
Cited on page(s): 7

[52] S. M. Flatté. Coupled-channel analysis of the $\pi\eta$ and $K\bar{K}$ systems near threshold. *Phys. Lett. B*, 63:224, 1976.
Cited on page(s): 83

[53] H. Fritzsch, M. Gell-Mann, and H. Leutwyler. Advantages of the color octet gluon picture. *Phys. Lett. B*, 47:365, 1973.
Cited on page(s): 1

[54] F. Gautheron et al. COMPASS-II proposal. CERN-SPSC-2010-014, SPSC-P-340, March 2010.
Cited on page(s): 16

[55] M. Gell-Mann and M. Lévy. The axial vector current in beta decay. *Nuovo Cim.*, 16:705, 1960.
Cited on page(s): 3

[56] A. Gersten. Ambiguities of complex phase-shift analysis. *Nucl. Phys. B*, 12:537, 1969.
Cited on page(s): 69

[57] K. Gottfried and J. D. Jackson. On the connection between production mechanism and decay of resonances at high energies. *Nuovo Cim.*, 33:309, 1964.
Cited on page(s): 59, 61

[58] S. Grabmüller. Cryogenic silicon detectors and analysis of Primakoff contributions to the reaction $\pi^-\,\mathrm{Pb} \to \pi^-\pi^-\pi^+\,\mathrm{Pb}$ at COMPASS. Dissertation, Technische Universität München, 2012.
Cited on page(s): 3

[59] F. Haas. Two-dimensional partial-wave analysis of exclusive 190 GeV $\pi^- p$ scattering into the $\pi^-\pi^-\pi^+$ final state at COMPASS (CERN). Dissertation, Technische Universität München, 2013.
Cited on page(s): 17, 25, 30, 32, 42, 44, 46, 47, 84, 92, 117

[60] L. A. Harland-Lang et al. The phenomenology of central exclusive production at hadron colliders. *Eur. Phys. J. C*, 72:2110, 2012.
Cited on page(s): 11, 41, 51, 52

[61] L. A. Harland-Lang et al. Dime Monte Carlo: event generator for exclusive meson pair production via double Pomeron exchange. *http://dimemc.hepforge.org/*, 2014.
Cited on page(s): 51

[62] L. A. Harland-Lang et al. Modeling exclusive meson pair production at hadron colliders. *accepted for publication in EPJC*, 2014.
Cited on page(s): 51

[63] B. Holzgartner. Water cooling for the frontend electronics and a modular phase separator for the COMPASS silicon detectors and alignment for the 2012 Primakoff run. Diplomarbeit, Technische Universität München, 2012.
Cited on page(s): 144

[64] B. Hyams et al. $\pi\pi$ phase-shift analysis from 600 to 1900 MeV. *Nucl. Phys. B*, 64:134, 1973.
Cited on page(s): 13, 92

[65] F. James and M. Roos. Minuit: A system for function minimization and analysis of the parameter errors and correlations. *Comp. Phys. Commun.*, 10:343, 1975.
Cited on page(s): 64, 108

[66] P. K. Jasinski. Analysis of diffractive dissociation of K^- into $K^-\pi^+\pi^-$ on a liquid hydrogen target at the COMPASS spectrometer. Dissertation, Johannes-Gutenberg-Universität Mainz, 2012.
Cited on page(s): 27, 54

[67] D. Joyce et al. Double Pomeron exchange studies in $p\bar{p}$ interactions at 0.63 TeV. *Phys. Rev. D*, 48:1943, 1993.
Cited on page(s): 9

[68] A. B. Kaidalov et al. Central exclusive diffractive production as a spin-parity analyser: from hadrons to Higgs. *Eur. Phys. J. C*, 31-3:387, 2003.
Cited on page(s): 11, 42, 116

[69] B. Ketzer. Precision studies of light mesons at COMPASS. *PoS*, Hadron 2013:011, 2013.
Cited on page(s): 32

[70] B. Ketzer et al. Performance of triple GEM tracking detectors in the COMPASS experiment. *Nucl. Instr. and Meth. A*, 535:314, 2004.
Cited on page(s): 17

[71] A. Kirk et al. New effects observed in central production by the WA102 experiment at ther CERN OMEGA spectrometer. *XXVIII symposium on MultiParticle Dynamics*, 1998, hep-ph/9810221.
Cited on page(s): 42

[72] E. Klempt. Glueballs, hybrids and $q\bar{q}$ mesons. *PSI Zuoz Summer School on Phenomenology of Gauge Interactions*, 2000, hep-ex/0101031.
Cited on page(s): 2, 3

[73] E. Klempt and J.-M. Richard. Baryon spectroscopy. *Rev. Mod. Phys.*, 82:1095, 2010.
Cited on page(s): 30, 114

[74] E. Klempt and A. Zaitsev. Glueballs, hybrids, multiquarks. experimental facts versus QCD inspired concepts. *Phys. Rept.*, 454:1–202, 2007.
Cited on page(s): 1, 3, 9, 10, 11, 12, 13, 33, 36, 42, 48, 80

[75] P. Lebiedowicz and A. Szczurek. Exclusive $pp \to pp\pi^+\pi^-$ reaction: from the threshold to LHC. *Phys. Rev. D*, 81:036003, 2010.
Cited on page(s): 39, 40

[76] L. Li et al. New composition of $\pi\pi$ S-wave interaction. *Phys. Rev. D*, 63:074003, 2001.
Cited on page(s): 13

[77] T. Åkesson et al. A study of exclusive central hadron production at the ISR as a search for gluonium states. *Phys. Lett. B*, 133:268, 1983.
Cited on page(s): 88

[78] T. Åkesson et al. A search for glueballs and a study of double pomeron exchange at the CERN Intersecting Storage Rings. *Nucl. Phys. B*, 264:154, 1986.
Cited on page(s): 8, 9

[79] C. J. Morningstar and M. Peardon. Glueball spectrum from an anisotropic lattice study. *Phys. Rev. D*, 60:034509, 1999.
Cited on page(s): 4, 5

[80] S. Neubert. First amplitude analysis of resonant structures in the 5-pion continuum at COMPASS. Dissertation, Technische Universität München, 2012.
Cited on page(s): 52, 87

[81] W. Ochs. The status of glueballs. *J. Phys. G*, 40:043001, 2013.
Cited on page(s): 1, 3, 10, 108, 116

[82] S. Okubo. ϕ-meson and unitarity symmetry model. *Phys. Lett.*, 3:165, 1963.
Cited on page(s): 12

[83] J. R. Pelaez. Recent progress on light scalars: from confusion to precision using dispersion theory. *PoS*, ConfinementX:019, 2012.
Cited on page(s): 1, 9, 108, 116

[84] M. Pennington. private communications, 2013.
Cited on page(s): 85, 86, 93

[85] K. Peters. A primer on partial wave analysis. *Int. J. Mod. Phys. A*, 21:5618, 2006.
Cited on page(s): 82, 84, 91, 117

[86] W. H. Press et al. *Numerical Recipes in C: The Art of Scientific Computing (Second Edition)*. Cambridge University Press, 1992.
Cited on page(s): 69

[87] L. D. Roper. Evidence for a P_{11} pion-nucleon resonance at 556 MeV. *Phys. Rev. Lett.*, 12:340, 1964.
Cited on page(s): 32

[88] L. Rosselet et al. Experimental study of 30 000 K_{e4} decays. *Phys. Rev. D*, 15:574, 1977.
Cited on page(s): 13

[89] D. Ryabchikov. PWA methods for diffractive and central-production reactions. presented at CERN Seminar, February 16$^{\text{th}}$ 2011.
Cited on page(s): 50, 116, 117

[90] S. A. Sadovsky. On the ambiguities in the partial-wave analysis of $\pi^- p \to \eta\pi^0 n$ reactions. IHEP 91-75, 1991.
Cited on page(s): 69

[91] F. Sauli. Principles of operation of multiwire proportional and drift chambers. CERN 77-09, 1977.
Cited on page(s): 19

[92] F. Sauli. GEM: A new concept for electron amplification in gas detectors. *Nucl. Instr. and Meth. A*, 386, 1997.
Cited on page(s): 15, 16

[93] R. Schicker. Central meson production in ALICE. *Proceedings of XIV International Conference on Hadron Spectroscopy*, 2011, hep-ex/1110.3693.
Cited on page(s): 11, 12

[94] T. Schlüter. The $\pi^-\eta$ and $\pi^-\eta'$ systems in exclusive 190 GeV $\pi^- p$ reactions at COMPASS (CERN). Dissertation, Ludwig-Maximilian-Universität München, 2012.
Cited on page(s): 64, 65, 96

[95] T. Schlüter et al. Large-area sandwich veto detector with WLS fibre readout for hadron spectroscopy at COMPASS. *Nucl. Instr. and Meth. A*, 654:219, 2011.
Cited on page(s): 26

[96] T. Schromm. Development of a set-up for the investigation of aging effects in GEM detectors. Bachelor thesis, Technische Universität München, 2013.
Cited on page(s): 20, 22

[97] M. Tasior. Performance studies for the COMPASS PixelGEM tracking detectors and development of a modular test bench for GEM detectors. Diplomarbeit, Technische Universität München, 2011.
Cited on page(s): 18, 19, 21, 144

[98] T. T. M. Tran, C. Friaud, F. M. M. Sutter, and A. Villanova. The atmospheric corrosion of copper by hydrogen sulphide in underground conditions. *Corrosion Science*, 45-12:2787, 2003.
Cited on page(s): 20, 21

[99] S. Uhl. Contruction and commissioning of the PixelGEM tracking system for the COMPASS experiment. Diplomarbeit, Technische Universität München, 2008.
Cited on page(s): 18, 144

[100] S. Uhl. Dissertation in preparation, Technische Universität München, estim. 2015.
Cited on page(s): 23, 44, 52, 84

[101] I. Uman et al. Hadron program at COMPASS. *Chin. Phys. C*, 34:1375, 2010.
Cited on page(s): 49

[102] F. von Hippel and C. Quigg. Centrifugal-barrier effects in resonance partial decay widths, shapes, and production amplitudes. *Phys. Rev. D*, 5:624, 1972.
Cited on page(s): 83

[103] K. M. Watson. The effect of final state interaction on reaction cross sections. *Phys. Rev.*, 88:1163, 1952.
Cited on page(s): 13, 84, 91

[104] T. Weisrock. Dissertation in preparation, Johannes-Gutenberg-Universität Mainz, estim. 2015.
Cited on page(s): 30, 43, 44

List of Figures

List of Tables

Appendix A

Mathematical Ambiguities

A.1 Formulae for *S*-, *P*- and *D*-waves

The coefficients of the forth-order polynomial

$$G(u) = a_4u^4 - a_3u^3 + a_2u^2 - a_1u + a_0 \tag{A.1}$$

for a system with S-, P- and D-waves and $M \leq 1$ may be written [35] as

$$\begin{aligned} a_0 &= S_0 + \sqrt{3}P_0 + \sqrt{5}D_0 \\ a_1 &= 2\sqrt{3}(P_- - \sqrt{5}D_-) \\ a_2 &= 2S_0 - 4\sqrt{5}D_0 \\ a_3 &= 2\sqrt{3}(P_- - \sqrt{5}D_-) \\ a_4 &= S_0 - \sqrt{3}P_0 + \sqrt{5}D_0 \end{aligned} \tag{A.2}$$

Reciprocally, the partial waves are expressed in terms of the roots u_k:

$$\begin{aligned} 6S_0 &= a_4(2u_1u_2u_3u_4 + u_1u_2 + u_1u_3 + u_1u_4 + u_2u_3 + u_2u_4 + u_3u_4 + 2) \\ 2\sqrt{3}P_0 &= a_4(u_1u_2u_3u_4 - 1.) \\ 4\sqrt{3}P_- &= a_4(u_1u_2u_3 + u_2u_3u_4 + u_3u_4u_1 + u_4u_1u_2 + u_1 + u_2 + u_3 + u_4) \\ 6\sqrt{5}D_0 &= a_4(u_1u_2u_3u_4 - u_1u_2 - u_1u_3 - u_1u_4 - u_2u_3 - u_2u_4 - u_3u_4 + 1) \\ 4\sqrt{15}D_- &= a_4(u_1u_2u_3 + u_2u_3u_4 + u_3u_4u_1 + u_4u_1u_2 - u_1 - u_2 - u_3 - u_4) \end{aligned} \tag{A.3}$$

The set of eight ambiguous solutions may be obtained using the following system:

$$\begin{aligned} &\{u_1, u_2, u_3, u_4\} \\ &\{u_1, u_2, u_3, u_4^*\} \\ &\{u_1, u_2, u_3^*, u_4\} \\ &\{u_1, u_2, u_3^*, u_4^*\} \\ &\{u_1, u_2^*, u_3, u_4\} \\ &\{u_1, u_2^*, u_3, u_4^*\} \\ &\{u_1, u_2^*, u_3^*, u_4\} \\ &\{u_1, u_2^*, u_3^*, u_4^*\} \end{aligned} \tag{A.4}$$

A.2 Formulae for *S*- and *D*-waves

The coefficients of the second-order polynomial

$$G(u) = a_2 u^2 - a_1 u + a_0 \tag{A.5}$$

for a system with S- and D-waves and $M \leq 1$ may be written [35] as

$$\begin{aligned} a_0 &= 4S_0 - 2\sqrt{5}D_0 \\ a_1 &= 2\sqrt{15}D_-) \\ a_2 &= S_0 + \sqrt{5}D_0 \end{aligned} \tag{A.6}$$

Reciprocally, the partial waves are expressed in terms of the roots u_k $(k = 1, 2)$:

$$\begin{aligned} 6S_0 &= a_2(u_1 u_2 + 2) \\ 6\sqrt{5}D_0 &= a_2(4 - u_1 u_2) \\ 2\sqrt{15}D_- &= a_2(u_1 + u_2) \end{aligned} \tag{A.7}$$

The two ambiguous solutions may be obtained using the following system:

$$\begin{aligned} &\{u_1, u_2\} \\ &\{u_1, u_2^*\} \end{aligned} \tag{A.8}$$

Appendix B

Momentum-Transfer Dependent Results

B.1 Centrally Produced $\pi^+\pi^-$ System

Bins in t_1 (GeV$^2/c^2$)	Bins in t_2 (GeV$^2/c^2$)
$[0.000, 0.040[$	$[0.000, 0.100[$
$[0.040, 0.080[$	$[0.100, 0.140[$
$[0.080, 0.140[$	$[0.140, 0.200[$
$[0.140, 0.255[$	$[0.200, 0.325[$
$[0.255, 2.000[$	$[0.325, 2.000[$

Table B.1: Binning in squared four-momentum transfers to the $\pi^+\pi^-$ system.

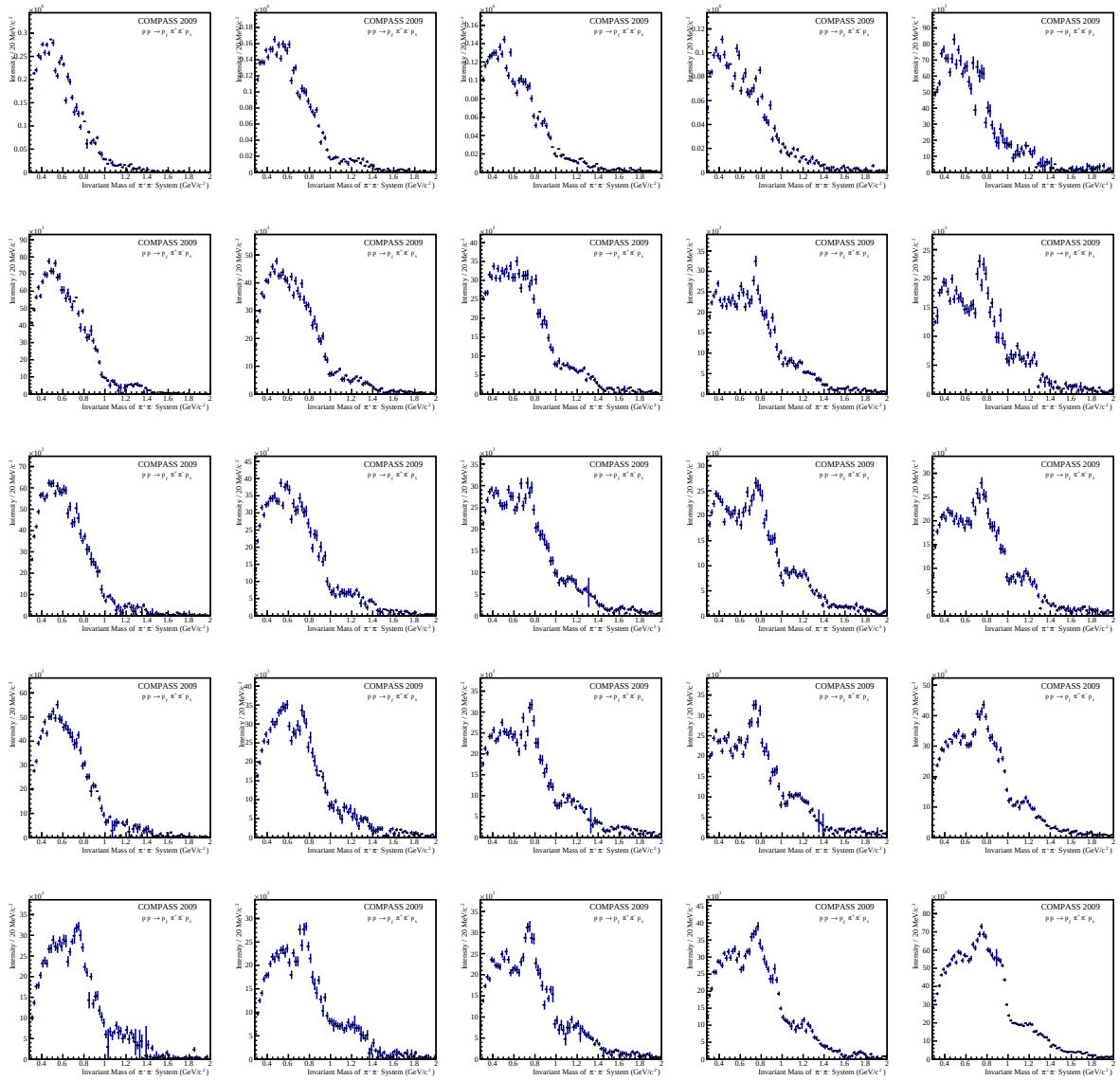

Figure B.1: Fitted S_0^--intensity of the $\pi^+\pi^-$ system in bins of t_1 (horizontal, increasing from left to right) and t_2 (vertical, increasing from top to bottom)

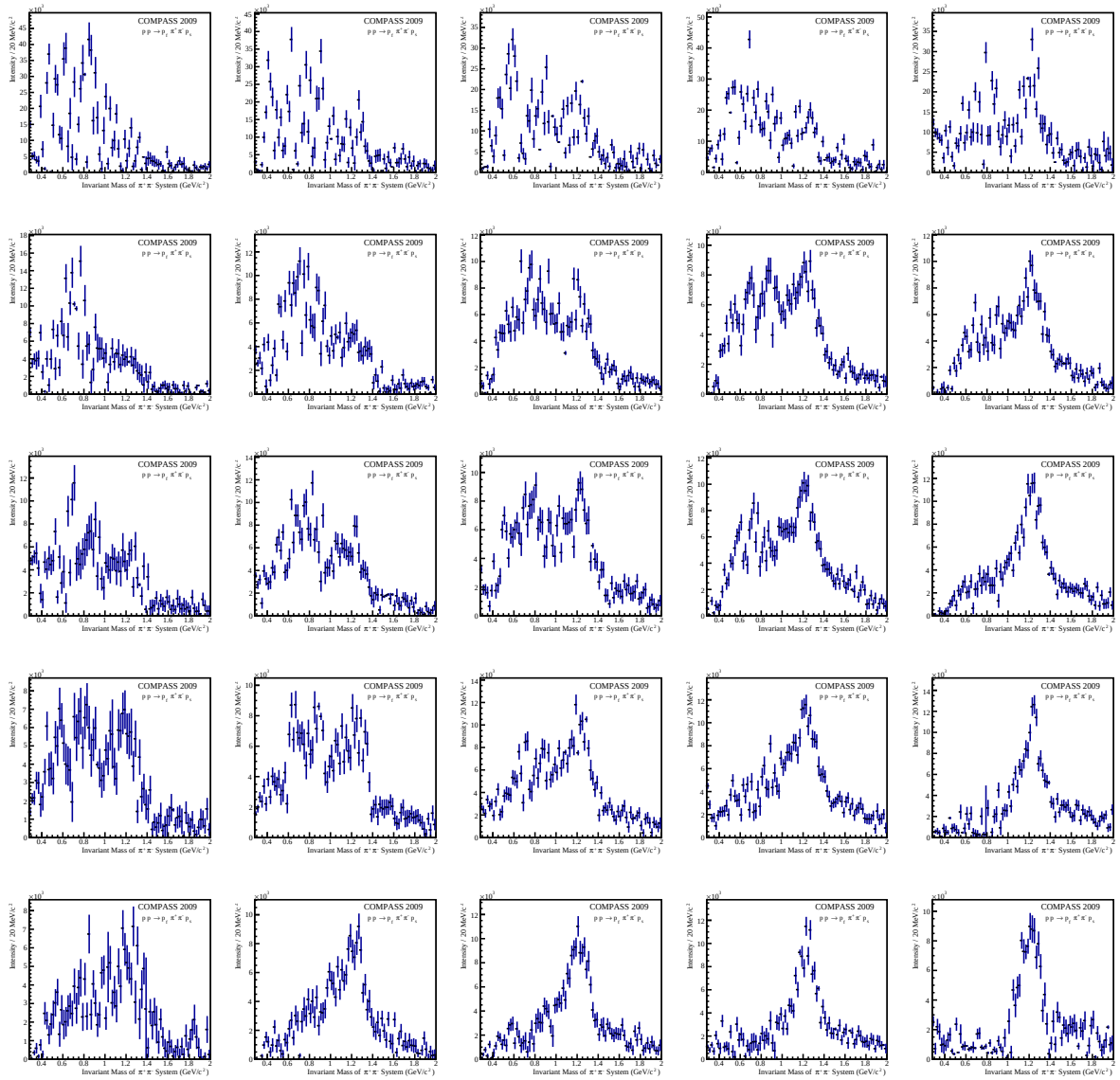

Figure B.2: Fitted D_0^--intensity of the $\pi^+\pi^-$ system in bins of t_1 (horizontal, increasing from left to right) and t_2 (vertical, increasing from top to bottom)

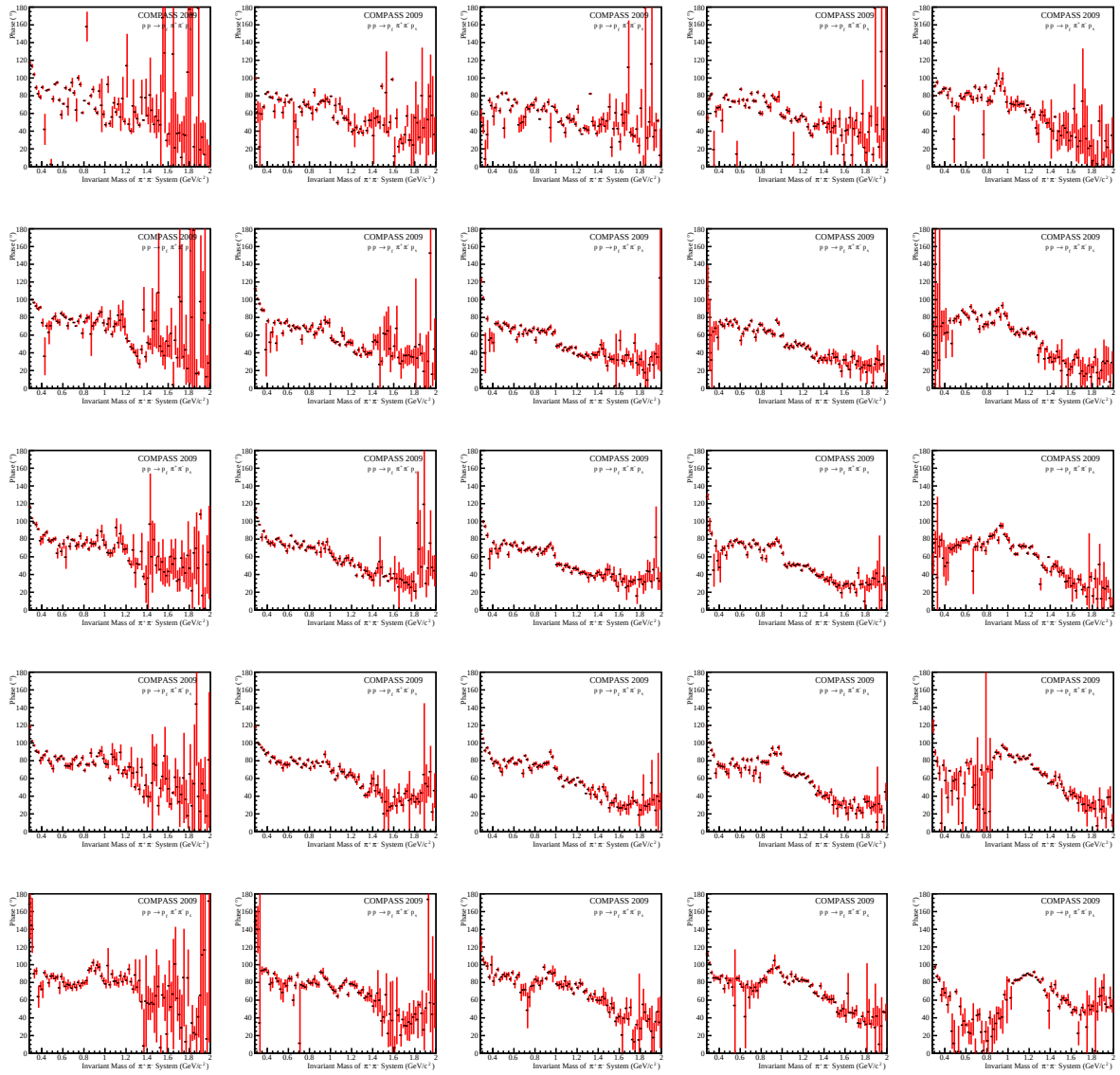

Figure B.3: Relative phase between S_0^-- and D_0^--amplitudes of the $\pi^+\pi^-$ system in bins of t_1 (horizontal, increasing from left to right) and t_2 (vertical, increasing from top to bottom)

B.2 Centrally Produced K^+K^- System

Bins in t_1 (GeV$^2/c^2$)	Bins in t_2 (GeV$^2/c^2$)
$[0.000, 0.105[$	$[0.000, 0.155[$
$[0.105, 0.265[$	$[0.155, 0.325[$
$[0.265, 2.000[$	$[0.325, 2.000[$

Table B.2: Binning in squared four-momentum transfers to the K^+K^- system.

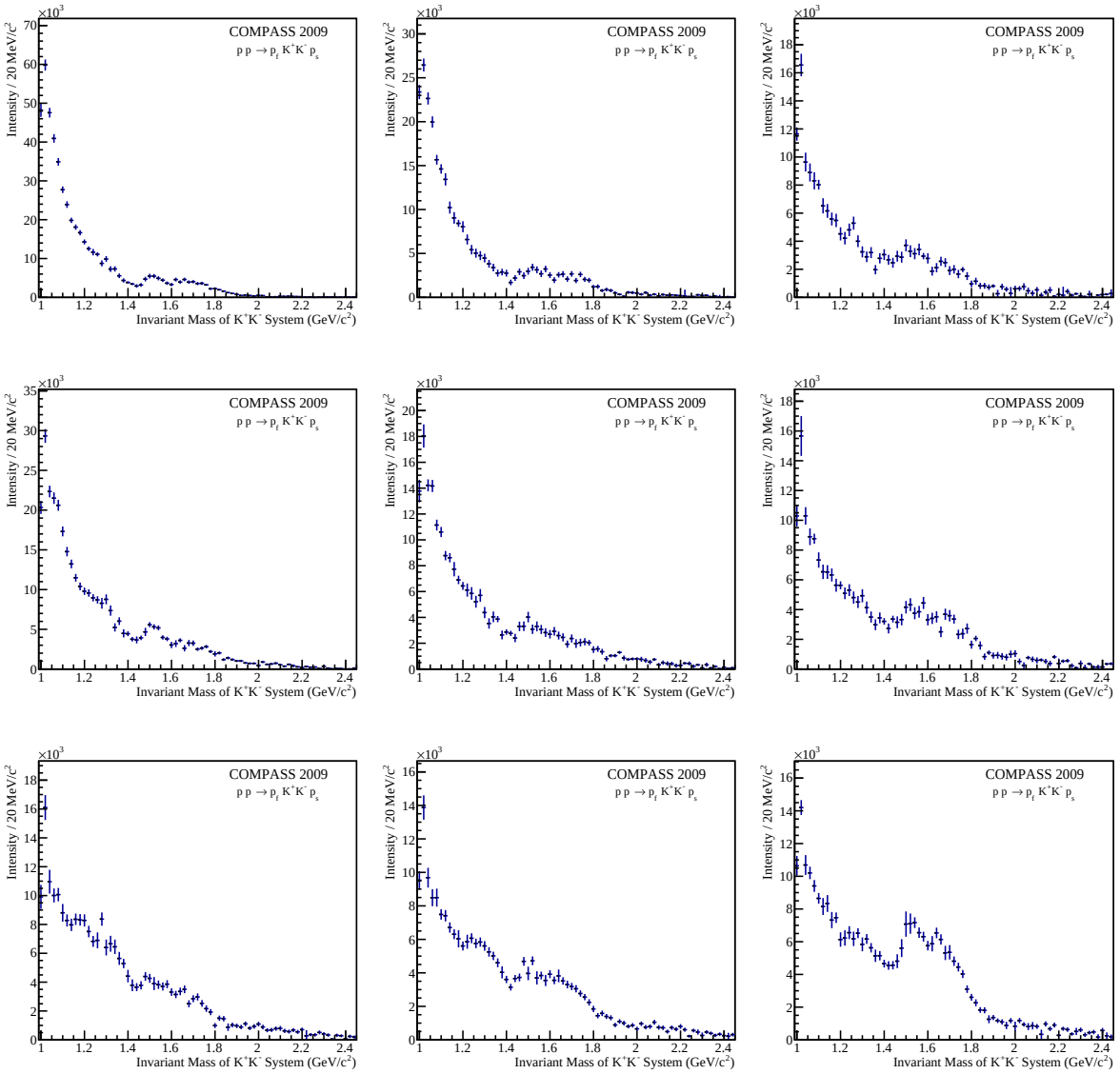

Figure B.4: Fitted S_0^--intensity of the K^+K^- system in bins of t_1 (horizontal, increasing from left to right) and t_2 (vertical, increasing from top to bottom)

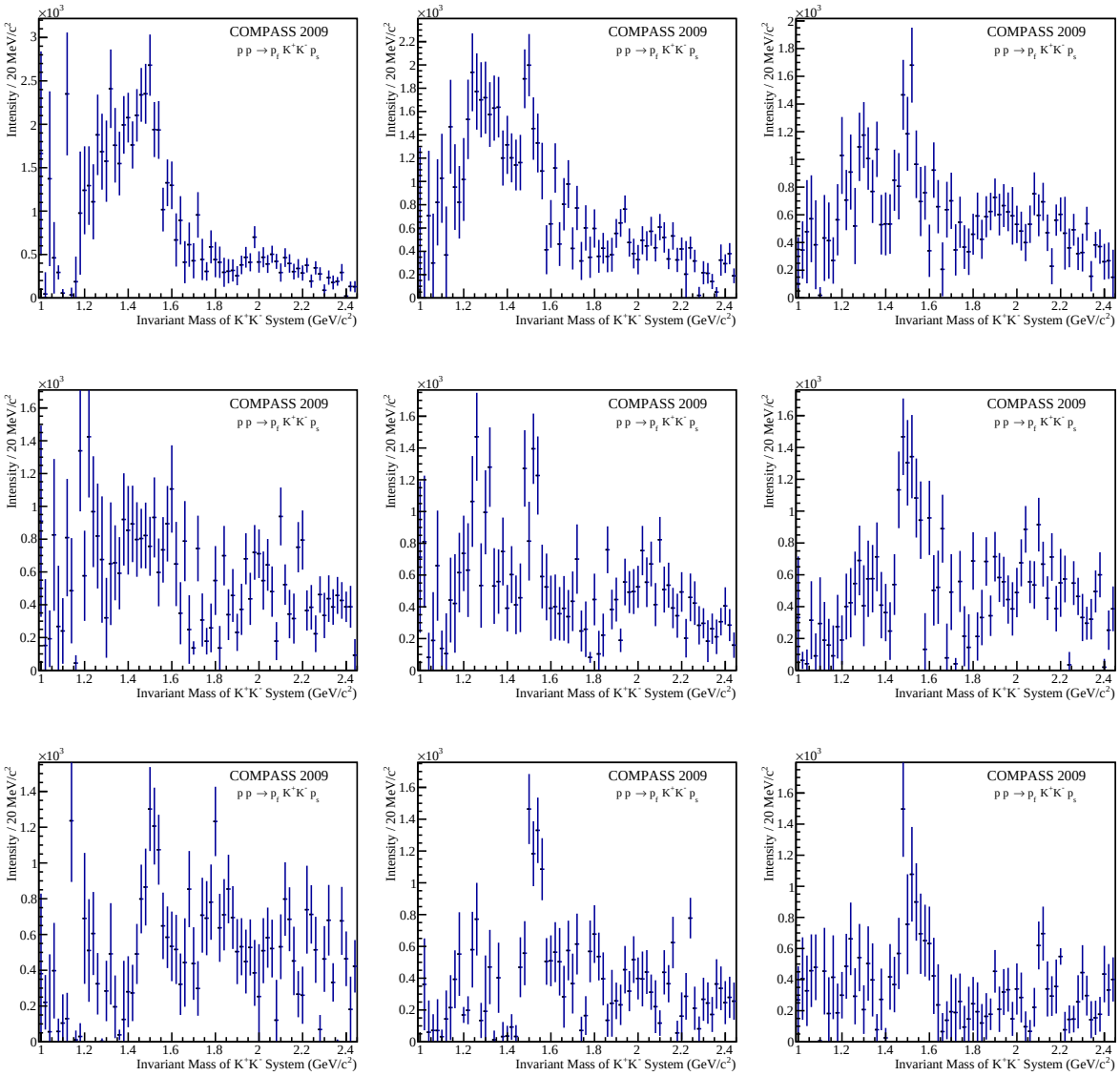

Figure B.5: Fitted D_0^--intensity of the K^+K^- system in bins of t_1 (horizontal, increasing from left to right) and t_2 (vertical, increasing from top to bottom)

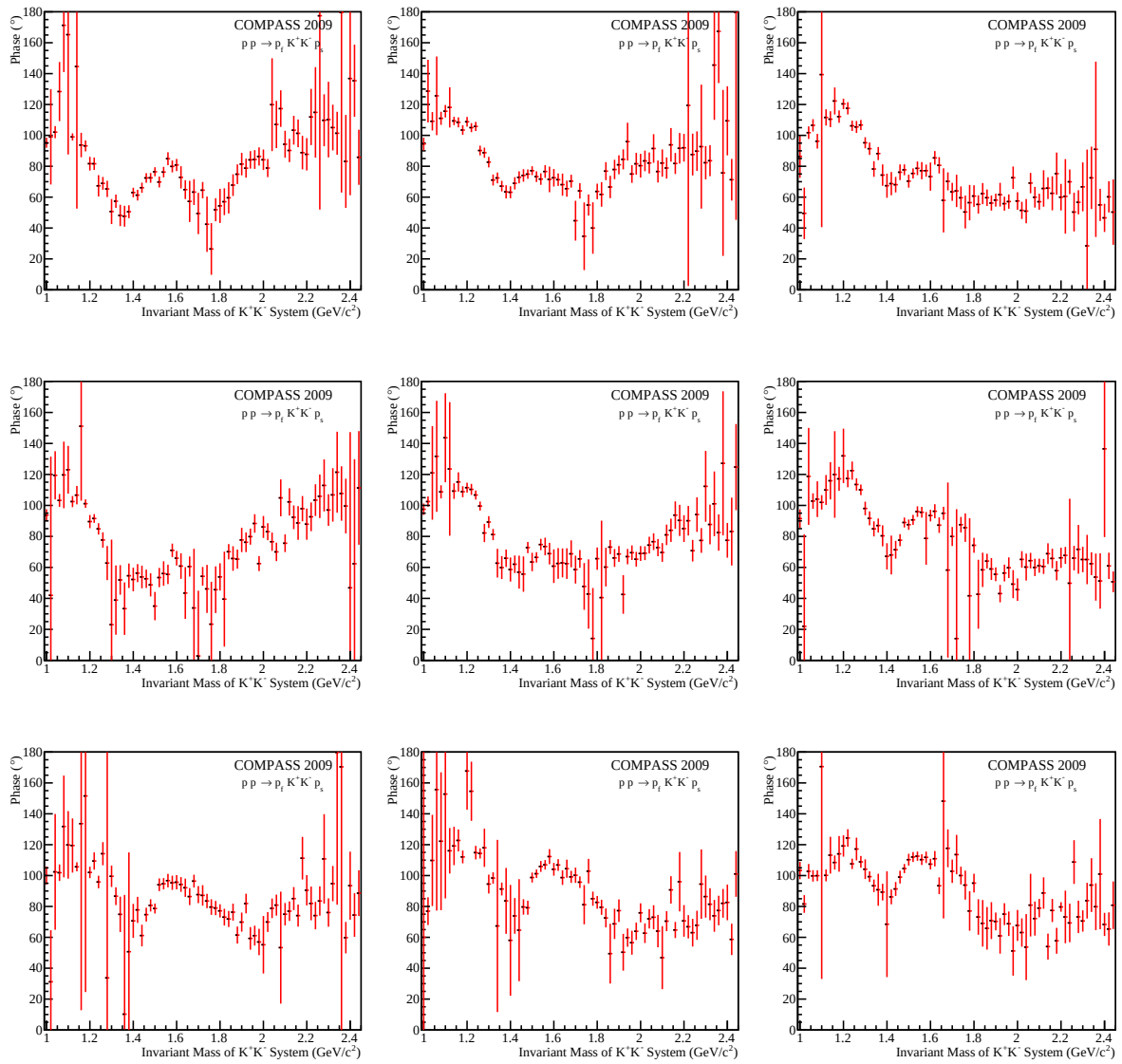

Figure B.6: Relative phase between S_0^-- and D_0^--amplitudes of the K^+K^- system in bins of t_1 (horizontal, increasing from left to right) and t_2 (vertical, increasing from top to bottom)

Acknowledgements

Above all, I would like to thank Prof. Stephan Paul for giving me the chance to work on this thesis. I am grateful for the confidence he had when he let me work at CERN for three years, beyond the reach of his direct supervision. He always trusted me to get involved where my skills were needed. After my return to Munich, I could pursue my ideas and interests with his support. In addition, I greatly appreciated the possibility to represent the collaboration on several occasions, sometimes even in very remote parts of the world.

I also would like to thank Gerhard Mallot for his part as my official supervisor during my three years at CERN. Even though I was acting under his responsibility, he let me make my own decisions concerning my involvement in the COMPASS experiment. Through this freedom, I was able to become acquainted with all parts of the experimental setup, including various detector types, readout electronics, data handling and analysis tools.

I am much obliged to Bernhard Ketzer, from whom I could learn a professional and scientific attitude in every way. He passionately guided the GEM detector group, but was always interested in the progress of the data analysis. More than once, his questions triggered the right thoughts.

I will be forever indebted to Boris Grube, to whom I could utter any question or problem regarding this analysis or the workaday life, and which he would friendly and wholeheartedly attend to. He proofread this entire document, which I am also very grateful for.

Sincerest thanks to my collaborator and friend Tobias Schlüter, who had the idea to adapt his own program for the analysis described in this thesis. It all started with an email saying "Also, ich bin mal gespannt, ob da irgendwas rauskommt". Even after his involvement in COMPASS ended, he was always helpful and enthusiastic. He provided useful comments on this thesis, too.

I want to express my gratitude to Prof. Suh-Urk Chung and Dima Ryabchikov, who shared their immense knowledge about hadron physics with us.

For an enjoyable atmosphere at CERN, I want to thank all colleagues in the COMPASS collaboration, but especially Johannes Bernhard, Karin Schönning, Nick DuFresne, Frank Nerling and Claude Marchand, who became real friends. The same is true for my fellow TUM colleagues Florian Haas, Sebastian Uhl, Jan Friedrich, Markus Krämer, Sebastian Neubert, Thiemo Nagel, Steffi Grabmüller, Christian Höppner, Daniel Greenwald, Sverre Dørheim, Florian Schneider, Charly Bicker and many more. Special thanks to my office mates Stefan Huber and Dima Levit, who facilitated this work with their calmness and helpfulness.

Thanks to the students Michael Tasior, Michael Leeb, Bernd Holzgartner, Jacopo Durandi, Christian Dreisbach and Thomas Schromm who contributed to the technical part of this work.

Last but not least, I sincerely thank Anja and my parents for their constant support.

Own Contribution

During my time as a doctoral student, I was involved in several different aspects of the COMPASS experiment. Detector development and maintenance, data taking and software reconstruction were integral parts of my occupation besides the data analysis presented in this work.

After working on the commissioning and performance evaluation of a PixelGEM detector prototype for my degree, I continued to work on the realisation of a PixelGEM tracking system for COMPASS with the group of B. Ketzer. Six detectors were manufactured in Munich, where my main responsibility was the calibration with radiation sources, but I also took part in all steps of the production. With the CERN doctoral student programme, I was based at CERN in Geneva, Switzerland, for three years. In the beginning, I was responsible for the installation and commissioning of the detectors in the experimental zone of COMPASS. During data taking, performance studies of the PixelGEM tracking system were done by diploma students [99, 97] with B. Ketzer's and my supervision.

In the two years of hadron beam time 2008 and 2009, I was responsible for the software alignment of all tracking detector planes in COMPASS. A fast feed-back about the data quality was as important as the precise calibration of the detector position and orientation in space. With the help of Sebastian Uhl, the pixel detector as a novel detector type providing two-dimensional information was included into the official alignment framework. As a result, the optimisation of both projections perpendicular to the beam was possible for the first time. In addition, I developed a system for the time-dependent alignment of the silicon microstrip detectors. It was gradually applied by me, or Diploma students under my supervision [63], to the reconstruction of the hadron beam data sets recorded in 2008, 2009 and 2012.

During the preparation for the 2010 beam time, I became responsible for the large-area tracking stations W4/5 in COMPASS as a part of the CERN group. Detector performance studies of these detectors were also started during this time, which were continued by the subsequent responsible Elena Rocco. During six beam times in total, I took shift and on-call duties as the expert on-site for all GEM and silicon micro-strip detectors or the W4/5. Especially the dismounting, maintenance, installation and the subsequent adjusting of the position of the large-size GEM detectors was necessary in the preparation for each run.

All steps of the analysis presented in this thesis were done by myself. The crude selection of the data was performed with Phast, the official COMPASS data analysis framework, in combination with detector specific-software provided by the COMPASS hadron analysis subgroup. My own framework was used for the final event selection, coordinate transformation and histogramming. The event selection was cross-checked by J. Bernhard and T. Weissrock. Parts of the selection scheme were later used for the published results on vector meson production with a proton beam at COMPASS [8].

The software framework used for the entire partial-wave analysis was T. Schlüter's idea. Originally specialised for $\eta^{(\prime)}\pi$ final states, it was generalised through my collaboration. All methods underwent extensive review during the analysis presented in this thesis. The treatment of the two-body ambiguities was implemented by me, as well as the weighted Monte-Carlo method to evaluate the fit results and the models for the mass-dependence of the $\pi\pi$ and $K\bar{K}$ systems.

I defended this analysis several times in front of the COMPASS collaboration. Including the analysis of the centrally produced four-pion system which I started together with J. Bernhard, five milestones of my work were released by the collaboration in order to be published as preliminary results. I presented these results and an overview of the work of the entire COMPASS hadron analysis subgroup at numerous national and international conferences and workshops. In total, I wrote eight proceedings about this analysis, the COMPASS hadron spectroscopy program and the PixelGEM central tracking system.